

**SEISMIC PERFORMANCE, ANALYSIS, AND DESIGN OF HYBRID
CONCRETE-MASONRY**

A Dissertation
Presented to
The Academic Faculty

by

Laura M. Redmond

In Partial Fulfillment
of the Requirements for the Degree
Doctorate of Philosophy in the
School of Civil and Environmental Engineering

Georgia Institute of Technology
May 2015

Copyright © by Laura M. Redmond 2015

**SEISMIC PERFORMANCE, ANALYSIS, AND DESIGN OF HYBRID
CONCRETE-MASONRY**

Approved by:

Dr. Reginald DesRoches, Advisor
School of Civil and Environmental Engineering
Georgia Institute of Technology

Dr. Lawrence Kahn
School of Civil and Environmental
Engineering
Georgia Institute of Technology

Dr. Russell Gentry
School of Architecture
Georgia Institute of Technology

Dr. Kimberly Kurtis
School of Civil and Environmental
Engineering
Georgia Institute of Technology

Dr. Barry Goodno
School of Civil and Environmental Engineering
Georgia Institute of Technology

Dr. Andreas Stavridis
Department of Civil, Structural, and
Environmental Engineering
University of Buffalo

Date Approved: November 19, 2014

ACKNOWLEDGEMENTS

I would like to thank my advisor, Dr. Reginald DesRoches, for placing me on the Caribbean Hazard Assessment Mitigation and Preparedness (CHAMP) Project, giving me the freedom to pursue this dissertation topic, and providing the resources to conduct the experiments. He has been a great mentor and advocate for me throughout my time as a PhD student at Georgia Tech. I would like to thank Dr. Lawrence Kahn, whose advice regarding the experimental program was instrumental to its success. I appreciated the time Dr. Andreas Stavridis took to teach me the finite element modeling method from which I began my analytical work. I am indebted to numerous undergraduate students who worked so diligently and weren't afraid to get messy in the lab: Andrew Johnson, Carlee Hayden, Derek Zittrauer, Parker Haren, Harrison Parker, Kasey Henneman, Coli Smith, Leonardo Rogliero, and George Chrysochos. I am also grateful for the donations from Simpson Strong Tie, United Forming and Jollay Masonry for the project. Finally, I would like to thank my husband, Matt. He continually supported me, helped put things into perspective when I took work too seriously, and lent me his muscles for a few late nights in the lab.

TABLE OF CONTENTS

ACKNOWLEDGEMENTS	iv
LIST OF TABLES	ix
LIST OF FIGURES	xii
NOMENCLATURE	xxv
SUMMARY	xxx
CHAPTER 1: INTRODUCTION	1
1.1 Motivation.....	1
1.2 Background.....	4
1.3 Overview.....	11
1.4 Document Outline.....	14
CHAPTER 2: LITERATURE REVIEW	16
2.1 Finite Element Modeling of Concrete and Masonry Structures	16
2.1.1 Cracking Models.....	17
2.1.1.1 Discrete Crack Models.....	17
2.1.1.2 Smearred Crack Models.....	18
2.1.1.3 Crack Band Models.....	23
2.1.1.4 Microplane Models	24
2.1.2 Material Models	26
2.1.2.1 Tensile Behavior	26
2.1.2.2 Compressive Behavior	28
2.1.2.3 Combined Failure Material Models	29
2.1.2.3.1 Mohr-Coulomb Yield Criterion	29
2.1.2.3.2 Drucker-Prager Yield Criterion	30
2.1.2.3.3 Wiliam-Warnke Yield Criterion	31
2.1.2.3.4 Modified Compression Field Theory.....	32
2.1.2.3.5 Disturbed Stress Model.....	33
2.2 Simplified Modeling of Unreinforced Masonry Infill	33
2.2.1 FEMA 356 and ASCE 41-06	34
2.2.2 TMS 402-11	35
2.2.3 Eurocode 8	35
2.3 Experimental Studies and Field Observations on the Seismic Performance of Concrete and Masonry Walls.....	36
2.3.1 Masonry Infill	37
2.3.1.1 System Description	37
2.3.1.2 Experimental Studies	37
2.3.1.3 Performance in Past Earthquakes.....	41
2.3.2 Confined Masonry	44
2.3.2.1 System Description	44

2.3.2.2 Experimental Studies	45
2.3.2.3 Performance in Past Earthquakes.....	46
2.3.4 Hybrid Masonry Systems.....	48
2.3.4.1 System Description.....	48
2.4 Chapter Summary	50
CHAPTER 3: CONSTITUTIVE FINITE ELEMENT MODEL AND VALIDATION STUDIES	51
3.1 Modeling Scheme	51
3.2 Element Formulation	53
3.3 Material Calibration.....	58
3.3.1 Concrete.....	58
3.3.2 Masonry Assembly	60
3.4 Model Validation	64
3.4.1 Pure Tension and Pure Compression.....	65
3.4.2 Flexure Column	68
3.4.3 Shear Column.....	70
3.4.4 Bare Frame.....	73
3.4.5 Masonry Walls.....	75
3.4.5.1 Test Set Up and Analytical Model.....	76
3.4.5.2 Material Calibration.....	78
3.4.5.3 Results.....	79
3.4.6 Three-Story, Three-Bay RC Frame with Unreinforced Masonry Infill.....	82
3.4.6.1 Specimen Description.....	82
3.4.6.2 Finite Element Model	84
3.4.6.3 Material Calibration.....	85
3.4.6.4 Results.....	87
3.5 Chapter Summary	91
CHAPTER 4: FINITE ELEMENT MODELING OF HYBRID CONCRETE-MASONRY	92
4.1 Modeling Scheme	93
4.2 Material Calibration for Partially Grouted Masonry	96
4.2.1 Compression Behavior of Grouted Masonry	98
4.2.2 Tensile Behavior of Grouted Masonry Units.....	99
4.2.3 Shear and Tensile Behavior of Grouted Bed Joints.....	100
4.2.3.1 The Concept of Shear Friction.....	101
4.2.3.2 Application of Shear Friction Principles to Grouted Bed Joints.....	103
4.2.4 Accounting for the Contribution of Reinforcement.....	111
4.3 Modeling Dowel Connections	119
4.3.1 Modeling Scheme for Dowel Reinforcement	120
4.3.2 Validation of Dowel Reinforcement Modeling Scheme.....	121
4.3.2.1 Finite Element Model and Material Calibration	121
4.3.2.2 Results.....	123
4.3.3 Studies on Variation of Effective Dowel Area	128
4.4 Initial Finite Element Models	129
4.4.1 Concrete Properties.....	130

4.4.2 UngROUTed Masonry Properties	131
4.4.3 Grouted Masonry Properties	133
4.5 Chapter Summary	137
CHAPTER 5: EXPERIMENTAL DESIGN	140
5.1 RC Frame	140
5.1.1 Design	140
5.1.2 Material Properties	143
5.1.3 Construction Details	144
5.2 Reinforced Masonry Infill and Connections to RC Frame	153
5.2.1 Design	153
5.2.2 Material Properties	157
5.2.3 Construction Details	160
5.3 Test Set Up	165
5.3.1 Overview	165
5.3.2 Loading Protocol	169
5.4 Instrumentation Plan	173
5.4.1 Strain Gages	173
5.4.2 Displacement Sensors	177
5.4.3 Load Cells	180
5.5 Chapter Summary	181
CHAPTER 6: EXPERIMENTAL AND ANALYTICAL RESULTS	183
6.1 Observations from Experiments and Analytical Models	184
6.1.1 General Behavior	185
6.1.1.1 Damage Sequence	185
6.1.1.2 Gravity Loads	208
6.1.1.3 Force-Displacement Behavior	209
6.1.2 Interface Behavior	213
6.1.2.1 Beam-Wall Interface	214
6.1.2.2 Column-Wall Interfaces	215
6.1.2.3 Foundation-Wall Interface	217
6.1.3 Masonry Wall Behavior	217
6.1.3.1 Shear Strains	218
6.1.3.2 Reinforcement	219
6.1.4 Column Behavior	222
6.1.4.1 Curvature and Shear Strain	222
6.1.4.2 Reinforcement	223
6.2 Influence of Masonry and Connections on the Behavior of the RC frame	225
6.3 Improvement of Finite Element Models Based on Experimental Observations	227
6.3.1 Masonry Modeling and Material Properties	228
6.3.2 Interface Properties	229
6.3.3 Dowel Reinforcement Modeling	229
6.3.4 Concrete Fracture Energy	230
6.4 Results of Revised Finite Element Models	231
6.4.1 Damage Sequence	231
6.4.2 Force-Displacement Behavior	238

6.4.3 Yielding of Reinforcement	240
6.5 Chapter Summary	241
CHAPTER 7: APPLICATIONS FOR ENGINEERING PRACTICE.....	245
7.1 Analytical Study on Design Changes	246
7.1.1 Alternative Connections of the Infill to the RC frame.....	246
7.1.2 Suggested Changes Based on Experimental Observations.....	248
7.2 Parametric Study on Infill Properties.....	249
7.2.1 Reinforcement Sizes and Spacing.....	250
7.2.1.1 Methodology	250
7.2.1.2 Results.....	251
7.2.2 Masonry Material Properties.....	253
7.2.2.1 Methodology	254
7.2.2.2 Results.....	255
7.2.3 Discussion	263
7.3 Simplified Models.....	264
7.3.1 Elastic Transformed Section Model.....	264
7.3.2 Cracked Section Model.....	266
7.3.3 Modification of TMS 402 Strut Model for Infills with Connections	267
7.4 Chapter Summary	271
CHAPTER 8: SUMMARY, CONCLUSIONS, AND RECCOMENDATIONS	274
8.1 Summary of Experimental Work	275
8.2 Conclusions from the Experimental work	275
8.3 Summary of Analytical Work.....	276
8.4 Conclusions from the Analytical Work	277
8.5 Recommendations.....	280
8.6 Significance	282
8.7 Future Work.....	284
APPENDIX A: NOTES FROM SITE VISITS TO THE CARIBBEAN	285
APPENDIX B: MATERIAL DATA	291
APPENDIX C: SUPPLEMENTAL DATA FOR FINITE ELEMENT MODELS	304
APPENDIX D: SUPPLEMENTAL DATA AND EXAMPLE CALCULATIONS FROM EXPERIMENTS	329
APPENDIX E: CALCULATIONS FOR SIMPLIFIED MODELS	339
APPENDIX F: PROPOSED MODIFICATION OF THE TMS 402 STRUT MODEL FOR PARTICIPATING INFILLS.....	344
REFERENCES	347

LIST OF TABLES

Table 1:Dimensions and applied stress for wall specimens.....	76
Table 2: Observed damage of the HCT specimen in the experiment (Ezzatfar et. al. 2014) and finite element model	89
Table 3: Test data on the bond strength of grouted prisms.....	104
Table 4: Summary of effect of vertical truss reinforcement elements on the shear capacity of grouted bed joints.....	114
Table 5: Observed damage of the MRM specimen in the experiment (Ezzatfar et.al. 2012) and finite element model	126
Table 6: Initial cracking in the finite element models	187
Table 7: Initial cracking patterns of revised finite element models.....	233
Table 8: Damage sequence for revised finite element models	235
Table 9: Influence of ungrouted prism strength on the damage sequence for Frame 1 (full connection)	256
Table 10: Influence of ungrouted prism strength on the damage sequence for Frame 2 (Connection only at the base).....	257
Table 11: Influence of fully grouting infill wall on the damage sequence for Frame 1 (full connection)	260
Table 12: Influence of fully grouting infill wall on the damage sequence for Frame 2 (connection only at the base).....	261
Table 13: Material and construction data gathered from site visits to the Caribbean....	285
Table 14: Notes regarding Caribbean design practices.....	289
Table 15: Concrete compressive strength.....	291
Table 16: Concrete tensile strength from split cylinders	292
Table 17: Concrete elastic modulus.....	292
Table 18: Rebar properties.....	293
Table 19: Masonry prism compressive strength.....	293
Table 20: Prism elastic modulus.....	297

Table 21: Concrete used for grouted cells-compressive strength	298
Table 22: Mortar compressive strength	299
Table 23: Tensile bond strength from bond wrench tests	300
Table 24: Mortar interface element parameters for study on the influence of masonry head joint bond strength on seismic performance of URM walls	304
Table 25: Head joint bond strength study: initial and final cracking patterns for URM wall MI1 4.92f t x 6.56ft (1.5m x 2m), 174psi (1.2 MPa).....	305
Table 26: Head joint bond strength study: initial and final cracking patterns for URM wall MI2 4.92f t x 6.56ft (1.5m x 2m), 58psi (0.4MPa).....	306
Table 27: Head joint bond strength study: initial and final cracking patterns for URM wall MI3 4.92ft x 9.84ft (1.5m x 3m), 174psi (1.2 MPa).....	307
Table 28: Head joint bond strength study: initial and final cracking patterns for URM wall MI4 4.92ft x 9.84ft (1.5m x 3m), 58psi (0.4MPa).....	308
Table 29: Material properties for FE models of column test (Nosho et. al. 1996)	313
Table 30: Material properties for FE models of column test (Lynn et. al. 1998)	314
Table 31: Model properties for cyclic test of RC frame (Teymur et al. 2012)	315
Table 32: Parameters for calibration to URM walls (Magenes and Calvi 1992).....	316
Table 33: Summary of material properties and model parameters for the 3-story 3-bay RC frame with HCT infills	318
Table 34: Summary of material properties and model parameters for the initial models of the hybrid concrete-masonry test frames.....	319
Table 35: Summary of material properties and model parameters for revised models of the hybrid concrete-masonry test frames.....	321
Table 36: Summary of material properties and model parameters for parametric study on masonry material properties-increased grout strength (x2).....	325
Table 37: Summary of material properties and model parameters for parametric study on masonry material properties-decreased grout strength ($\div 2$)	326
Table 38: Summary of material properties and model parameters for parametric study on masonry material properties-increased ungrouted prism strength (x2)	327
Table 39: Summary of material properties and model parameters for parametric study on masonry material properties-type N mortar	328

Table 40: Crack data Frame 1, column in tension during positive (push) cycles334
Table 41: Crack data Frame 2, column in tension during positive (push) cycles335
Table 42: Crack data Frame 2, column in compression during positive (push) cycles 336

LIST OF FIGURES

Figure 1: Construction of a duplex (left) and an apartment (right) in Belize	2
Figure 2: Soft story collapse observed during the 2010 Haiti Earthquake (DesRoches et. al. 2011)	2
Figure 3: Map of the Caribbean showing current building codes, the status of enforcement and the earthquake risk	4
Figure 4: Condominiums (left) and close up of CMU infill wall (right) under construction in Jamaica.....	6
Figure 5: Construction drawings for bracket connections of the infill wall and provision of an isolation gap.....	7
Figure 6: Typical Belizian construction, placing column rebar and the infill wall	8
Figure 7: Close up of vertical rebar spacing (left) and rebar connection to column (right)	8
Figure 8: Methods for connection of the reinforced CMU wall to the concrete frame	9
Figure 9: Examples of horizontal wall reinforcement	11
Figure 10: Diagram of cracked property axes.....	19
Figure 11: Illustration of stress-locking in smeared crack elements (Rots and Blaauwendraad 1989)	22
Figure 12: (a) illustration of microplane locations (b) mapping of strains from microplane to macroplane strain tensor (Ozbolt et. al. 2001).....	25
Figure 13: Characteristic nodes around a band of cracked elements (Bazant and Cedolin 1979)	28
Figure 14: Comparison of exponential and bilinear compression curves.....	29
Figure 15: Normalized Mohr-Coulomb yield surfaces with tensile cut-off (Chen, 2007)	30
Figure 16: Unreinforced masonry wall test showing interface cracking and bed joint sliding (Mosalam 2005)	37
Figure 17: Shear failure due to short-column effect from crushing of masonry at corners (Corte et. al. 2008)	38
Figure 18: Large diagonal crack formed during shake table test (Stavridis et. al. 2012) ..	38

Figure 19: Damage from the Wenchuan earthquake: shear failure and collapse of masonry (left) and collapse of a 5 story building (right) (Li et al. 2008)	42
Figure 20: Solid infill which helped prevent building collapse (Li et al. 2008).....	43
Figure 21: (a and b) Details of toothed connections to tie-columns and (c) shear connections (Meli et.al. 2011)	44
Figure 22: Comparison of behavior under seismic action of (a) an infill wall and (b) a confined masonry wall (Meli et al. 2011).....	45
Figure 23: Cyclic test of two bay confined masonry wall (Perez-Gavilan et al. 2009).....	46
Figure 24: (a) In-plane shear failure of first story (b) Out-of-plane failure of second story (Brzev et al. 2010).....	48
Figure 25: Buckling of rebar at foot of column (left) and shear failure of first story column (right) (Brzev et al. 2010)	48
Figure 26: Diagrams of hybrid masonry systems types I-III (left to right) (Hybrid Masonry Design 2009).....	50
Figure 27: Assembly of smeared crack elements, interface elements, and truss elements to model reinforced concrete (Stavridis and Shing 2010).....	52
Figure 28: Assembly of smeared crack and interface elements to model masonry (Stavridis and Shing 2010).....	53
Figure 29: Failure surface for masonry and concrete (Lotfi and Shing 1991).....	54
Figure 30: Equations governing compressive behavior (Lotfi and Shing 1991)	55
Figure 31: Stress vs. strain normal to the crack surface (Lotfi and Shing 1991).....	55
Figure 32: Local axis and complete yield surface diagram for interface element (Lotfi and Shing 1994).....	56
Figure 33: Effect of internal variables on interface element yield surface	57
Figure 34: Schematic of interface element tension test and resulting stress-displacement curve.....	59
Figure 35: Isotropic compression curve for concrete calibrated to orthotropic compression curve.....	60
Figure 36: Shear behavior of mortar interface elements calibrated to test data (Magenes and Calvi 1992).....	61
Figure 37: Results of pure tension tests with and without interface elements	65

Figure 38: Tensile stress vs. strain behavior with mesh refinement, with and without interface elements	66
Figure 39: Results of pure compression tests with and without interface elements	67
Figure 40: Compression stress vs. strain behavior with mesh refinement, with and without interface elements	67
Figure 41: Concrete compression behavior	69
Figure 42:Cracking and crushing of column after failure in the experiment (Nosho et al. 1996) and analytical models	69
Figure 43: Force displacement curves for the flexure column experiment (Nosho et. al. 1996) and analytical models	70
Figure 44: Concrete compression behavior	71
Figure 45: Force displacement curves for the shear column experiment (Lynn et. al. 1998) and analytical models	72
Figure 46:Cracking of column after failure in the experiment (Lynn et al. 1998) and analytical models	73
Figure 47:Test specimen and reinforcement details (Teymur et al. 2012)	74
Figure 48:Observed cracking in the experiment (Teymur et al. 2012) and analytical model. Failed interface elements have been colored red	74
Figure 49: Base shear vs. drift for the bare frame experiment (Teymur et. al. 2012) and analytical model	75
Figure 50: Geometry and test set up for the walls	77
Figure 51: Tracked reactions from experiment (Magenes and Calvi 1992) and analytical model for wall MI2	77
Figure 52: Assembly of smeared crack and interface elements to model masonry	78
Figure 53: Force-displacement behavior and cracking patterns of the finite element models compared to the test data (Magenes and Calvi 1992)	81
Figure 54: Test frame details (Ezzatfar et. al. 2012): (a) test frame dimensions (b) test set-up (c) hollow clay tile brick (d) column section detail (e) beam section detail (* denotes additional reinforcement and change in spacing in confined region, dimensions are in mm)	82
Figure 55: Ground motions (Ezzatfar et. al. 2012)	83

Figure 56: Finite element model showing the truss members used for load distribution .	85
Figure 57: Base shear vs. top story displacement of the experiment (Ezzatfar et. al. 2014) and the finite element model for the HCT specimen	90
Figure 58: Schematic for partially grouted reinforced masonry	94
Figure 59: Vertical cracking path compared to element modules	95
Figure 60: Connectivity of truss elements for different horizontal reinforcement types..	96
Figure 61: Preference for cracking along the grouted joints of reinforced cells (Minaie 2009). Crack 2 has been highlighted in red	97
Figure 62: Components of shear friction	101
Figure 63: Results from shear tests of concrete joints by Harries (2012).....	103
Figure 64: Hyperbolic yield surface of the interface element.....	104
Figure 65: Normalized bond strength of grouted masonry prisms as a function of grout strength (Test data from Table 3).....	105
Figure 66: Development of the equation for shear friction factor of grouted bed joints	106
Figure 67: Data for cohesion of grouted bed joints and proposed function.....	107
Figure 68: Comparison of data from shear tests of grouted and un-grouted assemblies to the data points calculated by the proposed calibration method. Weak grout-2080 psi (14.34 MPa), Strong grout-5350 psi (36.89 MPa).....	108
Figure 69: Example of linear fit to obtain the interface element failure surface. Weak grout-2080 psi (14.34 MPa), Strong grout-5350 psi (36.89 MPa).....	109
Figure 70: Triplet test model with reinforcement	112
Figure 71: Shear stress vs. lateral displacement for grouted bed joints with and without vertical reinforcement without pre-compression. Weak grout-2080 psi (14.34 MPa), Strong grout-5350 psi (36.89 MPa)	113
Figure 72: Shear stress vs. lateral displacement for grouted bed joints with and without vertical reinforcement at 100 psi (0.7 MPa) of pre-compression. Weak grout-2080 psi (14.34 MPa), Strong grout-5350 psi (36.89 MPa)	113
Figure 73: Shear stress vs. lateral displacement for grouted bed joints with and without vertical reinforcement at 200 psi (1.4 MPa) of pre-compression. Weak grout-2080 psi (14.34 MPa), Strong grout-5350 psi (36.89 MPa)	114

Figure 74: Additional steel elements to capture dowel action of reinforcement in grouted bed joints.....	117
Figure 75: Model results of shear tests without pre-compression on grouted bed joints with and without reinforcement. Weak grout-2080 psi (14.34 MPa), Strong grout-5350 psi (36.89 MPa).....	118
Figure 76: Model results of shear tests with 100 psi (0.7 MPa) pre-compression on grouted bed joints with and without reinforcement. Weak grout-2080 psi (14.34 MPa), Strong grout-5350 psi (36.89 MPa)	119
Figure 77: Model results of shear tests with 200 psi (1.38 MPa) pre-compression on grouted bed joints with and without reinforcement. Weak grout-2080 psi (14.34 MPa), Strong grout-5350 psi (36.89 MPa)	119
Figure 78: Modeling scheme for dowel reinforcement.....	121
Figure 79: Reinforcement details for the MRM infills (Ezzatfar et al. 2012)	122
Figure 80: Schematic of the modeling scheme for MRM specimen	123
Figure 81: Base shear vs. top story displacement of the experiment (Ezzatfar et. al. 2012) and the finite element model.....	127
Figure 82: Concrete properties.....	130
Figure 83: UngROUTED masonry properties	131
Figure 84: Set up and testing of masonry triplet.....	132
Figure 85: UngROUTED bed joint interface element shear stress vs. normal stress	133
Figure 86: Grouted masonry properties	134
Figure 87: Bond strength equation with results from bond wrench tests on grouted specimens.....	135
Figure 88: Cohesion equation with results from grouted triplet tests.....	135
Figure 89: Friction factor equation with results from grouted triplet tests	136
Figure 90: Grouted bed joint interface element shear stress vs. normal stress	136
Figure 91: Design of the RC frame.....	141
Figure 92: Proposed geometries and loading configurations.....	142
Figure 93: Variation in force-displacement behavior of the models	143

Figure 94: Position of centerline beam nodes during analysis for each model from 1.2% to 2.0% drift	143
Figure 95: Construction of the post-tensioned slab beginning with the end sections.....	145
Figure 96: Construction of the post-tensioned slab, continuing with the middle section	145
Figure 97: Installation of column forms and reinforcement	146
Figure 98: Lifting slab	146
Figure 99: Post-tensioning slab to strong floor.....	147
Figure 100: Construction of the beams	148
Figure 101: Conveyor used to pour the top half columns.....	148
Figure 102: Disassembly of the shoring and formwork (a) and close up of frame with dowel connections (b)	149
Figure 103: Reinforced concrete frame	150
Figure 104: Post-tensioned slab	151
Figure 105: Post-tensioned slab section detail.....	152
Figure 106: Masonry details for frame without dowel connections	155
Figure 107: Masonry details for frame with dowel connections	156
Figure 108: Construction of grout prisms made from weak concrete	158
Figure 109: Constructing and bagging the (a) ungrouted prisms and (b) grouted prisms	159
Figure 110: Masonry triplet (a) construction and (b) testing	159
Figure 111: Masonry-mortar bond specimen (a) construction and (b) testing	160
Figure 112: Volumetric batching of the mortar	160
Figure 113: Placement of first row of masonry showing (a) the dowel bars and (b) the mortar at the wall-column interface	161
Figure 114: Horizontal reinforcement (a) placed over grouted webs and (b) spliced with dowel bars from columns.....	162
Figure 115: Measuring slump for weak concrete used to fill reinforced cells.....	162

Figure 116: Reinforced cells filled with concrete (a) and consolidated with a rod (b) ..	163
Figure 117: Splicing vertical reinforcement	163
Figure 118: Dowel reinforcement extending down from the RC beam.....	164
Figure 119: At the top of the masonry wall, (a) face shell of the grouted cell was removed, (b) weak concrete was poured into the 3 courses below, and (c-d) the last course was dry packed	165
Figure 120: Test set up.....	166
Figure 121: Column loads applied through transfer beam.....	167
Figure 122: Gap between the top of the infill wall and the RC frame.....	167
Figure 123: Hydraulic used to apply lateral loads and stiffened plate on left side of loading cage	168
Figure 124: Stiffened plate on right side of loading cage.....	168
Figure 125: Set up for controller and data acquisition.....	169
Figure 126: Deformation controlled loading history (FEMA 461)	170
Figure 127: Force displacement results for finite element models with and without dowel connections	171
Figure 128: Loading protocol for testing of hybrid concrete-masonry frames.....	172
Figure 129: Strain gages in the masonry wall: (a) at base of vertical reinforcement, (b) at mid-height of vertical reinforcement, (c) at center of horizontal reinforcement, and (d) on dowel bars	174
Figure 130: Grinding vertical column reinforcement to apply strain gages	175
Figure 131: Strain gage layout.....	176
Figure 132: Column shear and flexural deformations measured by (a) string pots and (b) dial gages	178
Figure 133: Lateral displacement of the columns measured by (a) string potentiometers accounting for (b) slip at the foundation.....	178
Figure 134: String potentiometers measuring shear and flexural deformation of the masonry infill and dial gages to measure slip.....	179
Figure 135: Displacement sensor layout.....	180

Figure 136: Load cells to measure column load throughout the test	181
Figure 137: Damage in the experimental frames and finite element models at 0.05 inches (1.3 mm) of lateral displacement. Damage is predicted in the finite element models at this displacement, but no damage was observed in either frame during the experiment.	186
Figure 138: Cracking patterns in the experimental frames and finite element models at 0.15 inches (3.8 mm) lateral displacement. The cracks observed in the experiments are traced in black for the positive cycles and red for the negative cycles.....	189
Figure 139: Damage in the experimental frames and finite element models at 0.3 inches (7.6 mm) of lateral displacement. The cracks observed in the experiments are traced in black for the positive cycles and red for the negative cycles.....	191
Figure 140: Damage in the experiments and finite element models at 0.42 inches (10.7 mm) of lateral displacement. The cracks observed in the experiments are traced in black for the positive cycles and red for the negative cycles.	193
Figure 141: Close up of masonry wall in Frame 1 (full connection). The cracks in the experiments are traced in black for the positive cycles and red for the negative cycles.	194
Figure 142: Close up of the masonry wall in Frame 2 (connection only at the base). The cracks in the experiments are traced in black for the positive cycles and red for the negative cycles.....	195
Figure 143: Damage in the experimental frames and finite element models at 0.58 inches (14.7 mm) of lateral displacement. The cracks observed in the experiments are traced in black for the positive cycles and red for the negative cycles.....	196
Figure 144: Observing bend which formed in the tension column beginning above the second course of masonry	197
Figure 145: Close up of crushing of the masonry face shells near the diagonal cracks .	198
Figure 146: Damage in the experimental frames and the finite element models at 0.82 inches (20.8 mm) of displacement. The cracks observed in the experiments are traced in black for the positive cycles and red for the negative cycles.....	199
Figure 147: Damage in the experimental frames and the finite element models at 1.2 inches (30.5 mm) of lateral displacement. The cracks observed in the experiments are traced in black for the positive cycles and red for the negative cycles.....	201
Figure 148: Large portion of masonry face shell (a) fell out of plane and revealed (b) grouted cores with shear cracks in Frame 1	202
Figure 149: Large portion of masonry face shell (a) fell out of plane and revealed (b) grouted cores which had debonded from the vertical reinforcement in Frame 2	203

Figure 150: Top section of masonry wall of Frame 2 (connection only at the base) was in danger of out-of-plane collapse	204
Figure 151: Comparison of shear cracks in the columns of (a) Frame 2 (connection only at the base) and (b) Frame 1 (full connection).....	204
Figure 152: Damage in the experimental frames and the finite element models at 1.8 inches (45.7 mm) of lateral displacement. The cracks observed in the experiments are traced in black for the positive cycles and red for the negative cycles.....	206
Figure 153: Damage in the experimental frames and the finite element models at 2.4 inches (61.0 mm) of lateral displacement. The cracks in the experiments are traced in black for the positive cycles and red for the negative cycles.....	208
Figure 154: Force-displacement plot of the experimental and analytical Frame 1 (full connection).....	210
Figure 155: Force-displacement plot of the experimental and analytical Frame 2 (connection only at the base)	211
Figure 156: Comparison of the experimental force-displacement behavior for Frame 1 and Frame 2.....	211
Figure 157: Interface cracking for a) Frame 1 (full connection) and b) Frame 2 (connection only at the base).	214
Figure 158: Shear strain in the masonry infill vs. lateral displacement of experimental and analytical Frame 1 (full connection) and Frame 2 (connection only at the base).....	218
Figure 159: Yielding in the masonry reinforcement of the finite element model of Frame 1 (full connection).....	220
Figure 160: Yielding in the masonry reinforcement of the finite element model of Frame 2 (connection only at the base)	220
Figure 161: The horizontal reinforcement placed at the center of the unit caused the masonry web to split	221
Figure 162: Bending of horizontal reinforcement just past the termination of the dowel bar in the Frame 1	222
Figure 163: Strains in the flexural reinforcement of the columns in the finite element model of Frame 1 (full connection)	224
Figure 164: Strains in the flexural reinforcement of the columns in the finite model of Frame 2 (connection only at the base)	225
Figure 165: Strut mechanisms observed during the experiments	227

Figure 166: Force-displacement plot of the experimental and analytical Frame 1 (full connection).....	239
Figure 167: Force-displacement plot of the experimental and analytical Frame 2 (connection only at the base)	239
Figure 168: Strains in the reinforcement of the revised finite element model of Frame 1 (full connection).....	241
Figure 169: Strains in reinforcement of the revised finite element model of Frame 2 (connection only at the base)	241
Figure 170: Force vs. displacement of the finite element models with different connections of the infill to the bounding RC frame.....	247
Figure 171: Influence of increasing the length of the column close tie spacing zone from 20 inches (50.8 cm) to 40 inches (101.6 cm) on the force-displacement behavior of Frames 1 and 2	249
Figure 172: Percent change in peak strength for changes in masonry infill reinforcement detailing.....	252
Figure 173: Percent change in displacement at peak strength for changes in masonry infill reinforcement detailing	253
Figure 174: Percent change in peak strength for changes in masonry infill properties ..	262
Figure 175: Percent change in displacement at peak strength for changes in masonry infill properties.....	262
Figure 176: Schematic of the transformed section and shear flow for the test frames...	264
Figure 177: Schematic of cracked section model	266
Figure 178: Proposed strut overlaid on experimental frames at 0.82in (20.8 mm) lateral displacement	268
Figure 179: Resultant forces and forces for design from strut and tie models. Applied forces are labeled in blue, resultant forces are labeled in black and are shear forces, u.n.o.	270
Figure 180: Concrete mix design for RC frame.....	291
Figure 181: Test set up to determine the Elastic Modulus of concrete.....	292
Figure 182: Preparation of prisms.....	294
Figure 183: Prisms bagged for curing at ambient temperature.....	294

Figure 184: Gypsum plaster capping applied to all prisms.....	295
Figure 185: Test set up for compressive strength of masonry prisms	295
Figure 186: Failure patterns for ungrouted prisms: (a) face shell separation and crushing, (b) face shell separation and shear, and (c) cone and shear	296
Figure 187: Failure patterns for grouted prisms: (a) face shell separation, (b) face shell separation and shear, (c) shear and crushing	296
Figure 188: Test set up for Elastic Modulus of (a) ungrouted and (b) grouted prisms...	297
Figure 189: Grout cube mold as specified by ASTM 1019	298
Figure 190: Grout cube (a) testing and (b) failure	299
Figure 191: Mortar cube (a) testing and (b) failure	300
Figure 192: Bond wrench test set up.....	300
Figure 193: Failures of ungrouted bed joints	301
Figure 194: Failures of grouted bed joints	301
Figure 195: Shear stress vs. normal stress plot of ungrouted triplet tests.....	301
Figure 196: Shear stress vs. normal stress data from grouted triplet tests	302
Figure 197: Triplet test set up	302
Figure 198: Failure of ungrouted triplet.....	303
Figure 199: Failure of grouted triplet (a) while still on the testing platform and (b) removed from the testing machine.....	303
Figure 200: Influence of head joint bond strength on wall MI1 [4.92f t x 6.56ft (1.5m x 2m), 174psi (1.2 MPa) compression] *mortar properties from Table 24, Magenes and Calvi (1992)	309
Figure 201: Influence of head joint bond strength on wall MI1 [4.92f t x 6.56ft (1.5m x 2m), 174psi (1.2 MPa) compression] *mortar properties from Table 24, Mortar with 2x Bond Strength and Cohesion	309
Figure 202: Influence of head joint bond strength on wall MI2 [4.92f t x 6.56ft (1.5m x 2m), 58psi (0.4MPa) compression] *mortar properties from Table 24, Magenes and Calvi (1992).....	310

Figure 203: Influence of head joint bond strength on wall MI2 [4.92ft x 6.56ft (1.5m x 2m), 58psi (0.4MPa) compression] *mortar properties from Table 24, Mortar with 2x Bond Strength and Cohesion	310
Figure 204: Influence of head joint bond strength on wall MI3 [4.92ft x 9.84ft (1.5m x 3m), 174psi (1.2 MPa) compression] *mortar properties from Table 24, Magenes and Calvi (1992)	311
Figure 205: Influence of head joint bond strength on wall MI3 [4.92ft x 9.84ft (1.5m x 3m), 174psi (1.2 MPa) compression] *mortar properties from Table 24, Mortar with 2x Bond Strength and Cohesion	311
Figure 206: Influence of head joint bond strength on wall MI4 [4.92ft x 9.84ft (1.5m x 3m), 58psi (0.4MPa) compression] *mortar properties from Table 24, Magenes and Calvi (1992).....	312
Figure 207: Influence of head joint bond strength on wall MI4 [4.92ft x 9.84ft (1.5m x 3m), 58psi (0.4MPa) compression]*mortar properties from Table 24, Mortar with 2x Bond Strength and Cohesion	312
Figure 208: Concrete compressive stress vs. strain curve for finite element model of bare RC frame.....	315
Figure 209: Masonry material calibration for models of URM walls (Magenes and Calvi 1992)	316
Figure 210: Concrete, brick and mortar material calibrations for (a) tension and (b) compression in the model of the 3-story 3-bay RC frame with HCT infills.....	317
Figure 211: Compressive stress vs. strain for concrete, grouted masonry, and ungrouted masonry in the initial finite element models of the hybrid concrete-masonry test frames	320
Figure 212: Tensile stress vs. strain for concrete, grouted CMU, ungrouted CMU, mortar and bed joints in grouted cells* in the initial finite element models of the hybrid concrete-masonry test frames *bed joints in grouted cells are the grout and mortar interface	320
Figure 213: UngROUTED bed joint interface element failure surface in initial finite element models of hybrid concrete-masonry test frames and test data from bond wrench tests and triplet tests.....	321
Figure 214: Grouted bed joint interface element failure surface in initial finite element models of hybrid concrete-masonry test frames and test data from bond wrench tests and triplet tests.....	321
Figure 215: Compressive stress vs. strain for concrete, grouted masonry, and ungrouted masonry in the revised finite element models of the hybrid concrete-masonry test frames	322

Figure 216: Tensile stress vs. strain for concrete, ungrouted CMU, grout cores and mortar in the revised finite element models of the hybrid concrete-masonry test frames.....	323
Figure 217: UngROUTED bed joint interface element failure surface in revised finite element models of hybrid concrete-masonry test frames and test data from bond wrench tests and triplet tests	323
Figure 218: Portal frame	330
Figure 219: Frame 1 column loads	331
Figure 220: Frame 2 column loads	332
Figure 221: Shear deformation schematic	333
Figure 222: Gage length diagram	333
Figure 223: Processed and raw force-displacement data for Frame 1 with dowel connections on all edges of the masonry infill.....	337
Figure 224: Processed and raw force-displacement data for Frame 2 with dowel connections only at the base of the masonry infill.....	338
Figure 225: Shear flow through transformed section	339
Figure 226: Schematic of cracked section model	340
Figure 227: Transformed section of bounding column from test frames	341

NOMENCLATURE

A_{cv}	area of concrete in the shear plane of the joint
A_g	area of grout core
A_{gbj}	area of grouted bed joint
A_{gmu}	area of grouted masonry unit
A_{mort}	area of mortar
A_n	net area
A_{unit}	area of concrete masonry unit
A_v	area of shear reinforcement crossing the shear plane
a	width of equivalent diagonal strut
b	thickness
c	cohesion
d	distance
D_n	stiffness of interface element
D_t	shear stiffness of the interface element
E	stiffness
E_{bc}	elastic modulus of the bounding column
E_{fe}	elastic modulus of the frame material
E_g	grout stiffness
E_{gbj}	stiffness of grouted bed joint
E_m	elastic modulus of the masonry prism
E_{mort}	mortar stiffness

E_s	elastic modulus of reinforcement
E_{unit}	stiffness of the masonry unit
f	function of the yield surface
f_0	compressive strength at the point of initial softening
f'_c	uniaxial compressive strength
f_g	compressive strength of grout
f'_m	masonry compressive strength
f_{mort}	compressive strength of mortar
$f'_{t\,eff}$	effective tensile strength
$f'_{t\,g}$	tensile strength of grout
f'_t	tensile strength
f_{vn}	normal shear stress
f_y	yield stress of the reinforcement
$F(\sigma, s, r, \mu)$	yield function of the interface element
G	shear modulus
G_f^I	mode I fracture energy
G_f^{II}	mode II fracture energy
h_{inf}	height of the infill panel
h_{col}	height of the column
I_1	first invariant of the stress tensor
I_{bc}	moment of inertia of the bounding column in the bending plane
I_{col}	moment of inertia of the column in the plane of bending
I_{trans}	moment of inertia of the transformed section

J_2 second invariant of the deviatoric stress tensor
 k material parameter in Drucker-Prager yield surface
 k_1 and k_2 terms which represent the plastic work which governs strength degradation
 l_0 shear critical zone for seismically detailed columns
 N_v dead load
 P_1 Calibration point 1
 P_2 Calibration point 2
 P_3 Calibration point 3
 P_4 Calibration point 4
 P_5 Calibration point 5
 Q static moment of inertia
 $Q(\sigma, s, r, \mu)$ formulation for the plastic potential of the interface element
 r material parameter which is a function of the biaxial compressive strength
 r radius of the interface element failure surface
 r_0 initial value for radius of interface element failure surface
 r_{inf} diagonal length of the infill panel
 r_p ratio of residual compression
 $r_p f'_m$ residual compressive strength
 r_r residual value for radius of interface element failure surface
 r_t coefficient of residual tensile strength
 s tensile strength of interface element
 S sensitivity index
 s_0 initial tensile strength of interface element

s_{bj}	bed joint spacing
s_r	residual tensile strength of interface element
t	thickness
t_{inf}	thickness of the masonry infill
$t_{net\ inf}$	net thickness of the infill
V	applied shear force
$V_{cracking}$	cracking load
V_n	shear capacity of a joint
w_g	unit weight of grout
w_{inf}	width of the infill
X	modeling parameter being varied
X^b	baseline modeling parameter
X_1	distance 1
X_2	distance 2
Y	value of peak capacity of the model as a result of a change in the modeling parameter
Y^b	peak capacity of the baseline model
α	controls the rate of reduction of μ for the interface element
α_d	material parameter in Drucker-Prager yield surface
α_h	parameter which varies according to joint casting condition (Harries 2012)
α_1	shape factor
β	controls the rate of reduction of r
ε_1	strain at peak strength
ε_{1p}	plastic strain at peak strength

ε_2 strain at the transition point
 ε_{2p} the plastic strain at the transition point
 ε_{cr} strain at cracking
 η scales dilatency
 θ angle whose tangent is the infill height to length aspect ratio
 θ_{strut} the angle of the infill diagonal with respect to horizontal
 λ_1 coefficient used to determine equivalent width of infill strut
 λ_{strut} characteristic stiffness parameter for infill
 μ ..slope of the yield surface for the interface element, equivalent to shear friction factor
 μ_r residual slope of yield surface for interface element
 μ_0 initial slope of yield surface for interface element
 ν poissons ratio
 σ normal stress
 $\sigma_1, \sigma_2, \text{ and } \sigma_3$ principal stresses
 τ shear stress
 ϕ internal friction angle

SUMMARY

Caribbean-style hybrid concrete-masonry structures consist of a reinforced concrete frame with partially grouted and reinforced infill masonry walls. The infill walls are typically connected to the RC frame with cast-in-place dowel reinforcement along one or more edges of the wall. There is limited guidance in masonry codes to design these types of structures, and their seismic performance has not been characterized with experimental tests. In this work, an experimental program characterized the seismic behavior of hybrid concrete-masonry frames and showed they do not exhibit the typical strut mechanism observed in unreinforced masonry infill structures. In addition, a detailed finite element modeling scheme and calibration methodology was developed for modeling partially grouted masonry. This model includes a novel calibration method to account for the difference in the shear and tensile behavior of bed joints with grouted and ungrouted cells, and a method to account for the contribution of vertical reinforcement to the shear capacity of the bed joints with grouted cells. Finally, simplified models were proposed for use in engineering design. A modification of the TMS 402 strut model for hybrid concrete-masonry was suggested to incorporate the effects of the masonry infill and connections in large models.

CHAPTER 1

INTRODUCTION

1.1 Motivation

The 2010 Haiti earthquake (M7.0) was a strong reminder of the earthquake risk that exists in the Caribbean. The earthquake caused 28% of the buildings in Port-of-Prince to collapse, most of which were either unreinforced masonry (URM) or concrete frames with URM infill (DesRoches et. al. 2011). Moderate to Large earthquakes have also struck Puerto Rico (M6.4 2014), Cuba (M5.6 2010), the Virgin Islands (M6.1 2008), Martinique (M7.4 2008), Jamaica (M6.2 2007) and the Dominican Republic (M6.4 2003) (USGS 2014). Many buildings in the Caribbean are constructed informally and are very vulnerable in earthquakes. Even structures which are formally designed by engineers may not be adequate in seismic events because many countries in the Caribbean do not mandate designs be pursuant to a modern building code or require seismic forces be considered. Additional vulnerabilities stem from poor material quality, lack of oversight during construction and the inherent seismic risk associated with infill masonry buildings.

Within the Caribbean, the most common building design is a mid-rise (2-7 story) reinforced concrete (RC) moment frame infilled with hollow concrete masonry units (CMU) as shown in Figure 1. CMU is an excellent building material for the hurricane prone region since it is effective in resisting heavy wind and minimizing damage from debris. However, in seismic events, the lack of continuity between the URM infill and the concrete frame can cause the infill to fall out of plane and trigger soft-story collapses, which are a common cause of fatalities (See Figure 2).



Figure 1: Construction of a duplex (left) and an apartment (right) in Belize



Figure 2: Soft story collapse observed during the 2010 Haiti Earthquake (DesRoches et. al. 2011)

As a result of growing awareness of the seismic risk in the Caribbean, many engineers have begun to reinforce CMU infill walls and connect them to the RC frame to prevent them from falling out in a seismic event. This forms a hybrid concrete-masonry structure. Field observations and interviews with local engineers revealed that the CMU walls are reinforced both vertically and horizontally with various methods to connect the masonry wall to the RC frame. In Puerto Rico, Belize, Trinidad, and Jamaica, many practicing engineers expressed the challenge of reconciling their local construction methods with typical seismic design code procedures and the difficulty of incorporating

the effects of reinforced wall panels into their design models. The best currently available method for modeling reinforced infill panels is the use of finite elements, which is often too time consuming for use in commercial designs.

Because of this difficulty, a common practice is to assume that the infill wall does not interact with the bounding frame and to neglect the additional stiffness of the reinforced infill or any type of connection between the masonry and the RC frame. There is significant research in the literature on unreinforced masonry infill structures which show that the interaction between the infill and the bounding frame often causes significant damage to the columns under lateral cyclic loading (Guevara and García 2005; Kurt et. al. 2011; Mehrabi et. al. 1994). These interaction effects are likely to be amplified with reinforced infill. However, no experimental tests of this type of hybrid concrete-masonry structure have ever been conducted.

This dissertation assesses the seismic performance of infill frames designed according to current methodologies used in the Caribbean with full-scale cyclic tests. A detailed finite element modeling scheme for hybrid concrete-masonry is developed and used to model the experimental specimens. The finite element models are used to assess the seismic performance of other types of connections from the reinforced masonry to the RC frame which were not tested experimentally. A parametric study of the effect of various modifications to the infill properties and detailing is conducted using the finite element models. The results of these studies give insight to the best performing designs and the properties which most influence the seismic performance of the frames. In addition, the results of the experiments and the finite element models are compared to

several proposed simplified models which may be more practical to use for building design.

1.2 Background

Most of the other Caribbean islands have similar seismic and hurricane risk to Haiti, but the design practices, building codes and the degree of enforcement of building codes across the islands vary greatly (See Figure 3). Knowledge about the current design practices in Puerto Rico, Trinidad, Belize, and Jamaica was obtained from in-person interviews with design engineers and government officials, research institutions and building authorities with funding from the Speedwell Foundation as part of the Caribbean Hazard Assessment Mitigation and Preparedness (CHAMP) Project.

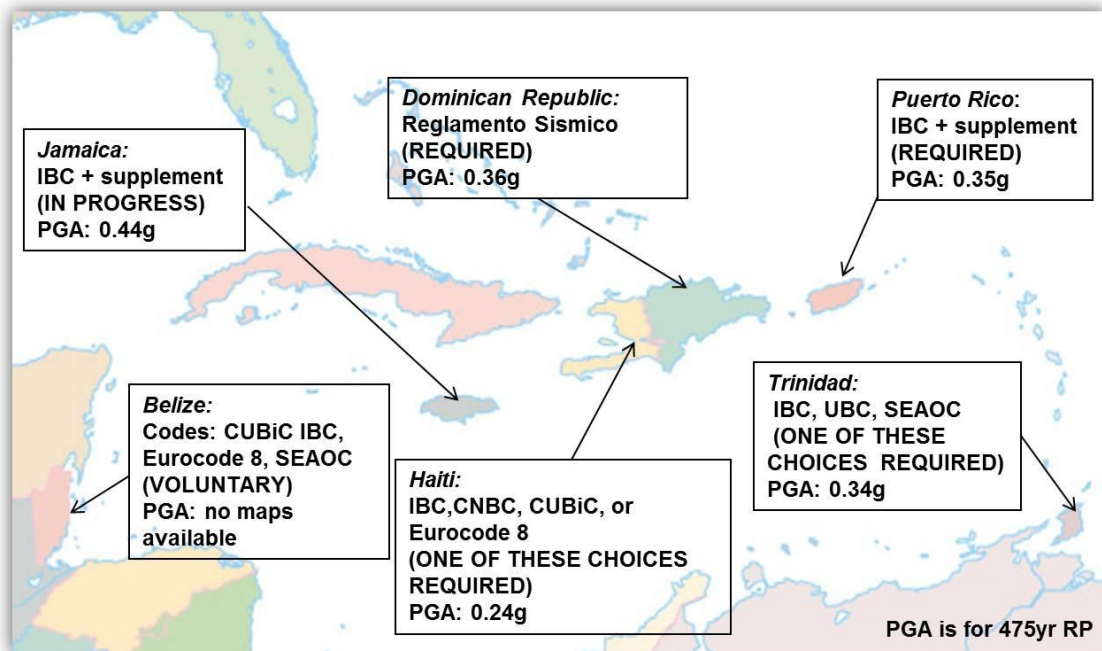


Figure 3: Map of the Caribbean showing current building codes, the status of enforcement and the earthquake risk

Interviewees expressed that since there is currently limited codified guidance for reinforced infill, their designs are often based on engineering judgment. Thus, reinforcement sizes and spacing within the CMU infills varied from firm to firm. However, in every firm where hybrid concrete-masonry was utilized, the CMU wall was reinforced both vertically and horizontally. There is also a lack of guidance regarding the connection of the infill wall to the concrete frame. The commentary of TMS 402 B.3.2 makes the following statement regarding connections of infill masonry, “while mechanical connectors, including the use of reinforcement are permitted, they must be detailed to preclude load transfer between the infill and the bounding frame.” Because of this ambiguity, there are many different methods used to connect the reinforced infill walls to the frame.

One method to connect the wall is to use cast-in place dowel reinforcement to connect the masonry to the RC frame either vertically (to the beams and foundation) or vertically and horizontally (to the columns, beams, and foundation) (See Figures 4, 8a, and 8b). The dowel reinforcing bars typically have a 90 degree hook and are embedded at least 4-6 inches into the concrete frame, although the depth of embedment varied among the firms interviewed (l_1 in Figures 8a and 8b). Additionally, there is no standard splice length for splicing the connection from the interior wall reinforcement to the dowel reinforcement. Some firms specified 30 bar diameters, while others specified 40 bar diameters or through one unit of masonry (l_2 in Figures 8a and 8b). Usually the CMU is placed directly up against the columns with mortar in the joint, and at the top of the wall bits of concrete may be shoved in with extra mortar to fill any void between the wall and the beam.



Figure 4: Condominiums (left) and close up of CMU infill wall (right) under construction in Jamaica

Another method to connect the walls to the RC frame is to try to isolate the reinforced CMU wall from the RC frame. L-brackets are sometimes used at the top of the masonry wall to connect it to the beam (See Figure 5). Dowel reinforcement is either cast-in-place, or drilled and epoxied into the foundation or beam below, then the reinforced CMU wall is constructed. An isolation gap is provided between the CMU wall and the columns and the beam above. This is sometimes filled with a flexible material. Like the first connection method, there does not seem to be a single methodology for determining the depth the dowel bars extend into the frame (l_1 in Figure 8c) or the splice length of the connection to the vertical reinforcement within the CMU wall (l_2 in Figure 8c).

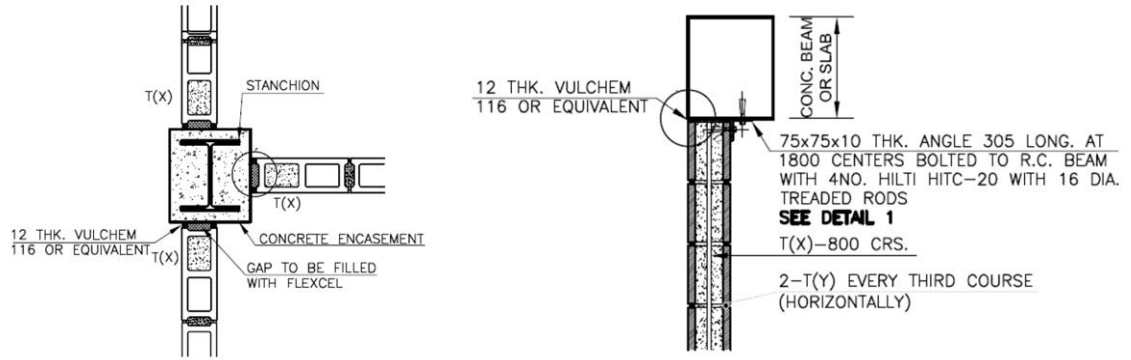


Figure 5: Construction drawings for bracket connections of the infill wall and provision of an isolation gap

The third method to connect the CMU walls is actually to reverse the construction order and finish the masonry wall before pouring the RC frame. The reinforcement from the CMU wall is run through the space where the columns and beams will be poured (See Figure 6, 7 and 8d). However, this practice was only observed in Belize. Like the reinforced infill structures, the wall is not designed to act integrally with the frame. In this type of construction, the RC frame is often designed for the majority of the gravity and lateral forces, and then the masonry walls are designed for the remainder of the loads.



Figure 6: Typical Belizian construction, placing column rebar and the infill wall



Figure 7: Close up of vertical rebar spacing (left) and rebar connection to column (right)

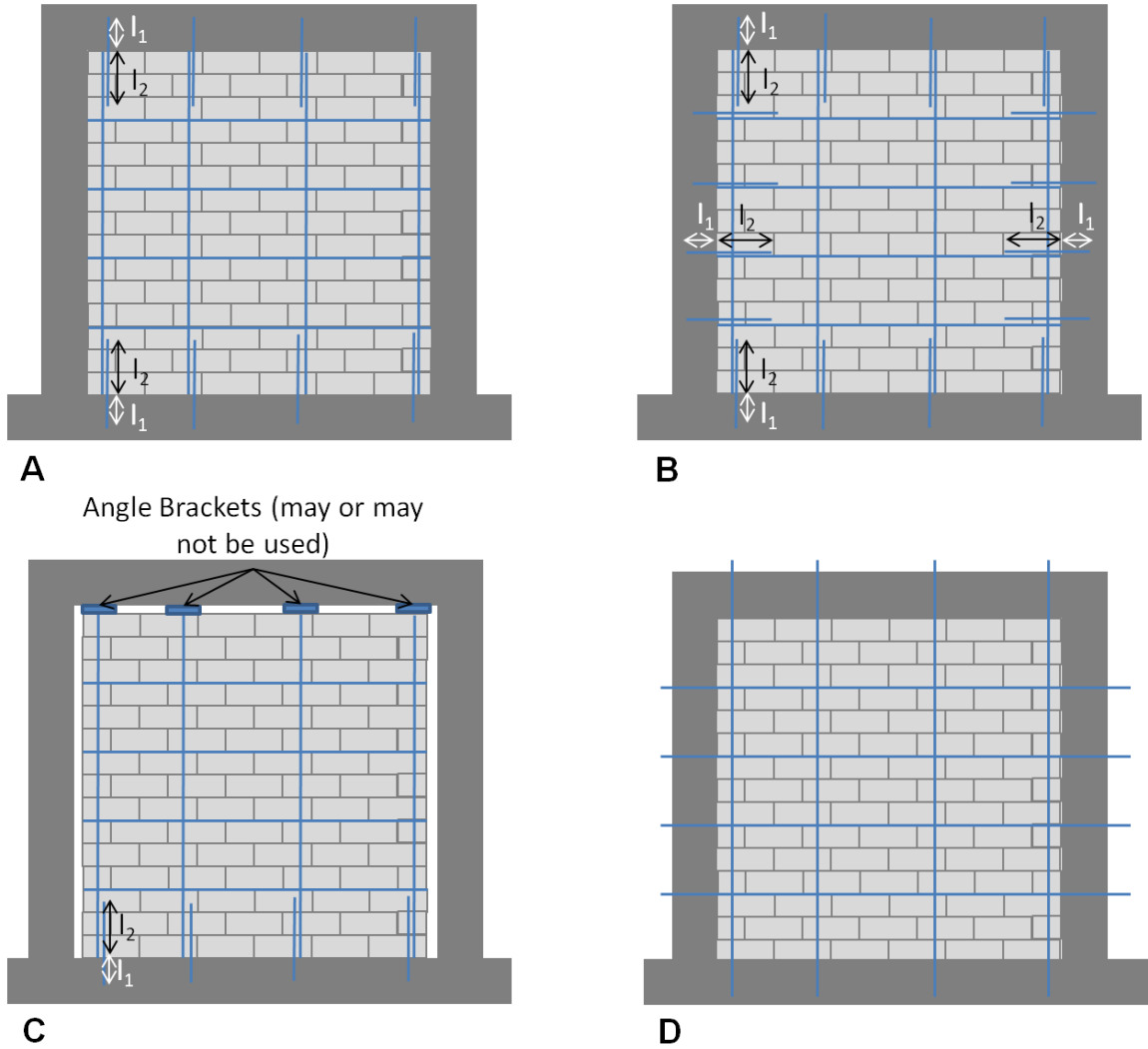


Figure 8: Methods for connection of the reinforced CMU wall to the concrete frame

The strengths of CMU and concrete in the Caribbean are much lower than the standard strengths achieved by CMU block and concrete manufactured in the United States. The aggregates are predominately limestone or a mix of limestone and quartz, which are weaker than the aggregate in the U.S. Additionally, the concrete mix designs are very lean; typically four sacks of cement per batch. The strength variation for concrete is between 3000 psi (20.7 MPa) and 4500 psi (31 MPa), and CMU unit strengths are between 2000 psi (13.8 MPa) and 3500 psi (24.1 MPa). CMU block in Jamaica is an

exception, which is very weak, typically 1000-1200 psi (6.9-8.3 MPa). It is typical practice to fill the cells in the CMU which have reinforcement, but grout is not typically used. Instead, the cells are filled with weak concrete 2000-2500 psi (13.8-17.2 MPa) having the same maximum size aggregate (MSA) as the column concrete (0.75 inches, 19.1 mm, on average). Masonry mortar in the Caribbean is specified as a 1:3 Portland cement: sand mix by every company interviewed. This is likely to be a very strong because of the high cement ratio, but may be brittle in comparison to a U.S. mortar because it lacks lime. Finally, because there is no production of ladder reinforcement in the Caribbean, it is typical practice to use one or two small reinforcing bars (#3 typical) as horizontal bed joint reinforcement, although one firm mentioned using mesh reinforcement within the bed joint. The reinforcement is typically placed closer to the center of the CMU block so that it is completely surrounded by the weak concrete (used as grout). However, this is not a continuous bond as only the cells which contain vertical reinforcement are filled (See Figure 9). This is also likely to slightly change the behavior of the masonry, since the bed joint thickness must be increased to accommodate the horizontal reinforcement. Experimental tests conducted as part of this dissertation give insight to the effects of these detailing methods which are not used in the United States.

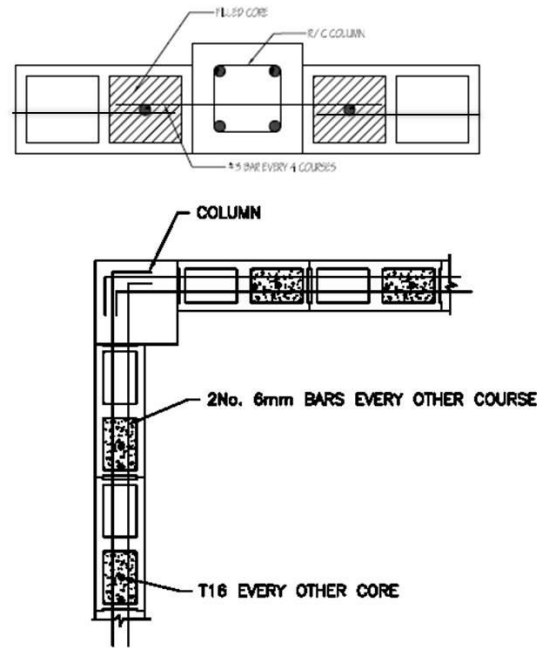


Figure 9: Examples of horizontal wall reinforcement

1.3 Overview

Detailed finite element models of hybrid concrete-masonry structures will allow for greater understanding of the seismic behavior of these structures through analytical studies. Finite element models are also the logical place to begin to develop simple models for design purposes. An extensive literature review was conducted on existing methods for modeling concrete and masonry, and led to the selection of the constitutive model from which the modeling scheme for hybrid concrete-masonry was developed. Review of experimental studies and field observations on the seismic performance of concrete and masonry walls was also conducted to gain insight into the possible failure mechanisms of hybrid concrete-masonry detailed according to practices in the Caribbean.

After compiling information from the available literature, finite element models for hybrid concrete-masonry were developed. First, extensive validation of the constitutive model was performed, beginning with element-level tests and progressing through component-level tests and finally validating the existing model with results from a 3-story 3-bay infill specimen tested dynamically. Then, since the validation established confidence in the constitutive model, it was adapted to include a modeling scheme for hybrid concrete-masonry. As part of this modeling scheme, a new methodology for calibrating the interface elements representing bed joints with grouted cells was developed based on the concept of shear friction in concrete. Shear and tensile tests on grouted bed masonry samples validated the proposed method to calculate the properties of grouted bed joints as a function of the compressive strength of the grout and mortar. Validation of the interface properties and the modeling of the connections between the reinforced masonry infill and the RC frame was postponed until after the data from the experimental program was obtained.

The initial finite element models calibrated with material test data were used to aid in the design of the experimental program. Models helped determine loading conditions for the frames and were used in tandem with hand calculations to bound the capacity of the structure, since there are no design tools to estimate the true capacity of hybrid concrete-masonry frames. The two test specimens were single-story, single-bay test frames with an additional half story to simulate the stiffness of the masonry wall above. The specimens were designed to be as similar to current design practices in the Caribbean. Because design and construction practices vary so greatly in the Caribbean, it was not practical to test every variation of concrete frame and connection of the CMU

infill to the RC frame. Two variations of connections of the CMU infill were assessed: Frame 1 had cast-in-place dowel reinforcement connecting all edges of the masonry infill to the RC frame, and Frame 2 had cast-in-place dowel reinforcement only at the base of the infill. The frames were tested using a displacement-controlled cyclic loading protocol which closely followed FEMA 461.

Cyclic tests of the two specimens were compared to one another to determine the effect of the different connections from the infill to the RC frame. Global force-displacement plots from the tests were compared to the expected behavior of a bare frame to determine the influence the reinforced masonry wall had on the frame behavior. Additional data was obtained regarding the slip at the interface between the masonry and the RC frame; the strains in the reinforcement of the columns and the infill wall; and the shear and flexural deformations at the top and bottom of the columns and the infill wall. This data was used to assess rather the infill participated as a structural element, even though it was designed as a non-structural element.

The results of the finite element models were compared to the data obtained during the experiments. Although the initial models provided very good predictions of the force-displacement behavior and generally captured the failure patterns of the frames, a revised model was created in order to better capture the effect of the dowel connections and fully calibrate the interface properties in the model.

The validated finite element models were then used for analytical studies. First, the finite element model was used to explore several changes to the design of hybrid concrete-masonry structures. This includes different types of connections which were observed in the Caribbean, but not tested experimentally and proposed improvements

based on observations during the experiments. Second, a parametric study was conducted to characterize the influence of the infill properties on the seismic performance of hybrid concrete-masonry frames. The study includes the influence of masonry material properties and the influence of reinforcement detailing.

Finally, several simplified models were developed and compared to the results of the finite element models and the experimental data. An elastic transformed section model was proposed to predict the cracking load and a cracked section model was proposed to predict the ultimate shear capacity of the experimental frames. A modification of the typical TMS 402 strut model was also suggested to account for the effect of the dowel connections on the geometry and behavior of the masonry diagonal strut in hybrid concrete-masonry structures.

Although major policy changes to address limited building regulation in the Caribbean and minimal guidance for hybrid concrete-masonry is unlikely to occur in the near future, many local engineers choose to engage in best practice design. These practices transfer down to contractors who mimic the typical construction details seen in large projects, for structures that are constructed informally. By providing data on the seismic performance of hybrid concrete-masonry, suggesting detailing methods which perform best in earthquakes, and proposing simplified models, this work will help engineers to expand and improve upon their existing design tools and methodologies.

1.4 Document Outline

Chapter 2 is a collection of the literature reviewed in preparation for this work. It contains a literature review of modeling methods for concrete and masonry structures, and a review of experimental studies and field observations on the seismic performance

of concrete and masonry walls. Chapter 3 is titled, Constitutive Finite Element Model and Validation Studies. It contains a detailed description of the constitutive model, followed by extensive model validation. Chapter 4 describes the finite element modeling method and newly proposed calibration methodology for hybrid concrete-masonry. It also presents the initial finite element models used to predict the behavior of the experimental specimens and aid in the experimental design. Chapter 5 covers the design of the experimental program including: the specimen design, the material properties, the construction details, the experimental set up, the loading protocol and the instrumentation plan. Chapter 6, titled "Experimental and Analytical Results," contains all the results of the experimental program and the initial finite element models. It also contains the rationale behind the changes that were made to the revised finite element models and compares these results with the experimental data. Chapter 7 describes the analytical studies conducted using the finite element models to determine the effect of design changes on the seismic performance of the hybrid concrete-masonry frames. It also contains the simplified models proposed to calculate the cracking load and peak capacity of the walls and a modification of the TMS 402 strut model for infill walls with connections to the RC frame. Chapter 8 contains the summary, conclusions and recommendations which resulted from this work.

CHAPTER 2

LITERATURE REVIEW

The development of a finite element modeling scheme for hybrid concrete-masonry structures is the starting point of this dissertation. The combined smeared crack and interface element constitutive model from which this scheme is developed has distinct advantages over other modeling methods which exist in the literature. In order to understand these advantages, an extensive review of existing finite element modeling schemes is presented. Finite element models are necessary for hybrid concrete-masonry because the existing simplified models for masonry infill structures are limited to unreinforced masonry infill without connections to the reinforced concrete frame. The current simplified modeling methods for unreinforced masonry infill structures are summarized.

Tests of hybrid concrete-masonry structures analogous to those in the Caribbean cannot be found in the literature. This necessitates testing of hybrid concrete-masonry walls to validate the finite element models and gain an understanding of the seismic performance of these structures. Experiments from the literature for other systems which are constructed of concrete and masonry are reviewed in order to establish a baseline for interpreting the failure mechanisms observed during cyclic tests of hybrid concrete-masonry walls.

2.1 Finite Element Modeling of Concrete and Masonry Structures

Modeling masonry or concrete in finite element is very similar because of their analogous material properties. Masonry and concrete both exhibit strain hardening and subsequent softening after yielding in compression, and are brittle in tension. The

primary difference between modeling masonry and modeling concrete is that masonry has mortar joints which are much weaker than the masonry bricks. This literature review does not elaborate on the different methods to model the mortar joints, but instead focuses on finite element (FE) models used to represent masonry bricks and concrete.

The most significant difference between existing finite element modeling schemes for concrete and masonry units is the method used for modeling cracking. The predominate methods are: discrete crack models, smeared crack models, crack band models and microplane models. For each of these methods, finite element material behavior must be defined to characterize the initial yield surface. Additionally, a plasticity model must be selected to determine the transformation of the yield surface after yielding of the element. Finally, a plastic potential should be defined, from which to derive the plastic strain increment beyond yielding. The plasticity model and plastic potential predominately affect the solution in the post-peak regime and have not received much attention in the literature. Thus the focus of this review will be on the cracking models and the material models which govern the initial yield surface.

2.1.1 Cracking Models

2.1.1.1 Discrete Crack Models

Discrete crack modeling is the earliest modeling scheme which was proposed to model concrete fracture. In a discrete formulation, cracks occur as displacement discontinuities at the element boundaries (Ngo and Scordelis 1967; Nilson 1968). The advantage of discrete formulations is that the stresses at the free surface on either side of the crack come down to zero, just as it does in the physical cracking process. The original formulations were very limited in their capability as cracks could only occur along

element boundaries. Some improvement to capturing cracking patterns was observed using Rigid Body Spring Networks, developed by Kawai (1978) discretely model cracking in spring elements which connect elastic elements of arbitrary shape. Because the mesh is not constrained to a quadrilateral or tetrahedral element, Bolander (1998) was able to successfully capture realistic cracking patterns for double edged notched concrete panels loaded in shear. However, because the elements are rigid, a rigid body spring network model cannot capture stress distribution.

Later formulations of discrete crack finite element models were proposed to allow discrete cracking inside an element (Goodman et. al. 1968; Ngo and Scordelis 1967) , but these methods also require re-meshing at every time step and thus were computationally expensive. Later models resolved the re-meshing issue by incorporating an interface element with initially coincident corner nodes to model this displacement (Lotfi and Shing 1994; Stavridis 2009). In this way, the crack was modeled discretely at predetermined locations where cracks were likely to occur, but did not permit a physical separation to form between the elements on either side of the interface. These interface elements were given large values of stiffness prior to violating the cracking criterion (stress condition), and then the interface elements were given a different set of properties to represent the cracked state.

2.1.1.2 Smearred Crack Models

Smearred crack models are commonly used in commercial software to represent the fracture of concrete or masonry because it has significantly less computational expense than a discrete formulation. In a smearred crack model, cracking is represented by

a change in the stiffness matrix from un-cracked isotropic properties to orthotropic ones representing the cracked state as shown in Figure 10.

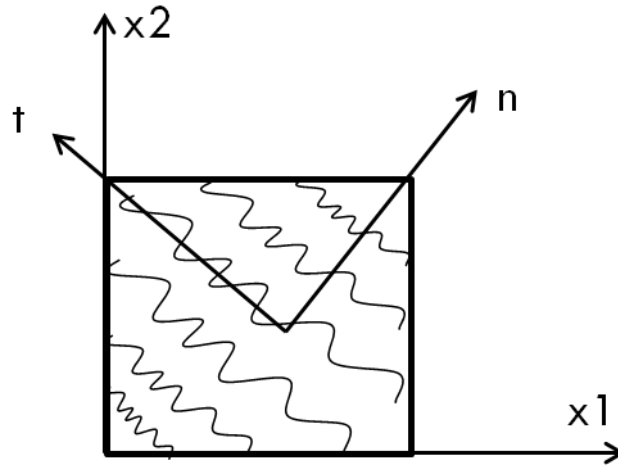


Figure 10: Diagram of cracked property axes

In the initial formulation (Rashid 1968), the smeared crack element orthotropic cracked stiffness matrix was formulated by zeroing out stiffness in the crack plane. This caused shear stresses along the crack to abruptly drop to zero and did not represent the ability of concrete to retain shear strength through aggregate interlock. In subsequent formulations, shear retention factors (Hegger et. al. 2004; Li et. al. 2003; Mahini 2005; Suidan and Schnobrich 1973) helped resolve much of the numerical difficulties associated with the original method. In the initial formulation, the cracking plane and material property axis was fixed after initial cracking of the element. This allowed tensile stresses to build up at angles different from the cracking axis. Stresses at these new orientations could exceed cracking stress without causing any change of tensile capacity in that direction, since a new cracking plane could not develop (Crisfield and Wills 1989). Softening rules in tension were developed to address this issue (Gopalaratnam and

Shah 1985; Gylltoft 1983; Li et. al. 2009; Manfredi et. al. 2008; Nilsson and Oldenburg 1983).

Some formulations of the fixed smeared crack element allow for the formation of multiple cracks in a single element (Cervenka and Papanikolaou, 2008; De Borst and Nauta 1985; Govindjee and Hall 1998; Mitra 2007). This is accomplished by decomposing the post-cracking stress and strain into a concrete (or masonry) component and a crack component. New cracks are permitted to form if the deviation of the principal stress from the last cracking axis exceeds a specified threshold value. Each crack is given its own local axis and stiffness matrix, and total stiffness (concrete and crack component) is determined as an assembly of the crack stiffness matrices and the concrete matrix.

Other smeared crack formulations allow the orientation of the crack to rotate with the axes of principal strain. Proposed formulations either continuously update the material property axes (Ayoub and Filippou 1998; Cope et.al. 1980; Gupta and Akbar 1984) or initiate a change in axes after exceedance of a threshold angle between the principal stress and existing crack (Cope and Rao 1981). In studies by Rots and Blaauwendraad (1989), the rotating crack formulation did not seem to produce better results than a fixed crack formulation and tended to have a slight directional bias for crack localization along the lines of the mesh. Ayoub and Fillipou (1998) noted better agreement with experimental results of shear panels and deep beams with a rotating crack formulation than a fixed crack formulation. Crisfield and Wills (1989) found that both rotating crack and fixed crack formulations overestimated the capacity of reinforced concrete panels that failed in shear.

Fixed single-crack, fixed multiple crack and rotating crack formulations all have the advantage of not constraining the crack path to predetermined locations, but each model has its own advantages and disadvantages.

Fixed single-crack smeared crack formulations can be easily integrated into current finite element schemes by simply adjusting the element stiffness matrix of existing common element types. The formulation is also very efficient, as no nodal renumbering is required after crack initiation, material properties do not need to be continuously updated, and there are no additional calculations to decompose strains into concrete (or masonry) and crack components. The predominate shortcoming of fixed single-crack smeared crack elements is their overestimation of shear capacity, which has been recounted by many researchers (Crisfield and Wills 1989; Manfredi et al. 2008; Sritharan et. al. 2000; Tajima et. al. 2004). Smeared crack elements also exhibit generally over-stiff behavior in shear (Bazant and Cedolin 1980; Spencer and Shing 2002). Stiff post-cracking behavior occurs regardless of the shear retention factor selected (Rots and Blaauwendraad 1989). Another inherent issue with smeared element formulations is the stress locking effects when inclined (shear cracks) are present in an element (Rots and Blaauwendraad 1989). As shown in Figure 11, when element 2 cracks, element 1 is subjected to a tensile stress caused by the cracking of element 2. Most of the time, the crack propagates into the next element above 2 and the tensile stress in element 1 is “locked” in. In reality, the crack should relieve stresses along the crack surface, but because the smeared formulation does not create a free surface (discrete crack) this stress relief does not take place. The effect does not diminish with mesh refinement, as it is an inherent deficiency of the smeared element formulation.

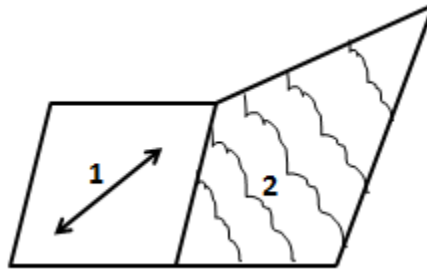


Figure 11: Illustration of stress-locking in smeared crack elements (Rots and Blaauwendraad 1989)

Fixed multiple-crack formulations can more accurately capture the progression of damage within a material and explicitly track crack behavior, but they are challenging to implement and have yielded mixed results. Crisfield and Wills (1989) attempted to implement the multiple crack formulation proposed by De Borst and Nauta (1985) but ultimately used a traditional single crack formulation, because they encountered many numerical instabilities involving the threshold angle. Rots and Blaauwendraad (1989) found if low threshold angles were used to initiate new cracks, multiple smeared crack models tended to have directional bias along the lines of the mesh, and if high threshold angles were used, they exhibited the same over-stiffening in shear as traditional smeared crack elements. Barzeyer-Jamshidi and Schnobrich (1986) successfully employed a multiple crack model based upon the work of De Borst and Nauta (1985) which captured shear failure of monotonically loaded panels, provided a sufficient shear retention factor was utilized.

Rotating crack formulations, which do not suffer from such stiff post-cracking behavior, have a slight directional bias (Rots and Blaauwendraad 1989) and cannot capture shear sliding (Spencer and Shing 2002). Failure of smeared crack elements

regardless of the type of cracking model is typically flexure dominated, because most formulations are governed by tensile strength. (Lotfi and Shing 1991). Using alternative material models which account for shear failure can improve this behavior, but cannot alleviate the stress-locking or overly-stiff post-cracking response inherent to continuum models.

2.1.1.3 Crack Band Models

Crack band models are essentially a cross-breed of the smeared cracking element and a discrete crack formulation. These models allow a bifurcation, or singular band, to form within the element. In the original formulations, crack widths were assumed based on previous material tests and all deformation once crack propagation began took place within this crack band. These models had the advantage of capturing localized behavior like a discrete model, without constraining crack propagation to predetermined paths (Belytschko et. al. 1988; Ortiz et. al. 1987; Pieruszczak and Moroz 1981). Subsequent improvements on the method decomposed strains into concrete strains and crack strains. Continuity of displacement in the singular band (crack) was maintained, but displacement gradients were not smooth. This allowed for crack widths to vary and they were calculated as a function of cumulative crack strain (Cervera et. al. 1987; Rots et. al. 1985). Other formulations allowed for the formation of coincident singular lines normal along the initial crack path. As the material cracks, the difference between the two initially coincident singular points in the displacement field on each end of the singular band was crack width (Oliver 1989).

This method is capable of capturing localization of cracks and relatively broad crack distributions, represented by the crack band width. It is also insensitive to mesh

size, so long as the finest mesh width is greater or equal to the expected crack width. However, crack band models are computationally expensive, and require input parameters which must be obtained through iterative calibration. Such parameters include: the characteristic crack length and crack band width limits, which contribute to the governing equations for the angle of crack propagation and energy based criterion for crack initiation and weighting functions to enforce compatibility between the crack band and the rest of the element (Bazant 1986; Bazant and Pijaudier-Cabot 1989; Oliver 1989). Additionally, the relations for a singular band occurring at any location within an element require nonlocal continuum formulations in which one must formulate some type of averaging operator to obtain a symmetric stiffness matrix (Bazant 1986).

2.1.1.4 Microplane Models

Microplane models are a modification of a smeared crack model used to model the brittle failure of concrete and masonry. In a microplane model, the concrete or masonry is divided into a series of planes which represent damage planes or weak planes like those between aggregate (See Figure 12). The microplanes have material failure surfaces which determine both the normal and deviatoric stresses and strains along those planes.

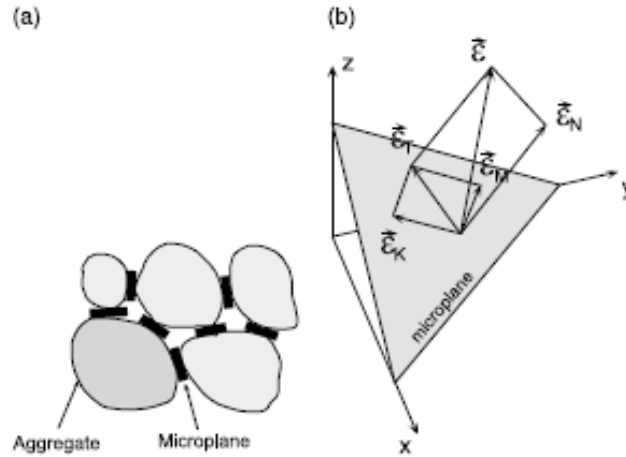


Figure 12: (a) illustration of microplane locations (b) mapping of strains from microplane to macroplane strain tensor (Ozbolt et. al. 2001)

Microplane models which follow a static constraint map the stresses from the microplanes onto the smeared crack elements representing concrete (Taylor 1938). This method was found to be unstable for tensile failure of concrete due to snap-back effects (Bazant 1984; Bazant and Gambarova 1984; Bazant and Oh 1983). Microplane models which follow a kinematic constraint map the strains from the microplanes onto the smeared crack elements representing concrete (Bazant and Prat 1988; Ozbolt and Bazant 1992). Kinematic microplane models have the advantage of being able to accurately predict failure along three-dimensional planes for multiple failure mechanisms including: tension, shear and compression. The model is also able to capture initial anisotropy from material defects.

One fallback with kinematic microplane models is that after tensile failure, the models incorrectly predict lateral expansion (Ozbolt et al. 2001). This occurs because the total stress is decomposed into the volumetric stress and deviatoric stress, which must sum to zero in the cracked state. The cracked state implies volumetric stress goes to zero as the volumetric (tensile) stiffness is greatly reduced after cracking. In order for the

deviatoric stress to equal zero, either (I) the deviatoric strain must equal zero, or (II) the deviatoric stiffness must reduce to zero. Because the deviatoric (compression) stiffness is 10 times the volumetric (tensile) stiffness for concrete, a softening curve which maintains numeric stability cannot satisfy condition II and thus condition I is imposed. However, if the material does not undergo negative deviatoric strain under tension, the material is expanding, which is physically unrealistic. Some work has been done to remove this expansion, but in doing so the material modeling must be discontinuous with a relaxation in the kinematic constraints after fracture (Ozbolt et al., 2001). This significantly increases the modeling complexity and can make calibration difficult due to excessive number of modeling parameters without a physical interpretation.

The other inherent issue with the microplane formulation is that the kinematic constraint necessitates the use of the Voight estimate for elastic modulus, which is an upper-bound for material stiffness (Bazant and Prat 1988). Excessive stiffness of numerical simulations compared to experimental data has been confirmed by several researchers (Eligehausen et. al. 2009; Ozbolt et al. 2001)

2.1.2 Material Models

Most finite element models for concrete and masonry either implements separate material models for tension and compression behavior, or utilize a combined failure surface model which accounts for multiple failure mechanisms.

2.1.2.1 Tensile Behavior

Rankine Theory is widely employed by many smeared crack modeling schemes (Cervenka and Papanikolaou 2008; De Borst and Nauta 1985; Lotfi and Shing 1991) to represent the failure surface of the element in tension. Rankine Theory states that failure

occurs whenever principal stress exceeds the tensile stress of the material at failure when loaded in pure tension (Rankine 1857). Most formulations utilize a form of exponential softening curve for the post-cracking tensile strength in order to avoid numerical instabilities (Gopalaratnam and Shah 1985; Gylltoft 1983; Li et al. 2009; Manfredi et al. 2008; Nilsson and Oldenburg 1983). Unfortunately, the use of the Rankine yield criterion as a crack criterion results in mesh sensitivity issues. As the width of the element ahead of the crack front decreases, the stress within that element will increase. Thus, with mesh refinement, the crack front propagates infinitely at virtually zero load (Bazant and Cedolin 1979).

To resolve the mesh sensitivity exhibited in the original models Bazant and Cedolin, in 1979 proposed the fracture energy crack criterion. It is based on theories of crack advance in elastic continuums (Rice 1968). This method alleviates mesh size bias but the computational expense is significantly greater than using a tensile stress crack criterion (Bazant and Cedolin 1979).

Another alternative to modeling tensile cracking is the use of a stress intensity factor (Bazant and Cedolin 1979; Saouma and Ingraffea 1981). When the computed stress intensity factor exceeds fracture toughness of the material, element cracking is initiated. The formulations for stress intensity factor are based on the expected length of crack propagation and its direction, as is typically done for discrete cracks. An equivalent crack length and direction is determined by fitting displacements at characteristic nodes around a band of cracked elements as shown in Figure 13. Solutions using this method are highly dependent on selection of characteristic nodes, and the algorithms can be very tedious to implement.

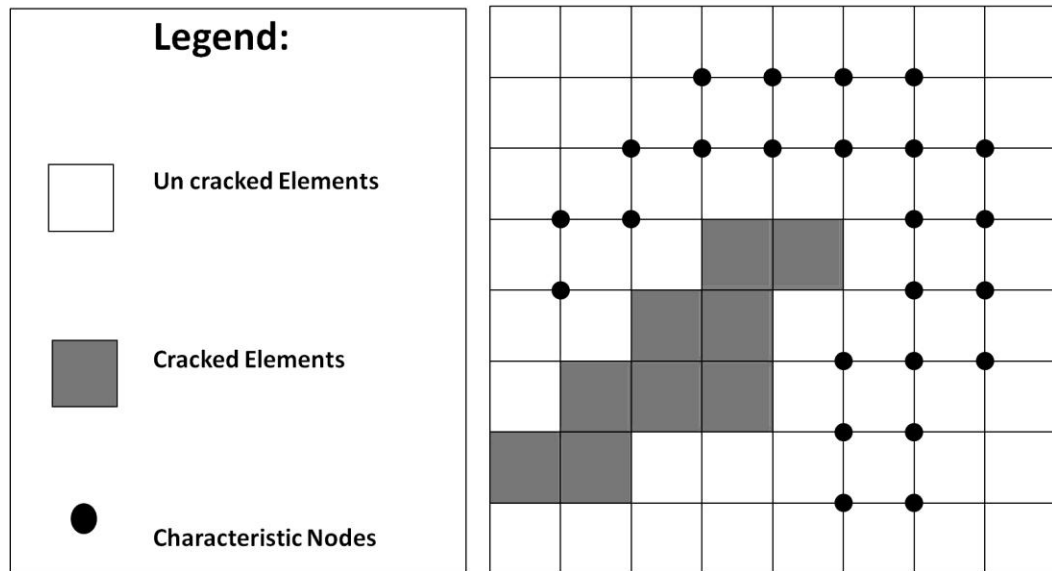


Figure 13: Characteristic nodes around a band of cracked elements (Bazant and Cedolin 1979)

2.1.2.2 Compressive Behavior

There is a great deal of agreement among researchers in the modeling of concrete and masonry in compression. Nearly all proposed models include some type of exponential curve for the material behavior, in order to capture the initial stiffness and subsequent softening after peak compressive stress has been exceeded (Chung and Ahmad 1995; Desayi and Krishnan 1964; Kent and Park 1971; Kupfer et. al. 1969; Lotfi and Shing 1991). Some formulations have more simplified bilinear equations representing initial stiffness state and a slightly reduced stiffness state after compression stress has exceeded 1/3 of peak strength (Tajima et al. 2004). A comparison between the two types of compression models is shown in Figure 14.

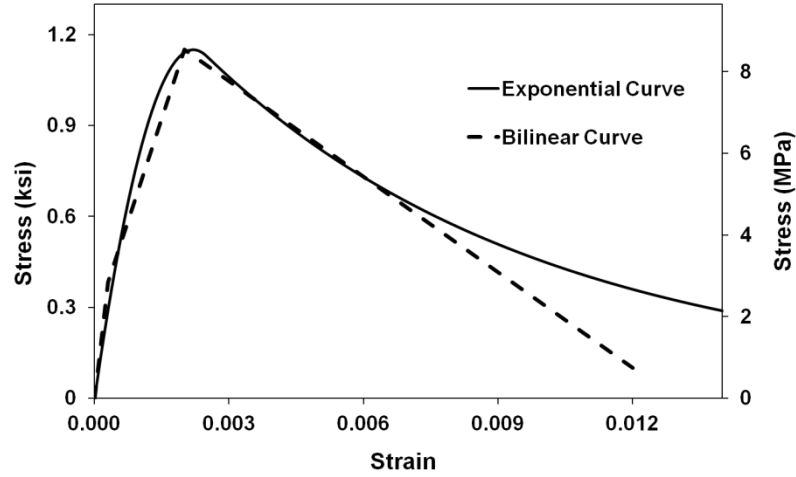


Figure 14: Comparison of exponential and bilinear compression curves

2.1.2.3 Combined Failure Material Models

2.1.2.3.1 Mohr-Coulomb Yield Criterion

The Mohr-Coulomb yield criterion is often combined with a simple tensile cut-off to form a failure surface for concrete (Cowan 1953; Mohr 1900). The Mohr-Coulomb yield criterion is defined by Equation 1, where the limiting shear stress of the material is a function of the cohesion c , the normal stress σ and the internal friction angle of the material ϕ .

$$\tau = c - \sigma \tan \phi \quad (1)$$

When combined with a tensile cut-off criterion, the failure surface for concrete is shown in Figure 15. The advantage to this type of model is that it accounts for the shear capacity of the concrete explicitly, and does not overestimate shear capacity like traditional tensile-based failure models. The main disadvantage to this type of model is that the

influence of intermediate stress prior to exceeding the yield criterion, are ignored (Chen, 2007). This means that the uniaxial compression strength of concrete is the same as the biaxial strength, even though experiments have shown confinement to significantly increase concrete compressive strength. Additionally, the failure surface is not smooth, and the singularities can be difficult to handle in numeric simulations (Chen, 2007).

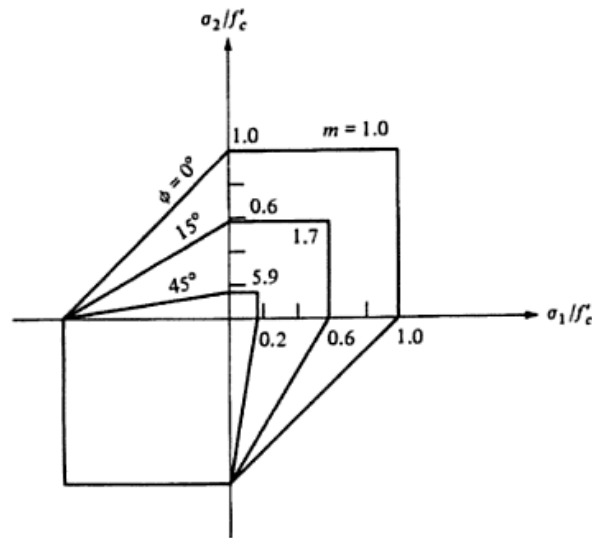


Figure 15: Normalized Mohr-Coulomb yield surfaces with tensile cut-off (Chen, 2007)

2.1.2.3.2 Drucker-Prager Yield Criterion

The Drucker-Prager yield criterion was originally used for modeling soils and represents the failure surface of a material as a function of its shear strength as a function of compressive load (Drucker and Prager 1952). It is essentially a smoothed version of the Mohr-Coulomb yield surface. Equation 2 shows the function of the yield surface f , which is characterized by the first invariant of the stress tensor I_1 , the second invariant of the deviatoric stress tensor J_2 , and material parameters α_d and k . These material parameters can either be calibrated to material tests or written as functions of cohesion c

and the internal friction angle of the material ϕ . When k is reduced to zero, the Drucker-Prager equation essentially becomes a Von Mises failure criterion.

$$f = \alpha_d I_1 + \sqrt{J_2} - k \quad (2)$$

The Drucker-Prager yield criterion alleviates the numerical instabilities exhibited from a Mohr-Coulomb type yield surface (Chen, 2007). However, the same assumptions about ignoring the effect of intermediate stresses on the compressive strength of the material which were in the Mohr-Coulomb model are also inherent to the Drucker-Prager yield criterion.

2.1.2.3.3 William-Warnke Yield Criterion

The William-Warnke (1974) yield surface is defined by three parameters: the uniaxial tensile strength, the uniaxial compressive strength, and the biaxial compressive strength of a given material. The yield surface for this model is given by Equation 3, where ρ and r are parameters which are functions of the tensile strength and the biaxial compressive strength of the material, f'_c is the uniaxial compressive strength, I_1 is the first invariant of the stress tensor, and σ_i s are the principal stresses.

$$f = \frac{1}{3\rho} \frac{I_1}{f'_c} + \frac{1}{r(\theta)} \frac{\sqrt{(\sigma_1 - \sigma_2)^2 + (\sigma_2 - \sigma_3)^2 + (\sigma_3 - \sigma_1)^2}}{\sqrt{15} f'_c} - 1 \quad (3)$$

This model correctly accounts for increased compression strength due to confinement, and adequately captures shear failures. There are many more failure surfaces which incorporate 4 or more parameters including the Ottosen (1977) criterion, the Reimann (1965) criterion, the Hsieh-Ting-Chen (1979) criterion and the 5-Parameter William-Warnke (1974) yield criterion. However, these are less commonly utilized and increase model complexity.

2.1.2.3.4 Modified Compression Field Theory

Modified compression field theory (MCFT) (Vecchio and Collins 1986) is somewhat different from the other material models, because it can be used to represent reinforced concrete as a single material rather than use discrete truss elements for reinforcement. MCFT was adapted from compression field theory by accounting for the ability of cracked concrete to transfer some tensile stress rather than assuming zero tensile capacity. Element failure mechanisms in MCFT are all a function of the direction of principal compression stress, which is determined iteratively. Failure mechanisms include: slipping on the crack, crushing, shear failure, or reinforcement yielding, which are all formulated with respect to average stress and strain in the element. Additional variables which must be determined are the parameters governing crack control. These include reinforcement ratio and spacing, which are used to calculate crack width, and max aggregate size which is used to calculate shear stress. Modified Compression Field Theory (Vecchio and Collins 1986) has been the basis for many different element formulations used to model concrete and masonry (Bhide and Collins 1989; Kaufmann and Marti 1998; Kollegger and Mehlhorn 1990).

Deficiencies with the formulation for modeling shear behavior have been noted. Kollegger and Mehlhorn (1998) found that MCFT underestimated the stiffness and shear strength of heavily reinforced panels. Bhide and Collins (1989) found that MCFT overestimated the stiffness and strength of lightly reinforced concrete panels subjected to uniaxial tension and shear.

2.1.2.3.5 Disturbed Stress Model

Another model which incorporates the effects of reinforcement is the disturbed stress model (Vecchio, 2000). It differs from MCFT because stresses are a function of the angle of principal tensile stress, principal stress and strain are not required to be coincident, and shear stress in the element is a function of local behavior at the crack boundary rather than global stresses. Shear stress is calculated from local reinforcement stresses. These local stresses are determined from local reinforcement strains, which are a function of the average element strains and the relative angle between the reinforcement at the normal to the crack plane. This method has not been widely used in literature compared to MCFT.

2.2 Simplified Modeling of Unreinforced Masonry Infill

The most widely employed method for modeling masonry infill is the equivalent strut concept. The masonry infill is assumed to act like a diagonal compression-only strut between the structural columns. The most recognizable and significant work on the topic was conducted by Bryan Stafford-Smith, who developed models to calculate the equivalent stiffness and strength of a compression-only strut to model unreinforced masonry infill (Stafford-Smith 1967). His equations were validated against results of four different series of experiments and are the basis for most simplified methods in current design codes.

Subsequent improvements on the model have incorporated effects of strength degradation and slip in hysteretic behavior (Madan et. al. 1997; Puglisi et. al. 2009; Rodrigues et. al. 2010), or added limit states to the strut model for other failures like corner crushing (Flanagan and Bennett 1999). Others have proposed methods to calculate

equivalent struts for unreinforced wall panels with openings (Kakaletsis 2009; Mohebkhah et. al. 2007; Schneider et. al. 1998). Investigations have also been conducted on changing the governing force-displacement behavior of the strut and the number of struts used to represent the infill panel (Fiore et. al. 2012; Uva et. al. 2012). Still, these improvements have not been codified, likely because most code procedures are based on an equivalent static linear analysis rather than dynamic analysis and these improvements vastly increase model complexity. The major codes which contain guidance for modeling unreinforced masonry infill are FEMA 356, ASCE 41-06, TMS 402-11, and Eurocode 8.

2.2.1 FEMA 356 and ASCE 41-06

The procedure to determine the equivalent diagonal compression strut for masonry infill is identical in FEMA 356 and ASCE 41-06 and is given in Section 7.5.2.1 of FEMA 356 and 7.4.2 of ASCE 41-06 (ASCE 2000, 2006) . The equivalent diagonal strut has the same thickness and elastic modulus as the infill it represents. The width a , is calculated using Equations 4 and 5.

$$a = 0.175(\lambda_1 * h_{col})^{-0.4} r_{inf} \quad (4)$$

$$\lambda_1 = \left[\frac{E_{me} t_{inf} \sin 2\theta}{4E_{fe} I_{col} h_{inf}} \right]^{0.25} \quad (5)$$

In Equation 4, λ_1 is a coefficient used to determine equivalent width of the infill strut, h_{col} is the height of the column between centerlines of the beams, and r_{inf} is the diagonal length of the infill panel. In Equation 4, E_{me} is the elastic modulus of the masonry, t_{inf} is the thickness of the masonry infill, θ is the angle (in radians) whose tangent is the infill height to length aspect ratio, E_{fe} is the elastic modulus of the frame

material, I_{col} is the moment of inertia of the column in the plane of bending, and h_{inf} is the height of the infill panel.

2.2.2 TMS 402-11

The equivalent strut method for masonry infill is given in Appendix B of the TMS 402-11 code and has a thickness equivalent to the infill thickness and elastic modulus equal to the elastic modulus of the masonry prism (MSJC 2011). The width w_{inf} , is calculated by Equations 6 and 7.

$$w_{inf} = \frac{0.3}{\lambda_{strut} \cos \theta_{strut}} \quad (6)$$

$$\lambda_{strut} = \sqrt[4]{\frac{E_m t_{net\ inf} \sin 2\theta_{strut}}{4E_{bc} I_{bc} h_{inf}}} \quad (7)$$

In Equation 6, λ_{strut} is the characteristic stiffness parameter for infill and θ_{strut} is the angle of the infill diagonal with respect to horizontal, in degrees. In Equation 7, E_m is the elastic modulus of the masonry prism, $t_{net\ inf}$ is the net thickness of the infill, E_{bc} is the elastic modulus of the bounding column, I_{bc} is the moment of inertia of the bounding column in the bending plane, and h_{inf} is the vertical dimension of the infill.

2.2.3 Eurocode 8

Although Eurocode 8 does not give a specific equation for calculating the width of the equivalent strut, guidance is given on the method by which to calculate it (CEN 2003). Additionally, several limitations to the design are imposed, and a different behavior factor (Section 6.3.2) is used for moment resisting frames with infills. The limitations on the design of the structure is given in Section 4.3.6 and includes requirements for regularity in the distribution of infill panels in plan and elevation, and a

requirement to detail the columns for the local effects of frame-infill interaction. Section 5.9 gives the details of accounting for these local effects. If a column bounding an infill wall does not have masonry on either side of it, the column must be detailed as though the entire height were the critical region. The length of the column over which the diagonal strut force is applied, must be capable of resisting the shear force induced by the masonry strut. The force is assumed to be equal to the horizontal shear strength of the masonry panel based on the bed joint strength. The width of the diagonal strut must be justified by calculation, but no direct procedure for determining the width is given.

2.3 Experimental Studies and Field Observations on the Seismic

Performance of Concrete and Masonry Walls

There are three main types of reinforced concrete and masonry construction: infill walls, confined masonry walls, and hybrid masonry systems. In reviewing the literature, it is clear that the specimens tested as part of this dissertation do not neatly fall into one of these structural types. However, an understanding of the behavior of previously studied reinforced concrete and masonry structures establishes a baseline for interpreting the failure mechanisms observed in the physical tests of the wall specimens designed according to practices in the Caribbean. Within this survey, each structural type is first defined. Then a summary of the major conclusions from past experimental studies is presented. Finally, a brief record of the performance in past earthquakes is given. The focus of this survey is on single panel behavior, without the presence of openings, as this is the type of structure to be tested in the experimental program.

2.3.1 Masonry Infill

2.3.1.1 System Description

Unreinforced masonry infill structures are by far the most extensively studied of combined concrete and masonry structural systems. Typically, the reinforced concrete frame is designed for all gravity loads, partition loads, and lateral loads from wind or seismic forces. The frame is constructed first, then "filled-in" with brick units to form the walls of the structure. The infill walls are not designed to carry any of the loads placed on the building. Reinforced masonry infill differs from unreinforced infill because internal reinforcement is added to the masonry wall. All of the experimental programs on reinforced infill structures do not contain connections to the reinforced concrete frame.

2.3.1.2 Experimental Studies

Unreinforced masonry infill panels can fail in any combination of six primary modes: interface cracking, corner crushing, diagonal cracking, horizontal sliding, shear failure in the column, or a combined sliding and diagonal cracking mode (Moghaddam and Dowling 1987) (See Figures 16-18).



Figure 16: Unreinforced masonry wall test showing interface cracking and bed joint sliding (Mosalam 2005)



Figure 17: Shear failure due to short-column effect from crushing of masonry at corners (Corte et. al. 2008)



Figure 18: Large diagonal crack formed during shake table test (Stavridis et. al. 2012)

The type of failure exhibited in the infill wall is influenced by several factors. These include: the strength of the infill relative to the reinforced concrete frame, aspect ratio, presence of gap joints, mortar strength, beam-column joint strength, type of masonry unit, and type of loading. For weak (typically hollow) infill with weak frame, the lateral resistance is governed by sliding of the panel along bed joints, followed by a significant drop in resistance, yielding of reinforcement and finally crushing of masonry (Hashemi and Mosalam 2006). For weak infill and a strong frame, the failure mechanism is typically masonry sliding, but the frame is not significantly damaged (Murty and Jain 2000). For a strong infill with a weak frame, diagonal cracking of the masonry is

followed by sliding along the bed joint and shear failure in the column being pushed. This type of failure leads to faster degradation of resistance than a weak frame with weak infill and a quick brittle failure of the frame columns (Corte et al. 2008). For strong infill with a strong frame, the failure is governed by corner crushing of the infill followed by immediate shear cracking in the columns, but not shear failure, due to the large amount of shear reinforcement in the columns.

Aspect ratio (h/l) primarily effects the diagonal cracking mode (Moghaddam and Dowling 1987). The higher the aspect ratio of the wall, the more likely diagonal cracking will occur and the initial stiffness of the wall decreases as aspect ratio increases. Increased mortar strength increases tensile capacity and reduces the likelihood of diagonal cracking and shear horizontal bed joint sliding (Moghaddam and Dowling 1987). The influence of mortar strength is more significant for hollow units because the shear capacity is solely a function of the bond strength. In infill walls constructed of solid brick, shear capacity is a function of bond strength and internal friction. The presence of gap joints between the masonry and the columns may facilitate bed joint sliding, especially for weak infill (Gostic and Zarnic 1999). The strength of beam-column joints probably has a great influence on the likelihood of column hinging after crushing of the masonry, as tests of frames without seismic detailing exhibit poor performance with shear failures through the joints and soft story collapses. The type of brick unit also has a large impact on the failure mode. Hollow units are more likely to exhibit shear sliding, and will generally be weaker and less stiff than solid units (Mehrabi et. al. 1996). Finally, the loading method can also greatly impact test results. Monotonic loading generally captures the same failure mechanisms as cyclic loading, but the crack patterns often do not

correspond exactly to cyclic patterns, particularly in capturing horizontal bed sliding (Moghaddam and Dowling 1987). Additionally, walls loaded cyclically tend to fail at lower levels of lateral load and displacement than monotonically loaded specimens (Brokken and Bertero 1981; Hashemi and Mosalam 2006).

When compared to tests of bare RC frames, the presence of unreinforced infill masonry increases the initial stiffness (Brokken and Bertero 1981). Experimental data from the literature shows that infill masonry sometimes increases and other times decreases the strength and ductility of the system over tests of RC frames without infill (Angel et. al. 1994; Buonopane and White 1999; Murty and Jain 2000; Zarnic and Tomazevic 1988). The presence of unreinforced masonry infill also changes the force distribution in the columns (Buonopane and White 1999; Mosalam 2005). Infill also affects the system's dynamic properties, decreasing the natural period (Buonopane and White 1999; Hashemi and Mosalam 2006; Stavridis et al. 2012) and increasing the damping (Hashemi and Mosalam, 2006). The out-of-plane behavior of unreinforced masonry infill has shown to be very poor, and out-of-plane capacity is greatly reduced if the specimen has previous in-plane damage (Angel et al. 1994; Chen et. al. 2012; Shapiro et. al. 2004).

Reinforced infill walls have virtually the same initial stiffness as an unreinforced infill wall. Horizontal bed joint reinforcement does not significantly change the peak strength, or ductility of the infill wall, although less strength degradation has been observed (Moghaddam and Dowling 1987). The addition of horizontal reinforcement significantly improves out-of-plane behavior of an infill wall (Calvi et. al. 2004; Moghaddam and Dowling 1987; Murty and Jain 2000). Fully grouted, doubly reinforced

infill walls with dowel connections to the RC frame have been shown to increase strength, ductility, and energy dissipation of the infill wall, if the reinforcement ratio is large enough to prevent break-up of the infill panel (Brokken and Bertero 1981; Klingner and Bertero 1976). However, it is important to note that both of these tests had specially designed ductile frames to act integrally with the reinforced infill, where most infills are not considered when designing the RC frame. Out-of-plane tests of doubly reinforced infill walls were not found in literature, but they would also be expected to perform similarly or better than reinforced infill with only horizontal reinforcement.

2.3.1.3 Performance in Past Earthquakes

An overwhelming number of damaged buildings and casualties in earthquakes around the globe have demonstrated the seismic deficiencies of unreinforced masonry infill frames. However, there are some cases where the infill masonry proved beneficial and likely prevented the collapse of buildings with seismically deficient frames. There are not well-documented cases of reinforced infill structures which have experienced a significant seismic event. Infill with horizontal reinforcement is commonly found as curtain walls in the Eastern United States (Klingner 1994). Although most of this region has little seismic risk, buildings in the southeast near the New Madrid Seismic Zone may experience significant seismic forces in the future.

Examples of poor performance of infill wall structures can be seen in Peru during the 1970 Chimbote earthquake (M 7.9), when out-of-plane collapse of infill walls was extremely common and sometimes led to the collapse of the reinforced concrete frame (Schultz 1994). Most of the casualties during the 1985 Mexico City earthquake (M 8.0) were due to extensive shear cracking of infill and out of plane collapse of the clay infill in

high rise concrete frame structures, which collapsed. This was primarily due to weak columns which were not detailed for seismic loading and could not remain stable once the infill panels collapsed (Stone et. al. 1985). During the 1999 Izmit (M 7.6) and Duzce (M 7.2) earthquakes in Turkey many concrete frame buildings over four stories with unreinforced clay infill collapsed due to soft story failures (Bayhan and Gülkan 2011). Most which collapsed had seismically deficient frames, but seismically designed frames had shear failures of the masonry both in-plane and out-of plane. These same failures were seen again in the 2011 Van earthquake in Eastern Turkey (M 7.1) (Alaluf et. al. 2011). In the 2003 Boumerdes earthquake in Algeria, (M 6.8) seismically deficient reinforced concrete frames collapsed due to soft-story effects after the masonry on the first story failed (Bendimerad 2004). During the 2008 Wenchuan earthquake (M 8.0) in China, most reinforced concrete frames were considered seismically deficient. In those frames infilled with hollow clay masonry, the infill failed and collapsed out-of-plane in the first few stories of many buildings, resulting in soft-story mechanisms (See Figure 19) (Li et. al. 2008).



Figure 19: Damage from the Wenchuan earthquake: shear failure and collapse of masonry (left) and collapse of a 5 story building (right) (Li et al. 2008)

There are, however, examples of infill masonry being beneficial to seismic performance by providing additional strength, stiffness and redundant load paths for seismically deficient frames. The 2008 Wenchuan earthquake, in buildings which were infilled with solid clay masonry, the infill worked integrally with the building's seismically deficient frame and prevented collapse (See Figure 20).



Figure 20: Solid infill which helped prevent building collapse (Li et al. 2008)

During the Northridge earthquake, many seismically deficient buildings in Los Angeles were aided by the additional stiffness and lateral load resistance of the infill and did not collapse (Bennett et. al. 1996). Infill may also be beneficial in soft soil conditions and moderate earthquakes where the additional stiffness from the infill reduces the period of the building and decreases damage due to inertial forces. This was observed for buildings on soft soils during the 1985 Mexico City earthquake and the 1992 Cairo earthquake (M 5.8) (Bennett et al. 1996). During the 2003 Tecoman earthquake (M 7.8) in Mexico, infill structures performed very well (Alcocer et al. 2006). Damage was primarily shear cracking of infill panels and some spalling of the joint regions at the top of columns due to combined axial and shear forces.

2.3.2 Confined Masonry

2.3.2.1 System Description

Confined Masonry consists of a load-bearing masonry wall confined by tie-beams and tie-columns which are poured after the wall is in place. According to the 2011 Seismic Design Guide for Low-Rise Confined Masonry Buildings, the wall should have "toothing" or shear connectors in order to ensure that the wall acts integrally with the confining column (See Figure 21). The masonry wall carries gravity loads and out-of-plane loads. The masonry wall and confining elements act as a shear wall to resist in-plane loads due to seismic action. The tie-elements provide confinement and stability for in-plane and out-of-plane loading of the walls, and help reduce the likelihood of brittle failure in the masonry. When compared to an infill masonry building, the columns are typically much smaller and do not resist lateral forces through frame action (See Figure 22).

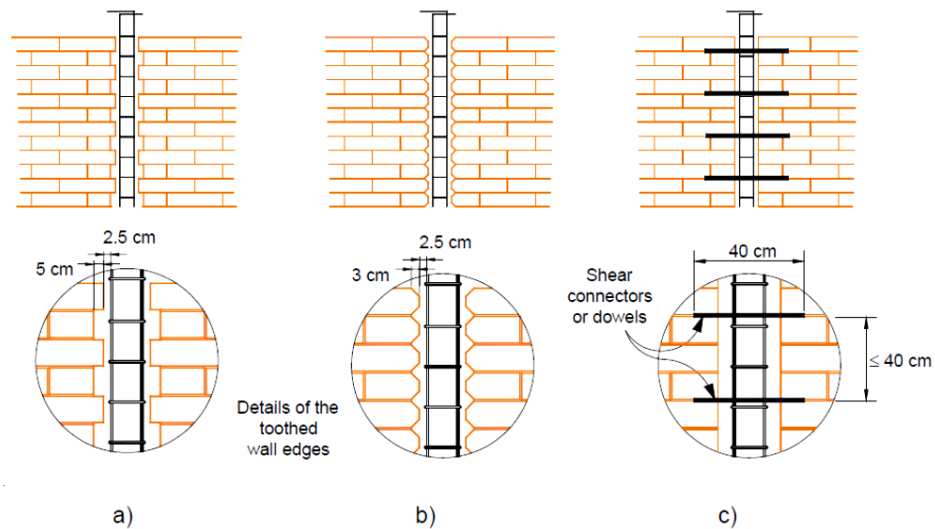


Figure 21: (a and b) Details of toothed connections to tie-columns and (c) shear connections (Meli et.al. 2011)

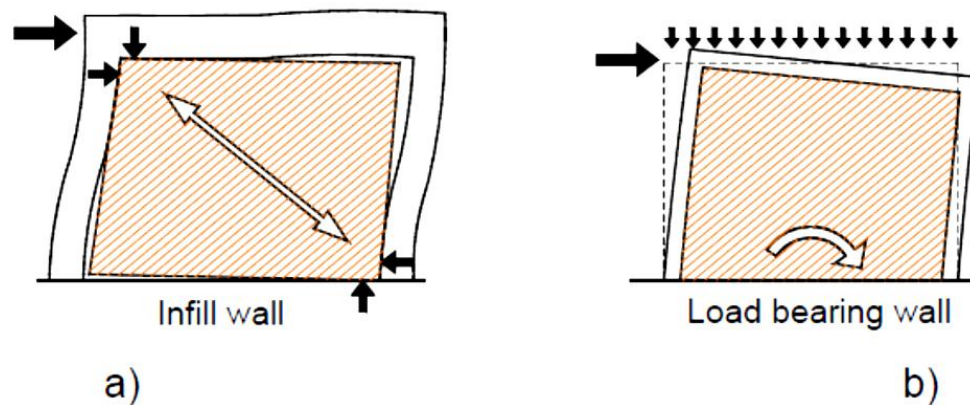


Figure 22: Comparison of behavior under seismic action of (a) an infill wall and (b) a confined masonry wall (Meli et al. 2011)

2.3.2.2 Experimental Studies

Few tests have been conducted to directly compare the performance of infill walls to confined masonry. It has been experimentally demonstrated that confined masonry shows less strength degradation and greater ductility under cyclic loads than unreinforced infill walls (See Figure 23) (Gostic and Zarnic 1999; Perez-Gavilan et. al. 2009). For tie-columns of width less than 1.5 times the masonry thickness, the tie elements and masonry act integrally and fail in shear (San Bartolome et. al. 2010). For tie-columns of width greater than two times the masonry thickness, the masonry separates from the tie-elements and behaves like an infill panel (San Bartolome et al. 2010). Both block type and mortar strength has a significant impact on the strength of confined masonry walls (Tena-Colunga et. al. 2009). Changing the amount of reinforcement in the tying elements does not significantly increase the strength of the panel, although the addition of vertical and horizontal reinforcement within the masonry greatly improves strength (Yoshimura et. al. 1996). The single study of the out-of-plane behavior of confined masonry found in

the literature showed that it behaves similarly to unreinforced infill walls, although the specimens tested did not have tothing or shear connections (Varela-Rivera et. al. 2011).

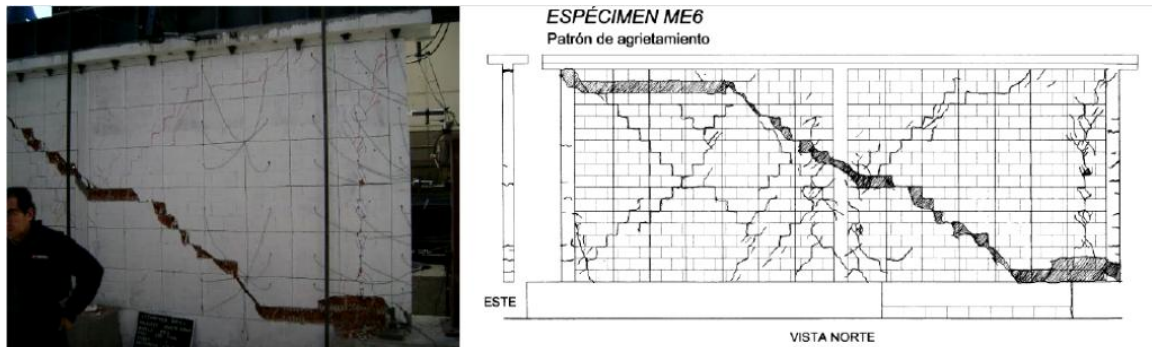


Figure 23: Cyclic test of two bay confined masonry wall (Perez-Gavilan et al. 2009)

2.3.2.3 Performance in Past Earthquakes

Confined masonry has gained a lot of momentum in recent research initiatives, primarily because of its record of good performance of low to medium rise structures in past earthquakes, even when many of these structures were not specifically designed to be earthquake resistant. From 1966 to 1974 Peru experienced three major earthquakes greater than magnitude 7.0; although nearly all the building stock in Peru was considered non-engineered, the confined masonry performed very well compared to reinforced masonry (Gallegos 1994). Most of the failures of reinforced masonry were the result of construction errors such as un-grouted cells or the substitution of mortar for grout. Confined masonry was advantageous because it was simple, and thus more likely to be constructed correctly. It also required less rebar, and the structural systems have less mass than reinforced concrete buildings. Confined masonry structures in Columbia showed almost no damage during the 1983 Popayan earthquake (M 5.5) (Schultz 1994). Most homes had only minor cracking around the window and door openings, but those

with confining elements around the opening showed no observable damage. Low-rise structures (less than four stories) performed well during the 1985 Mexico City earthquake (M 8.0), with only minor cracking (Schultz 1994). Taller structures exhibited diagonal cracking on the first floors due to shear, and out-of-plane failures on the top levels, which are subjected to the greatest inertial forces during earthquakes. Good seismic performance of confined masonry structures was also observed in the 1985 Llole, Chile earthquake (M 7.5). Only 22% of confined masonry buildings 3-5 stories tall had severe damage, whereas 63% of reinforced masonry structures had severe damage (Moroni et. al. 2004). As with most structures, poor construction quality will result in poor seismic performance. Two-story residencies in Ecuador showed extensive damage or collapsed during the 1990 Pomasqui earthquake (M 5.3), as most buildings were missing tie-members in some of the walls (Schultz 1994).

The most recent Chile earthquake in 2010, again showed that well-constructed confined masonry structures perform very well, as only two collapsed (Brzev et. al. 2010). The large magnitude of the 2010 earthquake (8.8) left significant damage in many confined masonry structures. Masonry walls had some in-plane shear cracking at the first story and out-of-plane damage at the upper stories as shown in Figure 24. A new failure mode was observed, wherein the rebar at the foot of the column buckled after masonry crushing, rather than a shear failure at the top of the column which is common in infill construction (See Figure 25). Some shear failures were observed at the tops of first story columns, but these structures did not appear to have shear connectors or tothing (See Figure 25).



Figure 24: (a) In-plane shear failure of first story (b) Out-of-plane failure of second story (Brzev et al. 2010)



Figure 25: Buckling of rebar at foot of column (left) and shear failure of first story column (right) (Brzev et al. 2010)

2.3.4 Hybrid Masonry Systems

2.3.4.1 System Description

The study of hybrid masonry systems was first introduced by David Biggs in 2007. Essentially, it is a system in which the infill panel is designed to act integrally with

the frame to carry a portion of the seismic load. Thus far, no experimental studies have been conducted, but research is currently in progress at the University of Illinois on steel-frame hybrid masonry structures. Daniel Abrams has suggested that hybrid masonry systems consisting of steel frames with reinforced masonry panels would help to reduce the cost of steel structures by eliminating the need for bracing, and still provide adequate seismic performance.

The International Masonry Institute and National Concrete Masonry Association has defined three types of hybrid masonry systems (Hybrid Masonry Design 2009). The three types are shown in Figure 26. In all cases, the infill panel is reinforced to accommodate the design forces in tension and shear. A type I system transmits out-of-plane loads and in-plane shear loads and gaps are provided between the masonry and the bounding frame. Out-of-plane loads are transferred through anchors at the top which should not transmit axial loads. Anchors may also be used at the column-masonry interface, but they should not transfer shear loads, and the columns should not bear against the masonry under the expected design-level drifts. A type II hybrid masonry system is constructed with the wall tight to the beam and top anchors are provided which transfer shear, out-of-plane load, and axial load into the masonry. Gaps are provided between the columns and the infill, and if anchors are provided they should not transfer shear loads. In a type II system the infill wall becomes a load-bearing wall, unlike the type I system. A Type III masonry system is confined within the framing and is designed to support axial, shear and out-of-plane loads. The behavior of these types of systems becomes more complex, and testing is underway to better understand the response of these structures to seismic loading (Abrams 2011; Abrams et. al. 2010).

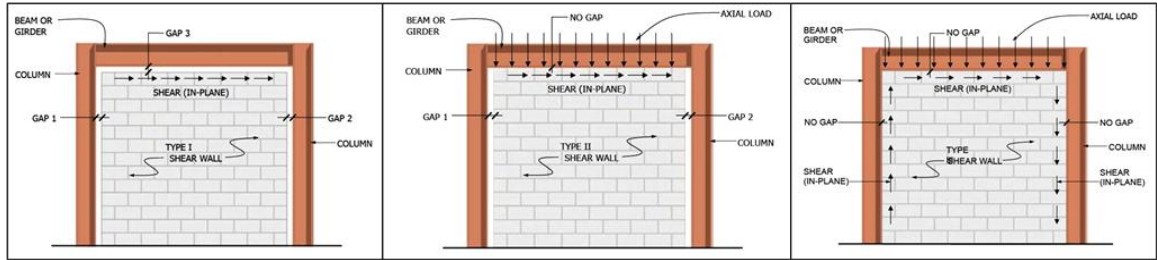


Figure 26: Diagrams of hybrid masonry systems types I-III (left to right) (Hybrid Masonry Design 2009)

2.4 Chapter Summary

In reviewing the existing finite element models for concrete and masonry, the lack of simplified models, and the existing literature on similar concrete and masonry structures, one can see the necessity of a new type of modeling scheme for hybrid concrete masonry and seismic testing of these structures. It is anticipated that like traditional masonry infill and confined masonry, hybrid concrete-masonry will exhibit complex failure mechanisms which must be captured by the finite element model. The models which are solely of a discrete crack or a smeared crack formulation all have distinct trade-offs with respect to model accuracy and complexity of the formulation. For this reason, a combined smeared crack and interface element constitutive model was chosen from which the modeling scheme for hybrid concrete-masonry is developed.

CHAPTER 3

CONSTITUTIVE FINITE ELEMENT MODEL AND VALIDATION STUDIES

This work utilizes and expands on the finite element modeling scheme first proposed by Lotfi and Shing (1991) and subsequently improved upon by: Lotfi and Shing (1994), Mehrabi and Shing (1997) and Stavridis (2009). The formulation uses fixed smeared crack elements to model compression and tension failure of the masonry and concrete, combined with discrete interface elements to model shear failure and tension failure. The interface elements prevent direct contact of smeared crack elements. This reduces the undesirable stress-locking, spurious mode effects, and mesh-sensitivity exhibited in traditional smeared crack element models. In the subsequent chapter, the modeling scheme is first outlined. Then details of the element formulation are described, followed by the procedure for calibrating the model to material data for concrete and masonry. Finally, a series of validation studies are presented ranging from single element tests to a model of a multi-story infill structure. The results of the validation studies indicate the constitutive model is robust and can be used with confidence as the basis for the development of finite element models of hybrid concrete-masonry structures.

3.1 Modeling Scheme

To model concrete, the interface elements are placed in a module with smeared crack elements such that crack locations do not need to be known a priori (Stavridis and Shing 2010). Each module consists of four triangular smeared-crack elements connected with four, diagonally placed, double-noded, zero-thickness interface elements as shown

in Figure 27. Each module is connected to the adjacent modules with horizontal and vertical interface elements. Using this meshing scheme, discrete cracks can develop at angles of 0° , 90° , and $\pm\theta$ with θ being as close to 45° as permitted, in order to represent possible diagonal shear cracks. Reinforcement is modeled with discrete truss elements which connect a node of the smeared crack element to the corresponding node in the smeared crack element below (See Figure 27). The behavior of the steel truss elements is governed by an elastic perfectly plastic stress-strain curve. Horizontal reinforcement is modeled with two truss elements placed in a cross pattern to ensure that they are effective in shear, rather than sliding along the horizontal interfaces.

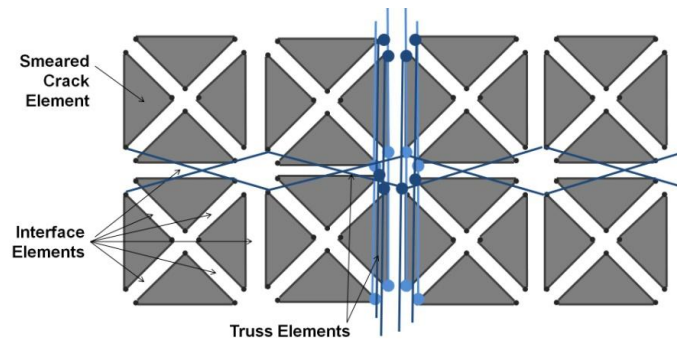


Figure 27: Assembly of smeared crack elements, interface elements, and truss elements to model reinforced concrete (Stavridis and Shing 2010)

The masonry infill wall is modeled with smeared crack elements that represent a half block with a vertical brick interface element in the center as shown in Figure 28. Mortar bed and head joints are also modeled using interface elements.

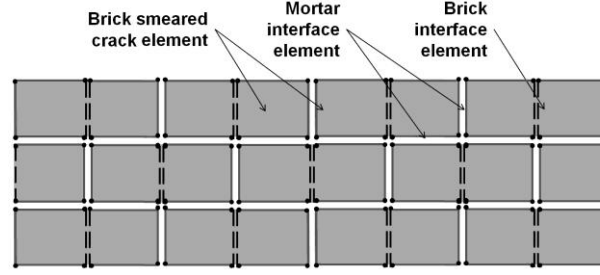


Figure 28: Assembly of smeared crack and interface elements to model masonry (Stavridis and Shing 2010)

3.2 Element Formulation

The smeared crack elements utilize a plasticity-based formulation for the compressive behavior of uncracked material. The failure surface is governed by a Von Mises failure criterion as shown in Figure 29. The compressive behavior of the element between the initial yield surface and the failure surface is governed by a curve that captures strain hardening and subsequent softening observed in concrete and brick (Figure 30a). The shape of the plasticity curve is governed by f_0 , the compressive strength at the point of initial softening; f'_m , the peak compressive strength; ε_{1p} , the plastic strain at peak strength; ε_{2p} , the plastic strain at the transition point; and $r_p f'_m$, the residual compressive strength.

The tensile failure is initiated when the maximum principal stress reaches a Rankine-type cut-off criterion. The material then becomes orthotropic with the axes of orthotropy fixed perpendicular and parallel to the crack. The compressive behavior parallel to the crack is captured with a parabola with an exponentially decaying tail that is shown in Figure 30(b). Like the plasticity curve, the orthotropic compressive behavior is a function of the peak compression strength, f'_m , and the residual compression strength of

the material, $r_p f'_m$, but the strain at peak strength, ϵ_1 , and at the transition point, ϵ_2 , are given with respect to the total strain in the material.

The stresses perpendicular to the crack are governed by an exponential softening curve (See Figure 31). The strain at cracking ϵ_{cr} , is determined from the elastic modulus of the material and the tensile strength, f'_t . The parameters α_1 , a shape factor, and r_t , the coefficient of residual strength, control the relative brittleness of the material. For both the compressive and tensile material curves, a relatively small amount of residual capacity is employed to help the model remain numerically stable.

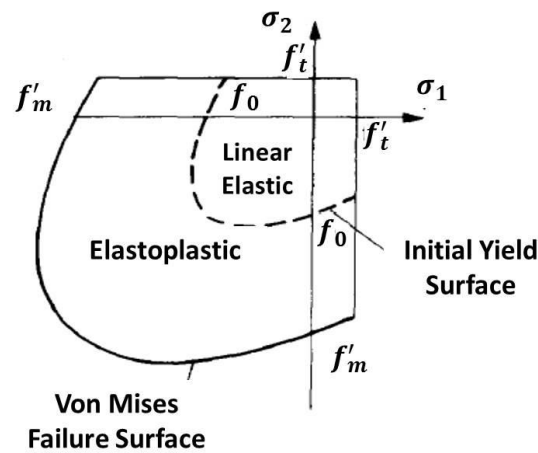
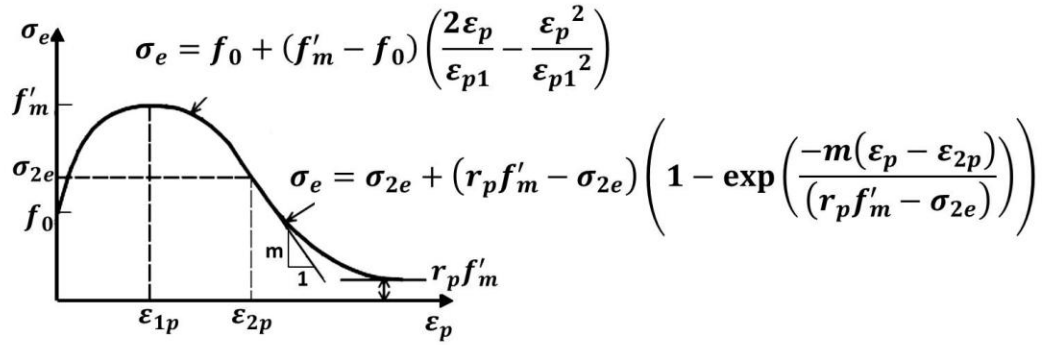
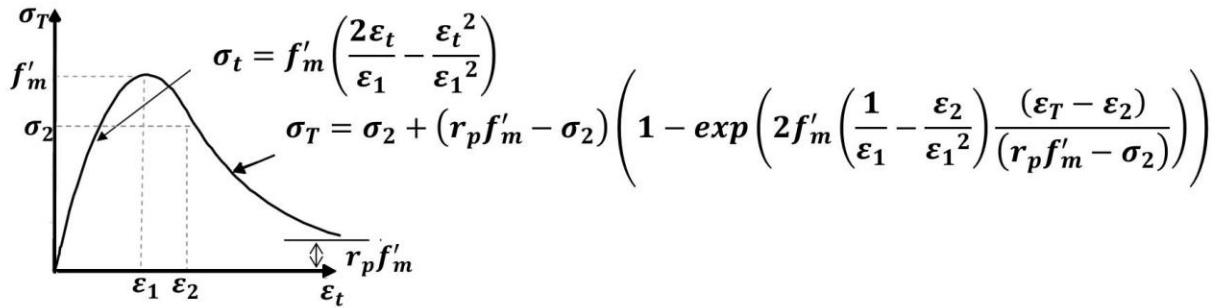


Figure 29: Failure surface for masonry and concrete (Lotfi and Shing 1991)



(a) Plasticity model



(b) Orthotropic model

Figure 30: Equations governing compressive behavior (Lotfi and Shing 1991)

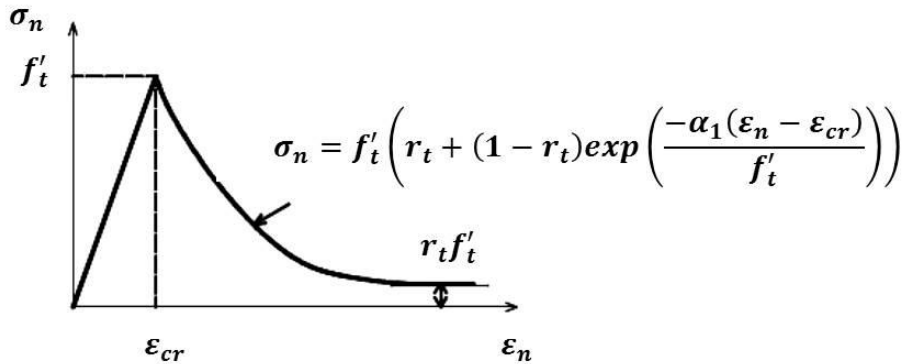


Figure 31: Stress vs. strain normal to the crack surface (Lotfi and Shing 1991)

The interface elements, developed by Lotfi and Shing (1991), are double-noded elements with zero thickness, as shown in Figure 32(a). The interface model is capable of modeling mode-I, mode-II and mixed mode fracture. The model was adopted from a

traditional discrete formulation to incorporate the effects of shear dilatation observed in concrete and masonry. The interface elements do not fail in compression, as their main function is to capture the opening of cracks. The stress strain relation is based on plasticity theory with a hyperbolic yield surface (See Figure 32b), which is described with Equation 8.

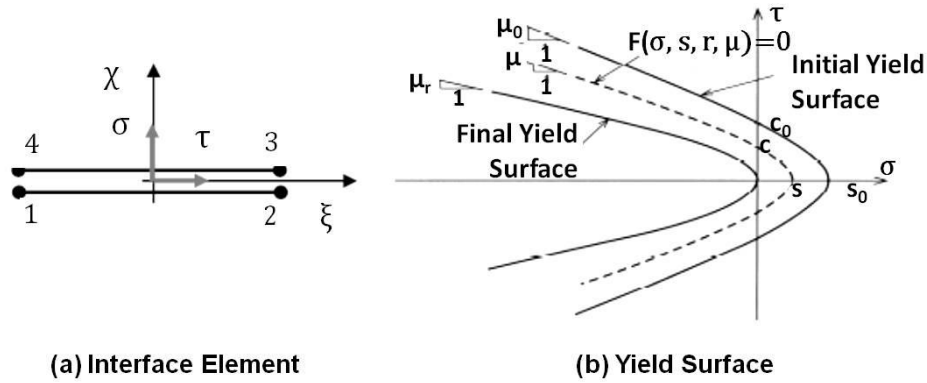


Figure 32: Local axis and complete yield surface diagram for interface element (Lotfi and Shing 1994)

$$F(\sigma, s, r, \mu) = \tau^2 - \mu^2(\sigma - s)^2 + 2r(\sigma - s) = 0 \quad (8)$$

Essentially the yield surface is a smooth transition from a Mohr-Coulomb to a tensile cut off criterion. The yield function becomes the Mohr-Coulomb criteria when r equals zero and the yield criteria is equal to the tension cut-off criteria for extremely large values of r and μ (See Figure 33).

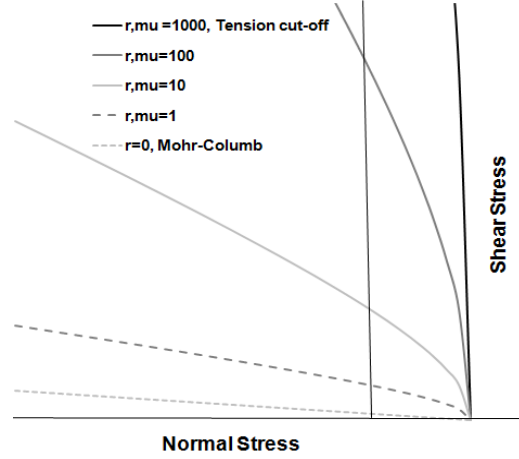


Figure 33: Effect of internal variables on interface element yield surface

The softening rules for each of the variables s , r , and μ , which govern the evolution of the yield surface from its initial to residual state, are provided in Equation set 9. In the equations, G_f^I and G_f^{II} are mode I and mode II fracture energies, α and β control the rate of reduction of r and μ , and the k_i terms represent the plastic work which governs the strength degradation.

$$s = s_0 \left(1 - \frac{k_1}{G_f^I} - \frac{k_2}{G_f^{II}} \right) \geq 0, \quad r = r_r + (r_0 - r_r)e^{-\beta k_3}, \quad \mu = \mu_r + (\mu_0 - \mu_r)e^{-\alpha k_3} \quad (9)$$

The displacements of the nodes during plastic flow are determined using the classical incremental plasticity definition of a flow rule ($d^p = \lambda \frac{\partial Q}{\partial \sigma}$). The formulation for the plastic potential, Q , takes into account the effects of shear dilatation with the appropriate calibration of the parameter η (Equation 10). This parameter scales the dilatancy, which decreases as the material wears.

$$Q(\sigma, s, r, \mu) = \eta \tau^2 + (r - r_r)(\sigma - s) \quad (10)$$

3.3 Material Calibration

3.3.1 Concrete

When calibrating the module of smeared crack and interface elements which represent concrete, the tensile relations of the smeared crack elements and the interface elements must be calibrated such that crack propagation is not favored in either element. To do this, the tensile behavior of the interface elements is first calibrated and then the constitutive relations for the interface element are used to calibrate the smeared crack elements.

It is sufficient to use split cylinder tests to calibrate tensile strength, f_t' , because the presence of rebar in the concrete columns and beams reduces the influence of the tensile strength of the concrete on the flexure behavior of the frame. Since the interface elements should not influence the concrete stiffness prior to fracture, the value for interface element stiffnesses, D_n and D_t , should be made artificially high, but not high enough to ill-condition the solution. Mode I fracture energy, G_f^I , can be taken from typical values or calculated using empirical formulas (Bazant and Becq-Giraudon 2002). Mode II fracture energy is difficult to obtain, but previous studies have shown G_f^I to G_f^{II} can be between 10 (Lotfi and Shing 1991) and 25 (Bazant 1986). Using these values and assuming typical values (Stavridis and Shing 2010) for r_0 , r_r , μ_0 , μ_r , α and β , a single-element tensile test can be conducted. Once the stress-displacement curve is determined, the values of r_0 , r_r , μ_0 , μ_r , α and β , can be adjusted to achieve the desired fracture energy (See Figure 34).

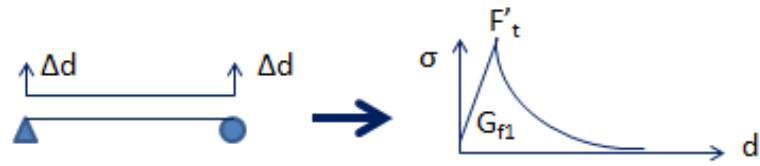


Figure 34: Schematic of interface element tension test and resulting stress-displacement curve

Tensile behavior of the concrete smear crack element is calibrated with the stress-displacement curve for the concrete interface element. Both tensile strength relationships are transformed to stress-displacement for comparison, as the interface elements have zero length and strains cannot be obtained. To do this, a characteristic length is defined with which the strains of the smeared crack element are multiplied to obtain displacements. For a CST element, a good approximation for this value is the square root of the element area (Papadrakakis et. al. 2005) . Because the smeared crack elements are calibrated with respect to characteristic length, separate material calibrations must be conducted for each of the mesh sizes used in the model. The value of elastic modulus for the smeared crack element can be determined from compression tests. Then, one must iterate on the value of the parameter α_1 in order to match the interface element tensile stress-displacement curve.

The compression behavior for the smeared crack element can be calibrated with uniaxial compression tests. The values for f'_c , ϵ_1 and ϵ_2 in the orthotropic model should be adjusted such that the orthotropic curve is fitted to the results of these tests. Once the orthotropic compression curve is obtained, the isotropic stress strain curve can be calibrated to match the behavior of the orthotropic model as shown in Figure 35. This

calibration insures a smooth transition in compression behavior from the uncracked to the cracked state.

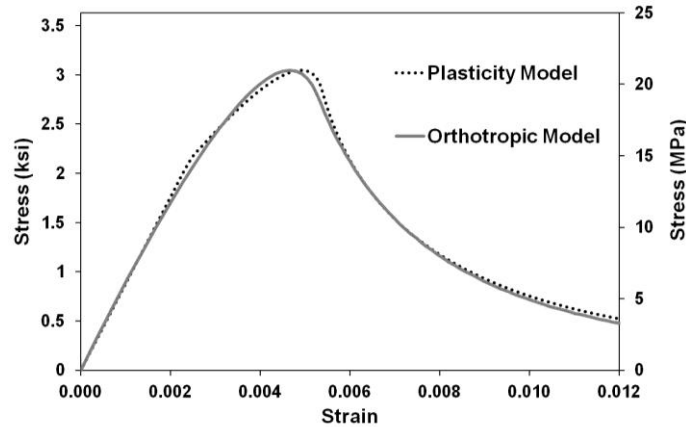


Figure 35: Isotropic compression curve for concrete calibrated to orthotropic compression curve

3.3.2 Masonry Assembly

The masonry assembly is modeled with three groups of elements: the smeared crack elements representing the brick units and the vertical interface elements representing the brick web or likely splitting location, and the interface elements representing the bed and head mortar joints. These groups of elements need to be calibrated considering the mechanics of the modeling scheme: the mortar interface elements represent the behavior of the mortar, as well as that of the brick-mortar interfaces and therefore simulate the tensile and the shear failure of the joints, while the smeared crack elements simulate the crushing of the masonry.

Calibration of the masonry assembly can begin with the mortar interface elements. For the calibration of the tensile behavior of the bed joints, data from direct tensile tests would be required. In lieu of these tests, data from bond-wrench or beam

tests can be used. The shear behavior of the mortar bed joints can be calibrated with data from masonry assembly tests that consider the interaction between the mortar joints and brick units. The peak and residual shear stress values can be obtained from direct shear tests (Amadei et. al. 1989; Manzuri 1995; Mehrabi 1994), triplet tests (EN 1052-3), or shove tests repeated under different values of normal stress. As shown in Figure 36, the peak strengths can be used for the calibration of the initial yield surface, i.e. parameters s_0 , r_0 , and μ_0 , while the residual strengths can be used for the calibration of the final yield surface that is defined by parameters s_r (equal to zero), r_r , and μ_r . Assembly shear tests can also provide information on the elastic tangential stiffness, D_t , and the mode II fracture energy, G_f^{II} . The elastic stiffness of the mortar joint under normal stress, D_n , can be assumed to be $2D_t(1 + \nu)$.

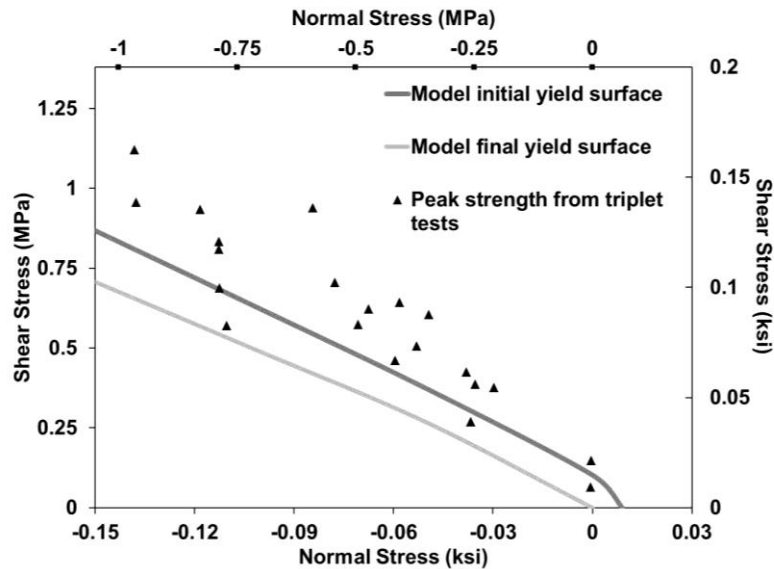


Figure 36: Shear behavior of mortar interface elements calibrated to test data (Magenes and Calvi 1992)

The mode I and II fracture energies express work per unit area and they are used to determine the rate of loss of the tensile strength of the interface elements as shown in Equation 9. The value of mode-I fracture energy, G_f^I , can be obtained considering that the ratio of G_f^I to G_f^{II} can be between 10 (Lotfi and Shing 1991) and 25 (Bazant 1986). The material parameters α and β which control the rate of loss of cohesive strength and frictional resistance as indicated in Equation 9, and the parameter η , which scales the shear dilatation as shown in Equation 8, can be calibrated with data from shear tests.

Mortar head joints are generally considered to have poor bond strength compared to mortar bed joints because they are more difficult to place and do not have the benefit of axial compression to reduce shrinkage stresses (Drysdale et. al. 1994; NCMA 2004). Numerical representations of mortar head joints typically fall in one of two categories. Either the bed joints and head joints are given the same properties (Lotfi and Shing 1994; Lourenco 1996) or the head joints are assumed to have little or no bond strength (Mojsilovic and Marti 1997; Schlegel and Rautenstrauch 2004). For the constitutive model presented here, the ratio of head joint bond strength to bed joint bond strength has very little influence on the peak lateral strength and initial stiffness of unreinforced masonry walls (See Appendix C for results of the parametric study). At very low ratios of head joint to bed joint bond strength, the cracking patterns change to significantly to favor head joint cracking. In light of the study, the head joint to bed joint bond strength will be initiated at 0.5 for all models and increased if cracking patterns are inconsistent with the experimental observations.

As illustrated in Figure 28, the brick units are modeled with a combination of smeared crack and interface elements, which must be consistently calibrated to capture

tensile failure. The brick interface elements are typically calibrated first as they represent cracks in a more direct manner and their calibration does not depend on the element size. The brick interface elements are not supposed to influence the behavior of the masonry panel before fracture. Therefore, their normal and tangential elastic stiffnesses, D_n and D_t , should be high, but not too high to make the model numerically ill-conditioned. The tensile strength of the bricks, f'_t or s_0 , can be estimated from tensile splitting or modulus of rupture tests. In lack of such data, one can assume that their tensile strength is approximately 10-15% of the compressive strength based on data from the literature. Data from the literature can also be used to obtain the mode I fracture energy, G_f^I , which in turn, can be used to obtain the mode II fracture energy, G_f^{II} , with the same relations used for the mortar interface elements. Information for the calibration of the parameters α , β , r , and the dilatation parameter, η , are generally not readily available and shear tests needed to obtain these values are difficult to conduct. The influence of these parameters has been characterized in the parametric study (Redmond et. al. 2014) and values from the literature can be selected in a conservative manner.

The calibration of the smeared crack elements in tension involves the shape factor α_1 which does not represent a physical quantity. However, it can be calibrated with the use of the calibrated stress-displacement curve of the interface element. This can be achieved if the stress-strain relation of the smeared-crack elements is converted to stress-displacement with the use of a characteristic length that can be assumed to be equal to the square root of the element area. Hence, one needs to come up with different shape factors for each different size of brick element.

The compressive failure of masonry is caused by the Poisson ratio mismatch between the brick units and the mortar joints which leads to tensile splitting of the bricks. The plane-stress elements used here cannot directly capture this phenomenon. However, the brick smeared crack elements can be calibrated to represent the compressive strength of the masonry assembly that is usually obtained from prism tests (Lourenco 1996). The flexibility of the mortar interface elements should be considered so that one brick smeared-crack element and one mortar interface element represent the prism stress-strain curve.

The uniaxial compressive behavior of the orthotropic model can be calibrated first as it requires the selection of only three parameters. The compressive strength, f'_m , can be selected as the strength of the prisms. With the stiffness of the mortar element already defined, one can select the strain at peak strength, ε_1 , and the strain which determines the onset of exponential decay, ε_2 , such that the assembly matches the prism behavior. The ratio of the residual compression, r_p , is typically taken as 5% of the compressive strength for numerical stability. Finally, the plasticity model employed to model the compressive behavior of the uncracked material can be calibrated to match the orthotropic compression curve so that there is a smooth transition to the latter once a crack initiates.

3.4 Model Validation

The finite element modeling scheme is evaluated in a series of models ranging from single element behavior to replicating large scale dynamic tests. First, element level tests in pure tension and compression are used to understand the influence of the interface element on the local behavior of the smeared crack elements. Next, the combined smeared crack and interface element model is compared to traditional continuum models

with only smeared crack elements for a column failing in flexure and a column failing in shear. Next, component-level validations are conducted by modeling a cyclic test of a bare RC frame and cyclic tests of a series of unreinforced masonry walls. Finally, the proficiency of the composite model to represent the behavior of the entire concrete and masonry system is demonstrated by modeling a pseudo-dynamic test of a three bay, three story, reinforced concrete frame with unreinforced masonry infill.

3.4.1 Pure Tension and Pure Compression

In order to characterize the effect of adding the interface elements to the boundaries of the smeared crack element, pure tension tests and pure compression tests were conducted on a 12x12 inch square discretized with one element, four elements and nine elements, with and without interface elements. Figure 37 shows the cracking patterns of the tensile specimens. The presence of interface elements at the boundaries does not influence the cracking patterns nor the displacement at which cracking occurs.

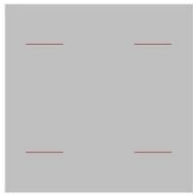
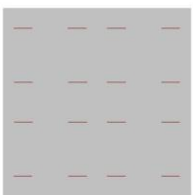

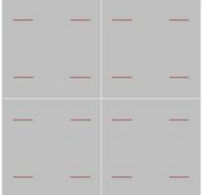
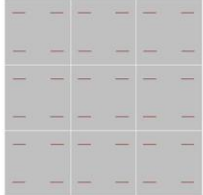
	1x1	2x2	3x3
No Interface Elements			
Interface Elements	N/A		

Figure 37: Results of pure tension tests with and without interface elements

Although interface elements do not directly correct the mesh sensitivity of the smeared crack elements in the post-peak softening behavior, the tensile calibration method assures consistent post-peak behavior with mesh refinement (See Figure 38).

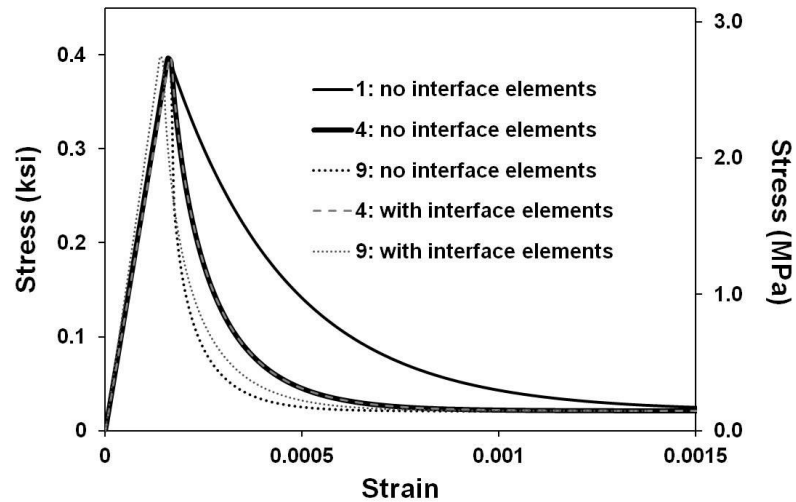


Figure 38: Tensile stress vs. strain behavior with mesh refinement, with and without interface elements

Figure 39 shows the crushing patterns of the compression specimens. The presence of interface elements at the boundaries does not influence the crushing patterns for the specimen or the displacement at which crushing occurred.

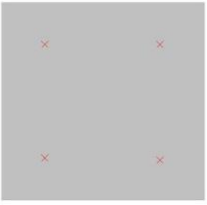
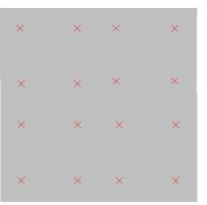


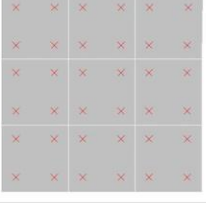
	1x1	2x2	3x3
No Interface Elements			
Interface Elements	N/A		

Figure 39: Results of pure compression tests with and without interface elements

The presence of interface elements does not correct the mesh sensitivity in the post-peak softening behavior present in smeared crack elements. This is shown in Figure 40. Thus, it is desirable to choose the element size based on expected failure area and calibrate the smeared crack element compression curve to material behavior.

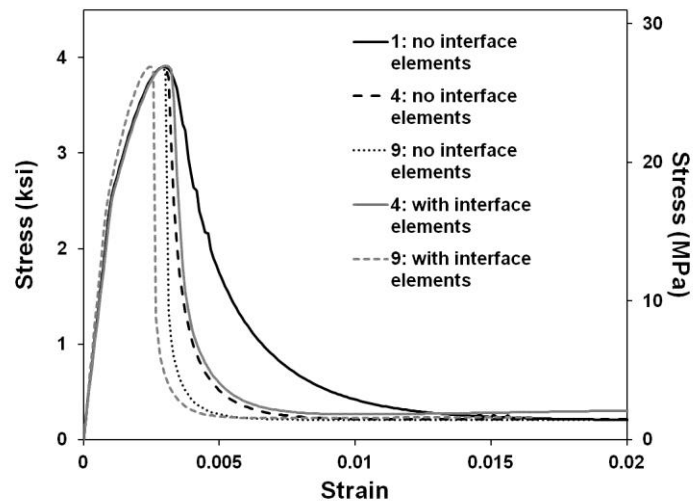


Figure 40: Compression stress vs. strain behavior with mesh refinement, with and without interface elements

3.4.2 Flexure Column

The concrete module presented in Section 3.1 and a traditional smeared crack elements were used to simulate the behavior of a column which failed in flexure under cyclic loading (Nosho et. al. 1996). Three models were created, one with a combination of interface elements and smeared crack elements placed in a module, and two models using only smeared crack elements different levels of mesh refinement. Values for compressive strength of the concrete, reinforcement yield strength, and rebar configurations were taken from the test data. As full stress-strain plots from concrete compression tests were not provided, the strain at peak compressive stress of the concrete was permitted to vary within the expected ultimate strain of concrete to obtain the best match to the initial stiffness of the experiment. The concrete ultimate strain is slightly different in each model, as traditional smeared crack elements tend to yield stiff results, and the combined model tends to yield more flexible results. The difference between the final calibrated compression behavior for the model with the interface elements and the models without interface elements can be seen in Figure 41. Fracture energy and initial and residual shear properties were initiated at values found in literature (Hillerborg 1983; Mehrabi 1994) and varied to achieve the desired cracking. A comparison of the material properties used in each model is given in Appendix C.

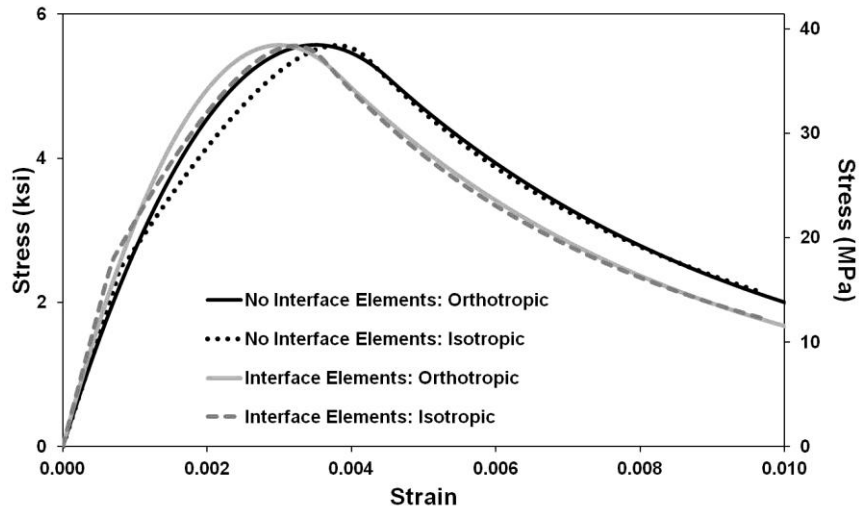


Figure 41: Concrete compression behavior

The cracking patterns for the experimental specimen, the model with interface elements and the two models without interface elements are shown in Figure 42. The failed interface elements are colored red to show the flexural cracking present in the first model. All models capture the flexural cracks and crushing of the bottom portion of the column.

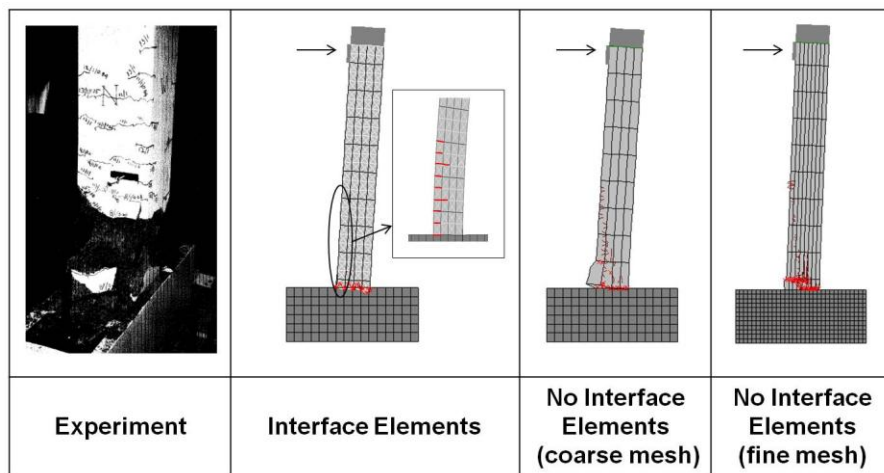


Figure 42: Cracking and crushing of column after failure in the experiment (Nosho et al. 1996) and analytical models

All of the models predict capacity within 7% of the peak column strength recorded in the experiment (See Figure 43). The model with interface elements permits more stress release as the interface elements open and thus does not fail as early as the models using traditional smeared crack elements. The model with interface elements predicts displacement at peak strength within 1% of the displacement recorded in the experiment. The model without interface elements using the coarse mesh has 18% error in predicting displacement at peak strength, and the model without interface elements using a fine mesh has 18.5% error.

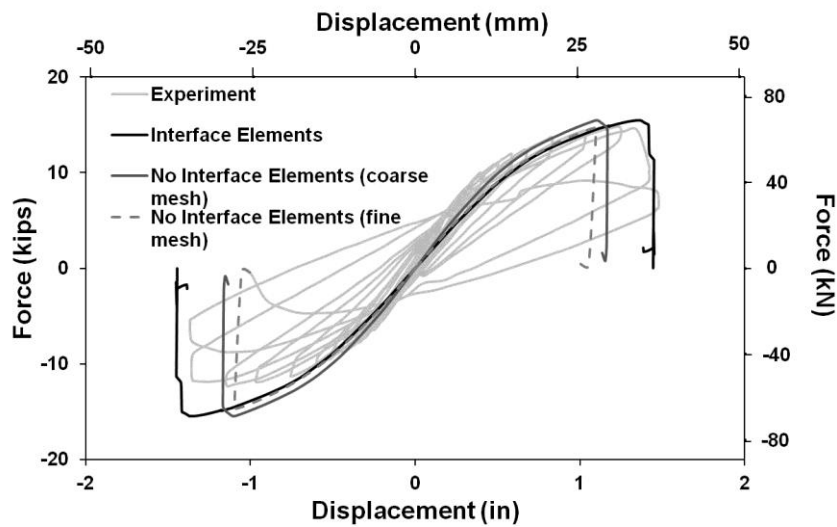


Figure 43: Force displacement curves for the flexure column experiment (Nosho et. al. 1996) and analytical models

3.4.3 Shear Column

The concrete module presented in Section 3.1 and a traditional smeared crack elements were also used to simulate the behavior of a column which failed in shear under cyclic loading (Lynn et. al. 1998). The study provided values for compressive strength of

the concrete, reinforcement yield strength, and rebar configurations. As with the flexure column models, the concrete compressive stress-strain curve for each model was calibrated separately and permitted to vary within the expected range of ultimate strain in concrete. The difference between the calibrated stress-strain behavior in compression for the two models can be seen in Figure 44. Fracture energy and initial and residual shear properties have been selected within the range of typical values from the literature (Hillerborg 1983; Mehrabi 1994) as no material data for these parameters was provided in the study. A comparison of the material properties used in each model is given in Appendix C.

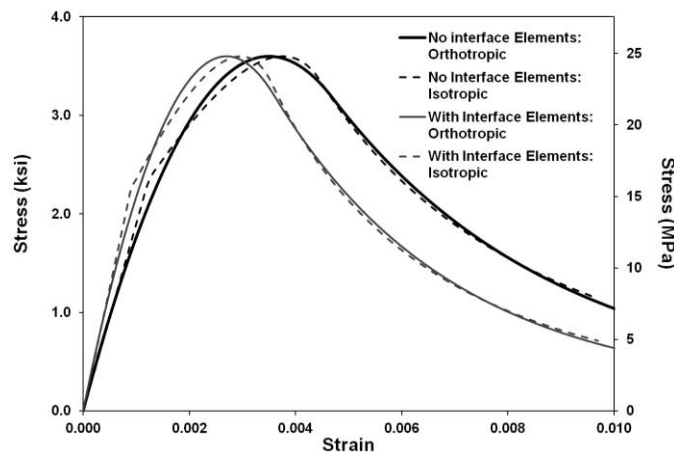


Figure 44: Concrete compression behavior

The results of the two models show that the model without interface elements vastly over predicts the strength of the column (See Figure 45). The composite model correctly predicts strength within 1% of the experimental peak, and the traditional smeared crack element model over predicts strength by 16.7%. The displacement at peak

strength is nearly the same between the model with interface elements and smeared crack elements and the model with only smeared crack elements.

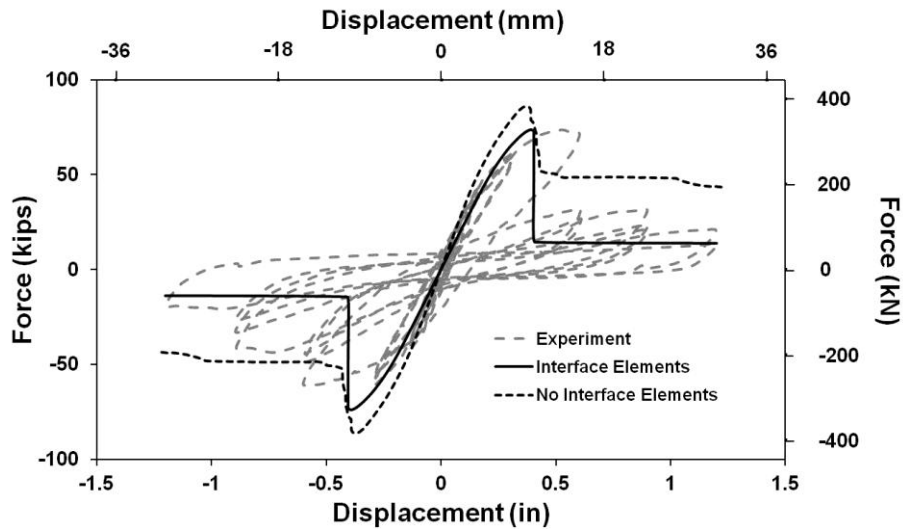


Figure 45: Force displacement curves for the shear column experiment (Lynn et. al. 1998) and analytical models

The cracking patterns of both models are representative of those which occurred in the experiment as shown in Figure 46. It is more difficult to see the shear crack in the model without interface elements as no crack opening occurs and the lack of stress relief causes additional crushing at the corner of the shear crack. Although the two models showed similar results in the flexural column test, the module of smeared crack and interface elements is far better at capturing shear behavior than smeared crack elements alone.

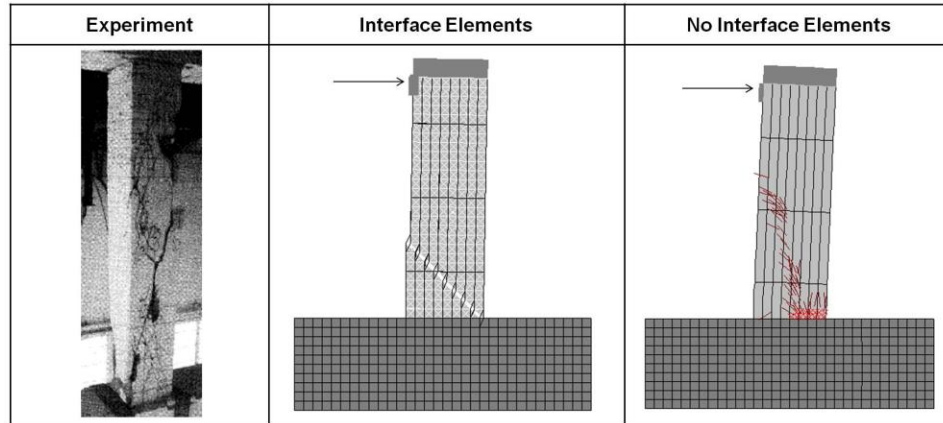


Figure 46:Cracking of column after failure in the experiment (Lynn et al. 1998) and analytical models

3.4.4 Bare Frame

In order to demonstrate the combined smeared crack and interface element model's ability to capture joint behavior and frame action, a cyclic test of a bare RC frame was modeled. The RC frame does not contain seismic detailing like hoops in the joint region, seismic hooks, or closely spaced horizontal reinforcement (Teymur et. al. 2012). Figure 47 shows the test specimen and reinforcement detailing. As with the previous column tests, only the concrete compression strength, reinforcement yield strength, geometry and rebar configurations were provided in the study. The concrete calibration was conducted in the same manner as the previous column tests. Interface element properties were initiated using values from Stavridis and Shing (2010) and permitted to vary within the ranges specified by their parametric study. The material properties used in the model are found in Appendix C.

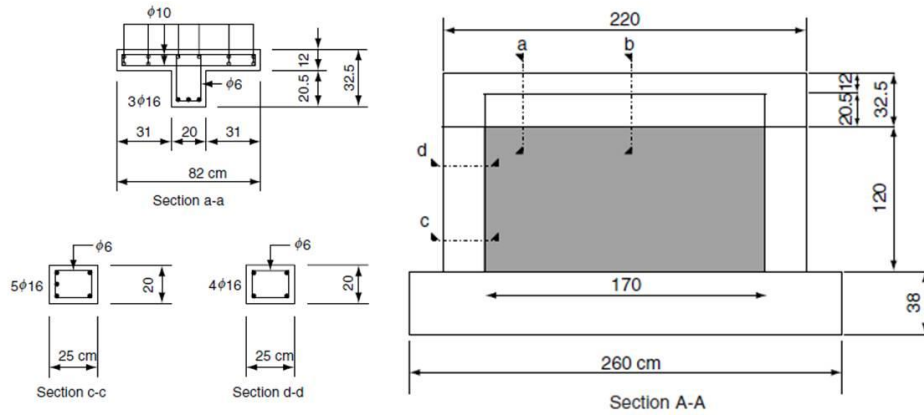


Figure 47: Test specimen and reinforcement details (Teymur et al. 2012)

The model does an excellent job of capturing the cracking patterns of the specimen. Figure 48 shows the cracking present in the experiment and in the analytical model.

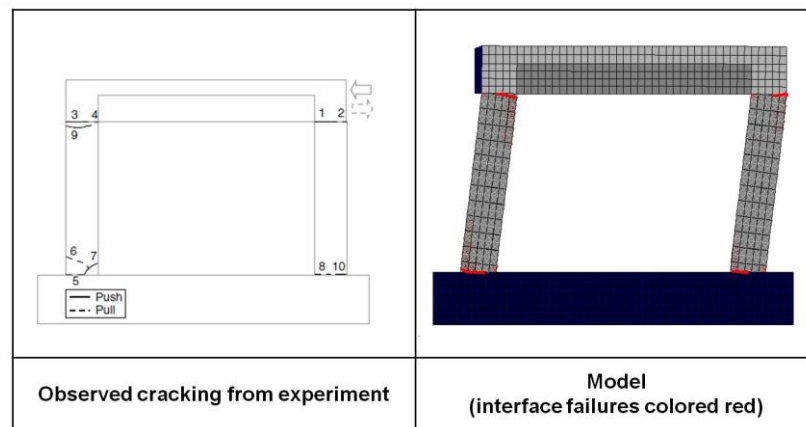


Figure 48: Observed cracking in the experiment (Teymur et al. 2012) and analytical model. Failed interface elements have been colored red

The model predicts peak strength within 2% of the experimental results (See Figure 49). However, the analytical model is slightly stiff compared to the experimental specimen and peak strength occurs earlier than in the physical test. This is in agreement

with the findings of Stavridis and Shing (2010). In this study, slight over-stiffness of the model for the bare frame specimen was observed, but the initial stiffnesses of frames with masonry infill were adequately captured by the model. Reinforced concrete frames with masonry infill are typically stiffer than open frames, so the slight over-stiffness of the model for modeling frame action is not likely to be significant when modeling infill structures.

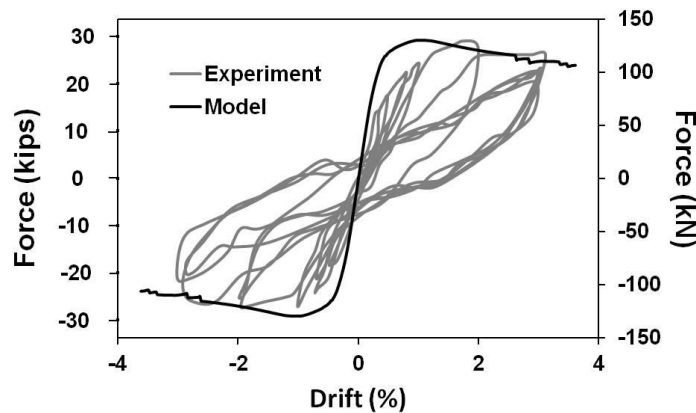


Figure 49: Base shear vs. drift for the bare frame experiment (Teymur et. al. 2012) and analytical model

3.4.5 Masonry Walls

A series of cyclic tests on four unreinforced masonry walls were used to evaluate the ability of the combined smeared crack and interface element model to capture the behavior of masonry subjected to lateral force (Magenes and Calvi 1992). The walls had varying aspect ratios and were subjected to different values of compression stress during cyclic loading. Additionally, the study had extensive materials tests from which to calibrate the model.

3.4.5.1 Test Set Up and Analytical Model

The wall dimensions and the vertical stresses applied on the four walls in the test series are summarized in Table 1, while the test setup is shown in Figure 50.

Table 1: Dimensions and applied stress for wall specimens (Magenes and Calvi 1992)

Specimen name	Wall dimensions (width x height) ft (m)	Initial compression psi (MPa)
MI1	4.92x6.56 (1.5x2)	174 (1.2)
MI2	4.92x6.56 (1.5x2)	58 (0.4)
MI3	4.92x9.84 (1.5x3)	174 (1.2)
MI4	4.92x9.84 (1.5x3)	58 (0.4)

Vertical jacks at the base of the specimens were used to apply a compressive stress to the masonry and apply pressure against a reaction slab at the top of the specimens. The compressive stresses of Table 1 were applied on the specimens prior to each test and then jacks are locked in place for the duration of the cyclic test. This caused a variation of the vertical load applied on the structure as the base of the structure was displaced laterally with a horizontal jack. The analytical model was constructed to represent the boundary conditions of the tests as shown in Figure 50. This required the estimation of a loading function for the compressive load in the analytical model so that it matched the vertical reactions recorded during the test, as illustrated in Figure 51.

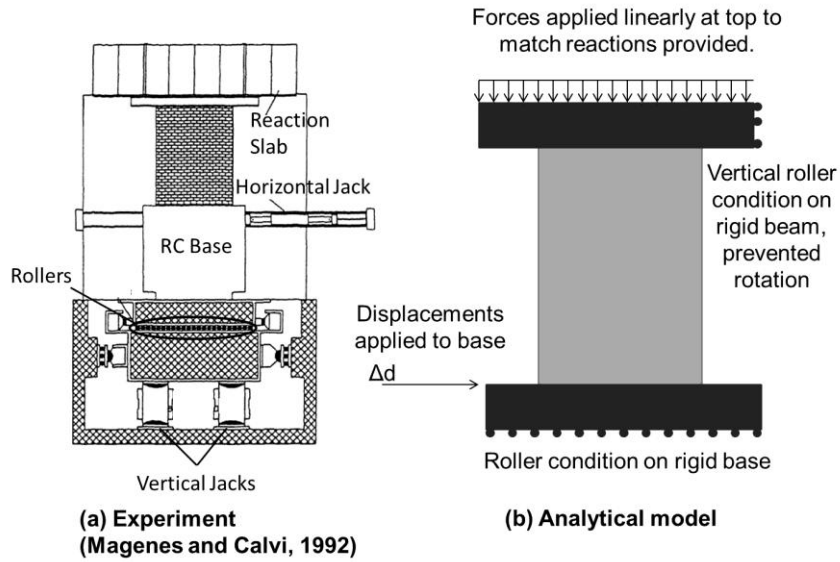


Figure 50: Geometry and test set up for the walls

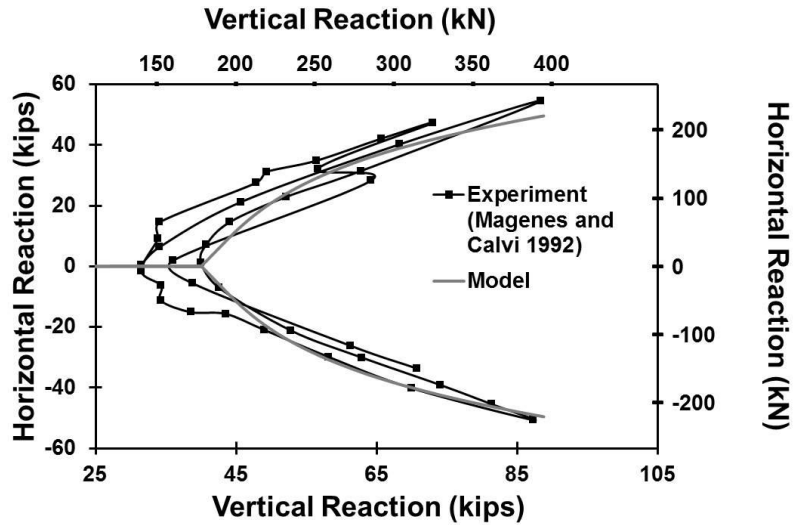


Figure 51: Tracked reactions from experiment (Magenes and Calvi 1992) and analytical model for wall MI2

The constitutive modeling scheme developed by Stavridis and Shing (2010) modeled walls with a running bond is shown in Figure 52(a). The modeling scheme was been modified to represent the English bond used in the walls by Magenes and Calvi

(1992) as shown in Figure 52(b). Two quarter block elements are connected to a half brick element with interface elements to represent the bricks in the stretcher rows. In the header rows, alternating bricks are represented by either one half brick element or two quarter brick elements. The horizontal interface elements connecting the rows of bricks represent the mortar bed joint.

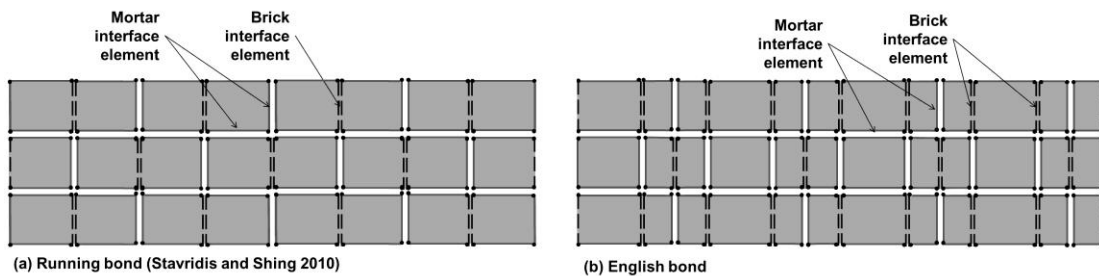


Figure 52: Assembly of smeared crack and interface elements to model masonry

3.4.5.2 Material Calibration

The material tests conducted by Magenes and Calvi (1992) have been used to obtain the compressive strengths of the bricks, masonry prisms, elastic modulus of the prism, tensile strength of the brick and mortar, and shear strength of the mortar. Fracture energy properties, G_f^I and G_f^{II} , and internal variables, α and β , which control softening of the interface element parameters have been selected based on values from literature (Bocca 1989; A. Mehrabi 1994). The vertical interface elements representing the mortar head joints were assigned the same properties as the bed joints, except their bond strength which was reduced by 50%. Appendix C contains the compressive curve for the masonry prism and the shear behavior of the mortar interface elements which were both calibrated

to tests conducted by Magenes and Calvi (1992). A list of all parameters used in the models is also given in Appendix C.

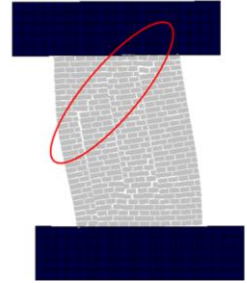
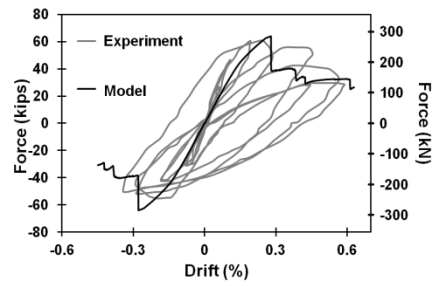
3.4.5.3 Results

The force-displacement behavior and cracking patterns of the finite element models are compared to the test results in Figure 53. In all four cases, the finite element models capture the important features of the response, as well as the failure mechanism of their experimental counterparts. The peak and residual capacities of the numerical models are in good agreement with the data from the experiment. For walls MI1 and MI2, that had aspect ratios equal to 1.33, the capacity of the heavily-loaded wall, MI1, is within 7% of the experiment while the capacity of the lightly-loaded wall, MI2, is within 15% of the experimentally measured capacity. For the walls with aspect ratios equal to 2.0, the capacity of the heavily-loaded wall, MI3, was within 10% of the experimental data, and the capacity of the lightly-loaded wall, MI4, is within 1% of the peak strength recorded in the experiment. The models in all cases predict accurately the failure patterns of the walls that is dominated by tensile splitting of the brick units or tensile and shear failure of the mortar joints. Both failure mechanisms are captured through the nonlinear behavior of interface elements. The failure of a number of these elements at one instant indicates the initiation of a dominant crack and results in a drop in the load carrying capacity as indicated by the force-displacement curves shown in Figure 53.

The initial stiffness and the stiffness after the apparent yield point up to the peak load also match well with the experimental behavior for all specimens except for MI1. In this case, the model is initially weaker than the experiment and the model reaches its full strength at a larger drift than in the experiment. This discrepancy may be due to batch-to-

batch variation of the mortar properties in the tests which is not reflected in the calibration of the numerical models. An analysis carried out with increased values for the stiffness and the fracture energy of the mortar element indicated that the initial stiffness of the numerical model can increase significantly. However, it was decided to use the same properties for the models presented here for consistency. For MI3, the other heavily loaded wall, which had an aspect ratio of 2.0, the model also reaches its strength at a slightly larger drift than the test specimen. For the two lightly loaded specimens, MI2 and MI4, the peak strength of the finite element models occurs at slightly lower drift levels than the drifts at peak strengths of the test specimens, but in all cases the difference is within 25%.

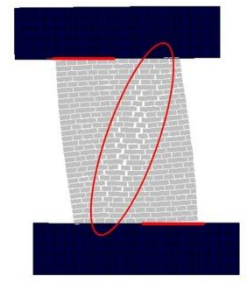
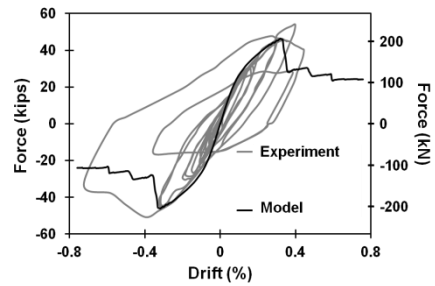
The comparison of the numerical and experimental results indicates that the modeling scheme can predict the failure mechanisms and cracking patterns of the masonry walls. Moreover, the numerical results for the peak strength are in all cases within 15% of the experimental values. The initial stiffness and stiffness degradation of the models is in good agreement with the experiment for all but one of the models, and this deviation could be attributed to test-to-test variability in the mortar properties.



MI1: (a) Force-displacement behavior

(b) Experiment

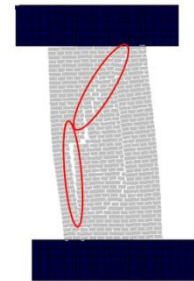
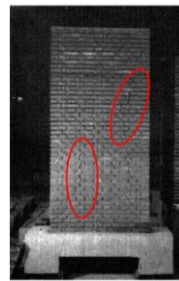
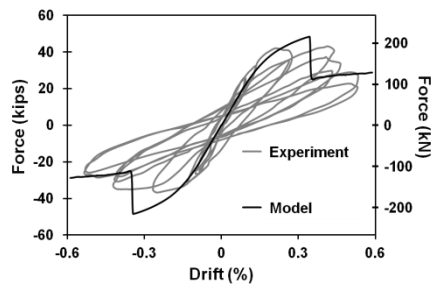
(c) FE model



MI2: (a) Force-displacement behavior

(b) Experiment

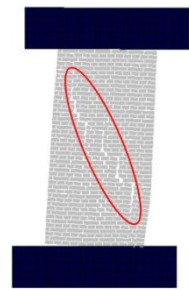
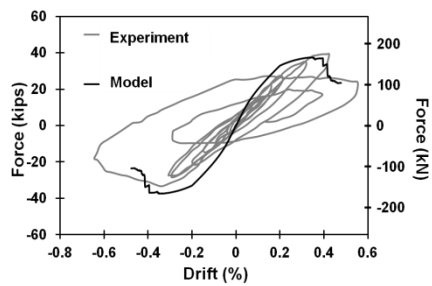
(c) FE model



MI3: (a) Force-displacement behavior

(b) Experiment

(c) FE Model



MI4: (a) Force-displacement behavior

(b) Experiment

(c) FE Model

Figure 53: Force-displacement behavior and cracking patterns of the finite element models compared to the test data (Magenes and Calvi 1992)

3.4.6 Three-Story, Three-Bay RC Frame with Unreinforced Masonry Infill

A 3-story 3-bay RC frame with hollow clay tile brick infill wall tested by Ezzatfar et al. (2012) was modeled to show that with the proposed modeling and calibration approach, the finite element model can capture the global force-displacement behavior, the cracking patterns in the masonry infill and the curvature of the RC columns.

3.4.6.1 Specimen Description

The test specimen is a half scale three-story three-bay RC frame (See Figure 54a). The reinforced frame is compliant with the Turkish seismic code and the reinforcement details of the frame components are presented in Figure 54d and 54e. The middle bay of the specimen is filled with hollow clay tile (HCT) infill walls in all stories (See Figure 54c).

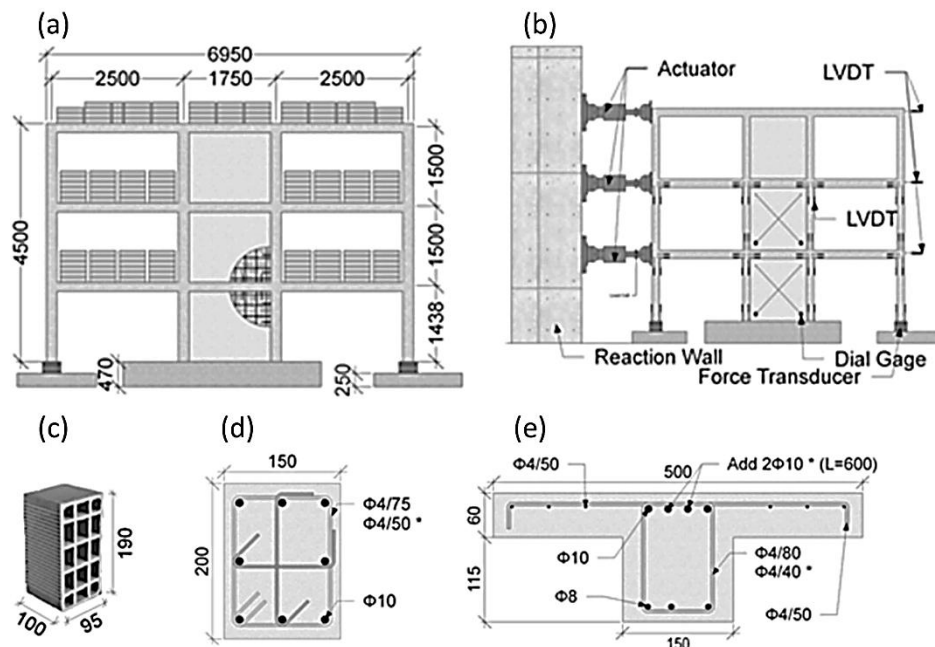


Figure 54: Test frame details (Ezzatfar et. al. 2012): (a) test frame dimensions (b) test set-up (c) hollow clay tile brick (d) column section detail (e) beam section detail (* denotes additional reinforcement and change in spacing in confined region, dimensions are in mm)

During the tests, story displacements were measured by two linear variable differential transformers (LVDTs) installed at each floor level, as shown in Figure 54b. Column and beam end rotations of the members in the first and second stories are measured with LVDTs. Shear deformation of infill walls were monitored by diagonally positioned LVDTs on infill walls of the first and second stories. Reactions (bending moment, axial force and shear force) at the base of external columns were measured using two special force transducers (Canbay et al. 2004).

Three different ground motions were applied to the test specimen with pseudo-dynamic testing technique. The ground motions were syntactically derived from Duzce city center site specific acceleration spectra corresponding to two levels of hazard and are shown in Figure 55. Spectral acceleration values were associated with 50% probability of exceedance in 50 years for stiff soil (D1), 10% probability of exceedance in 50 years for stiff soil (D2) and 10% probability of exceedance in 50 years for soft soil (D3).

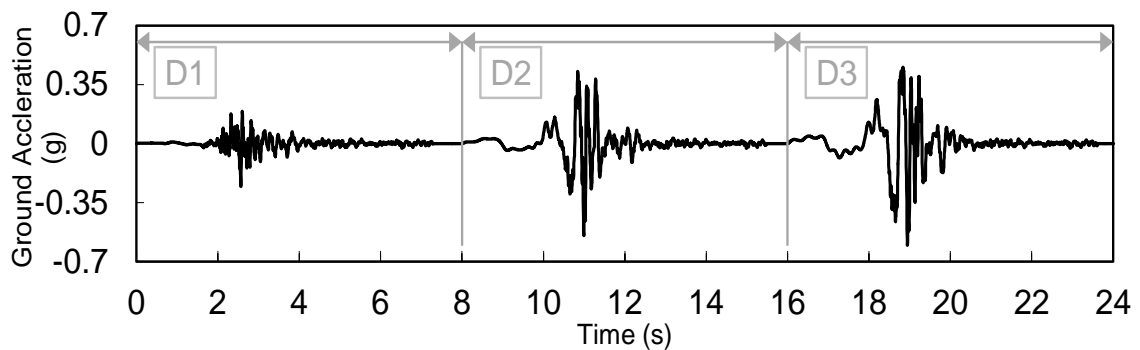


Figure 55: Ground motions (Ezzatfar et. al. 2012)

3.4.6.2 Finite Element Model

Most of the finite element model was constructed in the same manner as described by the constitutive modeling scheme. Modifications to the constitutive model were made in order to include the effect of plaster applied over the surface of the HCT infill walls. The out-of-plane thickness of the smeared crack elements representing the HCT units was approximated as the effective thickness based on net area of the unit. Mortar bed joints were also modeled using the effective thickness of the brick, but head joints were modeled using the full thickness of the HCT unit. The effect of the 10 mm (0.39 in) of plaster applied over the masonry was accounted for using a transformed section. The plaster thickness was converted to an equivalent thickness of brick in proportion to its compressive strength, as compressive strength has the greatest effect on global structural behavior. This same process was followed to determine the thickness of the mortar bed joints which represented both the mortar and the plaster applied over the mortar.

The mortar interface elements at the boundaries between the masonry and the concrete frame were given the same properties as the mortar interface elements in the interior of the masonry wall, with the exception of the interface between the top of the masonry wall and the beam. During construction, mortar was not injected between the last layer of masonry and the beam above, so the interface elements were given very low stiffness and tensile strength.

Figure 56 shows the structural model used for the analysis. Artificial truss elements are modeled to apply forces to the floor levels closely as possible to the forces applied during the experiment. The distances X_1 and X_2 were calculated by averaging the

first mode eigenvectors obtained from the time domain identification of the pseudo-dynamic test results.

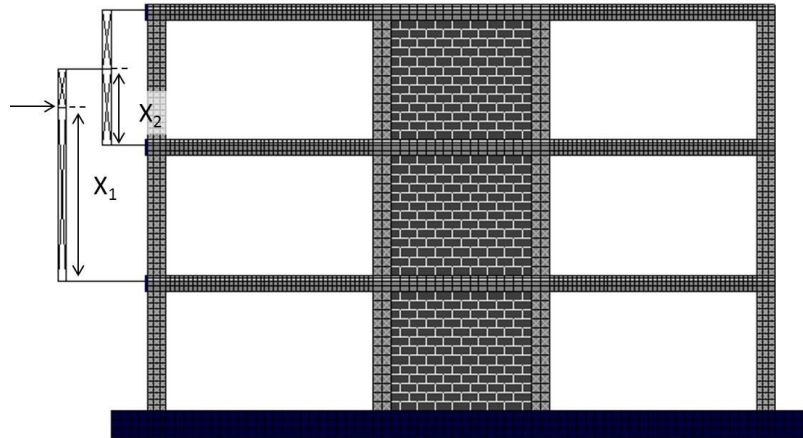


Figure 56: Finite element model showing the truss members used for load distribution

3.4.6.3 Material Calibration

Material data to calibrate the model was taken from the study and from other tests in the literature and followed the procedure outlined in Section 3.3. The calibration of the concrete is first discussed, followed by the calibration of the mortar and the masonry units.

The tensile behavior of the concrete interface elements is typically calibrated with data from split cylinder tests of concrete. Such tests were not conducted at the time of the experiment, hence the tensile strength of concrete was taken as 15% of the tested compressive strength as suggested by the literature (Oluokun 1991). The value for mode I fracture energy, G_f^I , was obtained from typical values for concrete with the same tensile strength (Hillerborg 1983). The tensile behavior of the concrete smear crack elements

was then calibrated with the stress-displacement curve for the concrete interface element following the calibration procedure in Section 3.3.1. The compression behavior for the concrete smeared crack element was calibrated with uniaxial compression tests.

The masonry walls include the following three groups of elements: the bed joint and head joint interface elements, the brick smeared crack elements, and the brick interface elements joining the half brick units. For this experiment, assembly tests like tensile pull off tests, triplet tests and prism tests to obtain the material properties were not conducted. In the absence of these tests, literature values and the compression tests of the brick units and mortar cubes were used to calibrate the model. The tensile strength of the mortar bed joint interface elements was approximated as 10% of the compression strength of the mortar cubes based on the tests reported by Stavridis (2009). The tensile strength of the mortar head joints was reduced by 50% to account for poor bond due to shrinkage cracking. Mode I fracture energy was taken as proportional to the tensile strength and the value used in the model was interpolated from values in the literature (Xu and Zhu 2007). In order to obtain shear properties for the mortar interface elements the slope of the yield surface (μ), and the radius of the yield surface (r), were initiated using values from Stavridis and Shing (2010) assuming shear strength and cohesion increased in proportion to the strength of the mortar. For the bed joints, these values were adjusted to account for increased cohesion due to mortar drippings which dried and partially filled the voids in the hollow units. An increase in cohesion of the bed joints was achieved by increasing the radius of the failure surface (r). Stiffness of the mortar bed joints and head joints were determined as part of the calibration of the compression behavior of the masonry assembly.

Due to the lack of data from prism tests, the compression tests of the brick units have been used to calculate the prism strength using a best fit line to the test data provided in the TMS 402-13 commentary. The estimated prism strength and stiffness has been verified to be within the ranges provided in statistical studies on masonry prism strength (Atkinson and Yan 1990). The stiffness of the prism has been assumed to be 300 times the compressive strength of the masonry prism (Kaushik et. al. 2007) and the stiffness of the brick smeared crack elements and the mortar interface elements are adjusted to achieve this stiffness following the procedure suggested by Stavridis and Shing (2010).

As was done for the concrete elements, the calibration of the tensile behavior of the brick was initially conducted for the brick interface elements, and then the constitutive relations for the interface element were used to calibrate the smeared crack elements. The tensile strength was assumed to be 15% of the compressive strength of the masonry unit. Mode I fracture energy was taken to be proportional to tensile strength and has been interpolated from literature (Bocca 1989).

The stress-strain curves for the tensile and compressive behavior of the concrete, the mortar and the masonry are found in Appendix C. Appendix C also contains a table with all of the modeling parameters.

3.4.6.4 Results

The observed damage during the experiment on the HCT specimen and cracking patterns from the finite element model are presented in Table 2. The photos presented in Table 2 were taken after the application of each ground motion and the experimental drift levels are the maximum first story drift when the damage was observed. The images from

the finite element model were taken at the step in which damage initiates and the specified drift corresponds to the first story drift at this step in the simulation.

During D1 earthquake, the specimen experienced minor damage at first story drift levels of 0.06-0.08%. Interface cracks between infill wall and frame and minor toe crushing were observed at the first level. In the finite element model, cracking initiates along the interface between the infill and the boundary column of the first story at 0.055% drift. There are also minor bed joint cracks in the finite element model.

Further damage occurred during the D2 earthquake between 0.4% and 0.7% first story drift. Diagonal and sliding cracks occurred in the first story infill walls and shear cracks formed at the boundary columns. A diagonal crack also opened in the second story infill wall. In the finite element model, combined diagonal and sliding cracks in the infill wall and slight shear cracking of the boundary columns are initiated at 0.1% first story drift. Minor diagonal cracking of the second story infill wall is observed at 0.44% first story drift.

During the D3 earthquake, intensive damage occurred in the boundary columns and the infill walls of the HCT specimen between 1.5-2% first story drift. The diagonal cracks and sliding mechanism of the first story infill wall extended and flexural cracks propagated along the height of the first story boundary columns. The diagonal crack of the second story infill wall also expanded and shear cracking of the second story boundary columns was also observed. Cracking patterns very similar to the experimental results are obtained from the finite element simulation. Additional shear and flexural cracks at the boundary columns and sliding cracks in the first story infill initiate at 0.73%

drift. The simulation also captures the diagonal cracking of the infill wall and shear cracks of columns in the second story.

Table 2: Observed damage of the HCT specimen in the experiment (Ezzatfar et. al. 2014) and finite element model

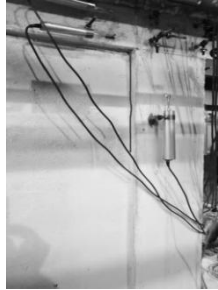
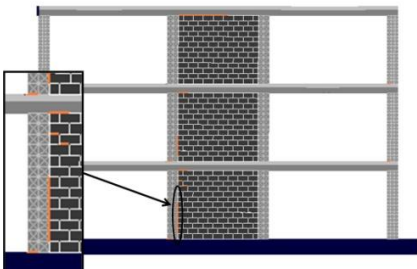
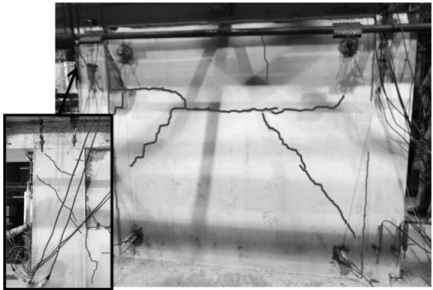
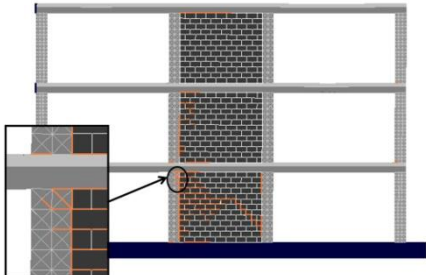
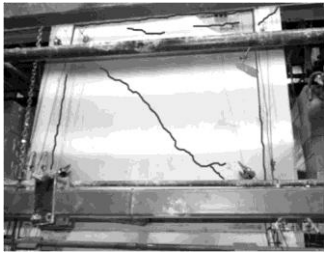
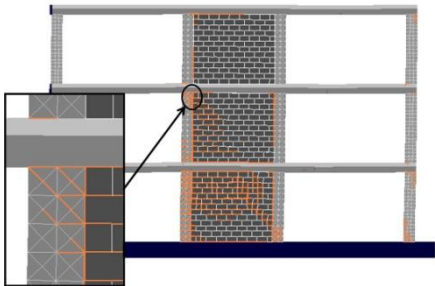
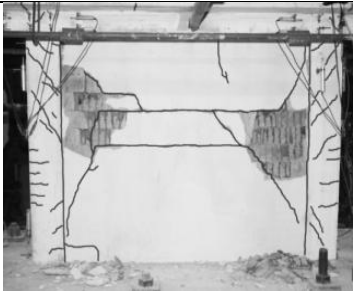
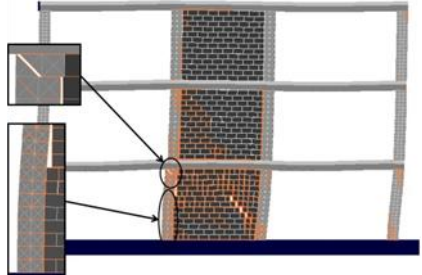
	Experiment	FE Model
D1 Earthquake	 <p>0.06-0.08%</p>	 <p>0.055%</p>
D2 Earthquake	 <p>(1)</p>	 <p>0.1%</p>
	 <p>(2)</p> <p>0.4-0.7%</p>	 <p>0.44%</p>
D3 Earthquake	 <p>1.5-2.0%</p>	 <p>0.73%</p>

Figure 57 presents the base shear vs. roof displacement for the three PSD tests on the HCT specimen and the envelope curve obtained from the finite element model. The initial stiffness of the model is 29% less than the stiffness calculated from the experimental data of the D1 ground motion. However, the slight underestimation in stiffness may also be due to interface cracking initiating earlier in the model than the experiment. The peak strength of the model is 8% greater than the experimentally measured strength. The model can capture the behavior of the test up until the second large shear crack opens at the base of the right boundary column adjacent to the masonry infill wall. This occurs just after peak capacity of the model is achieved and results in a drop of load in the force-displacement curve.

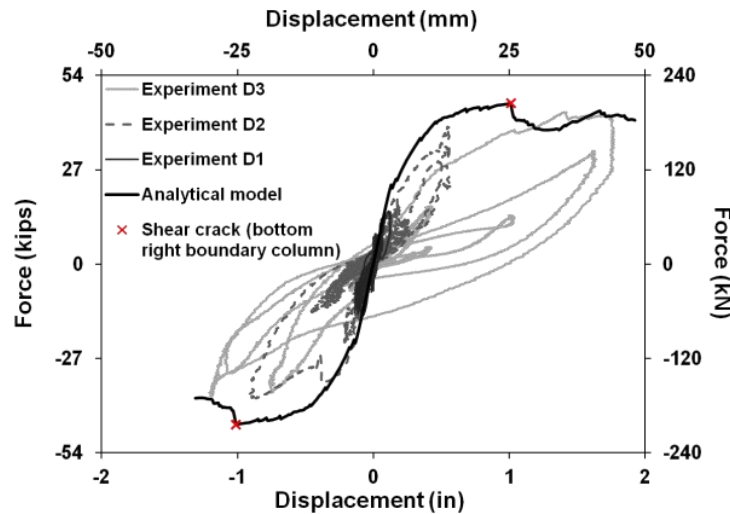


Figure 57: Base shear vs. top story displacement of the experiment (Ezzatfar et. al. 2014) and the finite element model for the HCT specimen

3.5 Chapter Summary

The constitutive modeling scheme, element formulation and material calibration process have been described in detail. The series of validation studies shows that the combined interface and smeared crack element yields consistent results over a range of models of increasing complexity.

Patch tests in pure compression and pure tension show that the use of interface elements does not affect the material behavior of the model with respect to the timing of failure. The calibration process alleviates tensile mesh sensitivity observed in traditional continuum models. The results of the single column tests indicate that the combined interface and smeared crack element model is equally able to model flexural behavior as traditional continuum models, and much superior in its capability to model shear failure. The results of the bare frame model were slightly stiff compared to the experiment. Given that infill structures tend to be stiffer than RC frames, the slight over-stiffness in modeling frame action is not expected to be significant for the models of hybrid concrete-masonry structures. The models of the series of cyclic tests on unreinforced masonry walls were in good agreement with the tests with respect to initial stiffness, peak strength and cracking patterns. The large model of the 3-story 3-bay RC frame with masonry infill also had predictions for initial stiffness, peak strength and timing of failure mechanisms which were close to the experiment.

The results of the validation studies confirm that the constitutive model is robust and appropriate for the basis of the modeling scheme for hybrid concrete-masonry.

CHAPTER 4

FINITE ELEMENT MODELING OF HYBRID CONCRETE- MASONRY

In order to model hybrid concrete-masonry in finite element, there are three components which must be properly characterized: the RC frame, the partially grouted masonry infill, and the connections from the masonry wall to the RC frame. Validation studies of the constitutive finite element model demonstrated its ability to model the RC frame in Chapter 3. In this chapter, modeling methods for partially grouted reinforced masonry infill and the connections from the masonry wall to the RC frame are proposed. Accurately modeling the exact types of connections used in the Caribbean is a challenge which requires tests of hybrid concrete-masonry structures to characterize the properties of the interface. For this reason, the proposed modeling method was validated with cyclic tests of full-scale hybrid concrete-masonry structures which are discussed in Chapter 6.

Within this chapter, the modeling scheme for hybrid concrete-masonry is described. Next, the material calibration for the partially grouted masonry infills is presented. The newly proposed methodology for calibrating the interface elements representing grouted bed joints is developed based on the concept of shear friction in concrete. Then, a method for modeling dowel connections from the masonry to the RC frame is presented. This method is validated using a model of a 3-story, 3-bay RC frame with infill and mesh reinforced mortar (MRM). Finally, preliminary models of the hybrid concrete-masonry frames used for the cyclic tests are presented. Material calibrations for the finite element models are compared to materials tests conducted on concrete, masonry, mortar and grout specimens. The shear and tensile tests on grouted bed

masonry samples validate the proposed method to calculate the properties of grouted bed joints as a function of the compressive strength of the grout and mortar. The summary for the chapter outlines the newly proposed process for calibrating the interface elements representing grouted bed joints using numbered steps.

4.1 Modeling Scheme

There are seven distinct elements in the proposed modeling scheme for partially grouted reinforced masonry: smeared crack elements for grouted cells, interface elements within grouted cells, smeared crack elements for un-grouted cells, interface elements for the masonry head joints, interface elements for the mortar head joints, interface elements for the bed joints in grouted cells, and interface elements for the bed joints in ungrouted cells, all of which are shown in Figure 58. In the figure, the interface elements are separated from the smeared crack elements in an exploded view in order to show which boundaries contain interface elements. Thus, the single lines shown represent the double-noded, zero-thickness interface elements used in the constitutive model. This convention is used for all the figures in this dissertation. The interface elements for the bed joints within grouted cells represent the mortar over the face shells and masonry webs and the grout within the cores. These will be referred to as grouted bed joints. The interface elements for the bed joints in ungrouted cells will be referred to as ungrouted bed joints.

The smeared crack elements representing grouted cells are the full unit thickness. They are configured in an eight element smeared crack module with interface elements to allow reinforcement to be placed at the center of each grouted cell and permit shear cracks to open within the grouted cells (See Figure 59b). This module also permits vertical cracking within the grouted cell which has been observed in the grouted cells

containing jamb reinforcement at the edges of partially grouted masonry walls (See Figure 59a). The new eight element module is used instead of the 4-element module proposed by Sayah et. al. (2013) (See Figure 59c) because the eight element module permits the horizontal truss elements to be connected at the same location as the vertical truss elements for horizontal reinforcement within the bed joints (See Figure 60a and b) or within a bond beam (See Figure 60c).

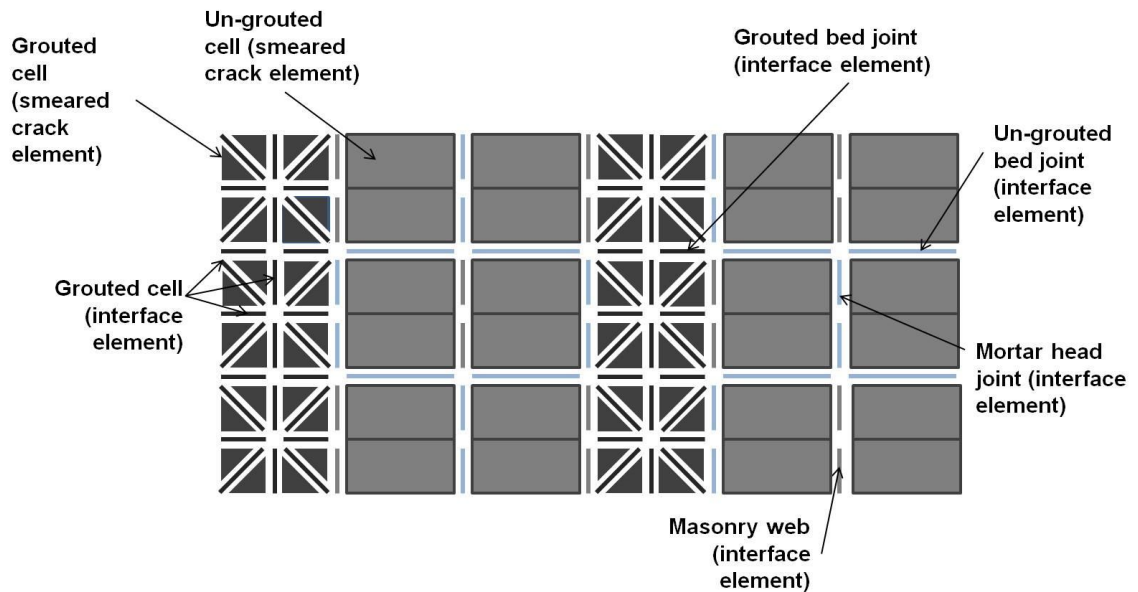


Figure 58: Schematic for partially grouted reinforced masonry

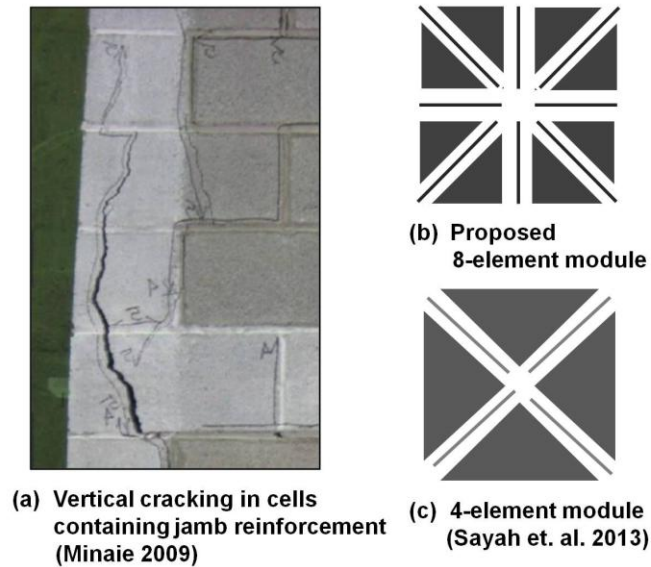


Figure 59: Vertical cracking path compared to element modules

The ungrouted cells are not modeled with the eight element module since crushing is expected to be the dominate failure of the hollow units. The smeared crack elements representing un-grouted cells have a thickness equal to the sum of the face shell thickness. The interface elements representing the masonry web are the full unit thickness. The thickness of the mortar bed joints is determined by calculating the net mortared area and dividing by the length of the CMU. The mortar head joints have a thickness equal to the thickness of the masonry unit and are given the same properties as the ungrouted bed joints, except for their bond strength which is reduced by 50% (See Section 3.3.2).

The method used to model reinforcement is shown in Figure 60. Twelve truss elements are used to model the vertical reinforcement in the grouted cells and joint reinforcement is modeled with two truss elements which connect at the center of each grouted cell regardless of whether bed joint or bond beam reinforcement is modeled.

For modeling hybrid concrete-masonry in the Caribbean, horizontal reinforcement is connected only in the grouted cells, as shown in Figure 60a, because the horizontal reinforcement is only bonded to the grouted cells. For modeling traditional horizontal ladder reinforcement the reinforcement is connected to every masonry unit across the bed joint, since it is continuously bonded in the mortar of the face shell (See Figure 60b). To model bond beam reinforcement and maintain mesh connectivity, the un-grouted cells are modeled using four smeared crack elements rather than two. The bond beam is modeled with the same eight element module used for vertically reinforced and grouted cells as shown in Figure 60c.

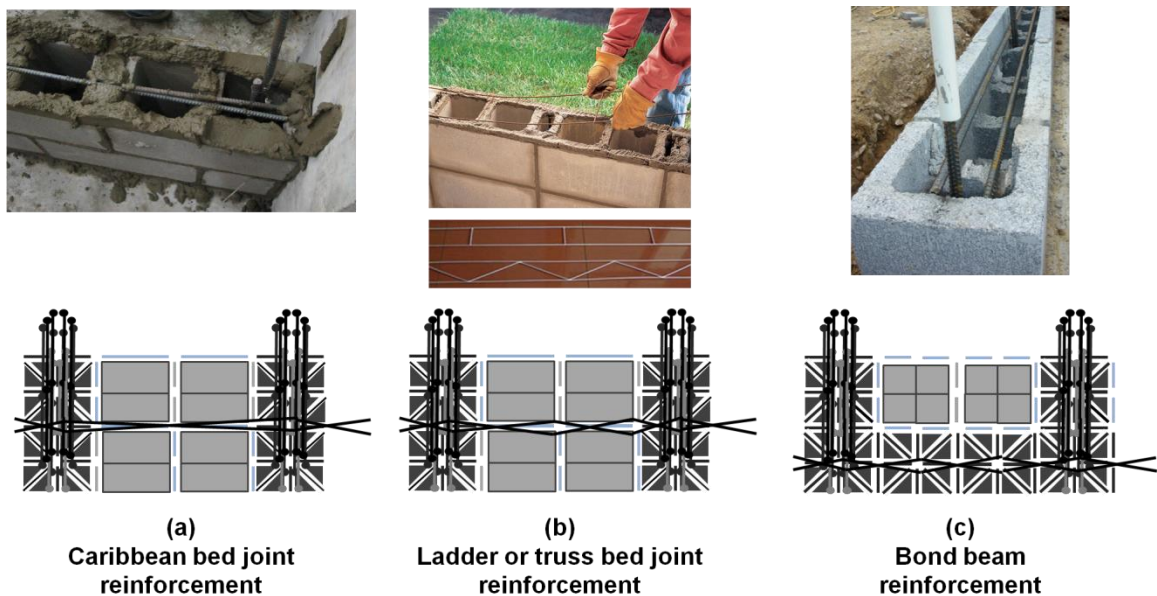


Figure 60: Connectivity of truss elements for different horizontal reinforcement types

4.2 Material Calibration for Partially Grouted Masonry

This Section describes the proposed material calibration for partially grouted masonry. The material calibration for the un-grouted cells is the same process used in the

constitutive model which was detailed in Chapter 3 (Stavridis and Shing 2010). It is important to remember that in the proposed modeling scheme, the characteristic length of the smeared crack elements used to represent un-grouted cells will be less than in the formulation by Stavridis (2010) as the elements are half the height.

While it is preferable to have assembly tests for calibration of the finite element model, limited data can be found in the literature for grouted masonry. Accurately modeling the shear behavior of grouted bed joints is particularly important for partially grouted masonry, which is likely to favor joints above and below grouted cells when sliding cracks or stair-stepped cracks propagate from the un-grouted masonry through the grouted cells (See Figure 61). Thus, a new calibration methodology which does not require assembly tests is proposed in the subsequent section.

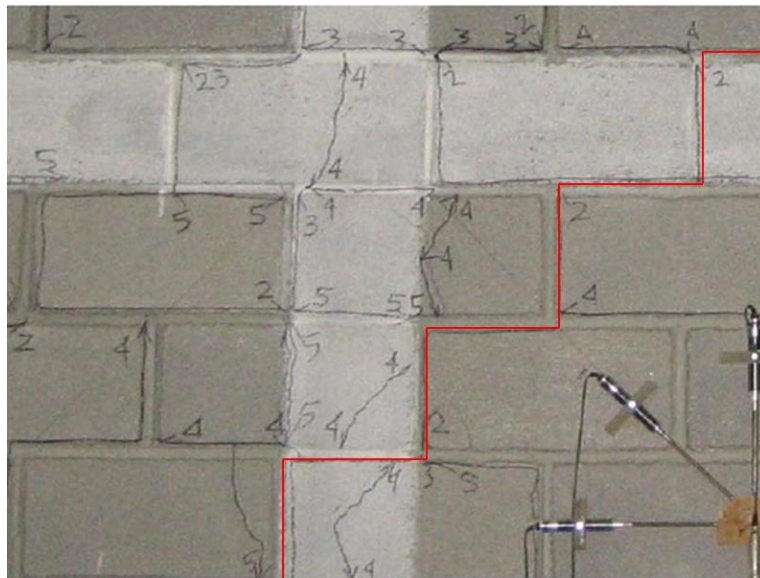


Figure 61: Preference for cracking along the grouted joints of reinforced cells (Minaie 2009). Crack 2 has been highlighted in red

The material calibration of the grouted masonry is divided into three sections: compression behavior of grouted masonry, tensile behavior of grouted masonry units, and shear and tensile behavior of grouted bed joints. In each section, the calibration method utilizing assembly test data is first described, followed by the mechanics-based approach using only data on the compressive strength of the masonry components.

4.2.1 Compression Behavior of Grouted Masonry

The basis for the material calibration of the grouted cells is based on studies of the compressive strength of prisms conducted by Cheema and Klingner (1986). Unlike ungrouted masonry prisms which almost exclusively fail due to splitting of the masonry unit, grouted masonry prisms have several distinct failure mechanisms. The failure mechanisms for grouted masonry prisms include: block splitting, block crushing, mortar crushing, mortar splitting and grout crushing.

In all cases except mortar crushing or mortar splitting, the stiffness of the grout is very similar to the stiffness of the masonry unit, which helps to distribute the strains more evenly throughout the prism height than in an un-grouted prism. For this reason, the compression behavior of the grouted cells is calibrated like a continuous material in a manner similar to concrete if the prism failure is governed by block splitting, block crushing or grout crushing. Interface elements are given an artificially high stiffness so as not to influence the compression behavior of the smeared crack elements, and the smeared crack element isotropic compression curve is calibrated to the grouted prism stress-strain behavior. Grouted prisms failing by mortar crushing or mortar splitting typically have very weak mortar, and damage first concentrates in the bed joint. This means that the bed joint region is significantly weaker than the rest of the prism and that

displacements may initially concentrate in the bed joint in a manner more similar to ungrouted masonry. In this case, the calibration of the four smeared crack element module and one grouted bed joint interface element is calibrated to the prism behavior in a manner similar to the procedure for ungrouted prisms suggested by Stavridis and Shing (2010).

The compressive failure mechanism for the grouted masonry used in the construction of the hybrid concrete-masonry walls was determined from prism tests conducted as part of this study. However, the most likely failure mechanism and the corresponding calibration method can also be determined using proposed equations from Cheema and Klingner (1986) if data from prism tests are not available. If no assembly data is available to obtain the compressive stress vs. strain curve, the process developed by Cheema and Klingner (1986) can be used to calculate the prism strength and expected failure mechanism. Alternatively, data from literature for grouted prisms with similar grout and unit strengths can be used to estimate the prism strength and elastic modulus from which to calibrate the compression behavior of the masonry assembly.

4.2.2 Tensile Behavior of Grouted Masonry Units

Within the grouted masonry units, it is important that the tensile strengths of the interface elements and of the smeared crack elements are calibrated consistently so that the failure of one is not favored over the other. Just as in the calibration process for the tensile behavior of concrete, the interface elements are calibrated first.

The effective tensile strength of the grouted masonry unit, $f'_{t\ eff}$ is determined by first converting the area of the unit into an equivalent area of grout using a transformed section approach. Then the effective tensile strength is calculated by dividing the total

tensile capacity of the transformed section by the actual area of the grouted masonry bed joint, A_{gbj} . This process is summarized by Equation 11, where A_g is the area of grout, E_{unit} is the stiffness of the masonry unit, E_g is the stiffness of the grout, A_{unit} is the area of CMU, and $f'_{t g}$ is the tensile strength of the grout.

$$f'_{t\ eff} = \frac{\left(A_g + \frac{E_{unit}}{E_g} A_{unit}\right) f'_{t\ g}}{A_{gbj}} \quad (11)$$

To finish calibrating the interface element, fracture energy of the grouted masonry unit must be determined. Tests for fracture energy are difficult to conduct, and tests for the fracture energy of grout have not been found in the literature. In lieu of test data, fracture energy of concrete or mortar with similar strength to the grout is used. The tensile behavior of the smear crack element is calibrated with the stress-displacement curve of the interface element. In order to compare the two element types, both tensile strength relationships are transformed to stress-displacement by multiplying the strains of the smeared crack elements by its characteristic length.

4.2.3 Shear and Tensile Behavior of Grouted Bed Joints

The tensile and shear behavior of the grouted bed joint interface elements can be calibrated with shear tests and bond wrench tests of grouted assemblies in the same manner as was done for ungrouted bed joints (Section 3.3.2). However, these tests are difficult to conduct and few tests can be found in the literature. Additionally, the calibration method described in Chapter 3 does not capture the effect of the reinforcement on the shear properties of the joint.

The grouted bed joint shear and tensile properties can also be calculated as a function of the compressive strength of the masonry components using the newly

proposed calibration methodology. The method is developed using shear friction equations for reinforced concrete joints and experimental studies on the tensile and shear properties of grouted masonry assemblies.

4.2.3.1 The Concept of Shear Friction

The concept of shear friction is adopted in both the ACI 318 and the AASHTO codes in order to formulate a simple equation for the shear capacity across a reinforced concrete cold joint. If there is no load normal to the joint, shear resistance comes from cohesion associated with the bonding properties of the matrix, aggregate interlock, clamping forces generated by the reinforcement, and dowel action of the reinforcement (See Figure 62) (Birkeland and Birkeland 1966; Mattock 1974; Walraven and Reinhardt 1981).

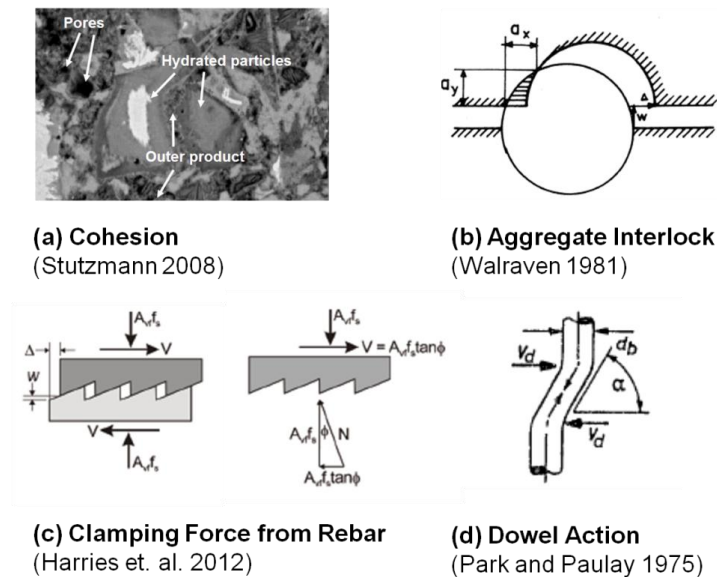


Figure 62: Components of shear friction

The last mechanism of dowel action is typically neglected since it has been shown through tests by Walraven (1981) to contribute only marginally to the shear capacity of the joint. With additional compression force applied normal to the joint, the clamping action of the reinforcement becomes negligible.

In the ACI 318 code, shear capacity of a joint (V_n) is given by Equation 12, where A_v is the area of shear reinforcement crossing the shear plane and f_y is the yield stress of the reinforcement. The shear friction factor (μ) accounts for both the clamping force from the reinforcement and the effect of aggregate interlock. The ACI 318 shear friction factor is not a function of concrete strength, but varies according to the roughness and initial bond condition of the joint surface. Several researchers have found that this form of equation may not reflect the true mechanisms of shear friction, as the reinforcement across concrete joints is typically only marginally engaged and does not reach yield prior to the peak shear strength of the joint (Harries et. al. 2012; Kahn and Mitchell 2002; Walraven and Reinhardt 1981).

$$V_n = \mu A_v f_y, \quad (12)$$

$\mu = 1.4$ for monolithic connection

$\mu = 1.0$ for a cold joint with 1/4in roughness amplitude

$\mu = 0.6$ for a cold joint with a smooth concrete surface

The majority of the shear capacity of the joint can be attributed to the concrete component which falls to a residual value while the steel component of the shear capacity continues to increase after the peak shear load is achieved (See Figure 63). The shear strength of the joint has been shown to increase for increasing concrete strengths (Harries et al. 2012; Kahn and Mitchell 2002). In light of the experimental data, Harries (2012) proposed Equation 13 for the calculation of the shear capacity of the concrete joint.

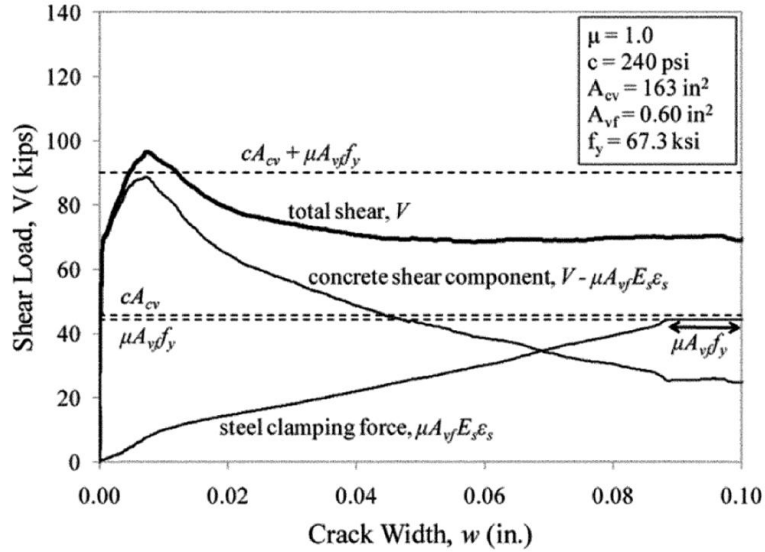


Figure 63: Results from shear tests of concrete joints by Harries (2012)

$$V_n = \alpha_h A_{cv} f'_c + \mu 0.002 E_s A_v \quad (13)$$

The parameter α_h varies according to the casting condition of the joint, A_{cv} is the area of concrete in the shear plane of the joint, f'_c is the compressive strength of concrete, and E_s is the elastic modulus of the reinforcement. The quantity $0.002 E_s$ is used instead of the yield strength of the steel as the steel has been shown experimentally to have stresses much below yield stress at the peak shear resistance of the joint.

4.2.3.2 Application of Shear Friction Principles to Grouted Bed Joints

Very similar shear friction mechanisms are present along the bed joints of grouted cells of reinforced masonry. The concepts of shear friction must be combined with experimental data on the flexural and shear properties of grouted masonry to develop a formula for the failure surface of the interface element. The first focus is to develop a model for the behavior of grouted cells without reinforcement.

The hyperbolic failure surface of the interface element is shown in Figure 64. The first point to be determined is s , is the tensile strength of the bed joint. Although the tensile strength of the bed joint is dominated by the grout, flexural tension (bond strength) of a grouted assembly is often less than the tensile strength of the grout (about 10% of compressive strength). Table 3 shows a compilation of the available data from the literature for bond strength of grouted prisms.

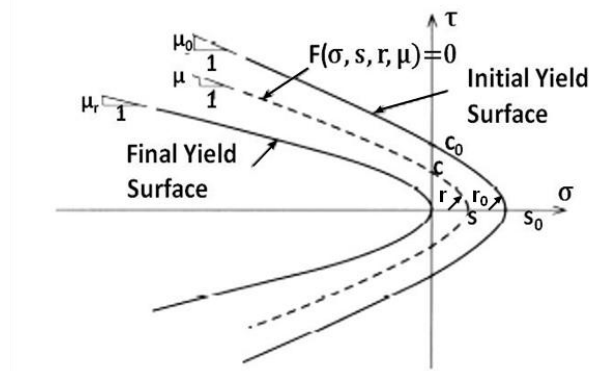


Figure 64: Hyperbolic yield surface of the interface element

Table 3: Test data on the bond strength of grouted prisms

Researchers	Mean Compressive Strength of Grout psi (MPa)	Mean Tensile Strength of Grout psi (MPa)	Mean Bond Strength psi (MPa)
Hamid and Drysdale (1988)*	GN-3060(21.1)	GN-304.6 (2.1)	GN-203.1 (1.4)
	GW-1987 (13.7)	GW-188.5 (1.3)	GW-203.1 (1.4)
	GS-5946 (41.0)	GS-522.1 (3.6)	GS-246.6 (1.7)
Hamid et. al. (1992)	3272 (22.6)	298 (2.1)	323 (2.2)
Brown and Melander (1999)	6192 (42.7)	N/A	152.4 (1.1)

*GN-normal grout, GW-weak grout, GS-strong grout

The bond strength of the grouted prisms ranges from about 2% of the compressive strength for strong grouts to 10% of the grouted strength for weak grouts. Based on the limited amount of data, the tensile strength of the grouted assembly is varied linearly

Figure 65 highlights that the proposed formulation is conservative, especially for low-strength grouts. The formulation may be improved if additional experimental work on the bond strength of grouted masonry is conducted.

Once the tensile strength of the grout has been determined, the concepts from shear fiction are applied to calculate the values for the friction factor (μ_0 in Figure 66) and cohesion (c_0 in Figure 66). The friction factor for grout is assumed to be a function of the compressive strength of the grout, to be consistent with the mechanics observed from tests of concrete joints. Equation 15a was developed from friction factors for grouted bed joints determined by (Hamid et. al. 1979) using assembly shear tests at varying levels of pre-compression for a strong and weak grout (See Figure 74 a and b). This study is the only set of shear assembly tests on grouted masonry to be found in the literature. Equation 15b is the metric equivalent to Equation 16a.

$$\mu_0 = 0.6 + 0.00015f_g \text{ (in psi)} \quad (15a)$$

$$\mu_0 = 0.6 + 0.0218f_g \text{ (in MPa)} \quad (15b)$$

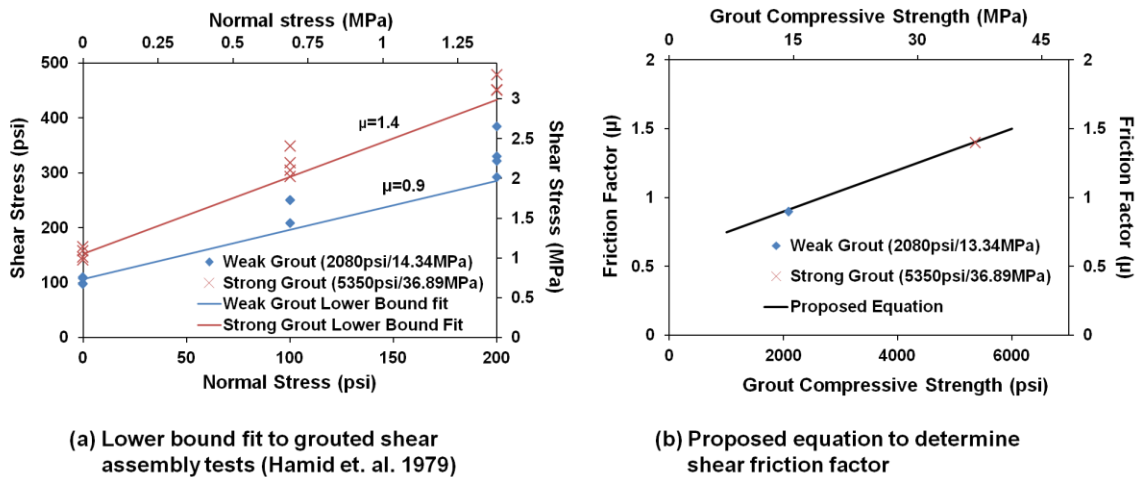


Figure 66: Development of the equation for shear friction factor of grouted bed joints

The cohesion of the grout was also assumed to be linearly related to the compressive strength of the grout, consistent with the formulation by Harries (2012) for concrete joints. Using data from Hamid et. al. (1979) and equation was fit to the values for cohesion of tests on a weak, normal and strong grout (See Figure 67 and Equation 16 a and b). It was decided to use a linear fit with a non-zero y-intercept, because constraining the linear fit to a zero intercept resulted in a very low r^2 value. Until more experimental data have been gathered on the shear behavior of grouted cells, the proposed formula should work well for normal grout strengths (1500 psi-6000 psi, 10.24 MPa-41.37 MPa).

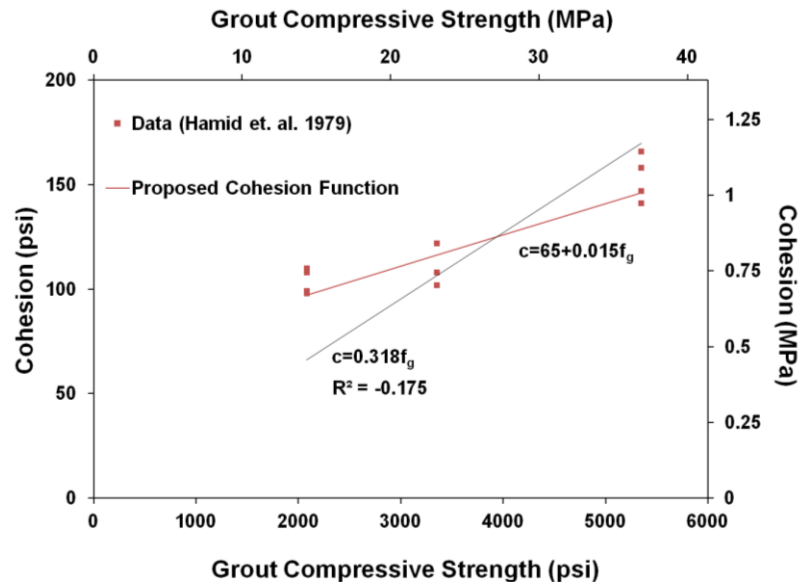


Figure 67: Data for cohesion of grouted bed joints and proposed function

$$c_0 = 65psi + 0.015f_g \quad (16a)$$

$$c_0 = 0.448MPa + 0.015f_g \quad (16b)$$

Going through the proposed calibration process for the weak and strong grout in the study by Hamid et. al. (1979) yields piece-wise linear functions which do not easily conform to the hyperbolic yield surface assumed for the interface element. This is because the shear friction values and the bond strength of the grouted masonry assembly are higher than the values typical for un-grouted bed joints, while the cohesion of the grouted assembly appears to be only marginally increased (See Figure 68).

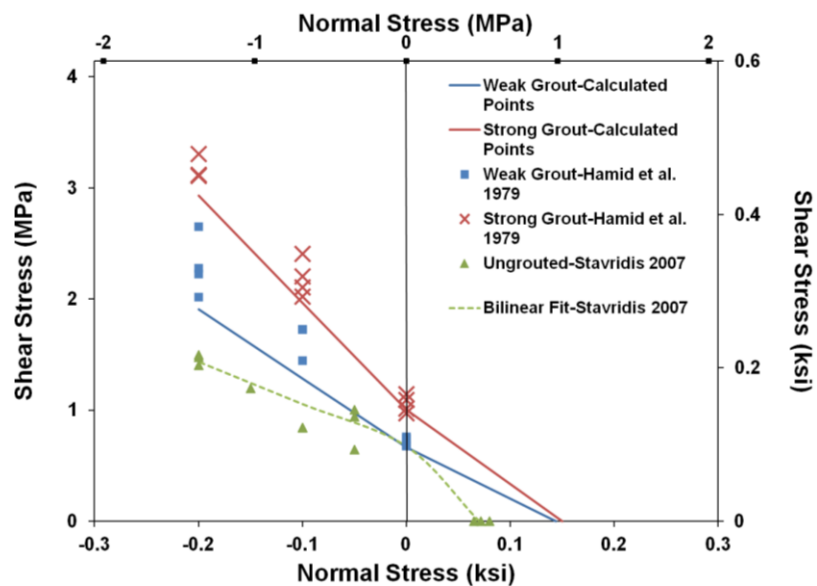


Figure 68: Comparison of data from shear tests of grouted and un-grouted assemblies to the data points calculated by the proposed calibration method. Weak grout-2080 psi (14.34 MPa), Strong grout-5350 psi (36.89 MPa)

There are no studies which contain both bond wrench tests and shear assembly tests of the same type of grouted masonry assembly by which to validate the methodology as a whole. Future work on the element formulation may include further testing of grouted masonry assemblies to establish the tensile bond, cohesion and shear friction value for the same masonry prisms. This will confirm or refute the trends observed from the data currently available in the literature and help to determine the form

of the interface element failure surface curve which better models the behavior of grouted bed joints.

Conducting a study to determine if these changes are necessary is beyond the scope of this research, but shear tests and bond wrench tests of grouted assemblies were conducted as part of the experimental program. This may be the first data set containing both tensile and shear assembly tests on the same batch of grouted masonry units. Until further data have been gathered, a sufficient match to the calculated values can be determined by a linear fit to five or more evenly spaced points on the bilinear curve between the maximum expected compressive stress in the bed joint and its tensile strength. An example for a fit with 0.2ksi (1.4MPa) maximum expected compressive stress for the strong and weak grout tested by Hamid (1979) is shown in Figure 69.

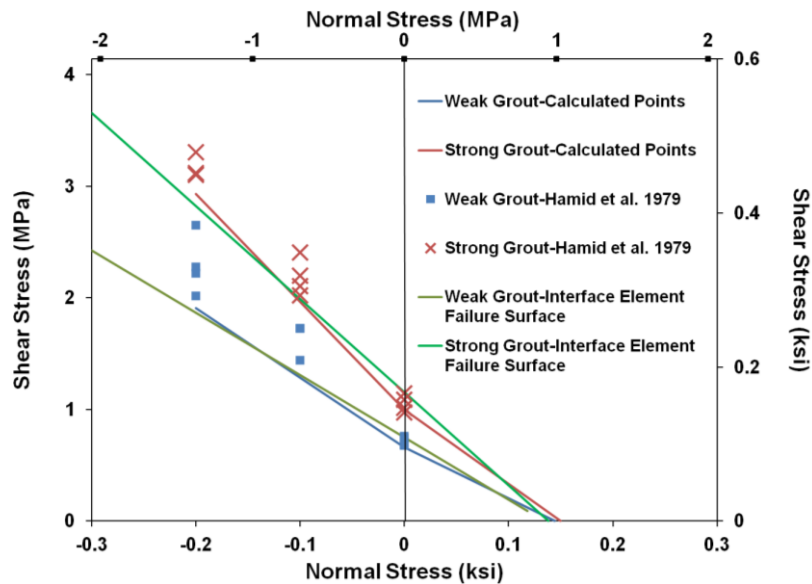


Figure 69: Example of linear fit to obtain the interface element failure surface. Weak grout-2080 psi (14.34 MPa), Strong grout-5350 psi (36.89 MPa)

No study has been conducted to characterize the residual shear resistance of grouted bed joints after the joint has failed. Until future experimental work is conducted, the shear strength of the grouted bed joint is expected to degrade in a manner similar to ungrouted bed joints. In tests by Mehrabi (1994) the residual shear strengths of bed joints under pre-compression ranged from 63% to 71.5% of the peak shear capacity. Conservative results are obtained by using the same friction factor ($\mu_r = \mu_0$) and setting the tensile capacity of the failed joint equal to zero.

Finally, it is important to calculate the shear modulus of the grouted bed joints for accurate representation of shear behavior. The elastic modulus of the grouted bed joint interface element is calibrated to prism behavior as part of the masonry assembly. Simply assuming the shear modulus is related to this elastic modulus by equations of elasticity would lead to over-stiff behavior in shear.

To more accurately determine the shear modulus of the grouted bed joint, the bed joint stiffness can be approximated as a composite material according to Equation 17. The variable E_{gbj} is the stiffness of the grouted bed joint and A_{gbj} is the total area of the grouted bed joint. The proportion of the grouted bed joint area occupied by the grout and mortar is denoted as A_g and A_{mort} , respectively. The grout stiffness, E_g is calculated with Equation 18 (Cheema and Klingner 1986), where w_g is the unit weight of grout in lbs/ft³ and f_g is the compressive strength of the grout in psi. The stiffness of mortar, E_{mort} is approximated as 500 times the mortar compressive strength (f_{mort}) (Cheema and Klingner 1986) (Equation 19). Once the stiffness of the bed joint (E_{gbj}) is established, the stiffness of the interface element representing the grouted bed joint (D_n) is determined by

dividing E_{gbj} by the bed joint spacing (s_{bj}) (Equation 20). Then the shear stiffness of the grouted bed joint interface element (D_t) can be calculated according to Equation 21.

$$E_{gbj} = \frac{E_g A_g + E_{mort} A_{mort}}{A_{gbj}} \quad (17)$$

$$E_g = 16.5 w_g^{1.5} \sqrt{f_g} \quad (18)$$

$$E_{mort} = 500 f_{mort} \quad (19)$$

$$D_n = \frac{E_{gbj}}{s_{gbj}} \quad (20)$$

$$D_t = \frac{D_n}{2(1+\nu)} \quad (21)$$

4.2.4 Accounting for the Contribution of Reinforcement

To determine if the addition of vertical reinforcement in a grouted cell merits altering the meshing scheme or material calibration of the grouted bed joint, the influence of the truss elements on the joint shear behavior must be characterized. Horizontal reinforcement has been shown to have a negligible effect on the shear capacity of bed joints (Hamid 1978).

In order to characterize the influence of the vertical reinforcement, a triplet test model was created in FEAP (See Figure 70). Several variants of the model were created, one model without reinforcement, and three models with the reinforcement area varied from #3 to a #5 bar. The material properties for the models were calibrated to the strong and weak grouts in the tests by Hamid (1979). This results in two versions of each model, one for the weak grout and one for the strong grout. Each of the eight models was run with applied pre-compression stresses of 0 psi (0 MPa), 100 psi (0.689 MPa) and 200 psi (1.379 MPa).

A comparison of the force-displacement behavior for the models with no pre-compression is shown in Figure 71. Figure 72 and Figure 73 show the same data for 100 psi (0.689 MPa) and 200 psi (1.379 MPa) of pre-compression. The percent difference in the peak shear capacity of each of the models with reinforcement over the case with no reinforcement is summarized in Table 4.

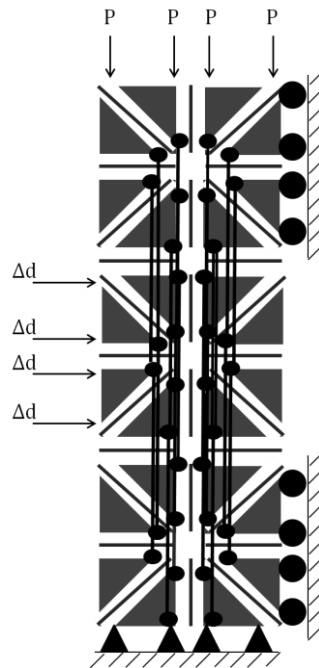


Figure 70: Triplet test model with reinforcement

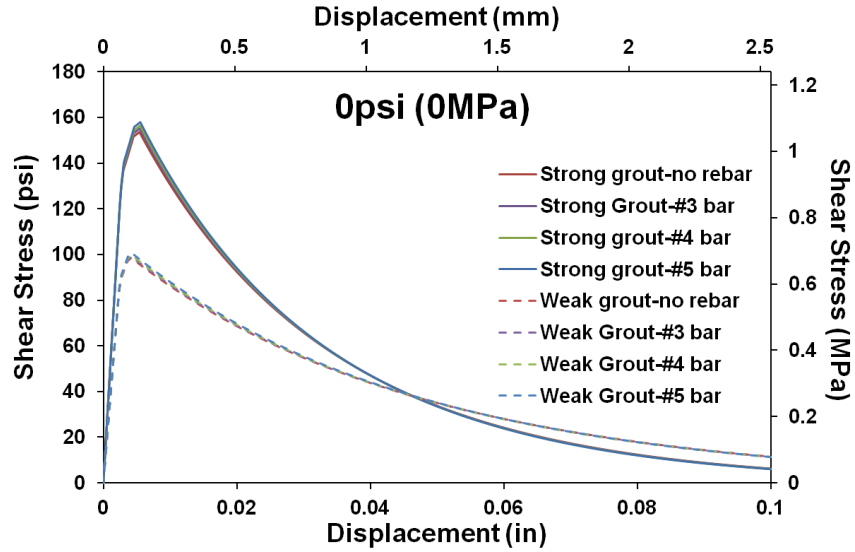


Figure 71: Shear stress vs. lateral displacement for grouted bed joints with and without vertical reinforcement without pre-compression. Weak grout-2080 psi (14.34 MPa), Strong grout-5350 psi (36.89 MPa)

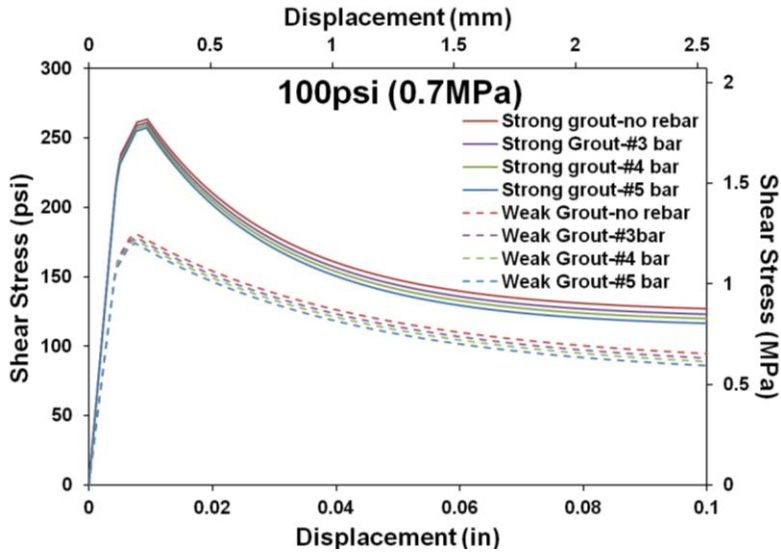


Figure 72: Shear stress vs. lateral displacement for grouted bed joints with and without vertical reinforcement at 100 psi (0.7 MPa) of pre-compression. Weak grout-2080 psi (14.34 MPa), Strong grout-5350 psi (36.89 MPa)

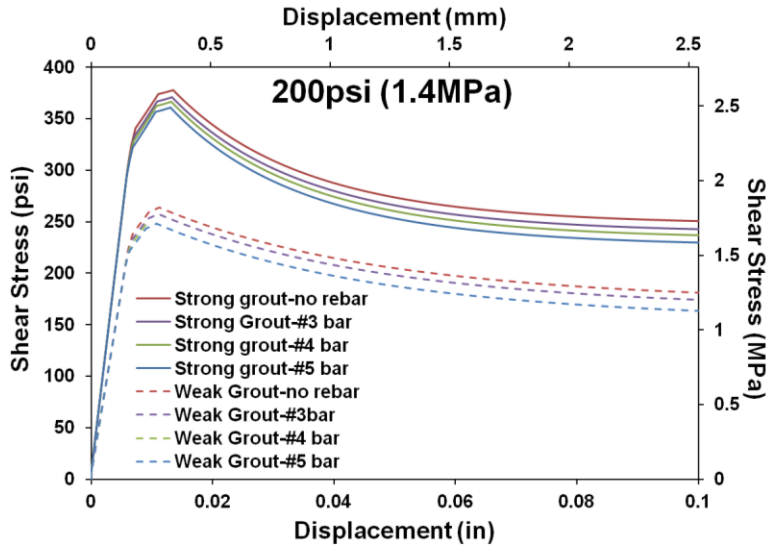


Figure 73: Shear stress vs. lateral displacement for grouted bed joints with and without vertical reinforcement at 200 psi (1.4 MPa) of pre-compression. Weak grout-2080 psi (14.34 MPa), Strong grout-5350 psi (36.89 MPa)

Table 4: Summary of effect of vertical truss reinforcement elements on the shear capacity of grouted bed joints

Pre-compression psi (MPa)	Weak Grout			Strong Grout		
	0	100 (0.7)	200 (1.4)	0	100 (0.7)	200 (1.4)
% Difference with a # 3 bar	+0.5%	-1.7%	-2.3%	+0.7%	-0.8%	-1.9%
% Difference with a # 4 bar	+1.5%	-2.8%	-4.2%	+1.6%	-1.5%	-3.17%
% Difference with a # 5 bar	+2.5%	-3.9%	-6.0%	+2.6%	-2.3%	-4.5%

*weak grout-2080 psi (14.34 MPa), strong grout-5350 psi (36.89 MPa)

The data indicates that the presence of the reinforcement has a minimal effect on the peak shear capacity of the joint. This makes sense because the truss elements have pinned end conditions. The peak difference in shear capacity occurs for the weak grout with a #5 bar and a pre-compression load of 200 psi (1.379 MPa), but even this case is only 6% less than the shear capacity without reinforcement. At no pre-compression, the rebar appears to minimally increase peak shear capacity and slightly reduce the residual

shear capacity of the joint. At moderate pre-compression and high levels of pre-compression, 100 psi (0.689 MPa) and 200 psi (1.379 MPa), the presence of reinforcement appears to slightly decrease both the peak and residual shear capacity of the joint. In reality, the normal stress in the bed joint is slightly reduced because the reinforcement serves to increase the effective area of the grouted joint. Less normal stress in the bed joint leads to a reduction in shear strength, which is captured by the slight reduction in shear capacity as reinforcement area is increased.

Because this does not accurately represent the physical behavior of reinforced joints subjected to shear, the contribution of the reinforcement to the shear capacity must be accounted for by altering the calibration of the grouted bed joint.

Two conditions should be satisfied from the presence of reinforcement across the grouted bed joint. First, initial failure surface of the interface element should reflect an increase in cohesion from the presence of reinforcement and a less significant change in the peak shear strength at higher levels of pre-compression. This is because the clamping force from the reinforcement is expected to become negligible with increasing pre-compression, consistent with findings from experimental studies on concrete joints (Harries et al. 2012). Second, the residual shear capacity of the grouted interface element should increase with increasing amounts of shear reinforcement, as the main contribution of reinforcement is to limit crack widths after the grout has cracked. Because the interface tensile capacity goes to zero after the element has failed, it is not possible to account for the residual cohesion by adjusting the failure surface of the interface element representing the grouted bed joint.

Thus it is necessary to add truss elements to the meshing scheme such that the additional steel elements could resist shear sliding across the bed joint once the interface element has failed (See Figure 74). The effective shear area for the added reinforcement can be determined based on literature values for dowel action of rebar in concrete. These values typically range from 25% to 50% of the physical bar area (Dulacska 1972; Soroushian et al. 1986; Paulay et al. 1974). The additional truss elements have a slight influence on the bending behavior of the grouted cell. However, the curvature for masonry in bending is typically very small, so these elements remain nearly horizontal and do not significantly influence the bending behavior of the masonry. In tension, the capacity of the joint is also marginally increased by the presence of the additional truss elements.

A validation study was conducted with models of stacks of 3 reinforced grouted cells as shown in Figure 70, with additional truss elements representing the shear contribution of the vertical reinforcement (See Figure 74). These models were subjected to pure tension and pure bending loading conditions. Two different grout properties were selected from the tests by Hamid (1979): a weak grout with 2080 psi (14.34 MPa) compressive strength and a strong grout with 5350 psi (36.89 MPa) compressive strength. Each model had a #4 vertical reinforcing bar and additional truss elements to model shear resistance of the vertical reinforcement. The additional truss elements in the baseline models were given zero area. For the strong grout, modeling effective dowel areas ranging from 25%-50% led to an increase in tensile capacity over the baseline model which were less than 0.5% and increases in bending resistance which were between 6% and 6.5% for all cases. For the weak grout with 25%-50% effective dowel area, the

tensile capacity of the grouted bed joint was increased by less than 0.5%, but the ultimate bending resistance was increased by 21-22%. Decreasing the effective dowel area to 10% or less reduced the increase in bending capacity to less than 10%. Based on the results of these models, 25% effective dowel area is recommended to capture the additional shear resistance of the vertical reinforcement unless the grout is weak (less than 2,500 psi (17.24 MPa)) and bending is expected to dominate the wall failure. In all cases, it is advisable to conduct a small study to verify the selected dowel area does not significantly influence the bending behavior of the reinforced and grouted masonry.

Any increase in bending resistance of the grouted bed joints is unlikely to have a significant effect on the models of hybrid concrete-masonry walls. The RC frames limit the curvature of the masonry infills and the masonry walls primarily resist lateral forces through shear mechanisms.

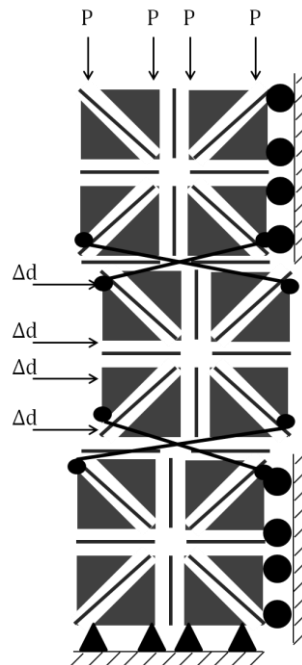


Figure 74: Additional steel elements to capture dowel action of reinforcement in grouted bed joints

The influence of variation in dowel area on the shear resistance of the grouted bed joint is shown for the weak and strong grout from tests by Hamid (1979) with a #4 reinforcing bar (See Figures 75-77). The results indicate that explicitly modeled reinforcement permits the interface element to fail first, resulting in softening prior to reaching peak shear capacity when the reinforcement yields. However, this effect diminishes with higher levels of pre-compression, which is in accordance with the observations in experimental tests from the literature.

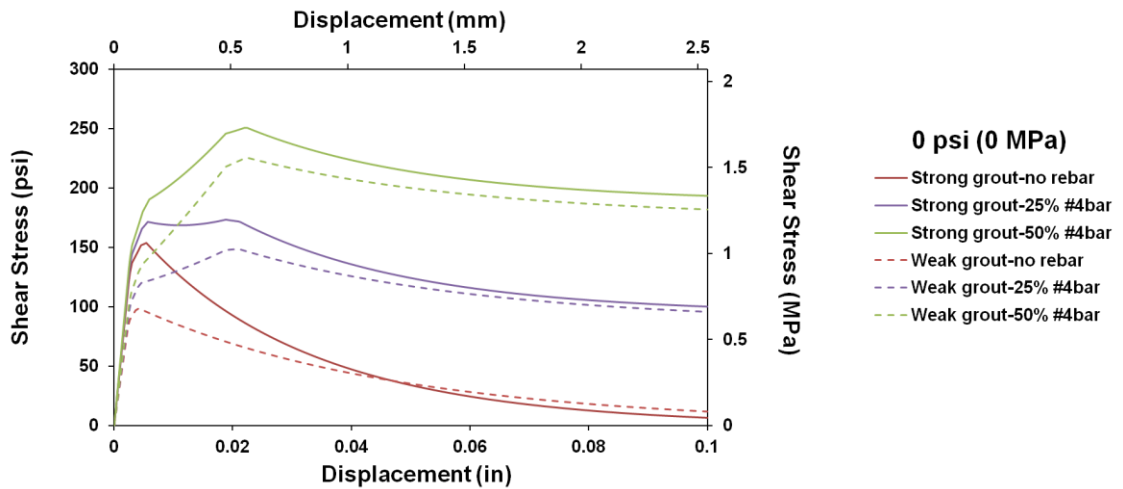


Figure 75: Model results of shear tests without pre-compression on grouted bed joints with and without reinforcement. Weak grout-2080 psi (14.34 MPa), Strong grout-5350 psi (36.89 MPa)

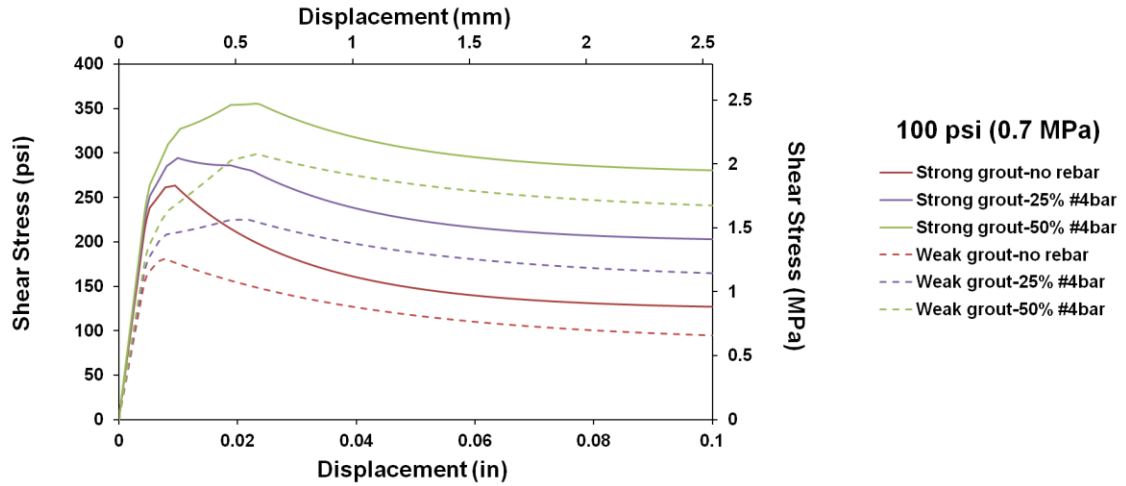


Figure 76: Model results of shear tests with 100 psi (0.7 MPa) pre-compression on grouted bed joints with and without reinforcement. Weak grout-2080 psi (14.34 MPa), Strong grout-5350 psi (36.89 MPa)

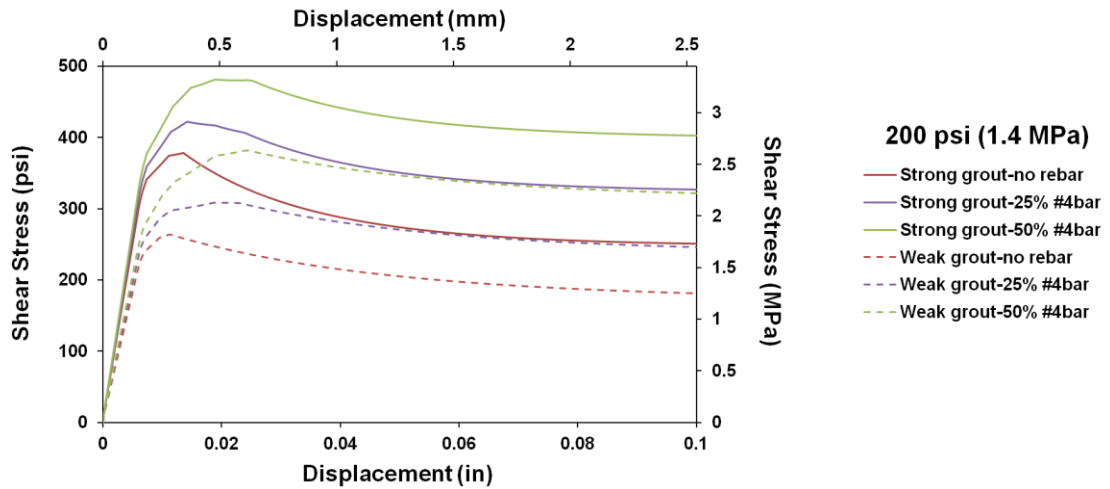


Figure 77: Model results of shear tests with 200 psi (1.38 MPa) pre-compression on grouted bed joints with and without reinforcement. Weak grout-2080 psi (14.34 MPa), Strong grout-5350 psi (36.89 MPa)

4.3 Modeling Dowel Connections

In some types of hybrid concrete-masonry, embedded reinforcing bars are used as connections from the RC columns to the masonry infill. These connections are located

within the masonry bed joints and provide resistance primarily through dowel action rather than bending. Thus, it is simplest to use two-elements in an X configuration to model the reinforcement. The effective area of dowel reinforcement to be used in the finite element model is formulated based on theories of dowel action in reinforcement embedded in concrete.

A 3-story 3-bay RC frame with hollow clay tile brick infill walls and externally applied mesh reinforced mortar (MRM) tested by Ezzatfar et al. (2012) is modeled using the proposed method for discrete modeling of anchorage dowels. The results show that this modeling technique adequately represents the behavior of the experimental specimen. Additional studies are conducted to demonstrate the importance of modeling anchorage dowels and characterize the sensitivity of the model's initial stiffness and peak capacity to a change in the effective dowel area.

4.3.1 Modeling Scheme for Dowel Reinforcement

Dowel reinforcement is modeled using a pair of truss elements connected from the masonry infill to the RC frame. The resistance provided by the truss elements to interface sliding is illustrated in Figure 78. The cross-sectional area of these truss elements must be selected so that the resistance from the element in tension added to the resistance of the truss element in compression is equivalent to the shear resistance of the dowel.

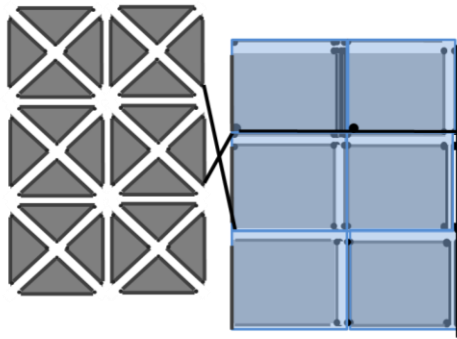


Figure 78: Modeling scheme for dowel reinforcement

4.3.2 Validation of Dowel Reinforcement Modeling Scheme

The test specimen is the retrofitted frame modeled in Section 3.4.6 to validate the constitutive model. For the second phase of testing, the frame was repaired and new infills with mesh reinforced mortar (MRM) were placed in the middle bays (See Figure 79). Because much of the specimen description and material calibration has already been reported in Section 3.4.6, only the aspects of the model which are unique to the MRM specimen are presented.

4.3.2.1 Finite Element Model and Material Calibration

The mesh consists of a 7.9 inch by 7.9 inch (200 mm by 200 mm) grid of 0.2 inch (5 mm) deformed bars attached to both sides of the HCT infill. These meshes are anchored to the boundary frame with 8-mm deformed anchor dowels and the entire mesh is covered in plastering mortar (See Figure 79). No repair action was taken for the frame elements.

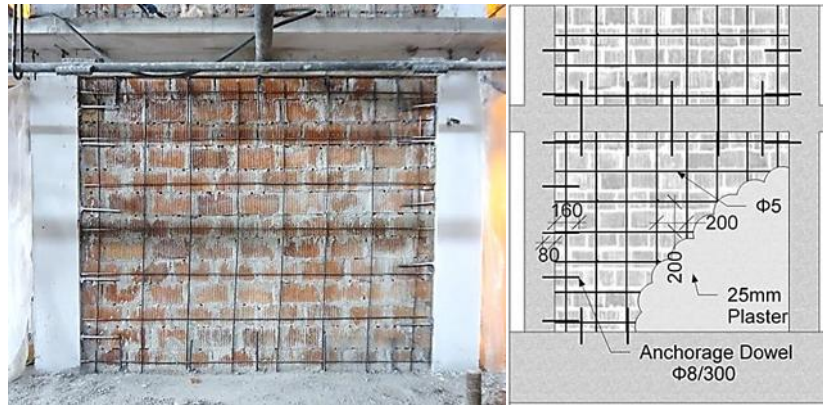


Figure 79: Reinforcement details for the MRM infills (Ezzatfar et al. 2012)

Three different ground motions were applied to the test specimen with pseudo-dynamic testing technique, just as was done for the unretrofitted specimen (Section 3.4.6). The D1 earthquake was completely applied. However due to the technical malfunctions encountered after the major peaks of D2 ground motion, the same ground motion (D2) was applied four times. These successive D2 motions were named as D2-1, D2-2, D2-3 and D2-4 respectively. At the end, quasi-static reversed cyclic test was conducted to obtain lateral load bearing and displacement capacity of the enhanced frame.

The details of the modeling scheme used for the MRM infill are shown in Figure 80. The smeared crack elements representing the hollow clay tile units is the thickness of two face shells and the plaster is modeled explicitly with overlay elements. The dowels are modeled using the proposed 2-element model, with each of the truss elements having an area equal to 12.5% of an 8mm bar, so that the total effective dowel area is 25% as suggested by Paulay et. al. (1974). The mesh reinforcement is modeled explicitly with truss elements. the stiffness of the concrete columns on the first story was reduced by 50% from the unretrofitted frame to account for the damage from the first phase of

testing. Since little to no damage was observed in the other parts of the RC frame after testing the unretrofitted specimen. The stiffness of the rest of the concrete frame members was kept the same as the model of the unretrofitted specimen (Section 3.4.6.3). A summary of all the material properties obtained from materials tests and the material parameters utilized in the structural model are presented in Appendix C.

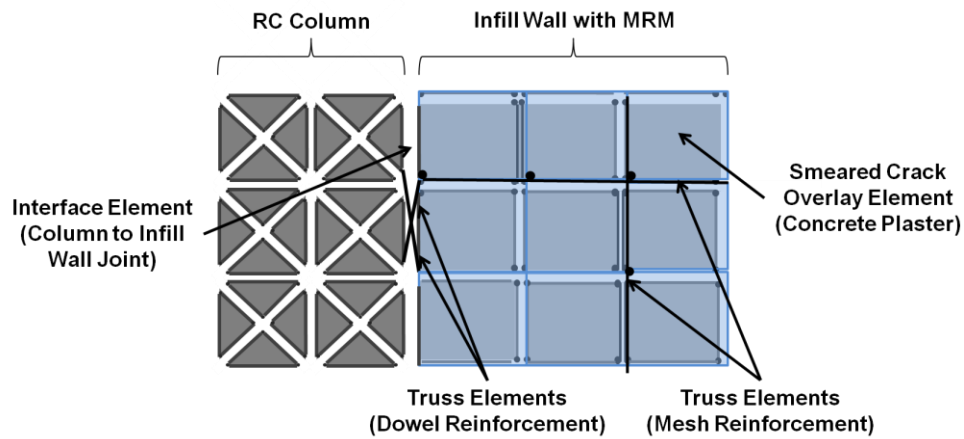


Figure 80: Schematic of the modeling scheme for MRM specimen

4.3.2.2 Results

The finite element model is in good agreement with the damage sequence observed in the experiment. The observed damage during experiments on the MRM specimen and cracking patterns from the finite element model are presented in Table 5. The photos presented in Table 4 have been taken after the application of each loading and the experimental drift levels are the maximum first story drifts for the three cycles with the largest amplitude of displacement during the specified ground motion. The images from the finite element model are taken at the step in which damage initiates and the specified drift corresponds to the first story drift at this step in the simulation.


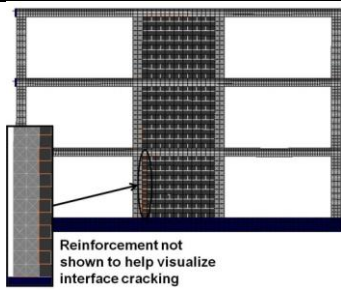
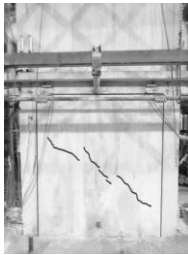
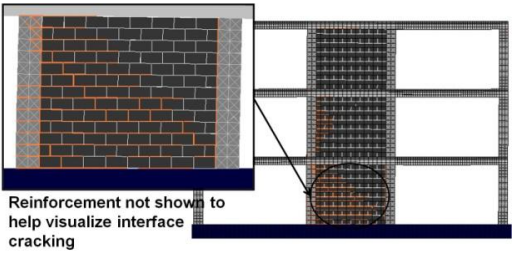

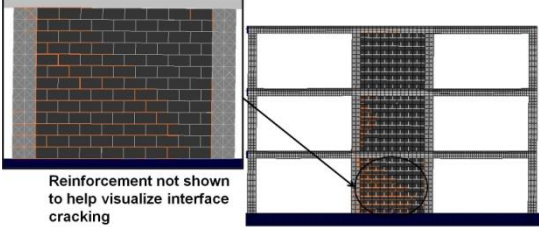

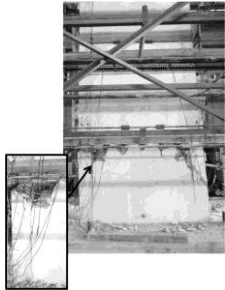
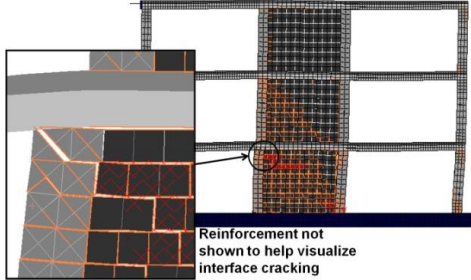
During D1 earthquake, the MRM specimen experiences only minor interface cracking between the columns and the first story infill and the maximum drift in the first story is 0.06%. In the finite element model, cracking initiates along the interface between the infill and the boundary column of the first story at 0.056% drift. There are also minor bed joint cracks in the finite element model.

The D2 earthquake was applied to the MRM specimen four times. Each time the experiment had to stop at around two seconds into the D2 experiment due to the technical problem in the actuators (these experiments are named as D2-1, D2-2, etc.). The maximum first story drifts observed during these trials are between 0.32% and 0.62%. At around 0.25% drift in the first story, a diagonal crack initiates in the first story infill. This same crack initiates in the finite element model at 0.14% drift. The onset of shear and flexural cracks are premature in the finite element model, initiating at the same time as the first diagonal crack. The next damage patterns observed during testing are distributed diagonal cracks which form within the first story infill wall and cracking of the first story boundary columns. A diagonal crack also initiates in the second story infill wall. All of this damage occurs during the first trial of ground motion D2 which has a maximum first story drift of 0.32%. Similar damage patterns are also observed in the finite element model at 0.39% first story drift, although slight cracking of the first story boundary columns had already begun at 0.13% drift. In the experiment, distributed cracking of the second story infill wall and the second story boundary columns occurs between 0.5% and 0.62% first story drift. In the finite element model, distributed cracking of the second story infill wall initiates after the diagonal crack and cracking of the boundary columns occurs simultaneously with the initial diagonal crack at a first story drift of 0.39%.

The cyclic tests on the MRM specimen result in crushing of the masonry at the top corners of the first story infill wall and ultimately shear failure of the first story boundary columns. Peak capacity of the frame was achieved at around 0.95% first story drift. In the finite element model, crushing initiates at 0.33% first story drift and the peak capacity of the frame is achieved at 1.23% drift.

(space left blank intentionally)

Table 5: Observed damage of the MRM specimen in the experiment (Ezzatfar et.al. 2012) and finite element model

	Experiment	FE Model
D1 Earthquake	 0.04-0.06%	 Reinforcement not shown to help visualize interface cracking 0.056%
	 (1)	 Reinforcement not shown to help visualize interface cracking 0.13%
D2 Earthquake	 (2)	 Reinforcement not shown to help visualize interface cracking 0.39%
	 (3) 0.32-0.62%	
Cyclic Test	 0.95%	 Reinforcement not shown to help visualize interface cracking 1.23%

The global force-displacement response of the model is also in good agreement with the experiment. Figure 81 presents the base shear vs. roof displacement for the three PSD tests on the MRM specimen and the envelope curve obtained from the finite element model. The initial stiffness of the model is within 5% of the initial stiffness of the experimental data, as interface cracking occurred at similar drift levels in the finite element model and the experiment. The softening of the analytical model is also consistent with the data from the D2-1 and D2-2 experiments, but the subsequent applications of D2-3 and D2-4 induce further damage to the structure which is not captured by the model. The peak strength of the model is 8.9% greater than the experimentally measured strength.

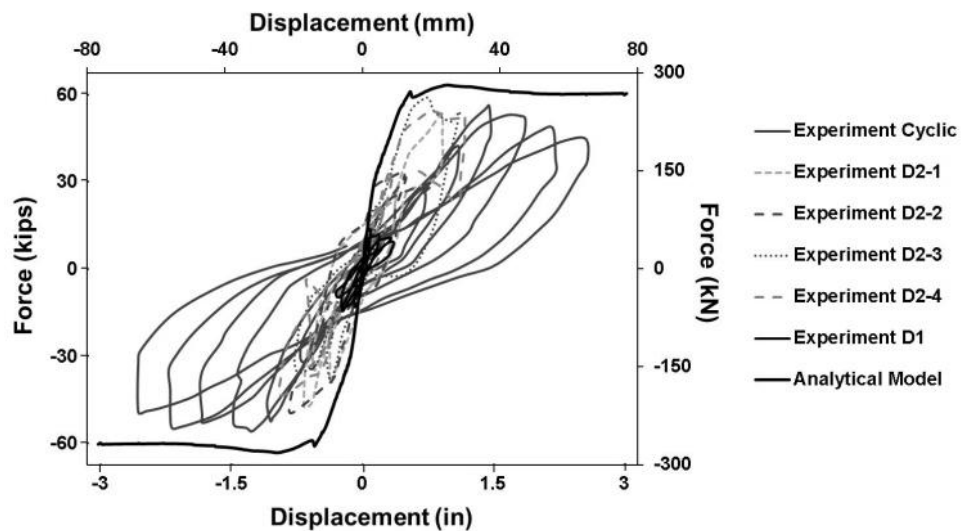


Figure 81: Base shear vs. top story displacement of the experiment (Ezzatfar et. al. 2012) and the finite element model

4.3.3 Studies on Variation of Effective Dowel Area

To model the anchorage dowels of the MRM specimen, 25% has been selected as the effective dowel area. Since many different equations exist for determining effective areas of dowel connections, a sensitivity study on the selected dowel area has been conducted with models using 0% dowel area, 25% dowel area (Paulay et al. 1974) and 100% dowel area. The maximum percentage change in capacity over the baseline model (25% dowel area) was a decrease in peak capacity of 22% by modeling 0% of the dowel area. This is a 14% underestimation of experimental capacity.

The sensitivity of the model to variation in effective dowel area is characterized by using an index, S , which has been used in the sensitivity analysis of URM infill structures modeled with FEAP by Stavridis and Shing (2010). The sensitivity index S , is calculated according to Equation 22, where Y is the value of the peak capacity of the model as a result of a change in the modeling parameter, and Y^b is the peak capacity in the baseline model. The variable X is the modeling parameter being varied, and X^b is the value of that modeling parameter in the baseline model.

$$S = \left| \frac{Y - Y^b}{Y^b} \frac{X^b}{X^b - X} \right| \quad (22)$$

The sensitivity of the peak capacity in the finite element model to the reduction of the effective dowel area is 0.22. This is much greater than the sensitivity of the peak capacity when the effective dowel area was increased to 100%, which yields a sensitivity of 0.012. Thus, it is important to consider the contribution of the dowels, but the peak capacity does not seem to be very sensitive to the overestimation of the effective dowel area.

4.4 Initial Finite Element Models

Initial finite element models of hybrid concrete-masonry structures were used to aid in the design of the experimental program and predict the behavior of the frames. These models are calibrated to materials tests which were conducted prior to the experiment and utilize the proposed modeling methodology and material calibration outlined in this chapter.

Testing of a hybrid concrete-masonry frame is required to adequately define the interface properties and the effectiveness of the dowel connections, so several assumptions were made in the preliminary models. First, the interface elements between the masonry infill and the RC frame were given the same properties as the mortar bed joints even though the mortar was unlikely to bond as well to the concrete as the masonry units. Second, the effective dowel area for the additional truss elements used to model the shear contribution of the vertical reinforcement within grouted cells was assumed to be 25% of the actual bar area. Third, all dowel connections from the partially grouted masonry were modeled as 100% of the actual bar area, because the previous models of concrete frames with masonry infill and mesh reinforced mortar indicated that the finite element models are more sensitive to an underestimation in the effective dowel area than an overestimation.

The material calibrations for the concrete, ungrouted masonry and grouted masonry are presented and compared to results from materials tests. The materials were selected to closely resemble properties of materials typically used in the Caribbean which is discussed in detail in Chapter 5, Experimental Design. Appendix B contains detailed

graphs, tables, and pictures from all of the materials tests. A table summarizing all of the parameters in the initial finite element models is found in Appendix C.

4.4.1 Concrete Properties

Most of the properties for the concrete were determined explicitly through materials testing. Results of compression tests and split tension tests of 6x12 in cylinders determined the concrete compressive and tensile strengths. Compression tests following the procedures outlined in ASTM C469 were used to obtain the concrete Elastic Modulus. The Shear Modulus of the concrete was then calculated as $G = \frac{E}{2(1+\nu)}$ assuming Poisson's ratio equal to 0.2. The fracture energy was assumed to be proportional to the compressive strength of the concrete and taken from data in the literature (Hillerborg 1983). The parameters μ_0 , μ_r, r_0 and r_r which govern the shear behavior of the concrete interface elements were initiated using values from Stavridis and Shing (2010). The compressive stress-strain curve for the smeared crack element is shown in Figure 82a. Figure 82b shows the failure surface of the concrete interface element.

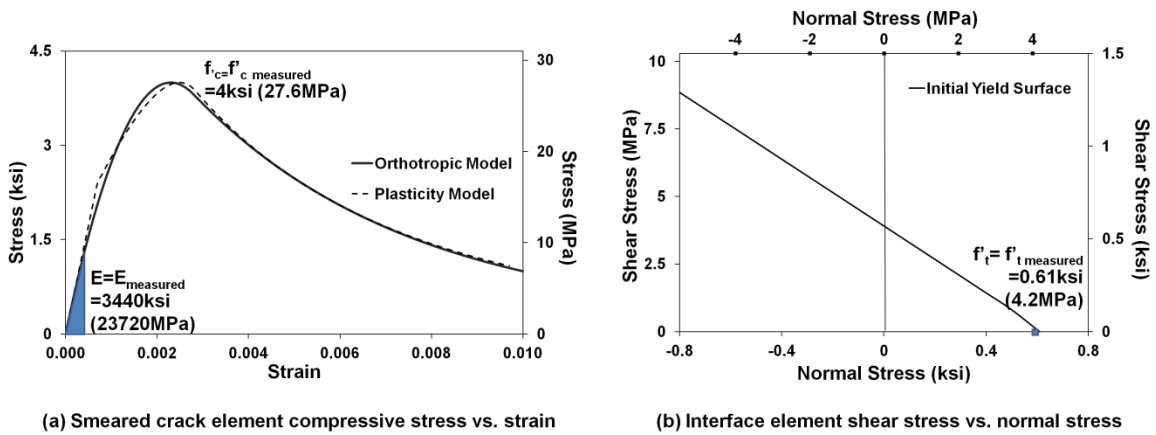


Figure 82: Concrete properties

4.4.2 UngROUTED Masonry Properties

The interface elements representing ungrouted bed joints and the smeared crack and interface elements representing the ungrouted masonry units were calibrated according to the procedure presented in the constitutive model (Section 3.3.2). The prism strength was obtained from compression tests of 2-unit prisms. The Elastic modulus was determined by conducting compression tests with dial gages mounted across the bed joint. The tensile strength of the ungrouted masonry unit was approximated as 10% of the unit compressive strength determined from testing. The fracture energy of the masonry unit and the shear properties from the unit were initiated using values from Stavridis and Shing (2010). The modeled compressive stress-strain curve for the ungrouted masonry prism is shown in Figure 83a. Figure 83b shows the failure surface of the interface element representing the ungrouted masonry unit.

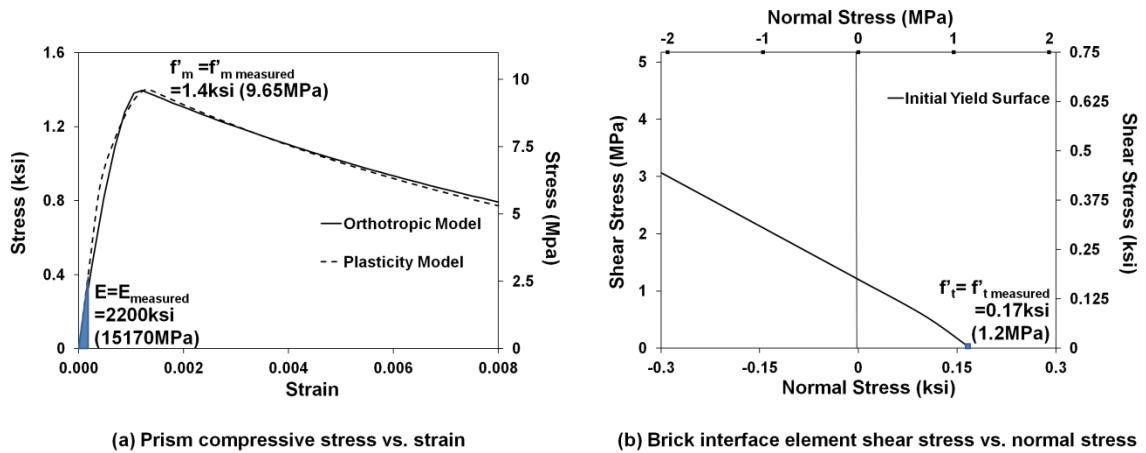


Figure 83: UngROUTED masonry properties

The failure surface of the interface element representing the ungrouted bed joint was also calibrated using the procedure of the constitutive model (Section 3.3.2). Bond

wrench tests were used to obtain the tensile strength of the bed joint. Triplet tests conducted at several levels of pre-compression to obtain points to calibrate the normal stress vs. shear stress relation of the interface element. The test set up and testing of the masonry triplet tests is shown in Figures 84a and 84b. Each triplet was initially compressed using the series of steel plates and threaded rods, then the specimen was rotated 90° and placed into a compression testing machine. The vertically applied compressive force was obtained from the testing machine, and the horizontal compressive force was monitored with a load cell. The peak shear stress was obtained from the peak force recorded by the testing machine and plotted against the average lateral compressive stress calculated using the data from the load cell. The failure surface of the interface element representing the ungrouted bed joint is shown in Figure 85. The interface element was calibrated with the aiming not to overestimate the cohesion of the bed joint, as the compressive stress on the infill during testing was expected to be very low.



(a) Precompression of triplet



(b) Testing of triplet

Figure 84: Set up and testing of masonry triplet

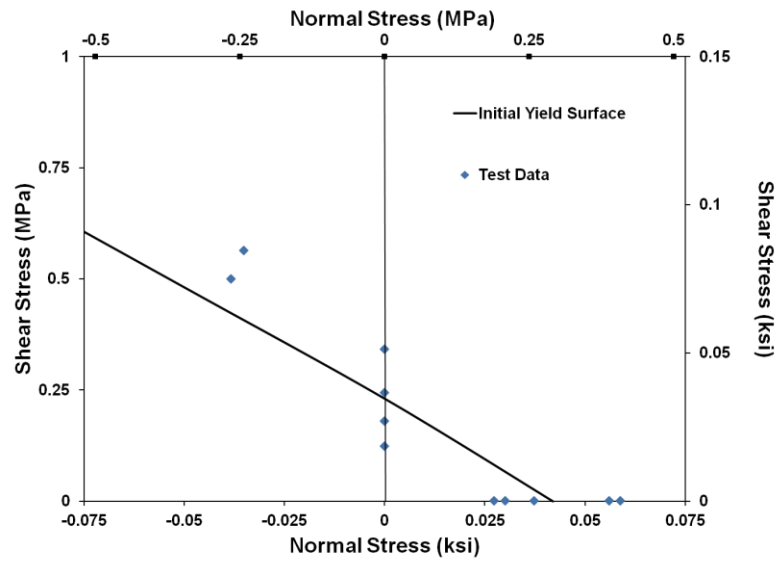


Figure 85: UngROUTED bed joint interface element shear stress vs. normal stress

4.4.3 Grouted Masonry Properties

The prism behavior of the grouted masonry was calibrated to the prism strength and Elastic modulus obtained through testing. The grouted prisms typically failed in a shear or cone and shear as defined by ASTM C1314. For this reason, the compression behavior of the grouted cells was calibrated like a continuous material in a manner similar to concrete. The interface elements are given an artificially high stiffness so as not to influence the compression behavior of the smeared crack elements and the smeared crack element isotropic compression curve is calibrated to the grouted prism stress-strain behavior. Then, the orthotropic curve was calibrated to the isotropic (plasticity) curve. The tensile strength of the grouted masonry unit was approximated as 10% of the grout compressive strength determined from tests of grout cubes prepared according to ASTM C1019. The fracture energy of the grouted masonry unit were assumed to be proportional to the compressive strength of the concrete grout and interpolated from values in the

literature (Hillerborg 1983). The values of μ_0 , μ_r , r_0 and r_r were initiated using values for concrete from Stavridis and Shing (2010). The modeled compressive stress-strain curve for the grouted masonry prism is shown in Figure 86a. Figure 86b shows the failure surface of the interface element representing the grouted masonry unit.

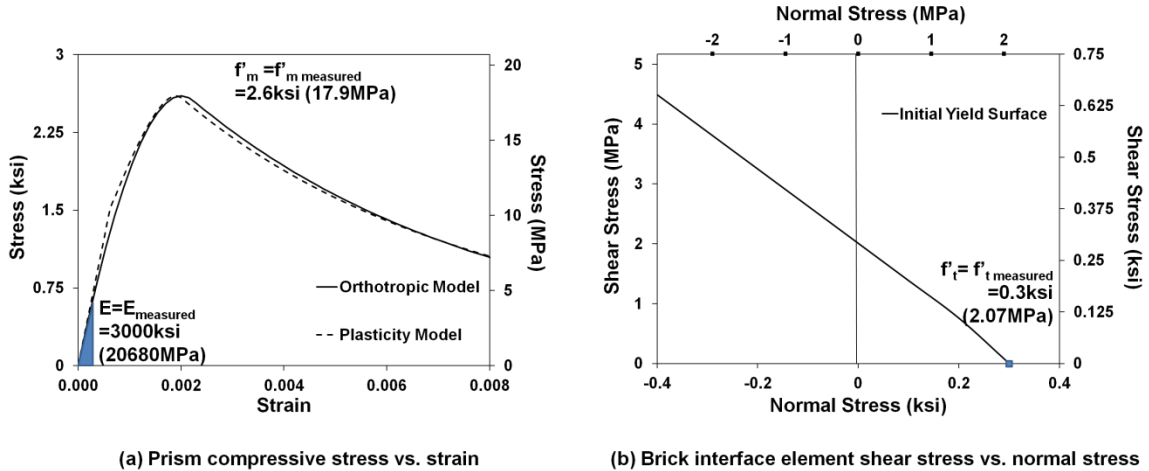


Figure 86: Grouted masonry properties

The proposed equations based on the compressive strength of the grout and mortar were used to calculate the tensile bond strength, cohesion and shear friction factor for the grouted cells. The equations are shown in Figures 87-89 with new data points from the tests of grouted shear triplets and bond wrench tests on grouted prisms added to the data collected from the literature. The tests confirm that the equations from the proposed calibration methodology yield close predictions for the bond strength, cohesion and shear friction of grouted bed joints. Note that the triplet tests under zero pre-compression have a very wide scatter, so the mean value for cohesion was taken as the y-intercept of the linear best fit to the shear stress vs. normal stress data collected from all the triplets. The data also confirms the trend of a bi-linear relation of shear stress to

normal stress in grouted bed joints which does not fit well with the current hyperbolic yield surface of the interface element (See Figure 90). Even so, the proposed methodology using a linear fit to determine the failure surface of the grouted bed joint interface element (Section 4.2.3.2) provides a close estimate of the grouted bed joint shear capacity (See Figure 90).

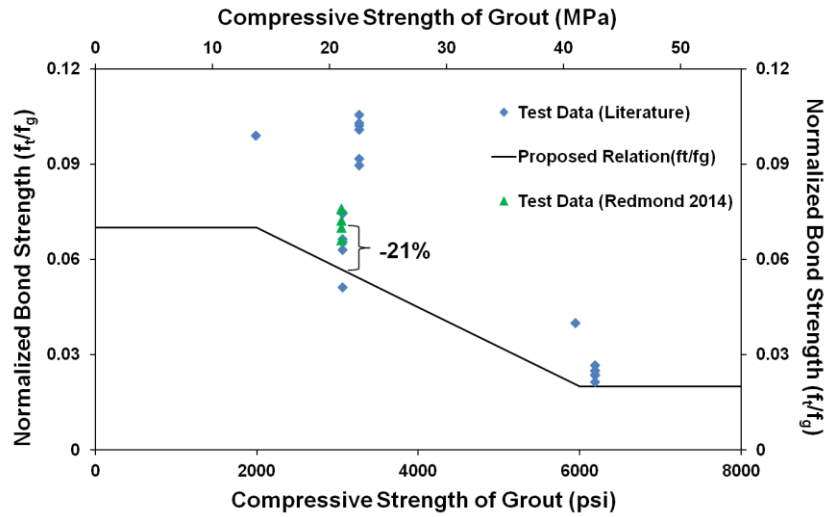


Figure 87: Bond strength equation with results from bond wrench tests on grouted specimens

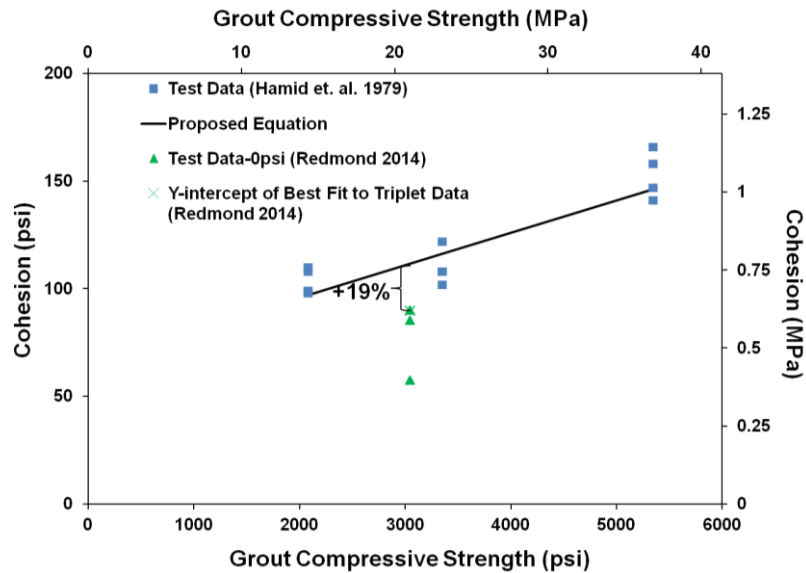


Figure 88: Cohesion equation with results from grouted triplet tests

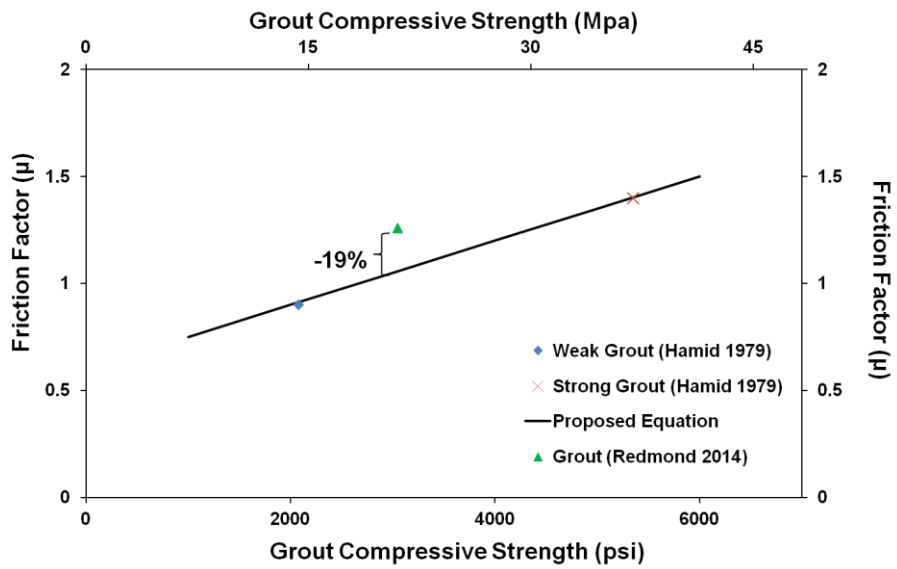


Figure 89: Friction factor equation with results from grouted triplet tests

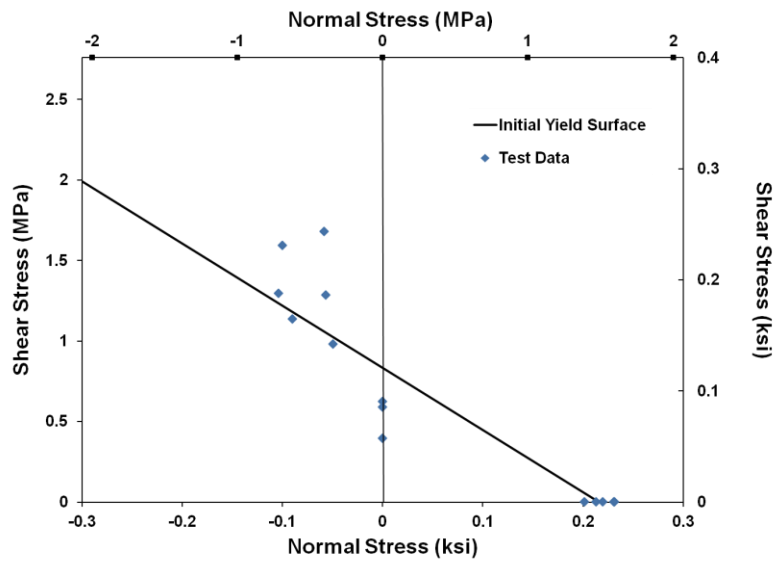


Figure 90: Grouted bed joint interface element shear stress vs. normal stress

4.5 Chapter Summary

The proposed meshing scheme for hybrid concrete masonry structures has the flexibility to model truss and bond beam reinforcement and explicitly accounts for the contribution of vertical reinforcement to the shear capacity of grouted bed joints. The material calibration of the newly proposed meshing scheme can be conducted using the same materials tests suggested for calibrating the constitutive model. However, many of the materials tests necessary to calibrate the behavior of grouted bed joints are difficult to conduct and not available in literature. Thus, an alternative calibration method has been proposed to calculate properties as a function of the compressive strength of the grout. This method is developed using concepts of shear friction in concrete joints. Although previous methodologies did not explicitly account for the contribution of vertical reinforcement to the shear capacity of the grouted bed joint, a methodology also was suggested to account for this effect. The steps for the calibration of grouted bed joints are listed below:

1. Obtain the compressive strength of the grout from compressive tests of grout cubes prepared according to ASTM C1019,
2. Calculate the tensile bond strength of the grouted bed joint using Equation 14,
3. Calculate the shear friction factor of the grouted bed joint using Equation 15,
4. Calculate the cohesion of the grouted bed joint using Equation 16,
5. Calculate at least 5 points from which to create a linear best fit line of the initial failure surface of the interface element representing the grouted bed joint, where the x is normal stress and y is shear stress and stresses σ_1 to σ_3 are normal stresses within the expected range of stress for the masonry being modeled:

- a. $P_1 = (0, c)$
 - b. $P_2 = (s, 0)$
 - c. $P_3 = (\sigma_1, c + \mu_0 \sigma_1)$
 - d. $P_4 = (\sigma_2, c + \mu_0 \sigma_2)$
 - e. $P_5 = (\sigma_3, c + \mu_0 \sigma_3)$
6. Select values for s_0 , μ_0 , and r_0 so that the initial failure surface of the interface element representing the grouted bed joint matches the linear fit to P_1 through P_5 ,
 7. Determine the residual failure surface by letting μ_r and r_r equal μ_0 and r_0 and setting the tensile capacity of the failed joint to zero,
 8. Determine the shear stiffness of the interface element representing the grouted bed joint by Equations 17-21,
 9. If the grouted bed joint contains vertical reinforcement, add two additional truss elements across the bed joint as shown in Figure 74. The total area of the two truss elements should equal 25% of the actual bar area, representing the shear resistance of the vertical reinforcement,

Further, a methodology for modeling dowel connections from masonry infill to RC column has been validated using a model of a 3-story, 3-bay RC frame with infill and mesh reinforced mortar (MRM). The results indicate that the proposed modeling method can adequately capture the influence of the dowel reinforcement on the peak strength of the RC frame with infill masonry. The results also suggest that the peak capacity of the frame has minimal sensitivity to overestimation of the effective dowel area

Finally, the preliminary finite element models used to design the experimental program and predict the seismic behavior of hybrid concrete masonry frames has been

presented. The triplet tests and bond wrench tests conducted on samples of grouted masonry validate the proposed methodology for calculating shear and tensile properties of the grouted bed joint as a function of the grout compressive strength.

CHAPTER 5

EXPERIMENTAL DESIGN

The main objective of the experimental program is to validate the proposed Finite element models. Of particular interest is the behavior of the interface between the reinforced masonry infill and the reinforced concrete (RC) frame. The scope of the testing regimen was limited to observing the effect of two different methods to connect the reinforced masonry infill wall to the RC frame on the seismic performance of the hybrid concrete masonry wall. These two tests serve as validation points for the Finite element models which can then be used to predict the seismic performance of other types of hybrid concrete masonry structures. The experimental program is the first laboratory tests of these types of structures and yields detailed information about the stiffness, progression of damage, peak strength and failure modes of hybrid concrete structures.

The design and construction details for the RC frames are identical between the two test specimens and are presented first. Then, the design and construction details for the masonry infill and the two different methods for connecting the infill to the RC frame are discussed. The test set up, including gravity loading and the application of lateral loads is explained next. Finally, the instrumentation plan for localized measurements of the RC frames and infill walls is presented.

5.1 RC Frame

5.1.1 Design

In order to isolate the effect of different connections of the reinforced masonry wall to the RC frame, both specimens were designed to be identical except for the

variation in connection type. The International Building Code was selected as the design code for the RC frame because it is the most commonly used code among the engineers surveyed during site visits to the Caribbean and a separate analytical study determined that the modern codes in the region seem to yield designs which have similar drift and demand to capacity ratios as the IBC (Redmond et. al. 2013).

The RC test frame was taken from the bottom story of a five story office building (See Figures 91 b and c) designed by the 2009 International Building Code (IBC) to the highest level of seismic hazard in Trinidad (See Figure 91 a). The RC frame was designed to carry all of the gravity and lateral loads, and the masonry infill was accounted for with a line load (500lb/ft, 7.3 kN/m), as is typically done by engineers interviewed on the site visits to the Caribbean. The design was based on a concrete strength of 4,500 psi (31.03 MPa) and reinforcement yield strength of 60,000 psi (413.69 MPa). The soil type was taken as an IBC 2009 site class D. The slab was designed as a one-way slab, and the experimental frame was taken from the direction of the beams rather than the girders as the stiff wall is more likely to influence the weaker beams than the girders.

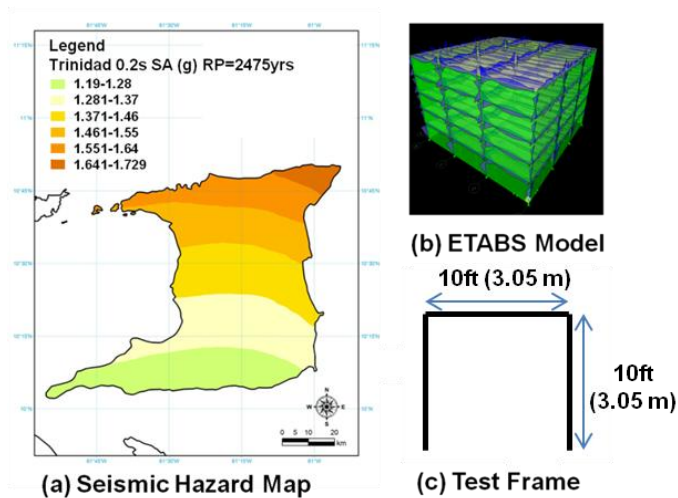


Figure 91: Design of the RC frame

In order to account for the effect of the stiffness of the infill wall above the beam on beam curvature, an extra half wall was constructed above each frame. The one and a half story frame was selected based on the results of finite element models for several proposed configurations. At this very early phase of the design stage, no material data for the actual structure was available and all material properties had to be assumed based on information from engineers in the Caribbean and data in the literature. The proposed configurations included: a single frame (See Figure 92a), a frame with an additional half story above (See Figure 92b), and a two-story frame (See Figure 92c). The resulting force displacement behavior of each model is shown in Figure 93. There is very little difference in the initial stiffness and peak capacities of the models. However, beam-curvature is influenced by the presence of a masonry wall above the beam (See Figure 94). There are less significant differences in beam curvature between the construction of an additional half or full story masonry wall. Ultimately, the one and a half story configuration was selected as it is simpler to construct and to load than a two-story frame.

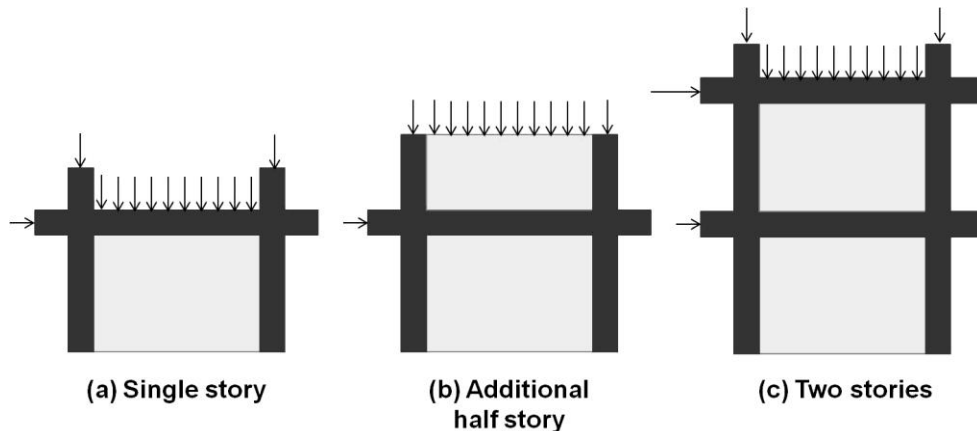


Figure 92: Proposed geometries and loading configurations

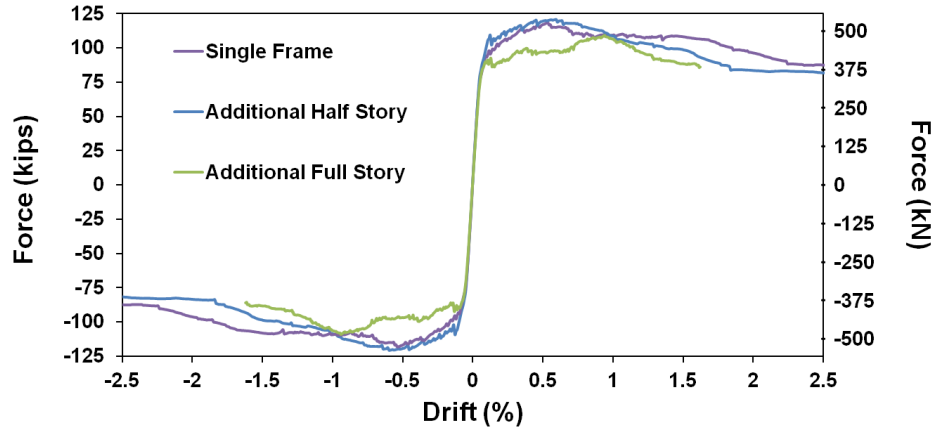


Figure 93: Variation in force-displacement behavior of the models

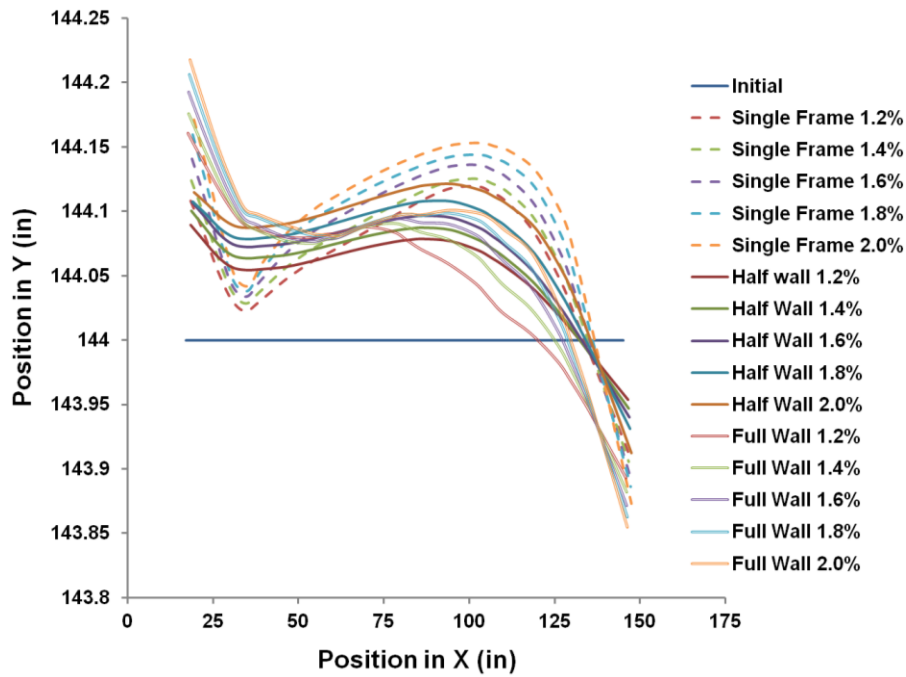


Figure 94: Position of centerline beam nodes during analysis for each model from 1.2% to 2.0% drift

5.1.2 Material Properties

Caribbean concrete typically uses limestone aggregate which typically uses less cement, and has a lower elastic modulus than concrete mixes made with granite aggregate. Because limestone aggregate is not readily available in Georgia, the concrete

mix was prepared using granite with the goal of achieving similar peak strengths, while recognizing that the material would be slightly stiffer than the concrete in the Caribbean.

The mix design had a 0.75 inch (19.1 mm) maximum aggregate size, water-to-cement (w/c) ratio within the range of 0.5 to 0.55 and was designed to achieve a maximum strength of 4500 psi (31.03 MPa). Because most concrete plants design a batch to achieve greater than specified strength, the greatest concern was that the concrete strength would be greater than in the Caribbean. To avoid this, the nominal specified strength of the final mix was been 3000 psi (20.68 MPa), and the average 28-day strength of the mix was tested to be 4055 psi (27.96 MPa). This is slightly under the design strength of 4500 psi (31.03 MPa), but well within the range of concrete strength in the Caribbean, which vary from 3000 to 4500 psi (20.68 to 31.03 MPa). The notes from interviews with design firms in the Caribbean regarding construction practices and material properties are presented in Appendix A. The elastic modulus of the concrete was determined using the procedure outlined by ASTM C469. The average value for the elastic modulus was 3,440,000 psi (23700 MPa).

The reinforcement was a standard mild steel rebar. The average tensile yield strength as calculated by the 0.2% offset method was 78,500 psi (541 MPa). Additional graphs and tabulated data for the materials tests conducted on the concrete and the reinforcement is given in Appendix B.

5.1.3 Construction Details

First, a deep post-tensioned slab was provided to allow for full development length of the #8 column bars and to allow for loading plates to be embedded in the foundation to post-tension the beam and columns with gravity loads. Figures 95 and 96

show the placement of the PVC pipes used as post-tensioning conduit, the anchorage plates embedded in the foundation and the shear reinforcement. The slab was cast in three pieces to allow for disassembly and reuse in future projects.

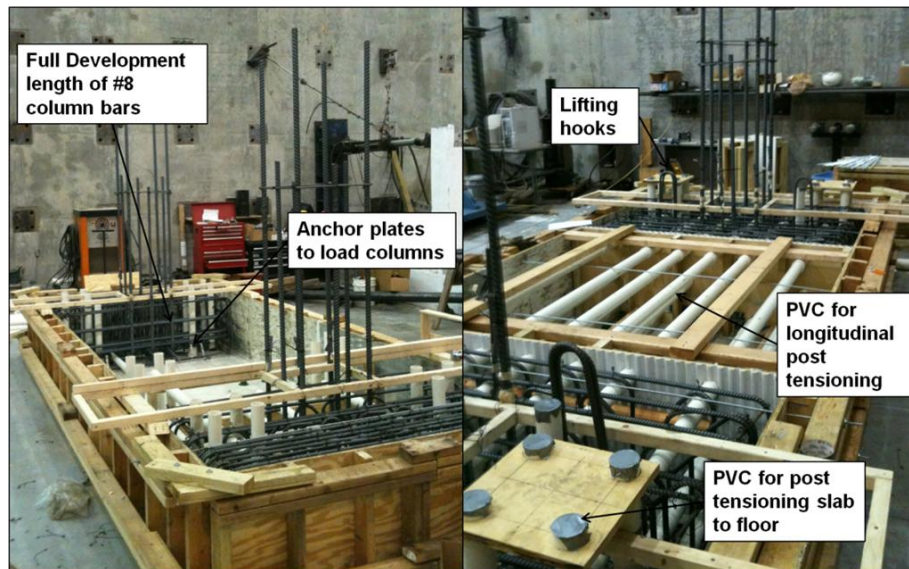


Figure 95: Construction of the post-tensioned slab beginning with the end sections



Figure 96: Construction of the post-tensioned slab, continuing with the middle section

Next, the column formwork and reinforcement were placed. Mechanical splices were used in the columns for ease of construction (See Figure 97). Then the slab was

post-tensioned and lifted to remove the forms and placed back over the anchors on the strong floor as shown in Figure 98. The slab was post-tensioned to the floor to provide additional resistance against sliding during the experiment (See Figure 99).



Figure 97: Installation of column forms and reinforcement

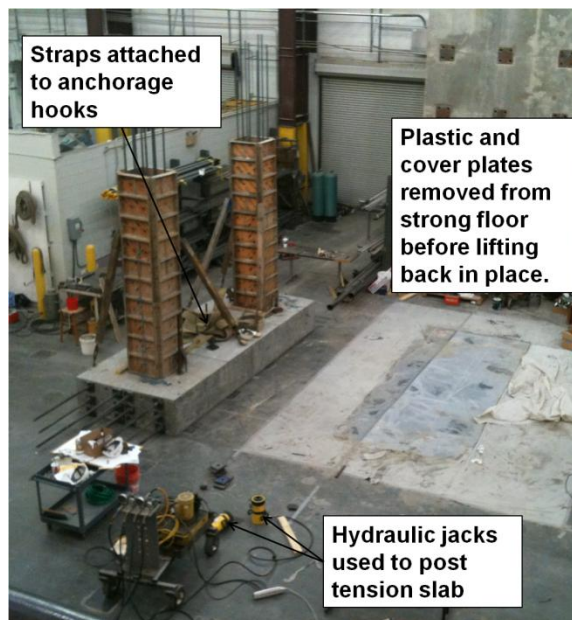


Figure 98: Lifting slab



Figure 99: Post-tensioning slab to strong floor

After the columns were cast, shoring was constructed for the beam forms and reinforcement was placed (See Figure 100). Stub beams were extended past the joint region to allow for a loading plate to be placed on the end of the stub beam rather than directly on the joint, permitting more realistic rotation of the beam-column joint during testing. The longitudinal beam reinforcement was extended through the joint and terminated in the stub beams without any lap splices.



Figure 100: Construction of the beams

Finally, the reinforcement for the top half columns was placed and the columns were poured using a conveyor truck (See Figure 101). Figure 102a shows the removal of the form work and Figure 102b shows the dowel connections which have been cast-in-place in one of the two frames. The complete construction drawings for the RC frame are shown in Figures 103-105. The cast-in-place dowels used to connect the masonry infill to the RC frame in one of the two frames are not shown.



Figure 101: Conveyor used to pour the top half columns



Figure 102: Disassembly of the shoring and formwork (a) and close up of frame with dowel connections (b)

(space left blank intentionally)

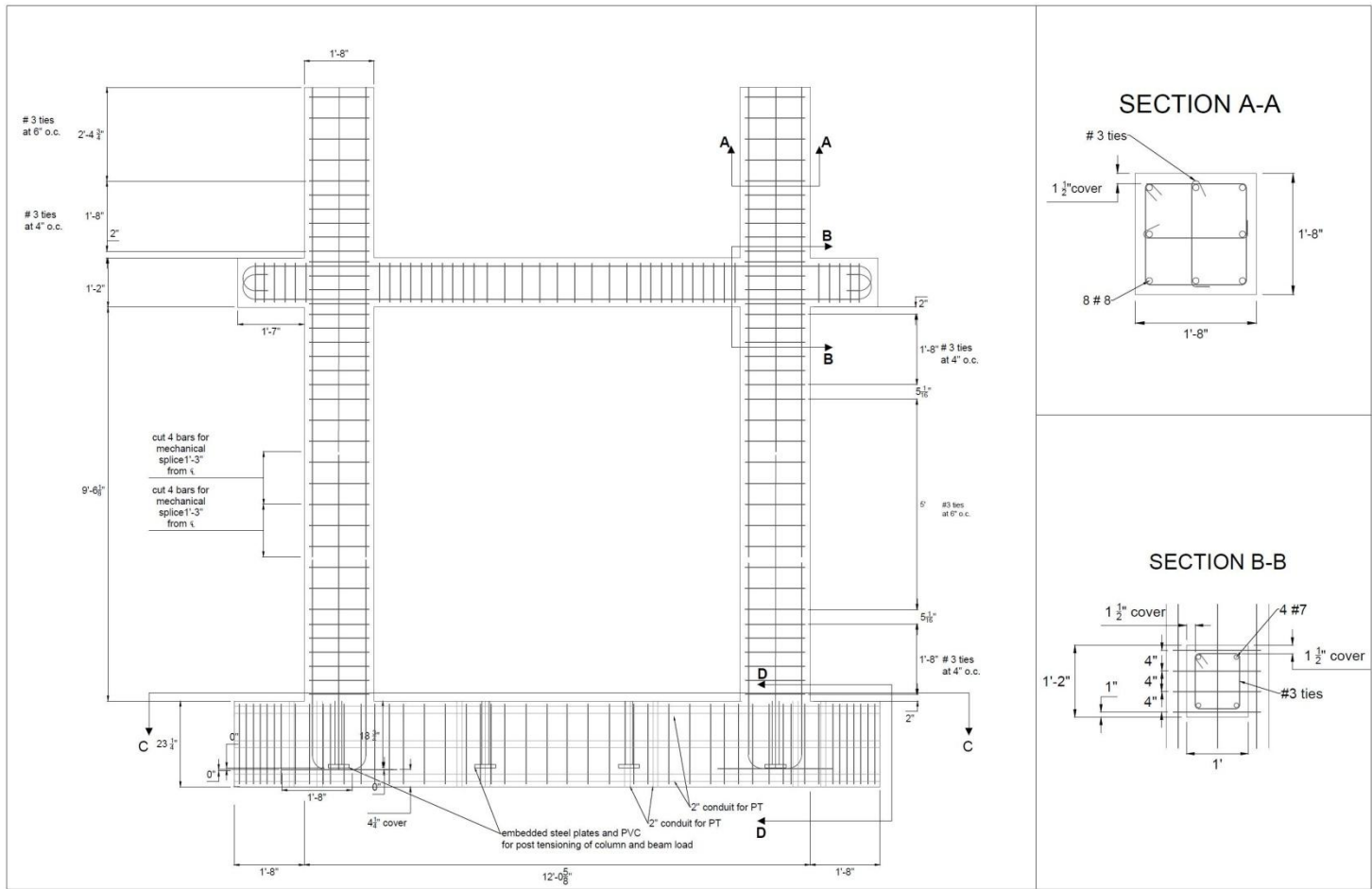


Figure 103: Reinforced concrete frame

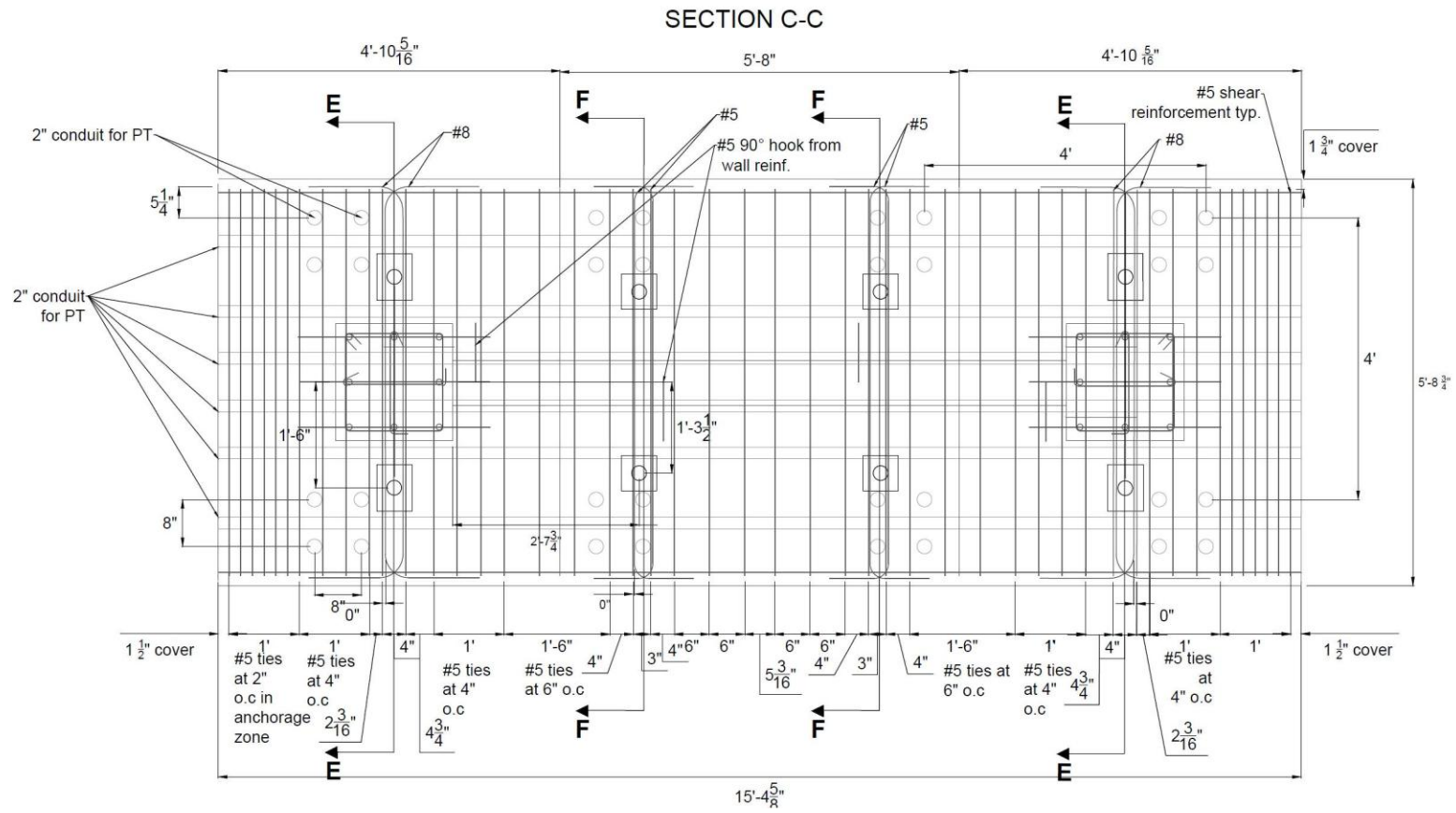


Figure 104: Post-tensioned slab

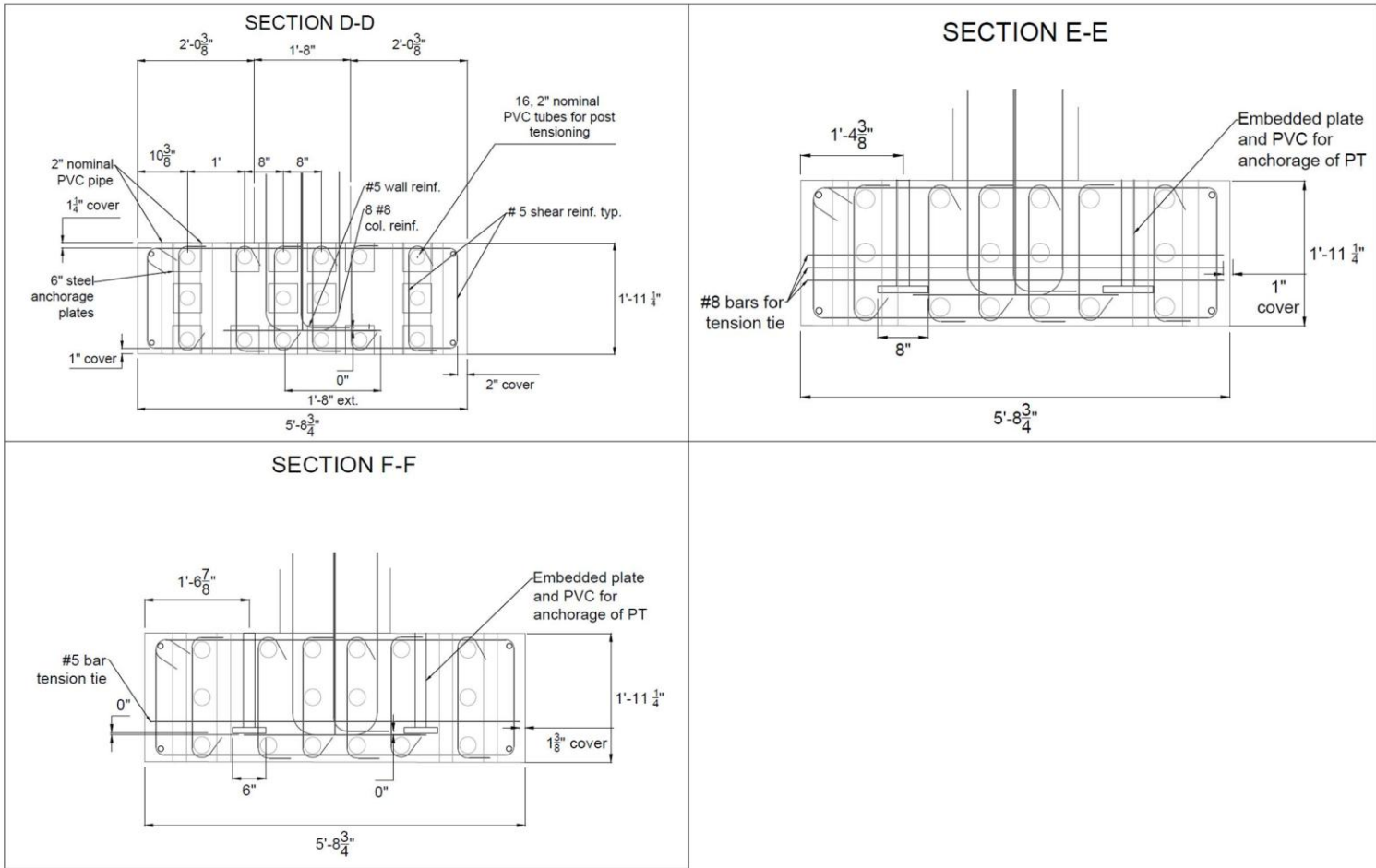


Figure 105: Post-tensioned slab section detail

5.2 Reinforced Masonry Infill and Connections to RC Frame

5.2.1 Design

The masonry infill walls of both test frames were constructed using 8x8x16 inch (20.3x20.3x40.6 cm) hollow CMU as is typical in the Caribbean. The strength of the units in the Caribbean is much lower than the typical strength of American CMUs, typically 1000-3500 psi (6.90-24.13 MPa). However, a low strength batch of CMU which had been improperly cured was obtained from an American supplier.

The internal wall reinforcement was kept the same between the two specimens. The masonry reinforcement sizes and spacing were based on what is most common among all the firms interviewed and does not reflect an exact detailing method for a particular firm. The horizontal reinforcement within the masonry wall was a single #3 rebar placed in the bed joint and down the centerline of the wall, spaced every three courses. This typically leads to a larger bed joint than given by TMS 402. Ladder reinforcement is not available in the Caribbean, and bond beams are not used. The vertical reinforcement was a #5 rebar spaced every 32 inches (81.3 cm). The cells with vertical reinforcement were filled with a watered-down concrete and consolidated every three to four courses with a rod, in accordance with practices observed in the Caribbean.

For both frames, #5 dowel bars for the vertical wall reinforcement were cast into the foundation. The splice lengths for the dowel bars and the lap splices within the walls were determined based on TMS 402 in order to adhere as much as possible to current design codes, although it is more common within the Caribbean to specify a splice length in terms of bar diameters ($30-40d_b$). Lap splices for the vertical masonry reinforcement

were placed every four courses, in accordance with the most common local practices. In one of the frames, cast-in-place connections were placed in the RC frame both vertically (#5 dowel bars) and horizontally (#3 dowel bars). The 90° hooks at the end of each dowel were extended as close to the far face of the columns and beams as possible to be consistent with typical ACI 318 detailing. The final construction drawing for the masonry infill wall without dowel connections is shown in Figure 106. The construction drawing for the infill wall with dowel connections is shown in Figure 107.

The concrete used to fill the reinforced cells was designed to be as close to the practices observed in the Caribbean. Often, the same concrete is used to fill the cells as would be used for the construction of an RC frame, except that water is added to the mix to achieve a large slump. The strength of the concrete used to fill the grouted cells is typically between 2000 and 3000 psi (13.79 and 20.68 MPa).

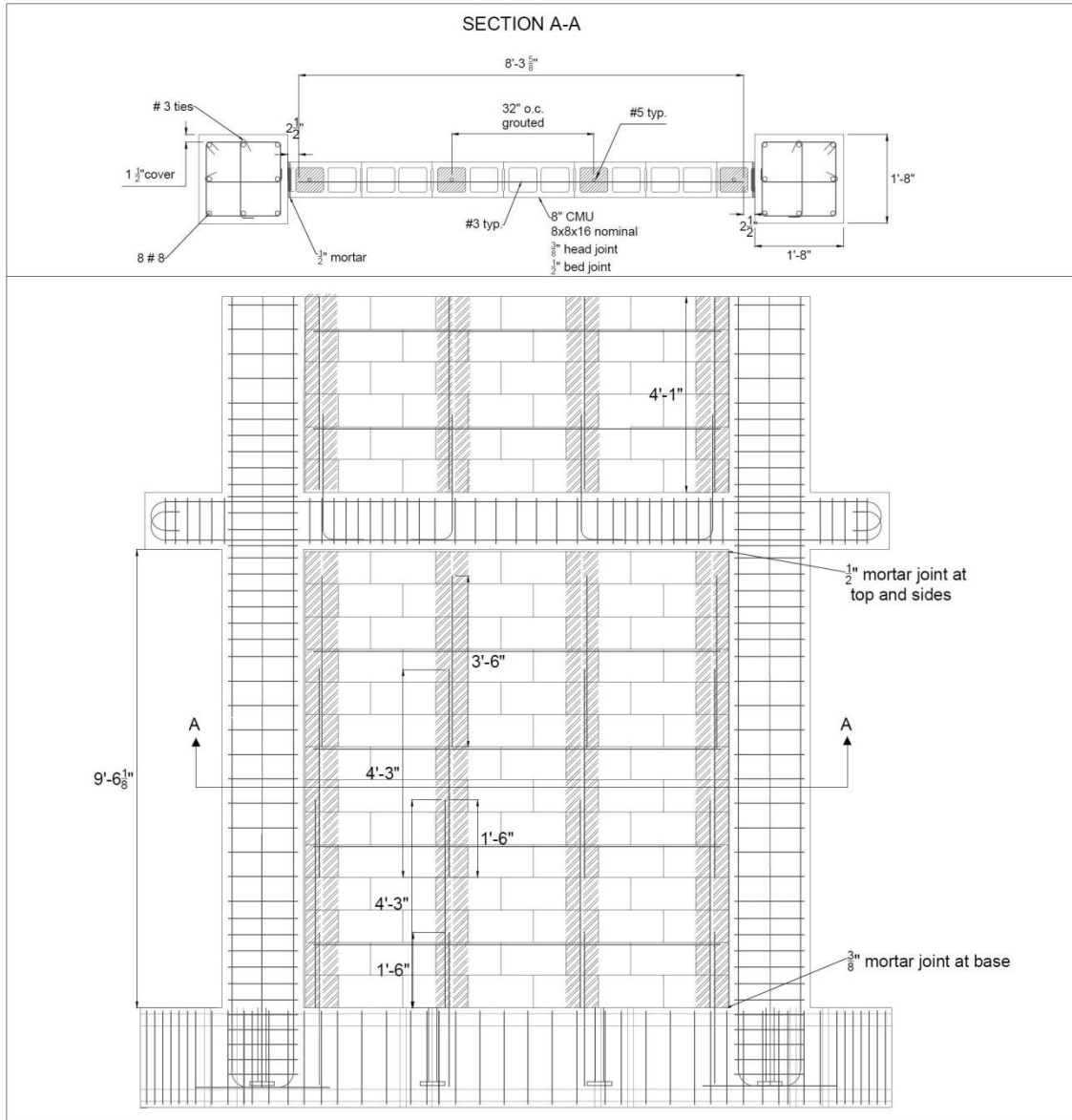


Figure 106: Masonry details for frame without dowel connections

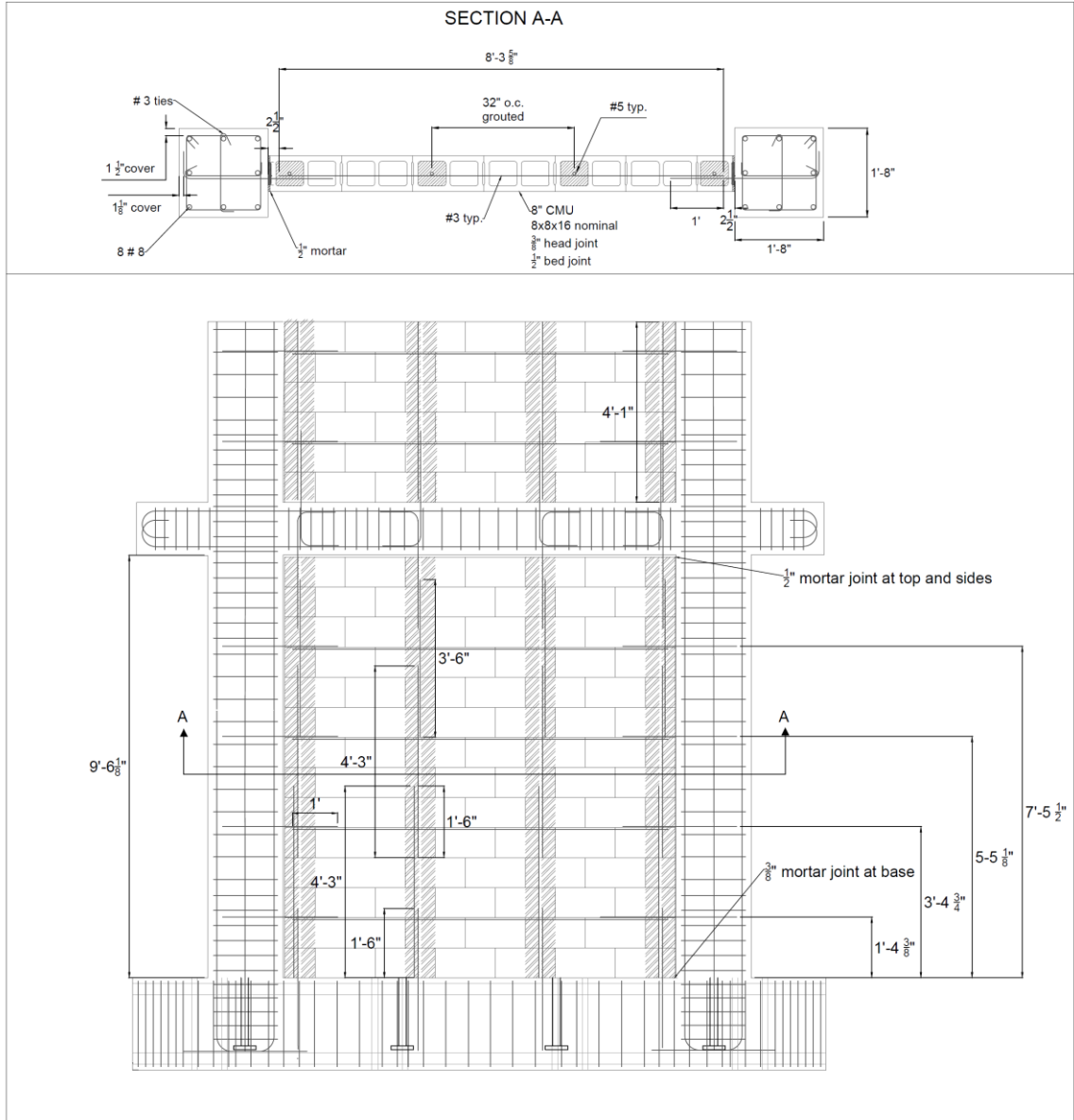


Figure 107: Masonry details for frame with dowel connections

5.2.2 Material Properties

The masonry infill walls of both test frames were constructed using 8x8x16 in (20.3x20.3x40.6 cm) hollow CMU with unit strength of 1700 psi (11.72 MPa). The CMU strength was selected based upon what was available from local U.S. suppliers and was within the range of CMU strengths typical to the Caribbean.

The mortar was mixed volumetrically in a ratio of three parts sand to one part Portland cement. Every firm interviewed used this type of mortar. To determine the compressive strength of the mortar, 2 inch (5.08 cm) cube specimens were taken at the time of construction and cured in the fog room for twenty-eight days. The average compressive strength of the mortar was 4430 psi (30.54 MPa).

The mix design for the weak concrete was designed using ACI 211 for 3000 psi (20.68 MPa) and a 7 inch (17.8 cm) slump. Then, during construction water was added to achieve a 9 inch (22.9 cm) slump. The compressive strength of the concrete was determined by two different methods. First, traditional 6x12 inch (15.2x30.5 cm) cylinder molds were cast and cured in the fog room. Second, grout prisms were formed according to ASTM C1019. The grout prisms are thought to better represent in-place properties of the grout, since the CMU block absorbs some of the water from the concrete which results in greater compressive strength (See Figure 108). The average compressive strength of the concrete as given by the grout prisms was 3040 psi (20.96 MPa), and the average compressive strength as given by the cylinder tests was 2760 psi (19.03 MPa).



Figure 108: Construction of grout prisms made from weak concrete

Masonry prisms were constructed for both ungrouted masonry and grouted masonry (See Figure 109 a and b). The average 28-day strength of the prisms was 1430 psi (9.86 MPa) and 2570 psi (17.72 MPa), for the ungrouted and the grouted prisms respectively. The shear and tensile properties of the grouted and ungrouted bed joints were determined using masonry triplets (See Figure 110 a and b) and prisms tested with a bond wrench machine (See Figure 111 a and b). Additional pictures of the test set ups, failed masonry samples and tabulated data for the materials tests conducted on the mortar, the concrete used to fill the grouted cells and the masonry assemblies are given in Appendix B.

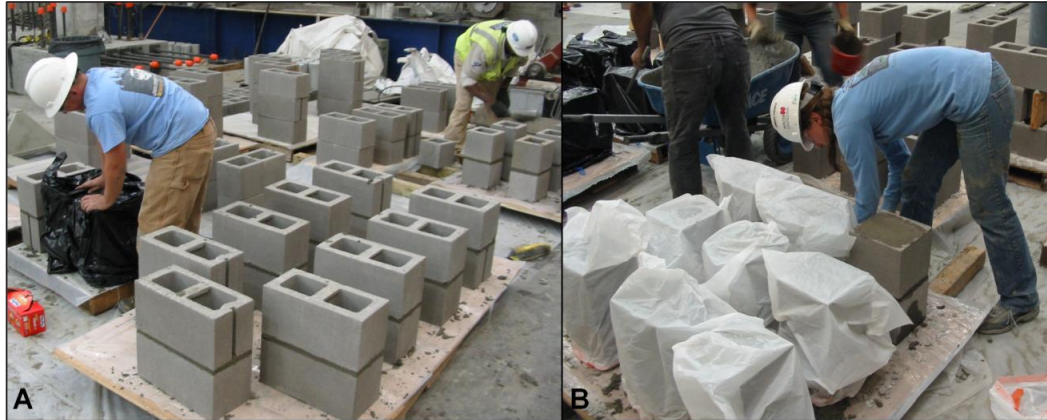


Figure 109: Constructing and bagging the (a) ungrouted prisms and (b) grouted prisms

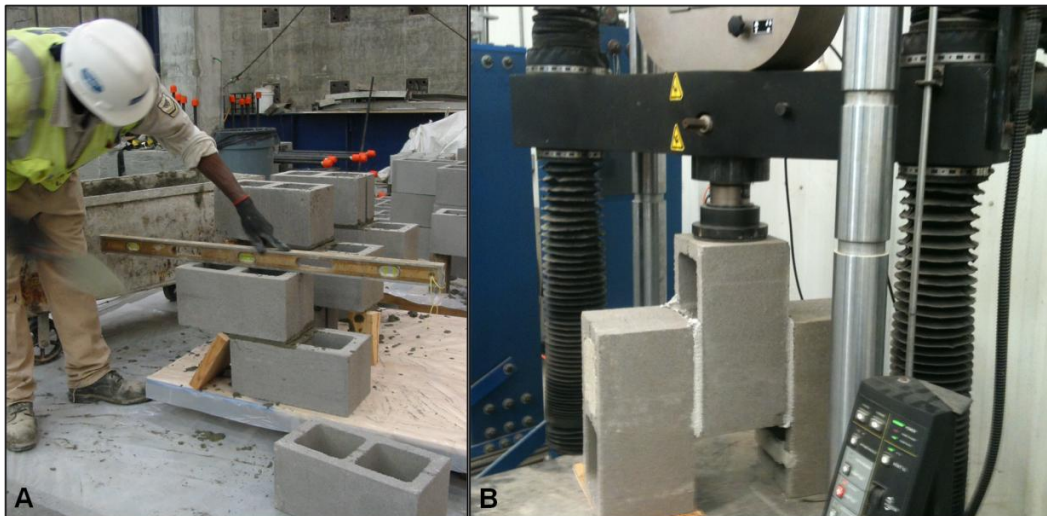


Figure 110: Masonry triplet (a) construction and (b) testing

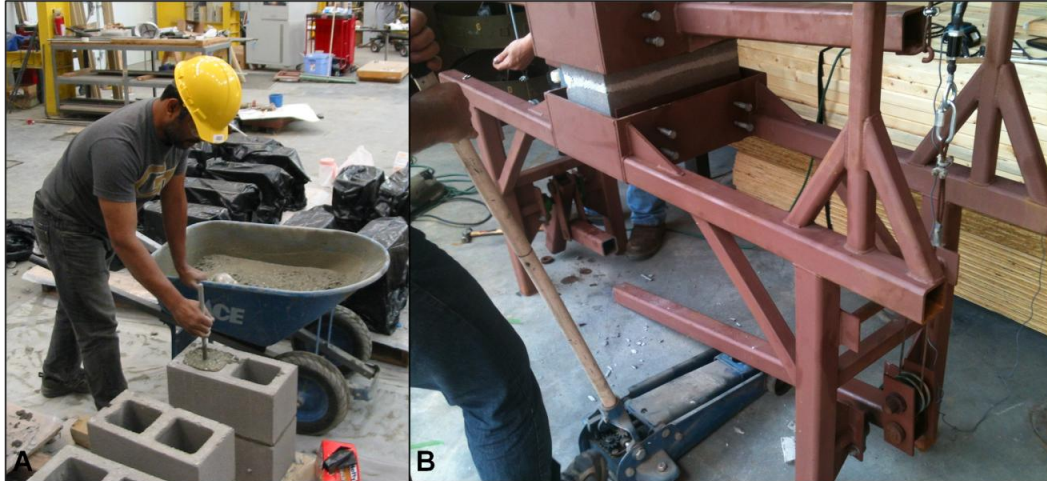


Figure 111: Masonry-mortar bond specimen (a) construction and (b) testing

5.2.3 Construction Details

The construction of the masonry wall primarily was done by a professional mason to ensure a consistent quality for both walls. The mortar for the masonry wall was volumetrically proportioned (See Figure 112). The bed joints were increased to a 0.5 inch (1.27 cm) thickness to accommodate the #3 reinforcing bars. The head joints were left at the standard 0.375 inch (0.952 cm) thickness. All mortar joints were tooled.



Figure 112: Volumetric batching of the mortar

For both specimens, the dowel bars were cast into the foundation to be spliced with the vertical reinforcement for the wall as shown in Figure 113a. At the end of each course mortar was placed in the gap between the CMU and the column (See Figure 113b).

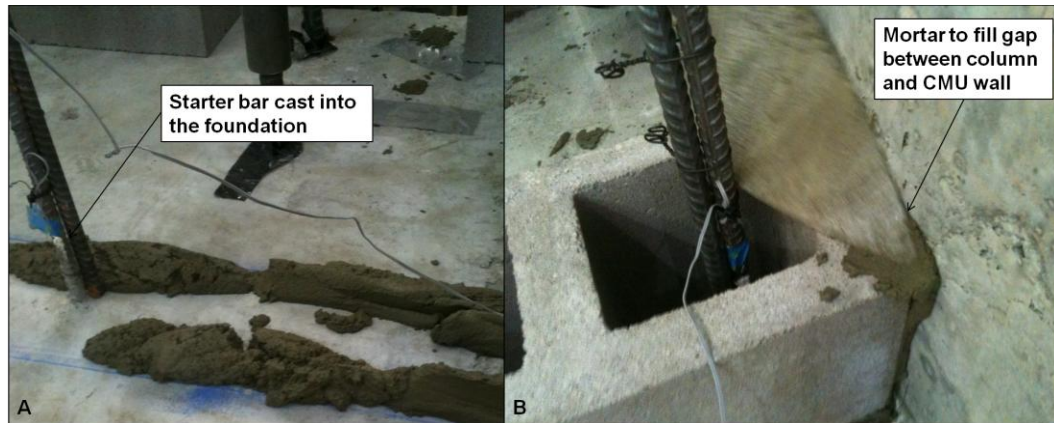


Figure 113: Placement of first row of masonry showing (a) the dowel bars and (b) the mortar at the wall-column interface

For each course, the masonry block was slid over the reinforcing bars and laid in place. Every third course, a single #3 reinforcing bar was placed in the center of the bed joint. The mortar was first placed on the webs before placing the reinforcement to ensure that the bar is fully encased in mortar (See Figure 114a). For Frame 1, the bottom of the block often had to be notched out to accommodate the horizontal dowel bar from the column and keep a consistent 0.5 inch (1.27 cm) bed joint thickness (See Figure 114b). Every four courses, construction was paused to fill the reinforced cells with concrete. The concrete was hand batched and watered down to achieve 8-10 inches (20.3-25.4 cm) of slump (See Figure 115). The concrete was placed in the reinforced cells and consolidated

with a rod (See Figure 116). The next vertical bar was then tied in place and construction of the wall resumed (See Figure 117).



Figure 114: Horizontal reinforcement (a) placed over grouted webs and (b) spliced with dowel bars from columns



Figure 115: Measuring slump for weak concrete used to fill reinforced cells



Figure 116: Reinforced cells filled with concrete (a) and consolidated with a rod (b)



Figure 117: Splicing vertical reinforcement

At the top courses of the wall with dowel connections, the webs of the masonry blocks were notched out to fit the block over the dowel bars which extended down from the RC beam (See Figure 118). For both frames, the face shells of the grouted cells in the last course of masonry were cut out in order to place the concrete in the cells. A dry pack was then used to fill in the top of the grouted cells where the face shells had been removed (See Figure 119).



Figure 118: Dowel reinforcement extending down from the RC beam

(space left blank intentionally)



Figure 119: At the top of the masonry wall, (a) face shell of the grouted cell was removed, (b) weak concrete was poured into the 3 courses below, and (c-d) the last course was dry packed

5.3 Test Set Up

5.3.1 Overview

Cyclic tests were conducted to determine the seismic performance of the frames and to gain insight into the behavior of entire buildings constructed with these types of infills. The test setup is shown in Figure 120.



Figure 120: Test set up

In order to simulate the gravity load from the four stories theoretically above the test frame, the columns were post-tensioned to the foundation using embedded anchors (See Figure 121). At the top of the column, a loading plate was welded to the longitudinal reinforcement which was purposely left exposed at the time of construction. A pin connection was machined out of steel and welded to the top of the loading plate and the bottom of the steel transfer beam. Hydraulic jacks were used to simultaneously load the post-tensioning bars on either side of the transfer beam. The load was selected such that the average gravity load, accounting for stretching of the post-tensioning bars would be equal to the load from four floors of office space above the column. The calculations for the column loads are presented in Appendix D. The beams were not post-tensioned with the load from the slab as the variation in load throughout the test would be over twice the initial loading.



Figure 121: Column loads applied through transfer beam

Placing all of the weight on the columns should have a minimal affect on the global behavior of the frame, as the large gap at the top of the infill walls means there is no initial compression on the masonry (See Figure 122). Thus, the beam acts only to transfer load to the column, and the loads on the columns account for the slab weight which is transferred through the beam.



Figure 122: Gap between the top of the infill wall and the RC frame

The lateral load was applied using a hydraulic actuator attached to a loading cage around the RC beam to permit a single actuator to both push and pull the specimen (Figures 123 and 124). The loading cage consisted of two stiffened plates attached to the RC stub beams with bolts and Simpson Strong-Tie cast-in-place loop anchors. These plates were tied to one another with four DYWIDAG bars and nuts.



Figure 123: Hydraulic used to apply lateral loads and stiffened plate on left side of loading cage



Figure 124: Stiffened plate on right side of loading cage

The cyclic tests were conducted using displacement control. The hydraulic was controlled manually with a MTS 407 controller. The voltage output from the LVDT and load cell on the hydraulic jack was monitored with the 407 controller. The output from the controller was fed into an SCXI1000 chassis and converted into force and displacement readings in LabView 2014. All of the other sensors from the structure were also wired to the SCXI1000 chassis and the data was recorded using LabView 2014. Figure 125 shows the set up for the 407 controller and the data acquisition system.

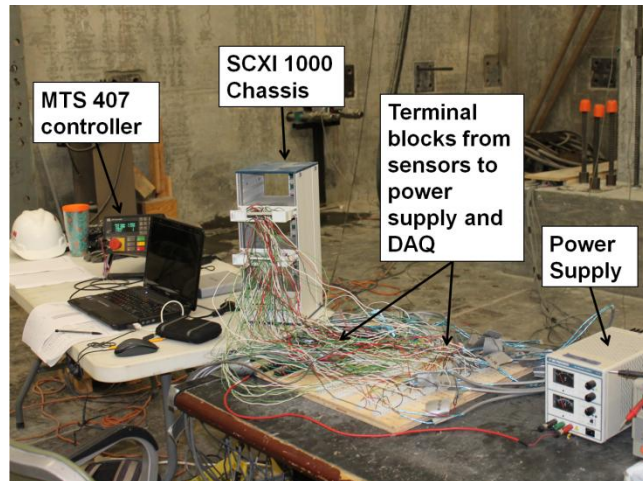


Figure 125: Set up for controller and data acquisition

5.3.2 Loading Protocol

The loading protocol was designed to adhere to the guidelines of FEMA 461, "Interim Testing Protocols for Determining the Seismic Performance Characteristics of Structural and Nonstructural Components." The guidelines for cyclic testing in FEMA 461 require that two cycles be performed at each amplitude, increasing the peak amplitude for each cycle by 40% until the desired damage state is reached, at a displacement of Δ_m . Prior to the first damage state, at least six cycles must be executed.

The amplitude may be further increased past Δ_m by increments of $0.3\Delta_m$ in order to examine further degradation of the structure. The total recommended number of cycles in a test is twenty. Figure 126 shows a plot from FEMA 461 of this proposed loading protocol.

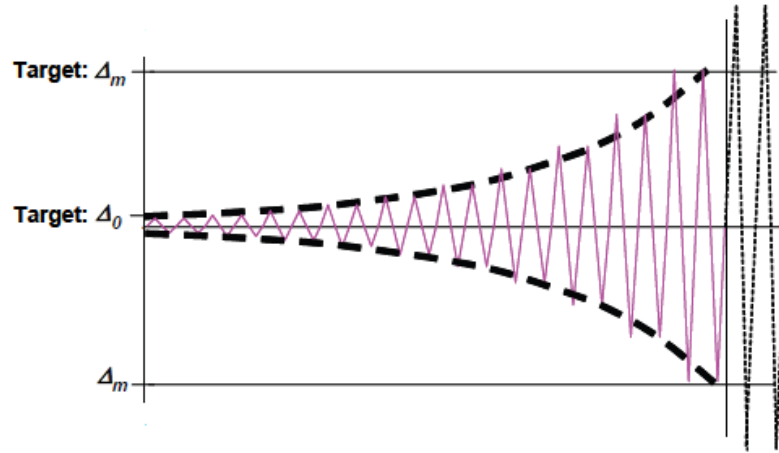


Figure 126: Deformation controlled loading history (FEMA 461)

In order to define damage states for the structures, preliminary finite element models were created of each frame. These were calibrated to the materials tests conducted prior to the experiment and utilized the proposed modeling methodology and material calibration outlined in Chapter 4. Because testing is required to adequately define the interface properties and the effectiveness of the dowel connections from the RC frame to the masonry infill, conservative assumptions were made. The aim of any assumption was to result in a model that may be stiffer or stronger than reality rather than more flexible and weaker as the assumption would ensure that the selected amplitudes for the initial cycles were small enough that at least six cycles would be completed prior to

the first damage state. Appendix D gives the parameters and material calibration for the initial finite element models.

The force displacement results of the two finite element models are shown in Figure 127. Since the structures were expected to be very stiff and it was anticipated that the interfaces between the masonry infill and the RC frame would fail at very low drift levels, the test would be excessively long if testing began prior to the finite element model's predictions for interface failure and continuously increased by 40%.

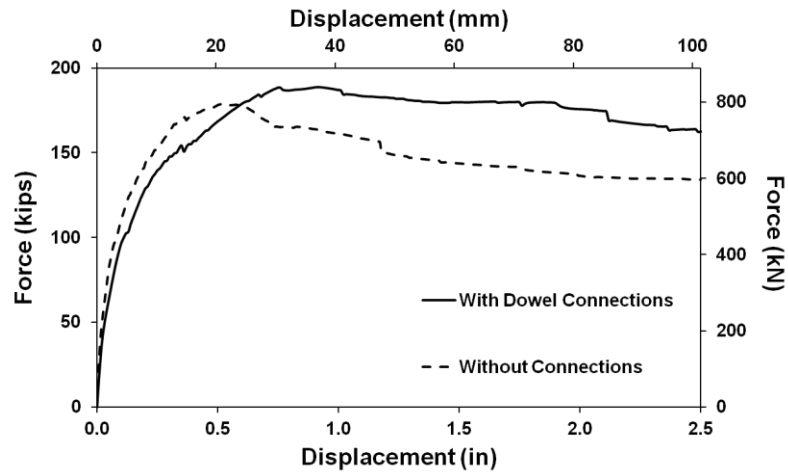


Figure 127: Force displacement results for finite element models with and without dowel connections

In order to capture the initial behavior of the masonry wall-RC frame interfaces, four cycles were conducted at very low amplitudes, two at 0.05 inches (1.3 mm) of displacement, and two at 0.15 inches (3.8 mm) of displacement. Then, testing followed the recommendations of FEMA 461 with displacements beginning at 0.3 inches (7.6 mm) and increasing by 40%. Based on the finite element models, this protocol meets the requirements for at least six cycles prior to the first damage state which was predicted to be crushing of the masonry for both test frames. The final damage state was determined

as the cycle in which the first degradation of strength is observed (Δ_m). After this cycle, the amplitudes were increased in increments of 0.5% drift up to 2% drift. The 2% drift level was selected to compare performance of the hybrid concrete-masonry wall to a traditional RC frame. The tests did not continue beyond this level of drift as the masonry in the top half story became unstable and was likely to fall. The loading protocol for the hybrid concrete-masonry frames is shown in Figure 128. Each ramp is named using a two-tiered numbering system. The first number corresponds to the set of cycles at the amplitude 1-8, where amplitude 1 is the first amplitude, 0.05 inches (1.3 mm), and amplitude 9 is the last amplitude, 2.4 inches (61.0 mm). The second number corresponds to the ramp number within the set at a particular amplitude, numbered 1-8. The loading rate was initially kept very small to permit pausing as soon as new cracks occurred (0.02 in/min, 0.4 mm/min) and increased up to 0.2 in/min (5.1 mm/min) for the 2.4 inch (61.0 mm) amplitude cycles. The amplitude of the negative cycles had to be increased during testing to account for stretching of the bars attached to the beam loading plates. Sample calculations for the adjusted cycle amplitudes are found in Appendix D.

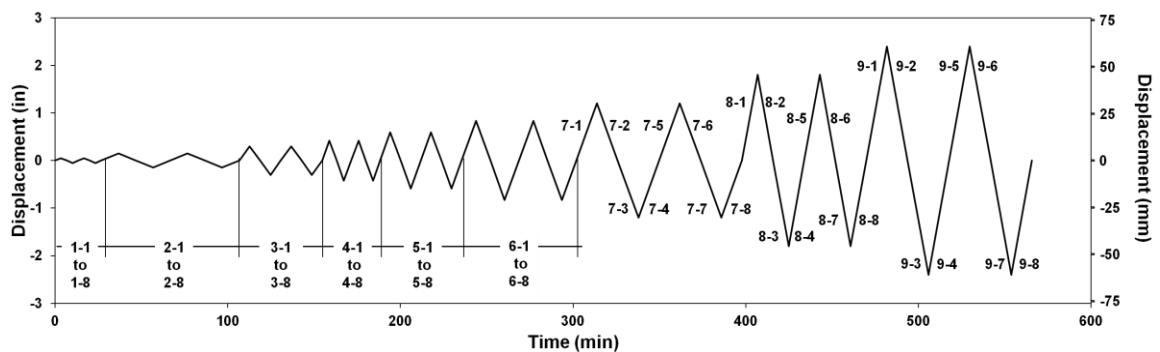


Figure 128: Loading protocol for testing of hybrid concrete-masonry frames

5.4 Instrumentation Plan

In order to gain further insight into the interaction between the RC frame and the reinforced masonry infill, the test specimens were heavily instrumented. The instruments can be divided into 3 groups: strain gages, displacement sensors and load cells.

5.4.1 Strain Gages

Determining the contribution of the reinforced infill wall to the behavior of the RC frame was the primary goal of the strain gages used for the test. First, electrical resistance strain gages were placed on the vertical reinforcement within the walls both at the base of the wall and at mid-height (See Figures 129 a and b). These were used to determine if the vertical bars in the masonry wall yielded before or after the column reinforcement and to observe the strain distribution within the wall. Next, electrical resistance strain gages were placed at the center of each horizontal bar to determine if they contribute to the lateral load resisting system (See Figure 129 c). For the frame with dowel connections to the columns, gages were placed on the dowel bars in each column at mid-height of the wall and at the ends of the horizontal bar which was placed in the same bed joint (See Figure 129 d). The aim of these gages is to determine if the dowel connections were transferring force to the horizontal reinforcement. The dowel action of these connections via bending cannot be measured with strain gages. In the columns, strain gages were placed on the longitudinal reinforcement near the base (See Figure 130). Data from these gages were used to determine when the reinforcement in the frame began to yield. The strain gage layout for the test specimen with dowel connections is shown in Figure 131.



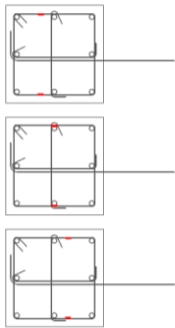
Figure 129: Strain gages in the masonry wall: (a) at base of vertical reinforcement, (b) at mid-height of vertical reinforcement, (c) at center of horizontal reinforcement, and (d) on dowel bars



Figure 130: Grinding vertical column reinforcement to apply strain gages

(space left blank intentionally)

Shear reinforcement strain gage arrangement



Strain gage arrangement for 1 row of dowels

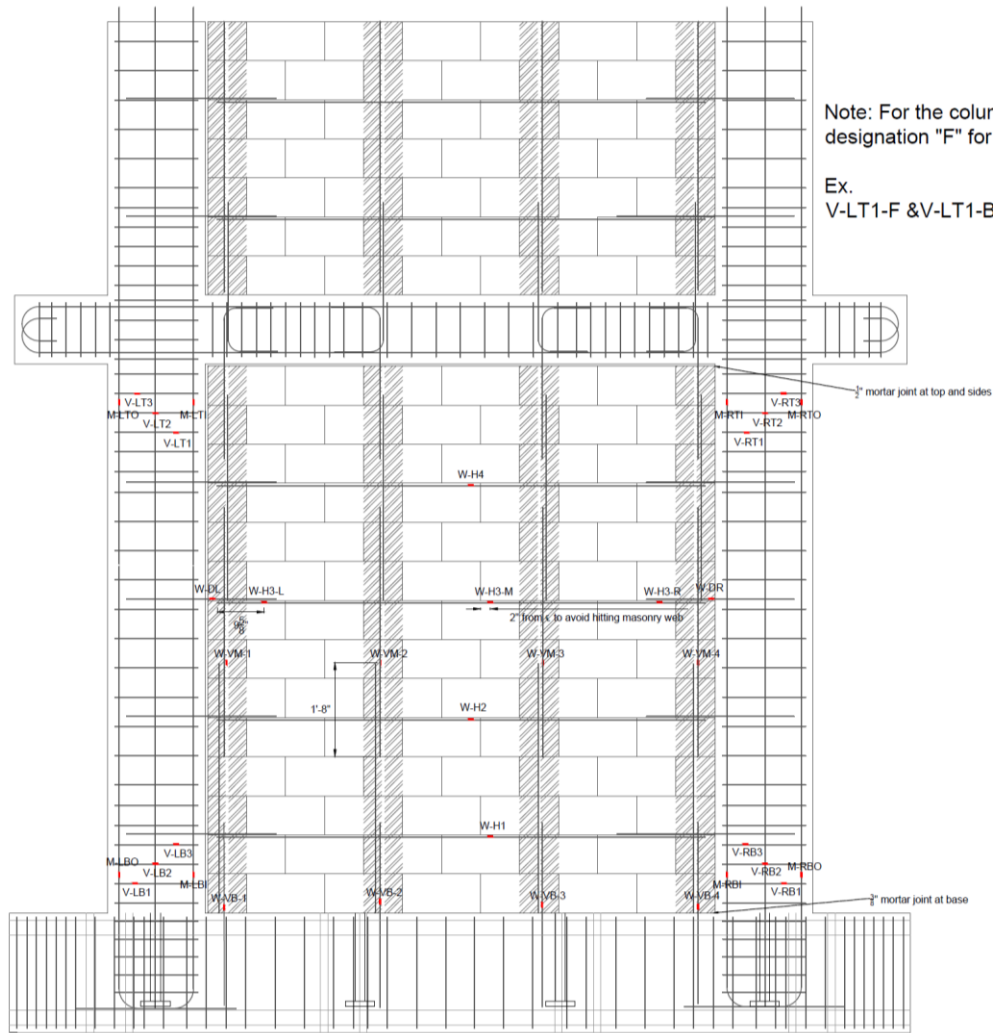
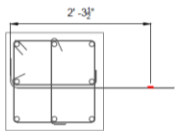


Figure 131: Strain gage layout

5.4.2 Displacement Sensors

The displacement sensors on the test specimens were a combination of string potentiometers and dial gages. On the columns, a set of six displacement sensors were placed in a 12 inch (30.5 cm) square and X configuration at the top and bottom of each column to measure the shear and flexural deformations in anticipated hinging zones (See Figure 132 a and b). At each of these locations, a string potentiometer was also used to measure the lateral displacement of the column at the top of each square (See Figure 133a). The slip at the base of the foundation was recorded with a dial gage and any slip was subtracted from the measurements for lateral displacement of the columns (See Figure 133b)

The shear and flexural deformations of the masonry wall were measured with string potentiometers placed in a square and X configuration 4 inches (10.2 cm) from the edge of the RC frame as shown in Figure 134. Around the perimeter of the wall, dial gages were used to detect slip between the masonry infill and the RC frame. The slip gages are also shown in Figure 134. A total of twenty-eight slip gages were used, with seven gages evenly spaced along each edge of the masonry wall. Figure 135 shows the instrumentation plan for the displacement sensors.

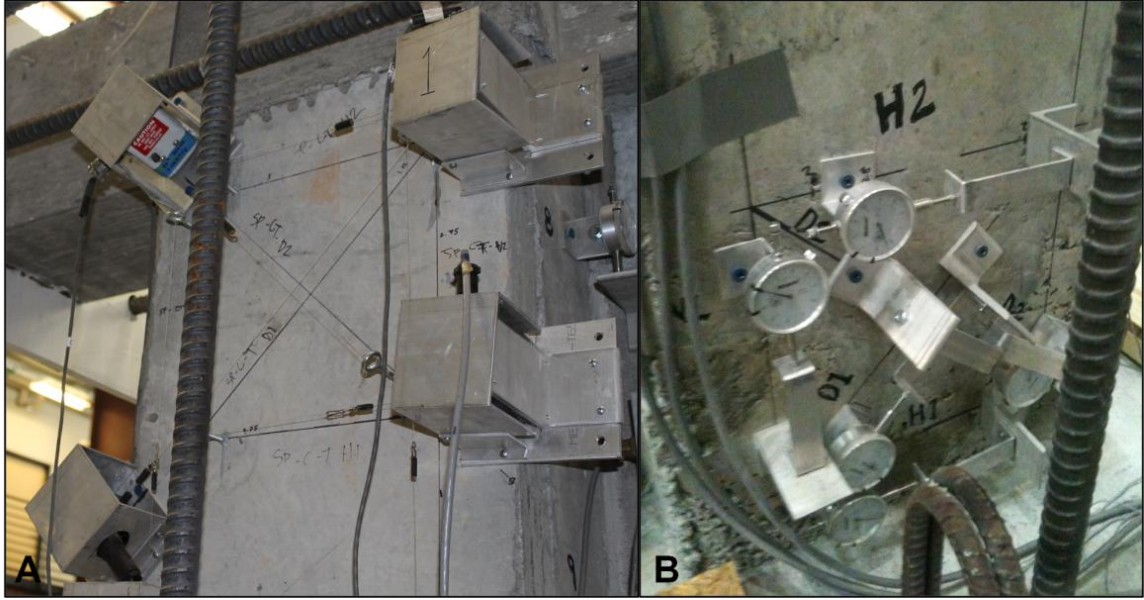


Figure 132: Column shear and flexural deformations measured by (a) string pots and (b) dial gages



Figure 133: Lateral displacement of the columns measured by (a) string potentiometers accounting for (b) slip at the foundation

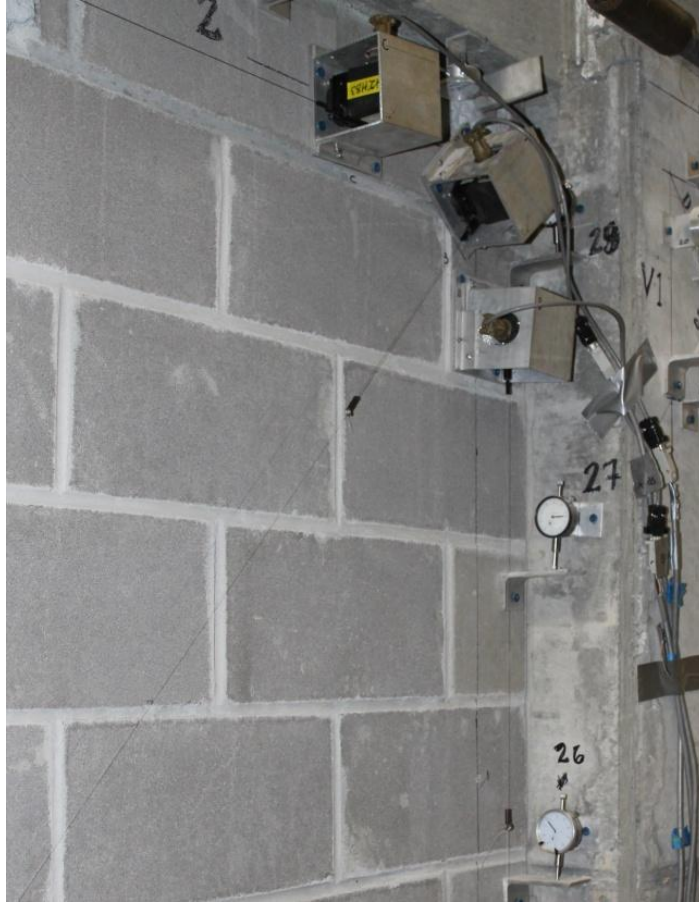


Figure 134: String potentiometers measuring shear and flexural deformation of the masonry infill and dial gages to measure slip

(space left blank intentionally)

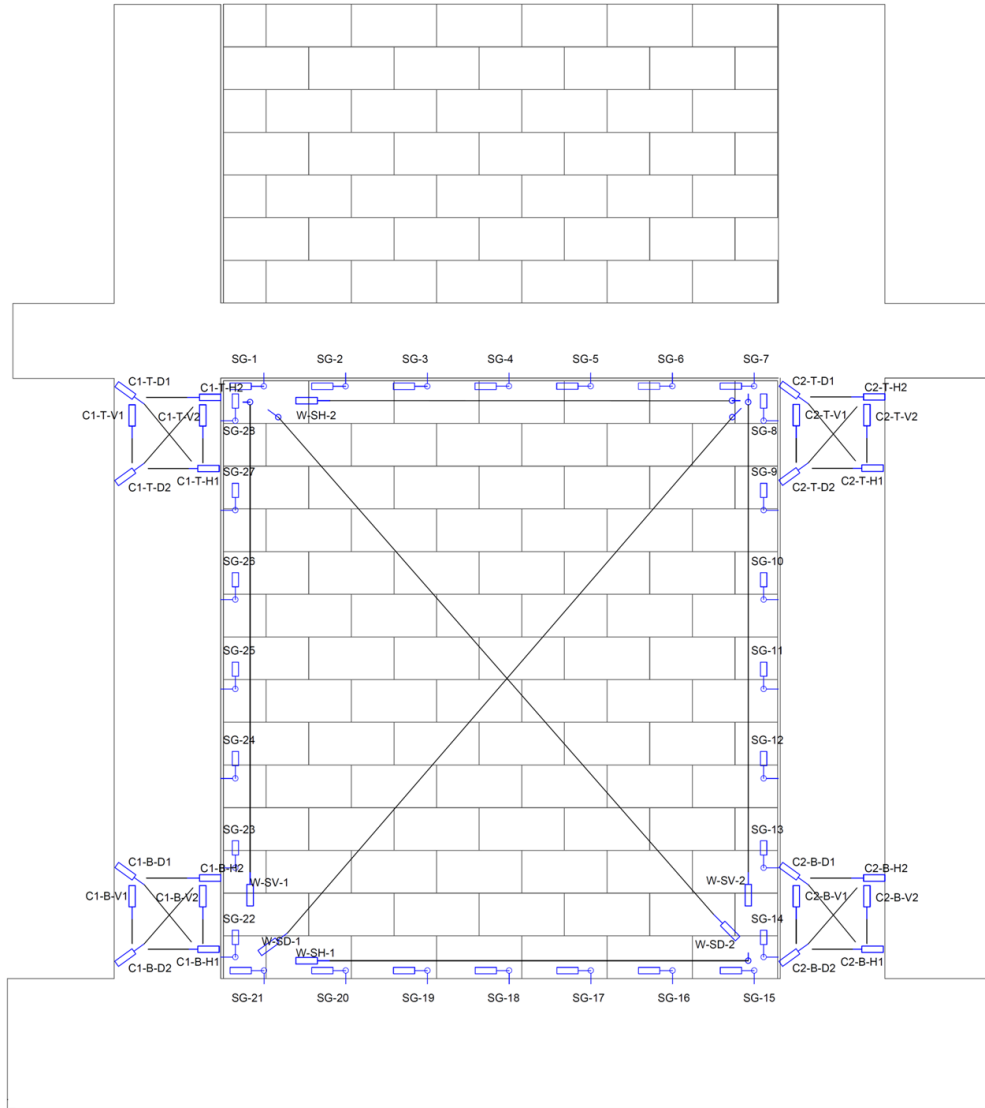


Figure 135: Displacement sensor layout

5.4.3 Load Cells

The simulated gravity loads on the columns were anticipated to change slightly throughout the test as the post-tensioning bars were stretched due to the displacement of the frame. In order to measure the initial load on the columns and the change in load during the tests, load cells were placed under the loading plates of the post-tensioning bars as shown in Figure 136.



Figure 136: Load cells to measure column load throughout the test

5.5 Chapter Summary

Best efforts were taken to replicate the construction practices observed in the Caribbean when building the two test specimens. The two specimens were full-scale models of frames of the exterior, bottom floor of a five-story office building, and they were identical except that one frame had cast-in-place dowel connections extending from the columns into the reinforced bed joints and dowel bars extending down from the beam into grouted cells. The material properties for the concrete in the RC frame, reinforcement, masonry units, mortar and weak concrete for the grouted cells were kept within typical ranges based on responses from engineers in the Caribbean. Detailed notes from site visits to the Caribbean regarding material properties and construction practices is presented in Appendix A. Comprehensive material data from all the various tests conducted is given in Appendix B.

The simulated building gravity loads were applied to the columns by externally post-tensioning the columns such that the average load throughout the tests would be

equal to the gravity load of four floors of office space. The calculations for the column loads are presented in Appendix D. The lateral loads were applied using a hydraulic jack and a system constructed of steel loading plates and DYWIDAG bars to permit one jack to pull and push the frames. The initial loading protocol was determined using finite models of the frames and FEMA 461.

The instrumentation consisted of electrical resistance strain gages, displacement sensors and load cells. Strain gages were placed on the reinforcement within the masonry infill wall, on the horizontal dowel reinforcement and at the base of the columns. String potentiometers and dial gages were used to measure shear and flexural deformations of the RC columns and the masonry infill walls. Dial gages were also used to measure the slip between the RC frame and the masonry infill. Load cells tracked the change in gravity load on the columns due to stretching of the post-tensioning bars as the structure displaces laterally. A load cell and an LVDT inside the hydraulic jack monitored the applied displacements and lateral loads.

CHAPTER 6

EXPERIMENTAL AND ANALYTICAL RESULTS

The experimental program consisted of two Caribbean-style hybrid concrete-masonry structures. Frame 1 had cast-in-place connections on all four boundaries of the partially grouted infill wall, but Frame 2 had cast-in-place connections at the base only. Both frames failed at similar loads and drift levels, exhibiting a compression strut mechanism and combined flexural and shear cracking in the columns of the bounding frame. The hybrid concrete-masonry frames had approximately twice the capacity of the bare frame and achieved peak strength at lower ductility levels. These results are very similar to observations from tests of unreinforced masonry infill structures found in the literature (Angel et al. 1994; Brokken and Bertero 1981; Mehrabi 1994; Stafford-Smith 1967). However, the cracking patterns of the columns in the hybrid concrete-masonry frames suggest that the typical strut mechanism observed in unreinforced masonry infill structures was altered due to the connections from the reinforced concrete frame to the grouted cores of the masonry infill. The dowel connections at the base of the masonry wall also significantly stiffened the courses of masonry though the height of the dowels and shifted the hinging of the columns up to the location at which the dowels were terminated.

The finite element models predicted the behavior of the hybrid concrete-masonry frames very well. Predictions for peak strength and were within 10% of the experiment strengths, and predictions for displacement at peak strength were within 21% of the experimental displacement. The predicted failure progression closely matched the experiments for both models, but damage generally occurred earlier in the finite element

models than in the experiments. Additionally, the hinging zone in the columns was predicted to be at the base of the columns by the model, but the columns in the experimental frames hinged just above the height of the dowel bars from the foundation.

Although the initial models provided very good predictions of the force-displacement behavior and generally captured the failure patterns of the frames, a revised model was created in order to better capture the effect of the dowel connections and fully calibrate the interface properties in the model. A better match to the cracking patterns in the masonry wall, the cracking order of the interfaces and the location of yielding in the reinforcement was achieved with the revised models.

6.1 Observations from Experiments and Analytical Models

The two experimental frames were subjected to the same loading conditions and are compared to one another to highlight the influence of dowel connections on the seismic performance of hybrid concrete-masonry structures. The results from the experiments are also compared to the behavior predicted by the initial finite element models, which were presented in Section 4.4.

First, the general behavior of the frames with regard to cracking patterns and force displacement behavior is presented. Second, the slip at the interfaces between the masonry infill and the RC frame is examined and the influence of the interface bond on the frame behavior is hypothesized based on cracking patterns observed in the experiments. Third, to determine if the masonry infill participates as a structural element, the shear deformation of the masonry panel and the yielding of the reinforcement within the wall are examined. Finally, the local behavior of the columns is presented, including curvature data, shear deformations, and the yielding of the reinforcement.

6.1.1 General Behavior

The general behavior of the frames was characterized by the observed cracking patterns, the displacements at which the damage occurred, and the force-displacement curves.

6.1.1.1 Damage Sequence

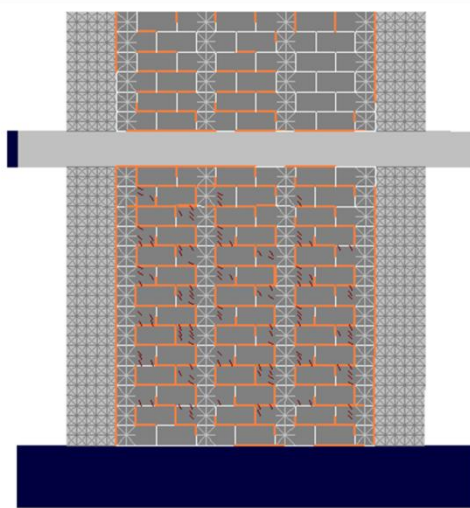
During the initial cycles at 0.05 inches (1.3 mm) amplitude (0.00417% drift), no observable damage occurred in either frame (See Figure 137 a and b). Damage initiated in the initial finite element models much sooner than was observed in the experiments (See Table 6). For both the models, the initial cracking began at the same displacement, with the interface along the left (tensile) column, and head joint cracking at the top left quadrant of the masonry wall. Then, the interfaces between the masonry wall and the top RC beam as well as between the masonry wall and right (compressive) column cracked. Simultaneously, diagonal cracking of the ungrouted cells and stair-stepped cracks through the mortar joints occurred throughout the wall. The timing of initial damage was slightly accelerated in the model of Frame 1, which had dowel connections on all edges of the masonry wall, compared to the model of Frame 2, which had connections only at the base. By 0.05 inches (1.3 mm) of displacement (0.00417% drift), both finite element models were virtually identical (See Figure 137 c and d). The top and side interfaces between the masonry infill and the RC frame cracked, and the interface between the wall and the foundation partially cracked. Some of the stair-stepped mortar joint cracks propagated through the grouted bed joints, and there were diagonal cracks in the ungrouted units.



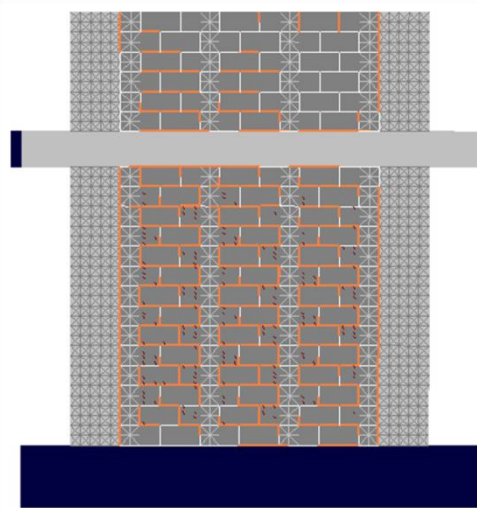
**(a) Experimental Frame 1
(Full connection)**



**(b) Experimental Frame 2
(Connections only at the base)**



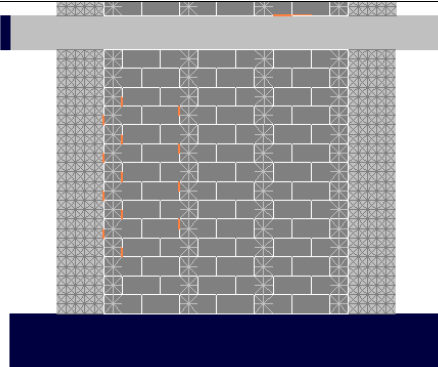
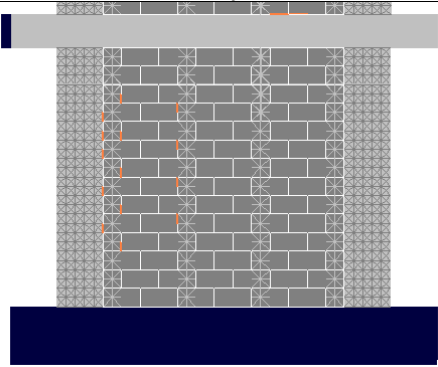
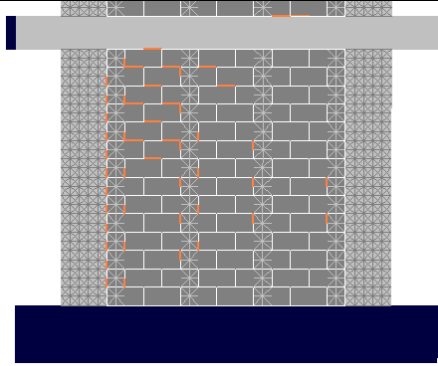
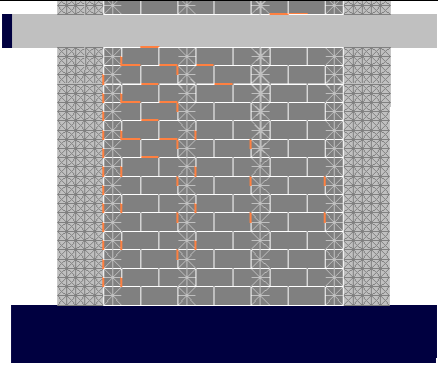
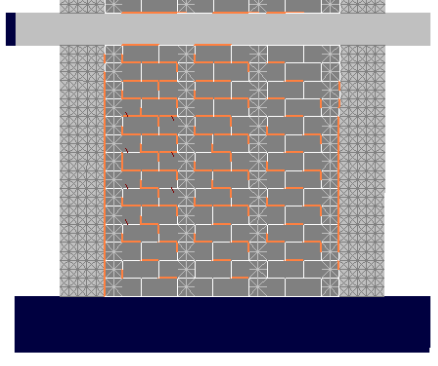
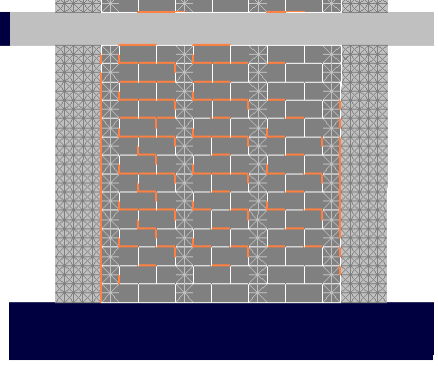
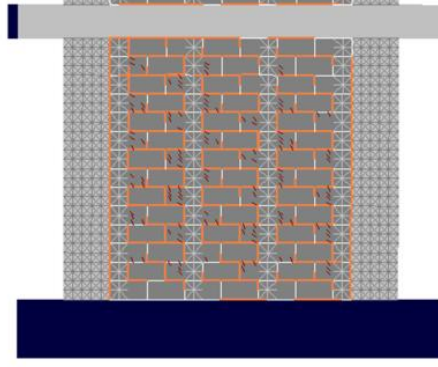
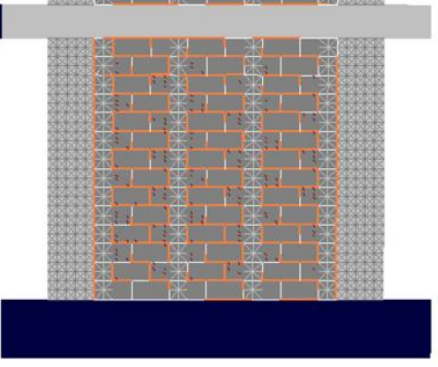
**(c) FE Model 1
(Full connection)**



**(d) FE Model 2
(Connection only at the base)**

Figure 137: Damage in the experimental frames and finite element models at 0.05 inches (1.3 mm) of lateral displacement (0.00417% drift). Damage is predicted in the finite element models at this displacement, but no damage was observed in either frame during the experiment.

Table 6: Initial cracking in the finite element models

FE Model 1 (Full connection)	FE Model 2 (Connection only at the base)
 <p data-bbox="342 653 777 695">0.007 in (0.2 mm), 0.00583% drift</p>	 <p data-bbox="891 653 1326 695">0.007 in (0.2 mm), 0.00583% drift</p>
 <p data-bbox="342 1058 777 1100">0.01 in (0.3 mm), 0.00833% drift</p>	 <p data-bbox="891 1058 1326 1100">0.01 in (0.3 mm), 0.00833% drift</p>
 <p data-bbox="342 1463 777 1505">0.02 in (0.5 mm), 0.0167% drift</p>	 <p data-bbox="891 1463 1326 1505">0.02 in (0.5 mm), 0.0167% drift</p>
 <p data-bbox="342 1869 777 1902">0.05 in (1.3 mm), 0.00417% drift</p>	 <p data-bbox="891 1869 1326 1902">0.05 in (1.3 mm), 0.00417% drift</p>

Just before the completion of the first cycle to 0.15 inches (3.8 mm) of displacement (0.125% drift), a small "pop" was heard in Frame 1. No visible damage was seen in the frame or the masonry wall (See Figure 138a). For Frame 2, the 0.15 inch (3.8 mm, 0.125% drift) cycles caused bed joint sliding cracks which were concentrated near the columns from courses two to twelve (See Figure 138b). The initial damage pattern of the finite element model of Frame 2 was consistent with the first observation of cracking in the experiment, but occurred between 0.007 inches (0.2 mm) and 0.02 inches (0.5 mm) of displacement (0.00583% and 0.0167% drift), rather than between 0.05 inches (1.3 mm) and 0.15 inches (3.8 mm) of displacement (0.0417% and 0.125% drift), as observed in the experiment (See Figure 138c). The cracking load in the Frame 2 model was 14.21 kips (63.21 kN), which was also much lower than the load recorded for experimental Frame 2, 30.8 kips (137.0 kN). The same cracking pattern and cracking load was observed in the model of Frame 1, which had connections on all edges of the infill (See Figure 138d). In both finite element models, cracks propagated through several grouted cells, and minor cracks formed at the base of the right (compressive) column and the top of the left (tensile) column by 0.15 inches (3.8 mm) of displacement (0.125% drift). The model of Frame 2 had slightly more cracking at the top of the left (tensile) column than the model of Frame 1.

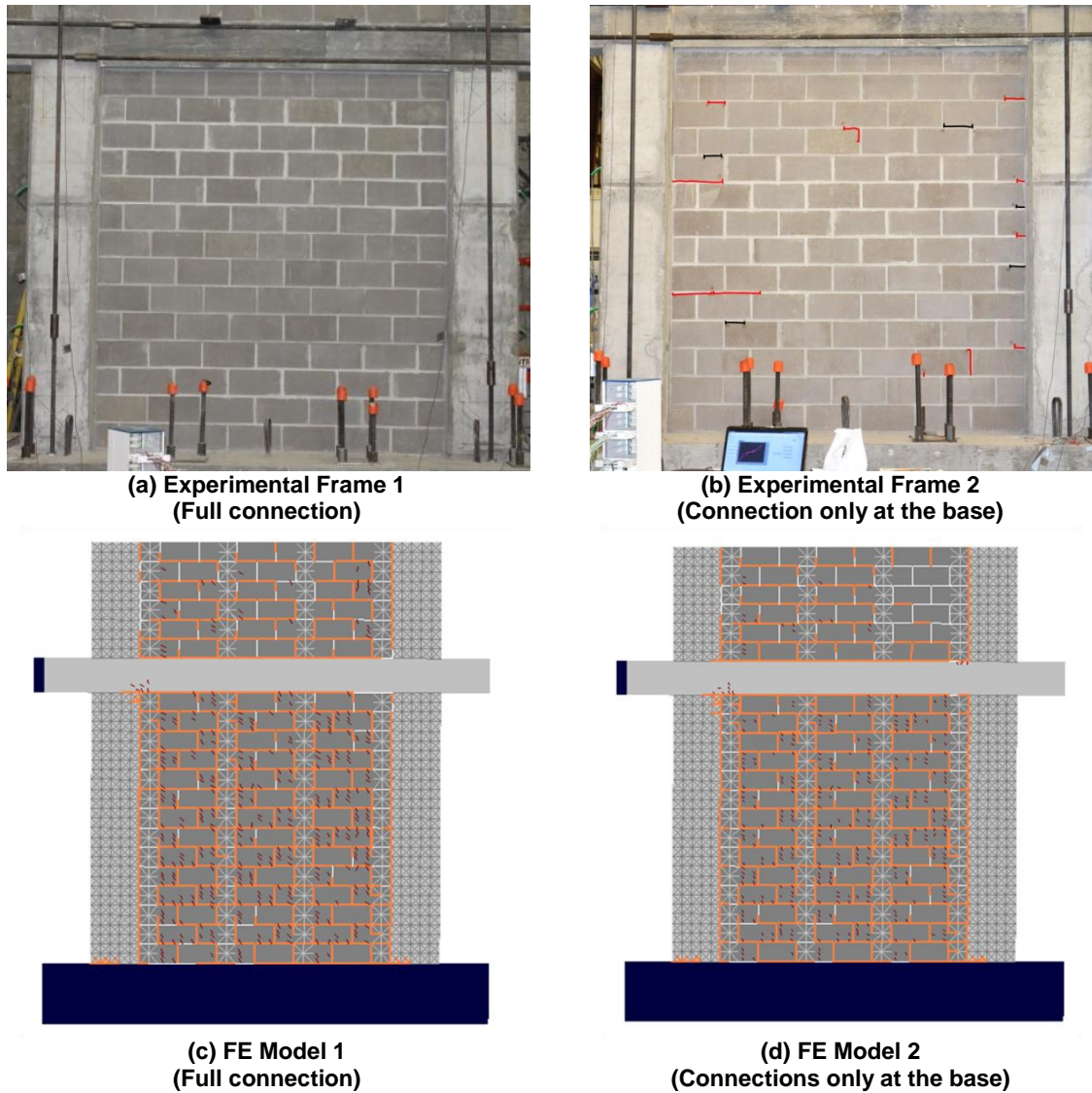


Figure 138: Cracking patterns in the experimental frames and finite element models at 0.15 inches (3.8 mm) lateral displacement (0.125% drift). The cracks observed in the experiments are traced in black for the positive cycles and red for the negative cycles

During the 0.3 inch (7.6 mm) displacement cycles (0.25% drift), a large diagonal crack opened from just above course two to course nine in Frame 1, which had dowel connections on all edges of the infill (See Figure 139a). The crack was stair stepped at the edges and cracked straight through the masonry between courses five to eight. Four smaller diagonal cracks also opened throughout the wall between courses three and thirteen, which primarily followed the mortar joints. Very little damage occurred in the

reverse cycles at this level of displacement. The dowel bars from the foundation to the masonry wall terminate at the top of course two, and the dowel bars from the beam terminate in course thirteen. These bars helped hold the top and bottom of the masonry wall in place and very few cracks propagated into this region for the remainder of the test. A hairline crack was also observed at the very base of the outside of each column.

Frame 2, which had dowel connections only at the base of the infill, also had several large diagonal cracks open from just above course two to course nine during the 0.3 inch (7.6 mm) displacement cycles (0.25% drift) (See Figure 139b). All the cracks were mainly through the mortar joints, but in three locations the cracks propagated through the masonry units. More damage was observed in the columns of this frame than the frame with connections around the entire perimeter of the masonry wall. Several flexural cracks opened in the outside of the columns from the top of course two, where the dowels terminate, to the top of course six. Hairline cracking was also observed at the very base of the columns near the foundation.

In the finite element models for both Frame 1 and Frame 2, the cracking in the tensile column propagated from the base of the column up to the height of the fifth course of masonry at 0.3 inches (7.6 mm) of displacement (0.25% drift) (See Figure 139 c and d). This is consistent with what was observed for experimental Frame 2. Since both models predicted flexural cracking at virtually the same displacement, the influence of the dowel connections on the cracking in the RC frame seems to be underestimated by the initial model. Shear and flexural cracking at the top of the left (tensile) column and bottom of the right (compressive) column was present in both models by 0.3 inches (7.6 mm) of displacement (0.25% drift). By this displacement, the shear transfer at the base of

the masonry wall was very minimal in the finite element models as the entire foundation-wall interface had cracked. This may explain why shear cracking at the base of the right (compressive) column was observed so early in the models compared to the experiments. A slight distinction can be made between the two models as the shear crack at the top of the left (tensile) column was larger in the model of Frame 2 than in the model of Frame 1. Both finite element models had slight crushing throughout the masonry wall which initiated at 0.25 inches (6.4 mm) of displacement (0.208% drift).

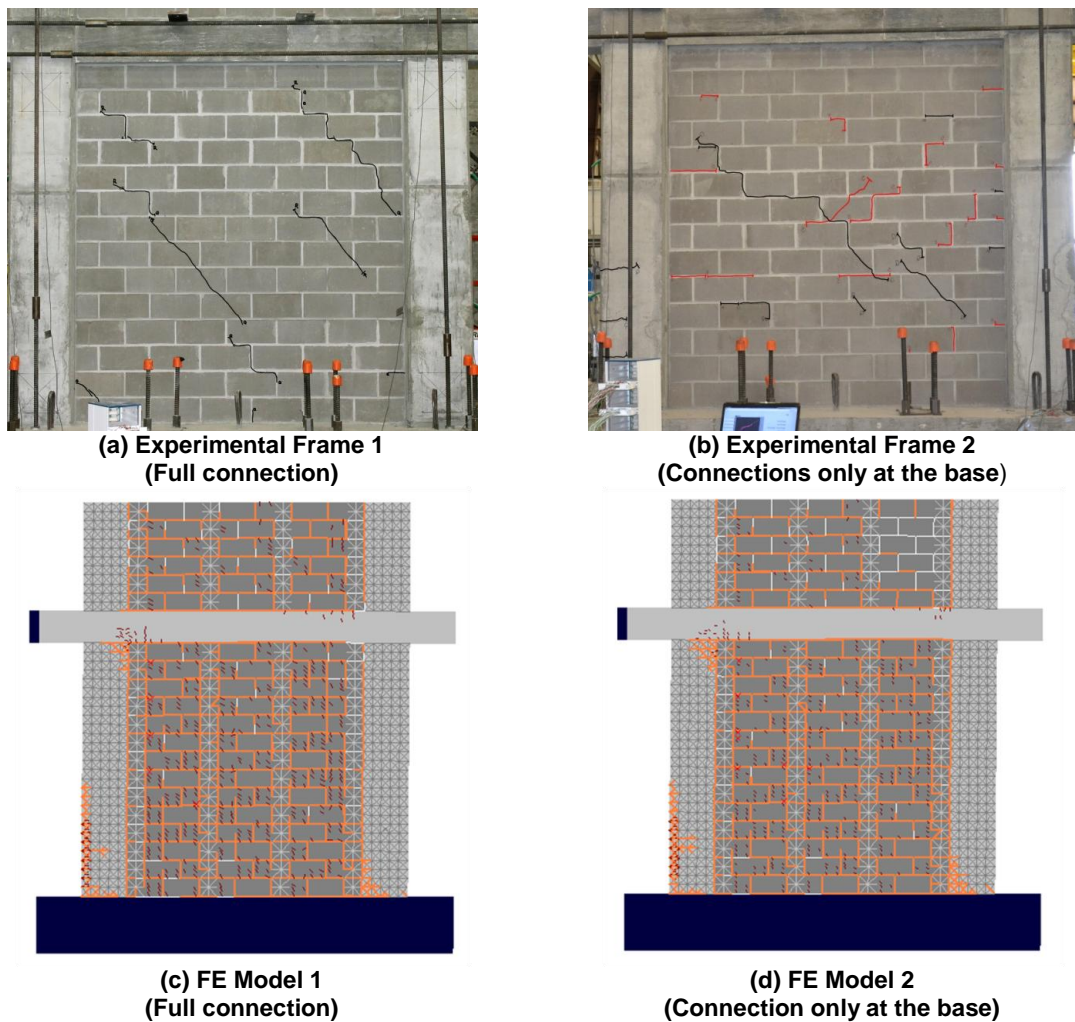


Figure 139: Damage in the experimental frames and finite element models at 0.3 inches (7.6 mm) of lateral displacement (0.25% drift). The cracks observed in the experiments are traced in black for the positive cycles and red for the negative cycles.

During the test of Frame 1, which had dowel connections around the entire perimeter of the infill, cracking of the columns did not initiate until the 0.42 inch (10.7 mm) amplitude cycles (0.35% drift) (See Figure 140a). Two large flexural cracks opened in the base of the columns, one at the top of course two and one just above course four. Additional diagonal cracks also formed throughout the masonry wall. These cracks were primarily diagonal, but a sliding type mechanism was observed at the top of course eight. Corner crushing at the top left of the masonry wall was also observed. In experimental Frame 2, which had dowel connections only at the base, additional diagonal cracks also formed in the masonry at 0.42 inches (10.7mm) of displacement (0.35% drift) (See Figure 140b). These cracks were primarily diagonal and closely followed the stair-stepped cracks from the 0.3 inch (7.6 mm, 0.35% drift) cycles. The flexural cracks which had formed in the columns during the 0.3 inch (7.6 mm, 0.35% drift) cycles also expanded, and a few new cracks formed spanning between the top of the second course of masonry to the top of the fifth course.

In both finite element models, the flexural and shear cracks of the columns which initiated earlier in the simulation expanded (See Figure 140 c and d). More crushing occurred throughout the walls, and a few more cracks opened through the grouted cells. At this stage of the simulation, both models looked nearly the same.

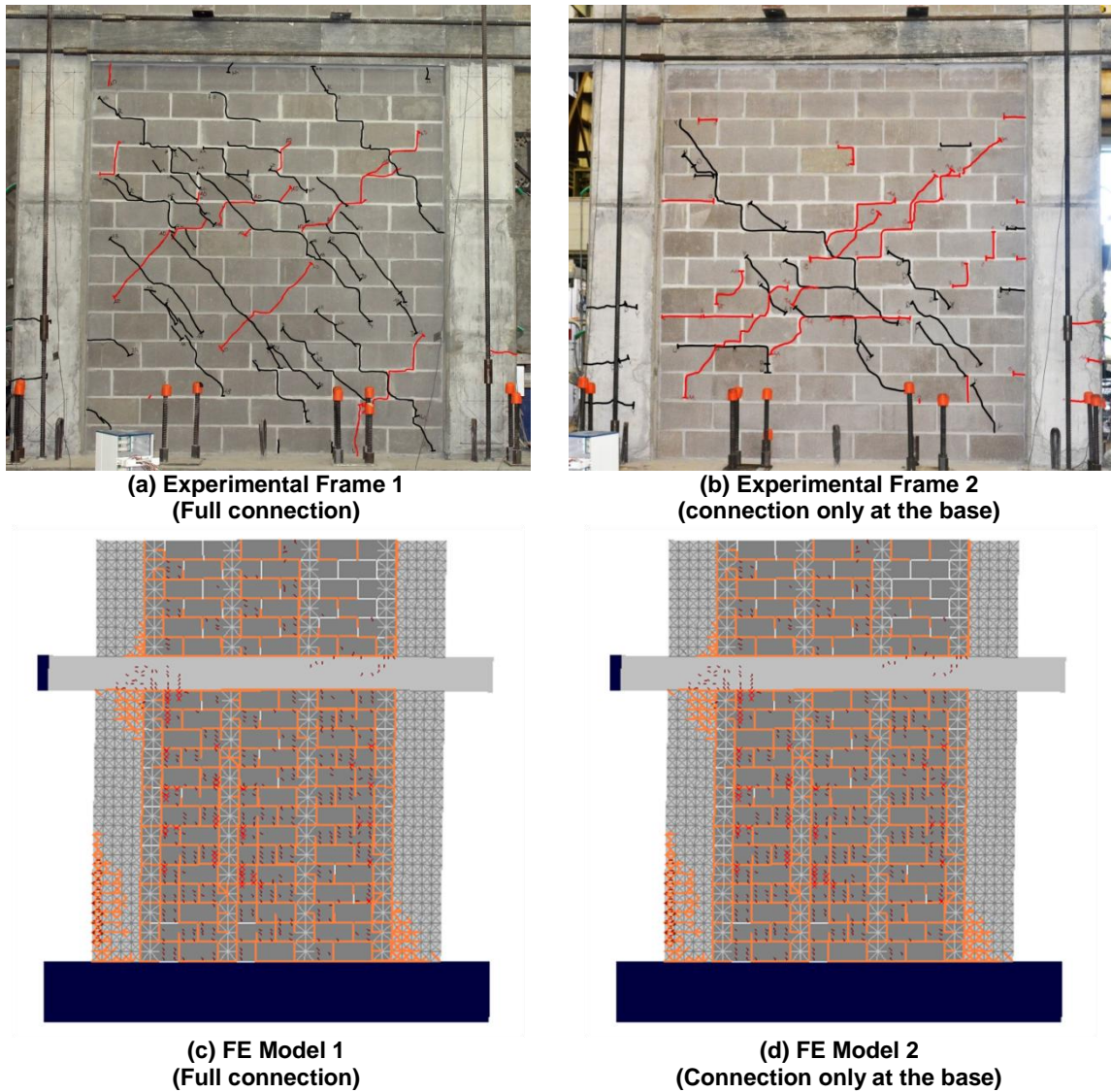


Figure 140: Damage in the experiments and finite element models at 0.42 inches (10.7 mm) of lateral displacement (0.35% drift). The cracks observed in the experiments are traced in black for the positive cycles and red for the negative cycles.

During 0.58 inch (14.7 mm, 0.483% drift) test cycles, many distributed diagonal cracks formed in the masonry wall (within courses 3-12) in Frame 1 (See Figure 143a). Small vertical cracks also opened at the top of the grouted cells in the middle of the unit where the dowel reinforcement was located (See Figure 141). Corner crushing also became more pronounced and slight crushing and spalling off of the masonry face shells was observed throughout the wall. Additional flexural cracks opened on the outside of the

columns from the height of the second course of masonry to the top of course eight. Small flexural cracks opened at the inside of the base of the columns within the height of the second course of masonry. Two cracks also opened at the top of the left and right columns within the top two courses of masonry, and one crack propagated across the bottom of the right beam-column joint. These cracks had a shallow angle to them suggesting they were due to combined flexure and shear forces.

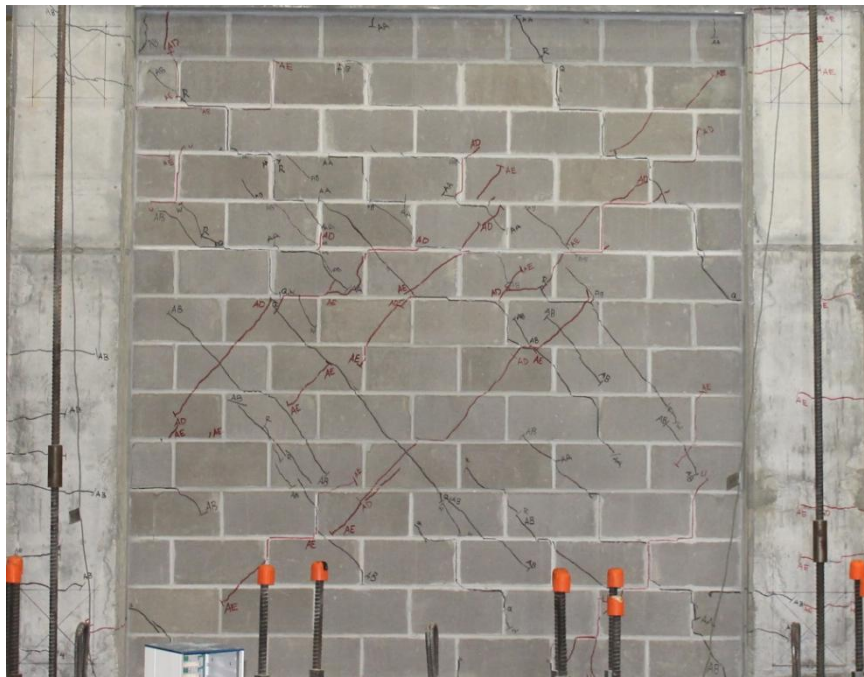


Figure 141: Close up of masonry wall in Frame 1 (full connection) at 0.58 inches (14.7 mm) of lateral displacement (0.483% drift). The cracks in the experiments are traced in black for the positive cycles and red for the negative cycles.

By 0.58 inches (14.7 mm) of displacement (0.483% drift), many small distributed diagonal cracks also formed within courses three to twelve in Frame 2 (See Figure 143b). A large vertical crack along the right of the second grouted core opened from the top of the masonry wall down three courses as shown in Figure 142. Slight spalling of the

masonry face shells was seen in a few locations in the center of the wall, but not as much crushing as was observed in Frame 1. Additional flexural cracks opened at the outside of each column, which were evenly distributed from two courses up to mid-height of the column. Additional flexural cracks were also observed on the inside of the columns at the base. At the tops of both columns, shear cracks opened following the shear cracks along the diagonal struts in the masonry (See Figure 143 a and b). The cracking patterns observed for Frame 2 at 0.58 inches (14.7 mm) of displacement (0.483% drift) were nearly identical to those in Frame 1, except that the cracks in the tops of the columns initiated slightly lower and had a much steeper slope, indicating they were more dominated by shear forces than the cracks in the columns of Frame 1.



Figure 142: Close up of the masonry wall in Frame 2 (connection only at the base) at 0.58 inches (14.7 mm) of lateral displacement (0.483% drift). The cracks in the experiments are traced in black for the positive cycles and red for the negative cycles.

The damage was nearly the same for both finite element models at 0.58 inches (14.7 mm) of displacement (0.483% drift) (See Figure 143 c and d). The shear cracking in the columns expanded, and crushing of the ungrouted units distributed throughout the height of the wall. Diagonal shear cracking through the grouted cores next to the crushed cells was also observed.

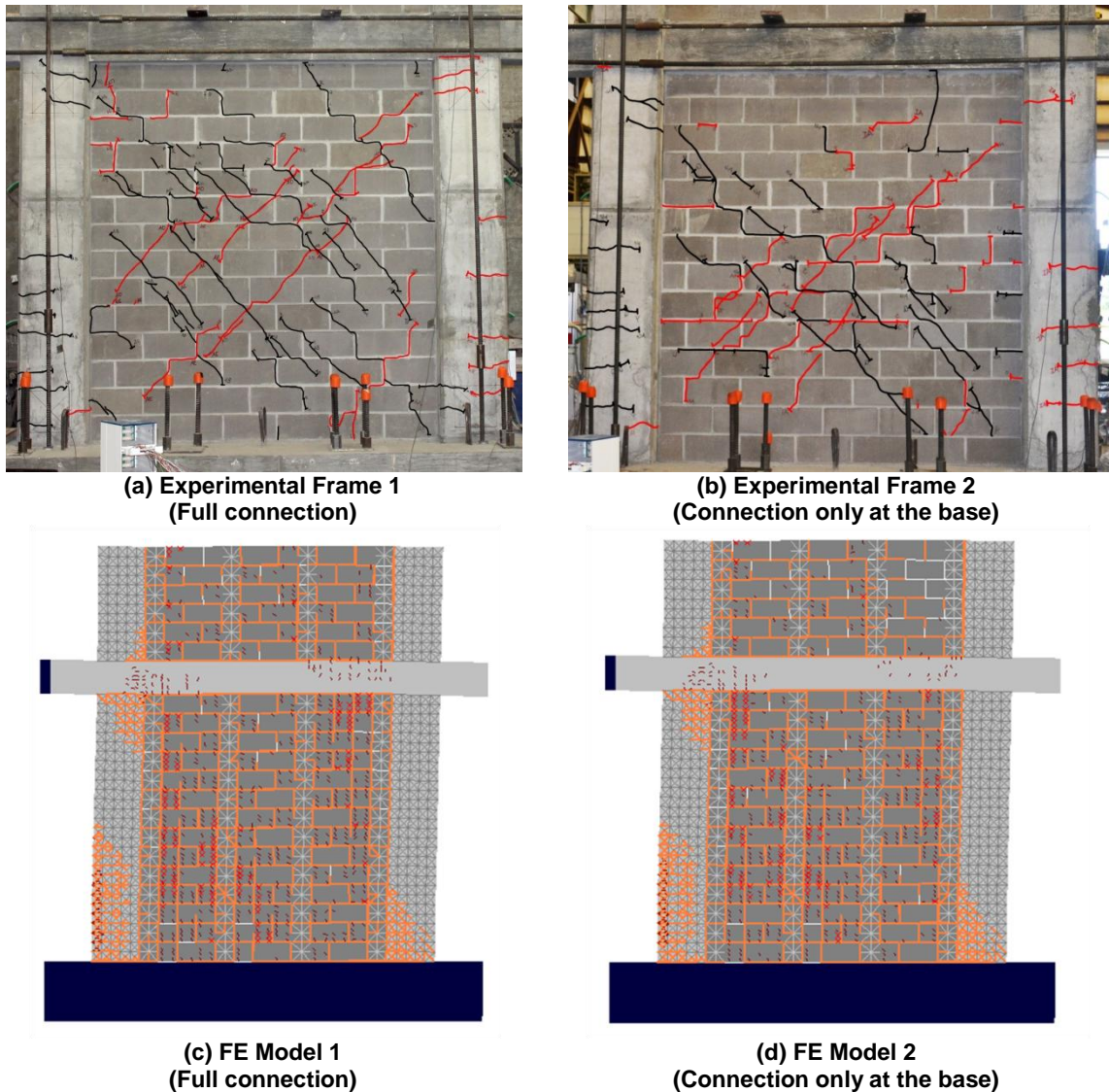


Figure 143: Damage in the experimental frames and finite element models at 0.58 inches (14.7 mm) of lateral displacement (0.483% drift). The cracks observed in the experiments are traced in black for the positive cycles and red for the negative cycles.

During the 0.82 inch (20.8 mm) amplitude cycles of the experiments (0.683% drift), two additional shear cracks opened at the top of the left column and one additional shear crack opened at the top of the left column in Frame 1, which had dowel connections on all edges of the infill (See Figure 146a). Small cracks were also observed at the base of the beam near each beam-column joint. The crack at the right end of the beam extended into the beam-column joint. Flexural cracks at the base of the column continued to extend and two more opened moving down towards the foundation. A large bend in the column of approximately 34° was observed with the rotation beginning at the top of the second course of masonry (See Figure 144). Additional crushing was also observed at the center of the masonry wall. Because no additional strength was gained after this cycle, the hinging observed just above the second course of masonry was most likely the cause of failure of the frame.

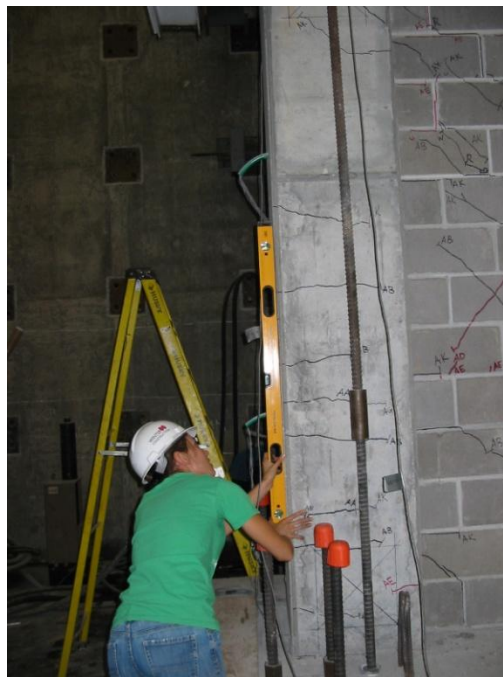


Figure 144: Observing bend formed in the tension column beginning above the second course of masonry at 0.82 inches (20.8 mm) of lateral displacement (0.683% drift).

In Frame 2, which had connections only at the base of the masonry infill wall, the cracking in the frame was fairly similar to Frame 1. More shear cracks opened and the initial shear cracks expanded at the top of both columns during the 0.82 inch (20.8 mm) amplitude cycles (0.683% drift) (See Figure 146b). Joint cracking was also observed and several large cracks propagated through the height of the beam, beginning at the base of the beam near the top corners of the masonry wall. A few flexural cracks also opened near the base of both columns. The initial diagonal strut crack opened to a width of 0.04 inches (1.0 mm) and slight crushing was observed near the diagonal cracks and at the top corners of the masonry wall (See Figure 145). The main difference between the two frames was that during these cycles the interface cracks at the sides and top of the masonry wall in Frame 2 had a visible gap at 0.82 inches (20.8 mm) of displacement (0.683% drift), but no gap had opened in Frame 1.



Figure 145: Close up of crushing of the masonry face shells near the diagonal cracks at 0.82 inches (20.8 mm) of lateral displacement (0.683% drift).

At 0.82 inches (20.8 mm) of displacement (0.683% drift), the damage to the columns in the finite element models looked fairly similar to the damage at 0.58 inches (14.7 mm) of displacement (0.483% drift) (See Figure 146 c and d). More crushing of the ungrouted units and shear cracking of the grouted units was present in both finite element models. The model of Frame 2 had a gap between the right (compressive) column and the masonry infill wall (See Figure 146d). No gap was predicted in the Frame 1 model (See Figure 146c). This behavior is consistent with experimental observations.

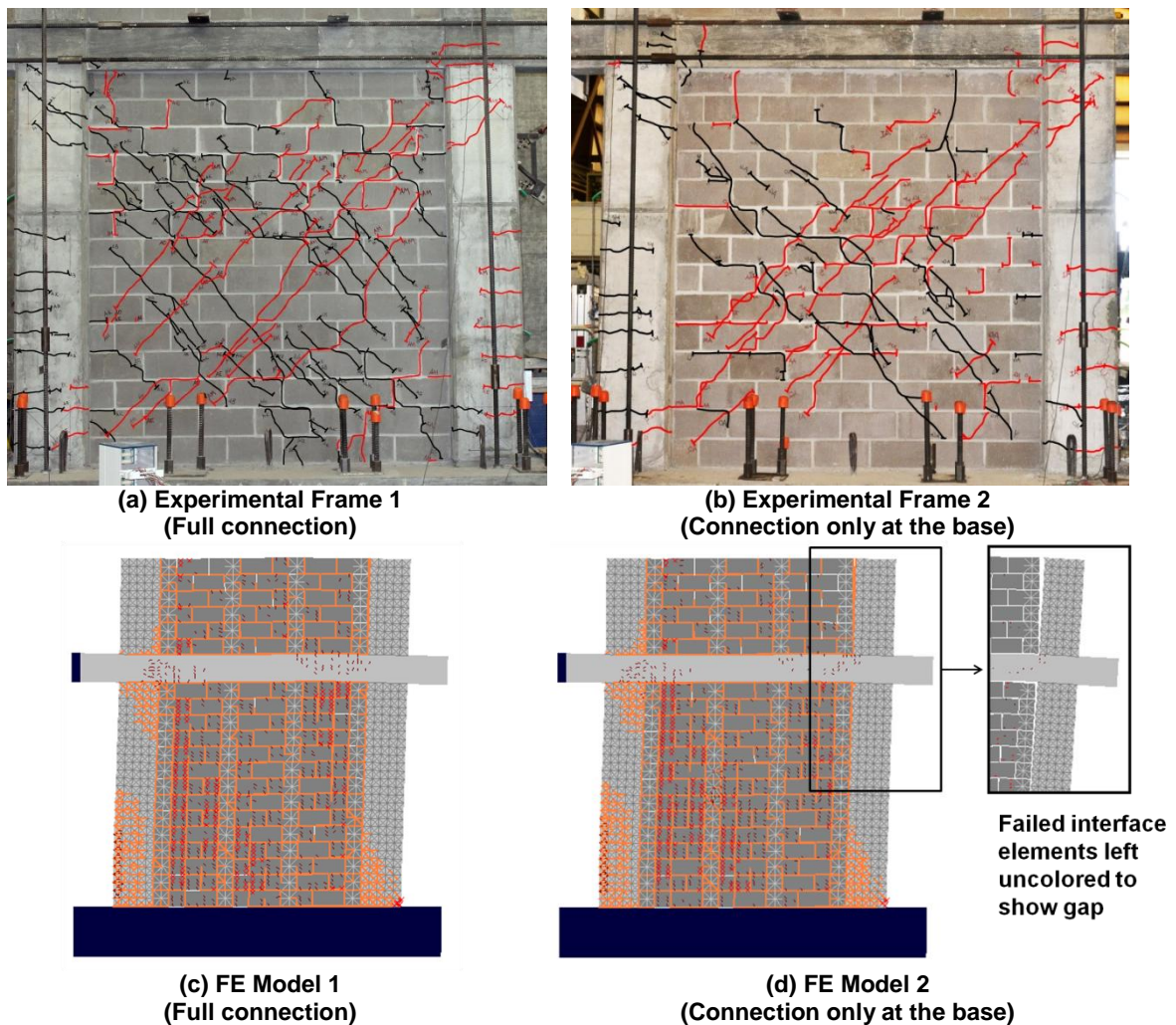


Figure 146: Damage in the experimental frames and the finite element models at 0.82 inches (20.8 mm) of displacement (0.683% drift). The cracks observed in the experiments are traced in black for the positive cycles and red for the negative cycles.

During the experimental cycles with an amplitude of 1.2 inches (30.5 mm, 1.0% drift), more crushing of the masonry was observed and the masonry at the top corners began to fall out of plane in Frame 1 (See Figure 147a). Additional cracks propagated up from the bottom of the beam at both ends near the joints. An additional shear crack formed in the top of the right column and the initial shear crack at the top of the left column opened to a width of 0.02 inches (0.5 mm). The flexural cracks along the outside face of the columns expanded, and a few new cracks formed on the inside face of the columns near the base.

The same general failure mechanisms were observed during the 1.2 inch (30.5 mm) amplitude cycles (1.0% drift) for Frame 2 as were observed for Frame 1 (See Figure 147b). The main differences between the behavior of the two frames at this stage was that Frame 2 had more cracking in the beam-column joints, along the inside faces of the columns near the foundation, and along the top of the beam, than Frame 1.

Again, the finite element models predicted more severe damage at 1.2 inches (30.5 mm) of displacement (1.0% drift) than was observed in the experiments (See Figure 147 c and d). The damage to the frame remains fairly constant for further displacement in the simulations. Crushing of the ungrouted masonry units increased in both models, but there was slightly more crushing at the top of the masonry wall in the Frame 2 model than the Frame 1 model.

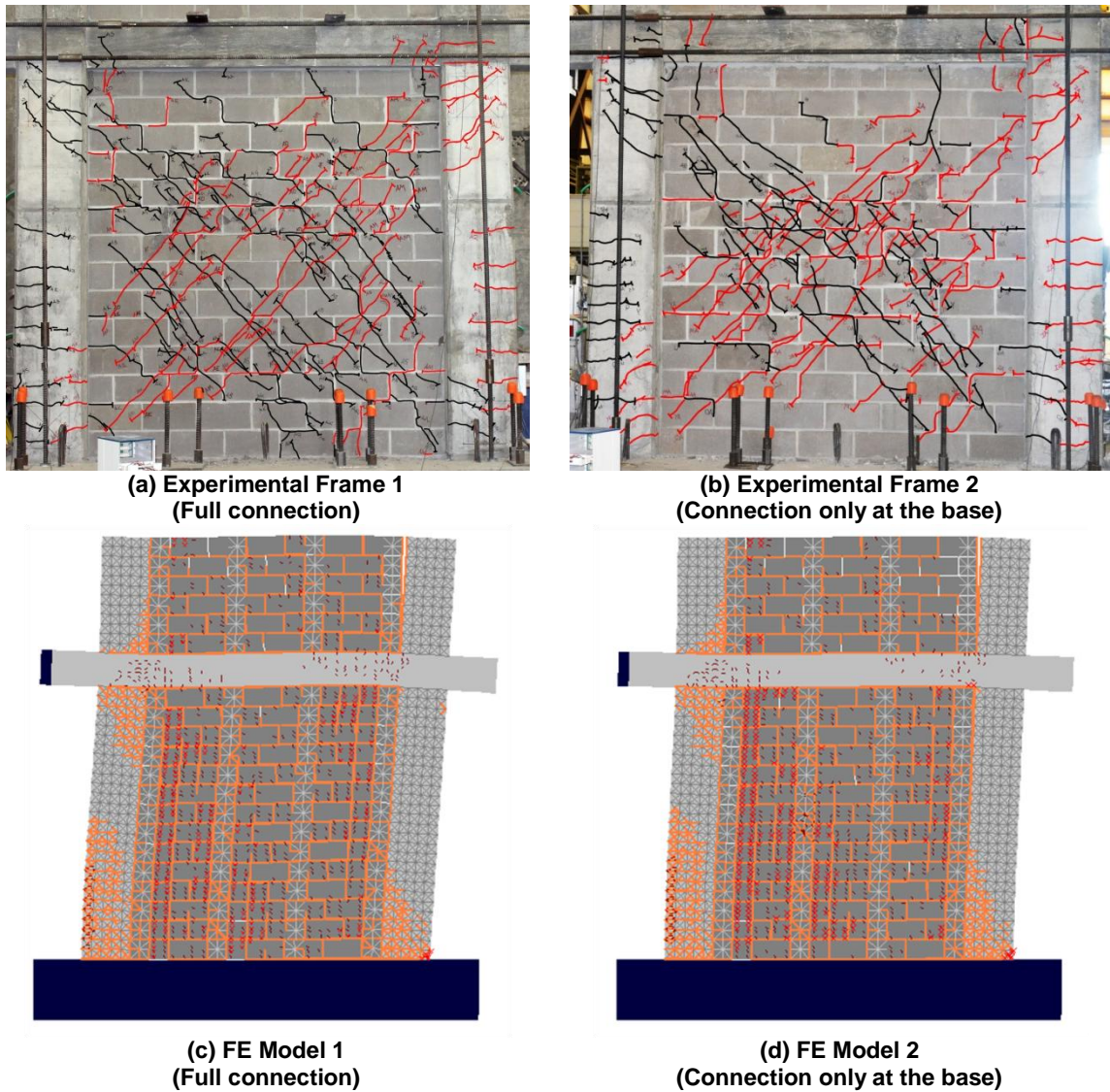


Figure 147: Damage in the experimental frames and the finite element models at 1.2 inches (30.5 mm) of lateral displacement (1.0% drift). The cracks observed in the experiments are traced in black for the positive cycles and red for the negative cycles.

By 1.8 inches (45.7 mm) of displacement (1.5% drift), the ungrouted units at the center of the masonry wall in experimental Frame 1 had crushed and large portions of the face shells began to fall out of plane (See Figure 152a). The grouted cores remained intact, but some of the diagonal cracks had extended through the grouted cores at the center of the wall as shown in Figure 148b. The dowel connections to the RC frame appeared to hold together the entirety of the top and bottom two courses of masonry.

Additional flexural cracks opened in the columns and more cracks were observed through the beam-column joints and the RC beam.



Figure 148: Large portion of masonry face shell (a) fell out of plane and revealed (b) grouted cores with shear cracks in Frame 1 at 1.8 inches (45.7 mm) of lateral displacement (1.5% drift).

During the 1.8 inch (45.7 mm) amplitude cycles (1.5% drift), there was a clear distinction in the behavior of the two frames. Frame 2 had much more damage to the masonry infill than Frame 1 (See Figure 152b). The ungrouted masonry fell out of plane in the center of the wall and across the diagonals where the compression strut had formed (See Figure 149a). This region extended from the top of course two all the way to the top of the infill wall. It exposed the grouted cores which in many places had de-bonded from the vertical reinforcement as shown in Figure 149b. The entire top section of the wall, between the regions where the masonry had already fallen out, was bent out of plane and in danger of collapsing. For safety reasons, no additional cracks were marked on the

masonry beyond these cycles (See Figure 150). Unlike Frame 1, new shear cracks opened in the columns of Frame 2, spreading down towards the mid-height of each column (See Figure 151). New cracks also opened in the beam, leaving all but the middle third cracked.

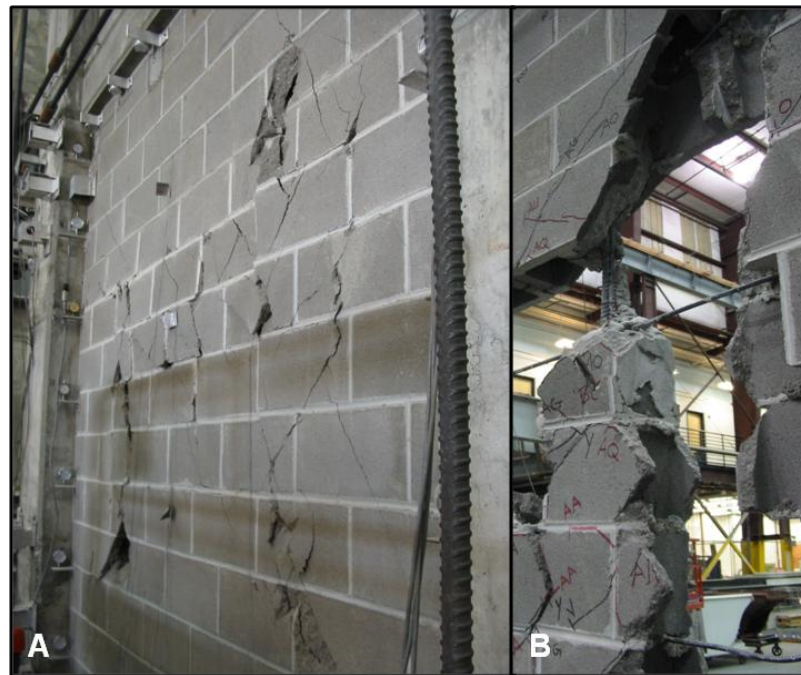


Figure 149: Large portion of masonry face shell (a) fell out of plane and revealed (b) grouted cores which had debonded from the vertical reinforcement in Frame 2 at 1.8 inches (45.7 mm) of lateral displacement (1.5% drift).



Figure 150: Top section of masonry wall of Frame 2 (connection only at the base) was in danger of out-of-plane collapse by 1.8 inches (45.7 mm) of lateral displacement (1.5% drift).

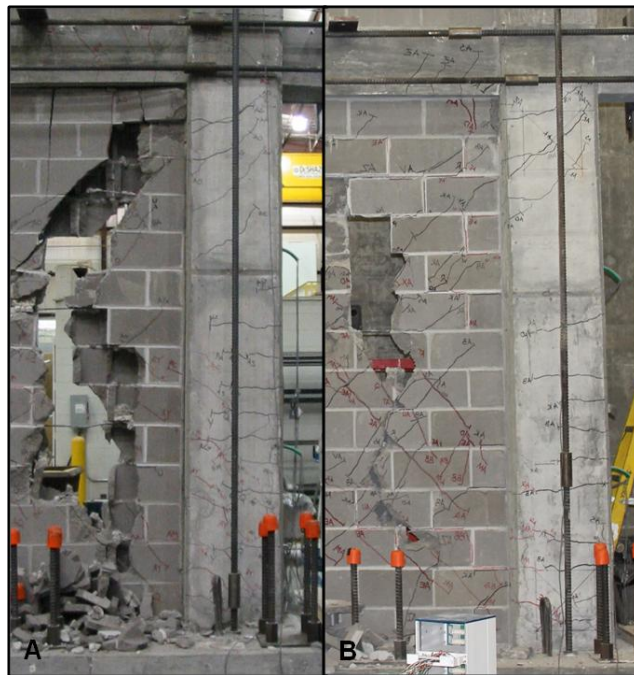


Figure 151: Comparison of shear cracks in the columns of (a) Frame 2 (connection only at the base) and (b) Frame 1 (full connection) at 1.8 inches (45.7 mm) of lateral displacement (1.5% drift).

There were only two noticeable differences between the finite element models at 1.8 inches (45.7 mm) of displacement (1.5% drift) (See Figure 152 c and d). First, there was a large gap in between the right (compressive) column and the masonry infill in the model of Frame 2, but there was no gap in the model of Frame 1. Second, there was cracking on the outside of the top left (compressive) column in the model of Frame 1 which was not present in the model of Frame 2. There was little difference in the degree of crushing of the masonry units between the two finite element models, whereas the experimental frames had widely varying degrees of damage to the masonry infill at 1.8 inches (45.7 mm) of displacement (1.5% drift). The cracking and crushing patterns of both models closely resembled Frame 2.

(space left blank intentionally)

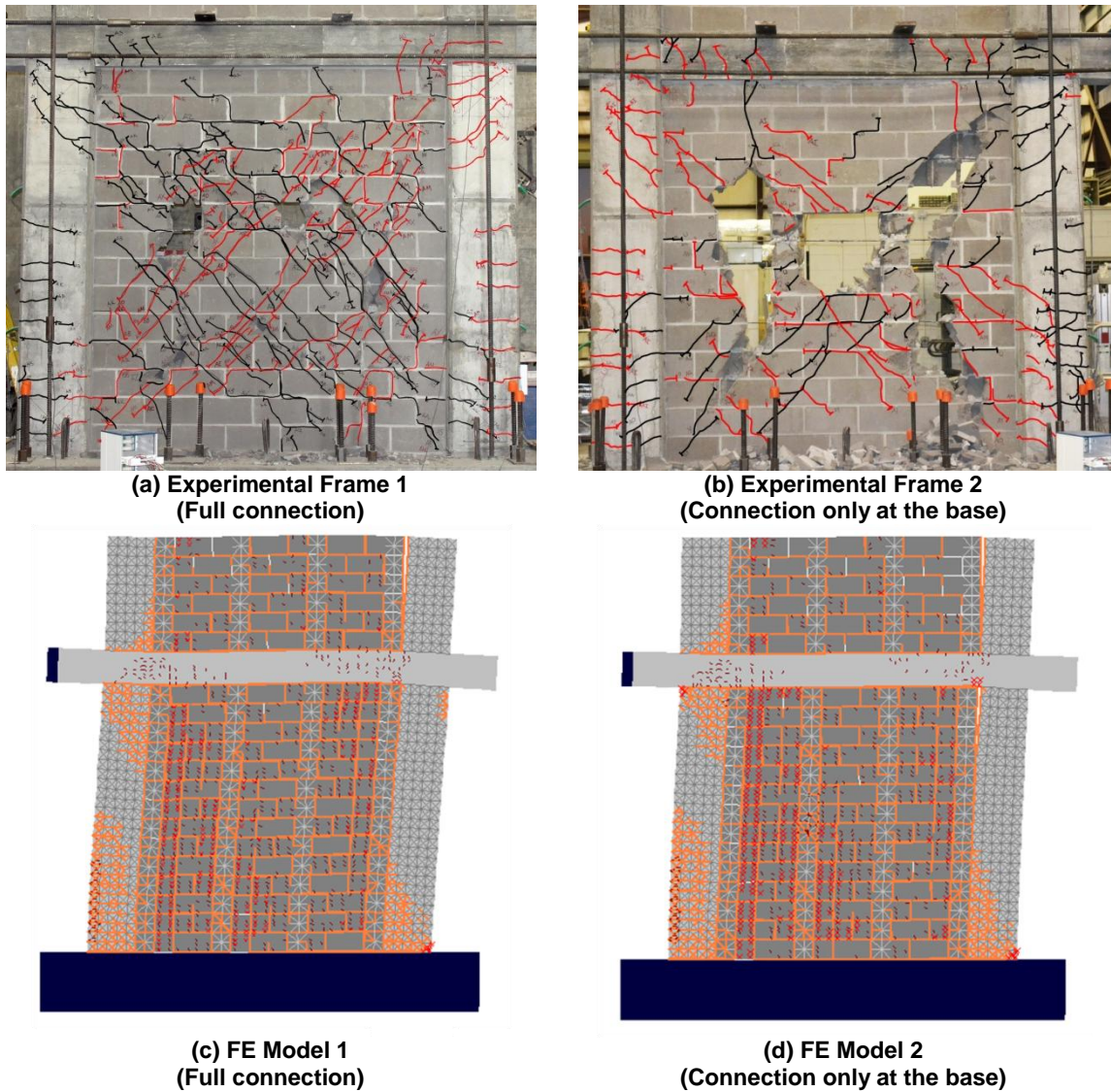


Figure 152: Damage in the experimental frames and the finite element models at 1.8 inches (45.7 mm) of lateral displacement (1.5% drift). The cracks observed in the experiments are traced in black for the positive cycles and red for the negative cycles.

During the final experimental cycles which had an amplitude of 2.4 inches (61.0 mm, 2.0% drift), the ungrouted cells fell out from the center of the masonry wall in Frame 1 (See Figure 153a). No new cracks formed in the beam or the beam-column joints. The flexural cracks in the frame continued to expand, and at the peak displacement (2.4 inches, 61.0 mm, 2.0% drift), the crack between the base of the tensile column and the foundation was 0.1 inches (2.5 mm) wide.

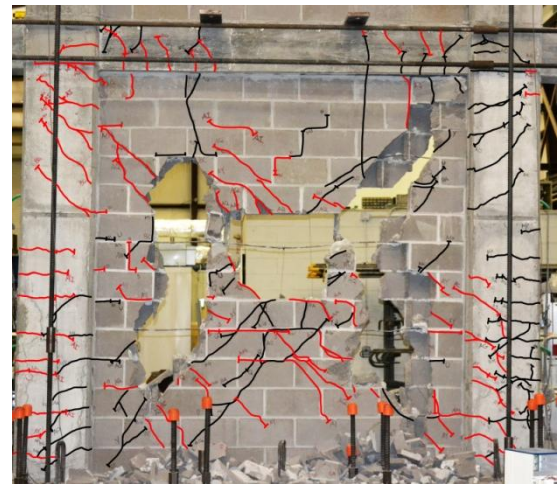
Frame 2 had slightly more damage to the frame by the end of the 2.4 inch (61.0 mm, 2.0% drift) cycles (See Figure 153b). Due to the unstable portion of the masonry wall, no additional cracks were marked out on the beam or the beam-column joints. The masonry wall continued to crush and the grouted cores at the center of the wall had also fallen out of plane due to debonding from the reinforcement. At each cycle, a very large separation was observed between the masonry wall and the columns of the infill frame.

Very little change was predicted in the finite element models from 1.8 inches (45.7 mm, 1.5% drift) to 2.4 inches (61.0 mm) of displacement (2.0% drift) (See Figure 153 c and d). Crushing of the ungrouted masonry continued to expand and the corners of the RC columns near the foundation and beam-column joints crushed slightly. The primary differences between the models were still the same as those observed at 1.8 inches (45.7 mm) of displacement (1.5% drift): crushing which was present in Frame 1 but not Frame 2, and a gap which was present in Frame 2 but not Frame 1.

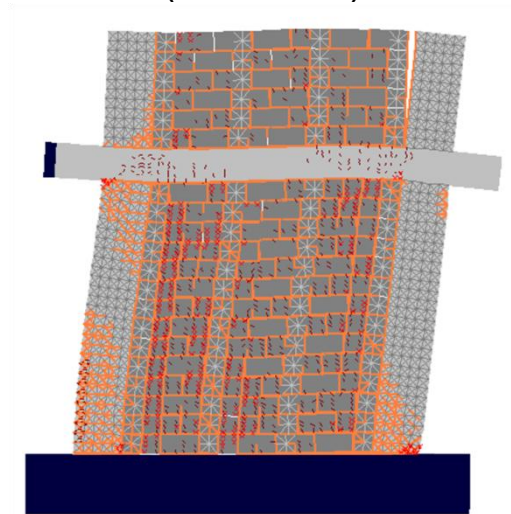
(space left blank intentionally)



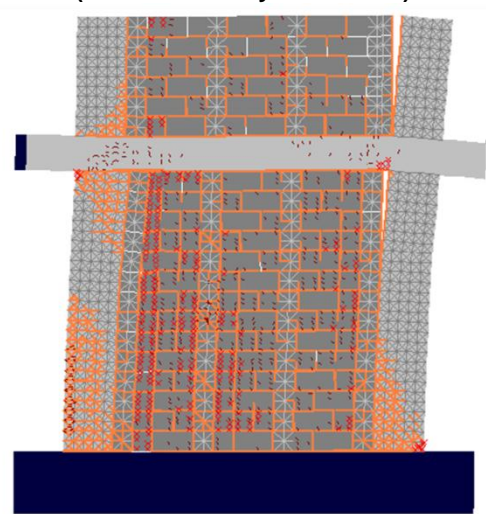
**(a) Experimental Frame 1
(Full connection)**



**(b) Experimental Frame 2
(Connection only at the base)**



**(c) FE Model 1
(Full connection)**



**(d) FE Model 2
(Connection only at the base)**

Figure 153: Damage in the experimental frames and the finite element models at 2.4 inches (61.0 mm) of lateral displacement (2.0% drift). The cracks in the experiments are traced in black for the positive cycles and red for the negative cycles.

6.1.1.2 Gravity Loads

In order to compare the force displacement behavior of the experimental frames to the analytical models, the gravity load data from the load cells was examined. The gravity loads had been applied to the columns in the experimental frames using DYWIDAG bars to post-tension a steel section down over the top of each column. The initial loads were

applied such that the average monitored load over the course of the cyclic tests would equal the gravity load of the five-story design structure (See Appendix D for calculations). Hinge connections were used at the tops of the columns to minimize any moment imposed by the loading. The average recorded load on the columns in each frame was within 1% of the desired gravity load. Although at the peak displacement of 2.4 inches (61.0 mm) (2.0% drift) when the post-tensioning bars were stretched most, the average load on the columns in both experiments was 40% above the gravity load for the tension columns and 21.5% below the gravity load for the compression columns. Because the gravity loading was less than 10% of the compressive strength of the column, the additional load at these large displacements was unlikely to have a significant effect on the capacity of the frames. Additionally, the maximum deviation from gravity load on the columns at any time during the experiments prior to the failure of the frames was only 20% (See Appendix D for additional graphs). The gravity load applied in the analytical models was the constant, targeted, gravity load.

6.1.1.3 Force-Displacement Behavior

Figures 154 and 155 show the force displacement behavior for the two frames and the results of the initial finite element models. Frame 1, which had connections around the entire perimeter of the infill, achieved a peak strength of 197.16 kips (877.01 kN) at 0.86 inches (21.8 mm) of displacement, or 0.7% drift. Frame 2, which had connections only at the base of the infill, had a peak strength of 193.4 kips (860.30 kN) which occurred at 1.1 inches (27.9 mm) of displacement. This is equivalent to a drift of 0.9%. The Frames achieved peak strength at much lower drift levels than a seismically detailed RC moment frame without masonry infill, which typically can sustain a 2.0% drift before

reaching its peak capacity. However, the capacities of the Frames were also increased by about 200% over the capacity of a bare RC moment frame with the same reinforcement detailing and concrete strength. A portal frame calculation for the bare frame capacity was 91.2 kips (405.7 kN) and the capacity predicted by the finite element models with the infill removed was 109.4 kips (486.6 kN) (See Appendix D for calculations). The force-displacement curves of the two experiments are shown together in Figure 156. Frame 2 slightly more pinching in the hysteresis curve than Frame 1. The secant stiffness at 0.05 inches (1.3 mm) of displacement was 37% greater in Frame 1 than the Frame 2.

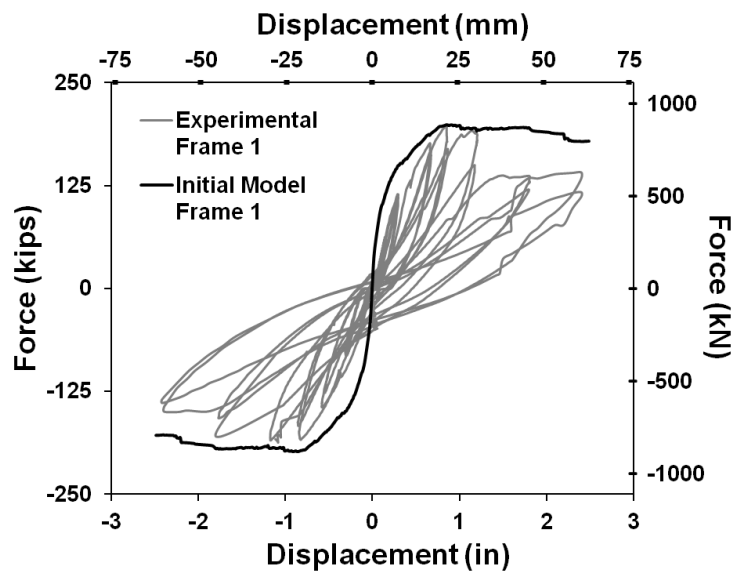


Figure 154: Force-displacement plot of the experimental and analytical Frame 1 (full connection)

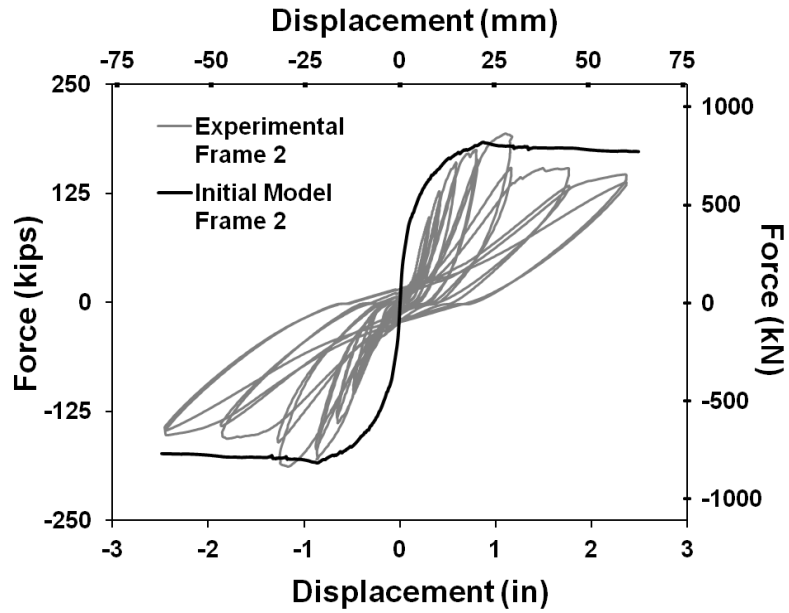


Figure 155: Force-displacement plot of the experimental and analytical Frame 2 (connection only at the base)

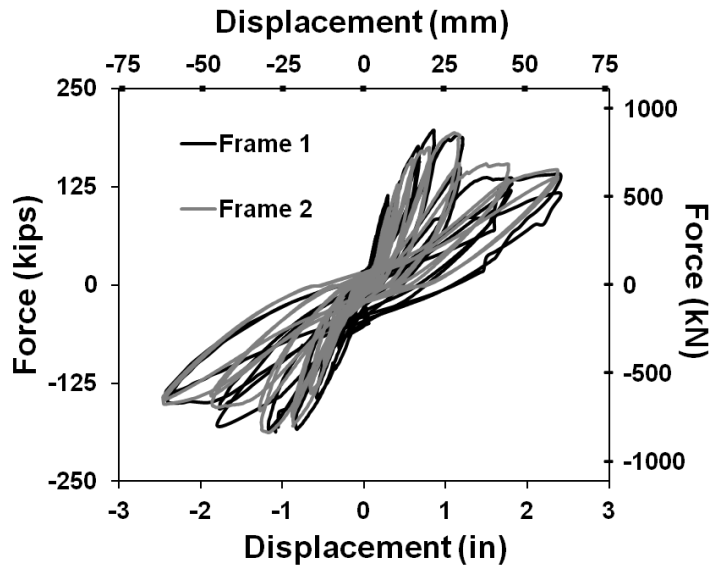


Figure 156: Comparison of the experimental force-displacement behavior for Frame 1 and Frame 2

The predictions of the initial finite element models for peak force and displacement at peak force were very close to the experimental results. The analytical model of Frame 1 with connections on all edges of the masonry wall predicted peak capacity to be 198.31 kips (882.13 kN) at 0.85 inches (29.6 mm) of displacement and is shown in Figure 154. These results were both within 2% of the experimentally recorded data. The analytical model of Frame 2 predicted peak capacity of 183.82 kips (817.67 kN) at 0.87 inches (22.1 mm) of displacement (See Figure 155). These results trend with the results from the experiments, but the analytical model underestimated the capacity of the frame by 9.6% and underestimated the displacement at peak capacity by 20.9%.

The initial stiffness of both models was greater than the stiffness observed experimentally. Since these frames had a weak masonry infill, the force-displacement behavior is dominated by the behavior of the RC frame. In validation studies of the constitutive model (Section 3.4.4) and in the work by Stavridis and Shing (2010), the constitutive model was found to overestimate the initial stiffness of bare frames. The finite element models also showed less strength degradation than the experimental frames. This may be related to how the ungrouted masonry units were modeled. When the initial finite element models were created, it was assumed that the ungrouted masonry would primarily fail due to crushing. Thus, they were modeled using smeared crack elements only to simplify the meshing scheme. However, since shear cracking through the ungrouted masonry was present in the experimental frames, it is probably more appropriate to model them with a combination of smeared crack and interface elements.

6.1.2 Interface Behavior

The interfaces between the partially grouted infill wall and the RC frames played a crucial role in altering the shear transfer zone for the masonry compression struts in both experimental frames. The influence of the reinforcement on the behavior of the interfaces can clearly be observed by comparing the slip gage data gathered from the two experiments, shown in Figure 157. The dial gages had a resolution of 0.001 inches (0.03 mm). Slip was defined to have occurred once a dial gage read at least 0.01 inches (0.25 mm) of displacement. These results are compared to the cracking of the interfaces in the initial finite element models. Each interface is discussed separately in the order in which it failed, beginning with the beam-wall interface.

(space left blank intentionally)

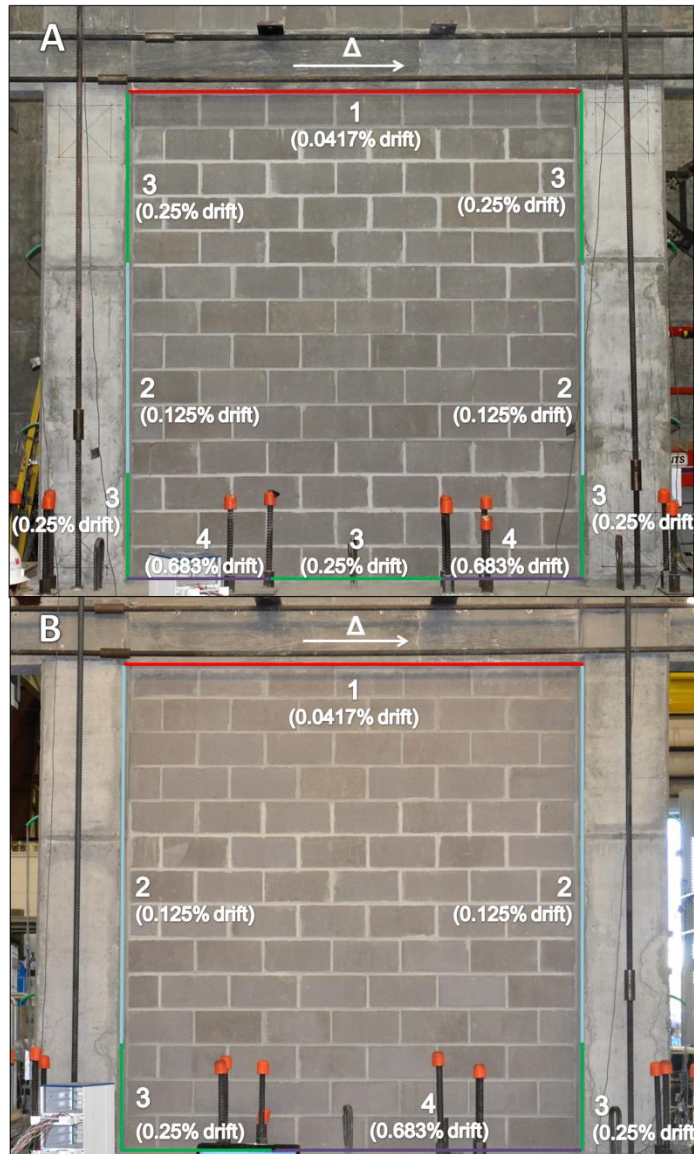


Figure 157: Interface cracking for a) Frame 1 (full connection) and b) Frame 2 (connection only at the base).

6.1.2.1 Beam-Wall Interface

The top interface cracked almost immediately in both frames. The entire interface slipped when the experiment was stopped for the first time to collect dial gage data at 0.05 inches (1.3 mm) of lateral displacement (0.0417% drift) (See Figure 157). The connection was probably very weak due to the fact that during construction, a small gap

was left at the top of the masonry wall between the masonry and the concrete beam. This gap was filled with mortar, but the bond did not appear to be very effective. The maximum slip recorded at the top interface of the masonry wall for both walls was about 0.2 inches (5.1 mm) at 1.2 inches (30.5 mm) of lateral displacement (1.0% drift). After this point, most of the gages fell off the masonry walls.

The connections from the reinforced concrete beam to the top of the masonry infill wall were crucial to preventing out-of-plane failure of the masonry. During the cyclic test of Frame 2, which did not have connections to the beam, the masonry shifted out of plane several inches and would have likely fallen out in a dynamic test (See Figure 150). Frame 1, which had connections at the top of the wall to the RC beam, did not have the masonry wall shift out of plane during testing.

In the initial finite element models, the interface between the beam and the masonry wall was assumed to have the same properties as the bed joints. The models predicted cracking at about the same time as bed joint cracking initiated in the model (See Table 6). This boundary should be revised in the finite element models to reflect the weak bond between the beam and the masonry wall.

6.1.2.2 Column-Wall Interfaces

The timing of cracking in the column-wall interfaces suggested that the connections from the reinforced concrete columns into the bed joints of the masonry had little to no influence in delaying the cracking of the interfaces between the masonry wall and the reinforced concrete columns. For both Frame 1 and Frame 2, the slip initiated during the 0.15 inch (3.8 mm) amplitude (0.125% drift) cycles (0.05-0.15 in, 1.3-3.8 mm) and the entire interface had slipped by the 0.3 inch (7.6 mm) amplitude cycles (0.25%

drift). However, it appears the vertical dowel connections in Frame 1 delayed interface cracking within the height of the vertical dowel connections. For Frame 1, the middle portion of the column-wall interface from course three to course nine slipped first, then the regions within the height of the vertical dowel connections. For Frame 2, the column-wall interface from course three to the top of the wall cracked first, followed by the interface from course one to three within the height of the dowel. This behavior is probably related to the bending mechanism observed in both columns suggests the dowel connection at the base of the wall served to stiffen the bottom portion of the masonry wall and move the hinging zone up in the column. If the connection at the top of the wall also stiffened that zone, it would make sense that the more flexible portions of the wall would permit slip to initiate first. The dial gages at these interfaces recorded a maximum slip of 0.16-0.2 inches (4.1-5.1 mm) for both frames at 1.2 inches (30.5 mm) of lateral displacement (1.0% drift). Beyond this point, many of the gages broke off the masonry walls.

The finite element models predicted the onset of cracking of the column-wall interface to be the same in both frames (See Table 6). This suggests that the effect of the dowel connections on the column-wall interface was underestimated by the model. Additionally, this interface was predicted to crack before the masonry wall. This is not consistent with the observations from the experiments. In experimental Frame 1, cracking in the wall did not initiate until between 0.15 and 0.3 inches (3.8 and 7.6 mm) of displacement (0.125% and 0.25% drift). In experimental Frame 2, cracking in the masonry initiated between 0.05 and 0.15 inches (1.3 and 3.8 mm) of displacement (0.00417% and 0.125% drift).

6.1.2.3 Foundation-Wall Interface

The foundation-wall interface behaved very similarly between the two frames. The interface on the compression side of the wall did not slip until the 0.82 inch (20.8 mm) cycles in either frame (0.683% drift). Slip along this interface initiated during the 0.3 inch (7.6 mm) amplitude (0.25% drift) cycles for both frames, but in different locations. For Frame 1, which had dowel connections on all edges of the infill, the slip initiated in the zone between the two grouted cells in the middle of the wall, beginning with the tensile portion and propagating through the ungrouted bed joints laterally to the center of the wall. In Frame 2, which connections only at the base of the infill, the bottom interface slip began at the corner of the tension side of the propagated across the bottom interface.

In the finite element models, the boundary between the masonry wall and the foundation was the last interface to crack, consistent with the trend observed in the experiments. The cracking began in the ungrouted bed joints at 0.05 inches (1.3 mm) of displacement (0.0417% drift) (See Figure 137) and went through the entire foundation-wall interface by 0.42 inches (10.7 mm) of displacement (0.35% drift) (See Figure 140). The crack propagation was slightly faster in the foundation-wall interface of the model with connections only at the base of the masonry wall. Because the gage readings were only taken at the beginning and end of each cycle, this trend cannot be verified or refuted by the experimental data.

6.1.3 Masonry Wall Behavior

The shear and flexural deformations of each masonry infill wall was determined using data from string pots around the perimeter and across the diagonals of the masonry

walls. Details of the calculations are found in Appendix D. The primary deformation of the masonry walls was in shear, and the curvature was negligible for the range of lateral displacements that the string pots recorded data. After the 0.82 inch (20.8 mm, 0.683% drift) cycles, too much debris fell on the cables to accurately measure the wall deformations. Strains in the vertical and horizontal rebar within the wall and the dowel connections at the base and to the columns were recorded by strain gages

6.1.3.1 Shear Strains

The shear strain in each of the masonry infill walls for the experimental and analytical frames is shown in Figure 158. Although there is more noise in the data from Frame 2, the data shows Frame 2 experienced less shear strain than the infill in Frame 1. This trend was confirmed by the finite element models, but the difference is not very significant until beyond 0.5 inches of lateral displacement (0.417% drift).

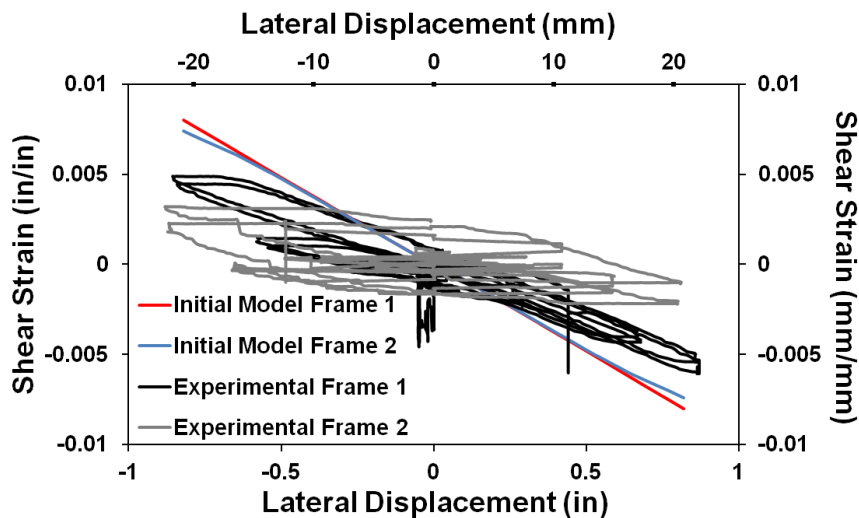


Figure 158: Shear strain in the masonry infill vs. lateral displacement of experimental and analytical Frame 1 (full connection) and Frame 2 (connection only at the base)

This trend makes sense if the connections to the RC frame constrain the masonry wall to deform more in conjunction with the frame. Although these connections did little to influence the slip at the column-wall interface, they prevented a gap from forming between the column and the masonry wall. A gap was observed in Frame 2 which had connections only at the base.

6.1.3.2 Reinforcement

The vertical reinforcement in both masonry walls had strain gages at the base, at a location 4.0 inches (10.2 cm) above the foundation, and at the mid-height of the wall. These gages did not show any yielding of the bars in these locations for either test. Based on the cracking patterns in the grouted cores once the face shells were removed, most of the damage to the cores was concentrated in the center of the wall for Frame 1. The damage to the grouted cores was both at the mid-height and the top of the wall in Frame 2. The yielding of the reinforcement in both finite element models was consistent with the observations from the experiments (See Figures 159 and 160). Both finite element models predicted the vertical reinforcement to yield first at the base of the right (compression side) of the masonry wall, followed by yielding within the height of the second course of masonry. Yielding propagated further up the vertical bars in the finite element model of Frame 1, but only reached mid-height in one of the bars at the very end of the simulation. In the finite element model of Frame 2, the yielding occurred later in the simulation and the reinforcement was most strained at the base of the masonry wall.

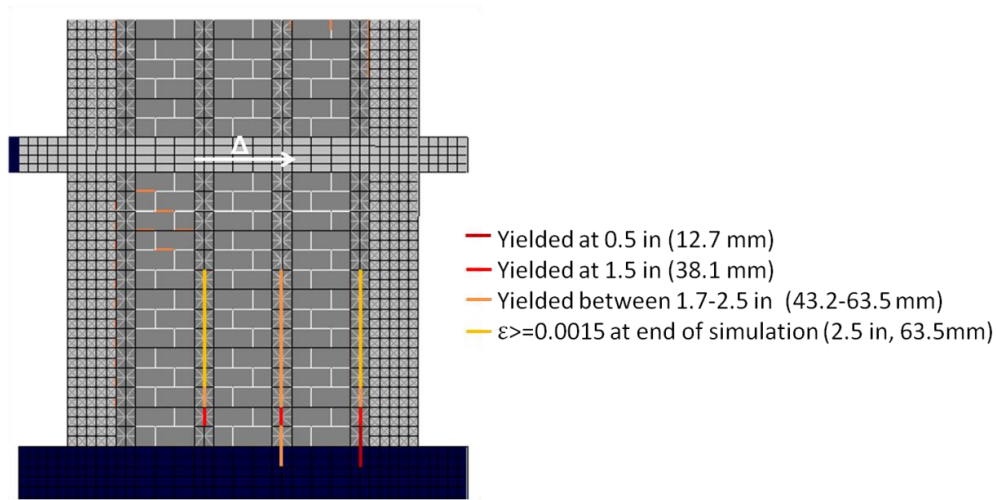


Figure 159: Yielding in the masonry reinforcement of the finite element model of Frame 1 (full connection)

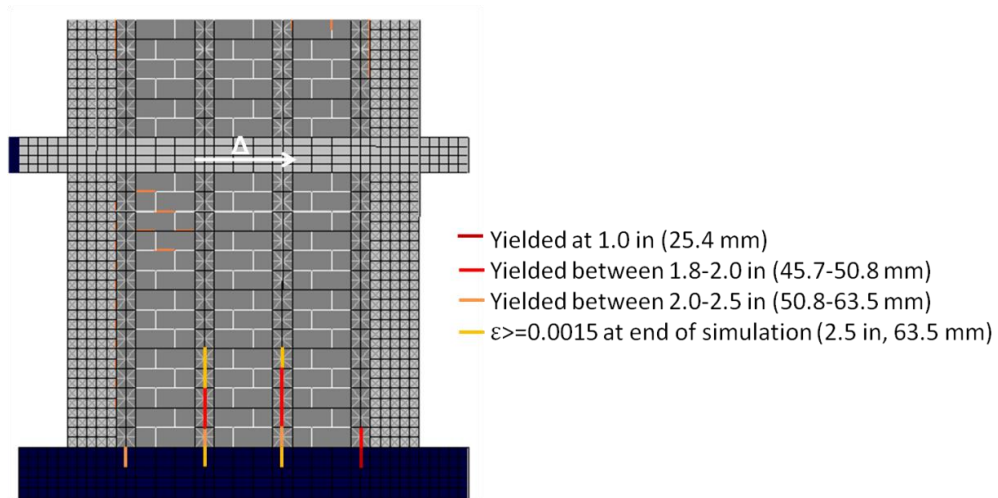


Figure 160: Yielding in the masonry reinforcement of the finite element model of Frame 2 (connection only at the base)

The gages placed at the center of the horizontal bars indicated no yielding during the entire test for either frame. As the ungrouted bricks fell away, these bars did not appear to have any deformation, and likely did not contribute much to the capacity of the

infill walls. In some of the bricks it was noted that the bar placed at the center of the masonry unit actually caused the masonry web to split (See Figure 161).



Figure 161: The horizontal reinforcement placed at the center of the unit caused the masonry web to split

In Frame 1, which had connections around the entire perimeter of the infill, the gages placed just past the dowel bar connecting the horizontal reinforcement to the columns indicated a large sudden increase in strain during the late stages of the test (1.8 inch (45.7 mm, 1.5% drift) cycles and 2.4 inch (60.9 mm, 2.0% drift) cycles. This was probably due to the bending of the bar, which occurred after the middle section of the masonry wall began to fall apart, shown in Figure 162.



Figure 162: Bending of horizontal reinforcement just past the termination of the dowel bar in the Frame 1

6.1.4 Column Behavior

Dial gages and string potentiometers in a 12 inch (30.48 cm) square configuration with diagonals were used to calculate the shear strain and curvature at the top and bottom of the columns. Example calculations are given in Appendix D. Strain gage data was also recorded for the flexural reinforcement at the base of each column. Crack sizes and spacing were used to estimate the strains in the reinforcement further up the height of the columns. Appendix D contains a table with the recorded crack data and the calculations for estimated strain in the rebar.

6.1.4.1 Curvature and Shear Strain

The data indicated that very little flexural deformation occurred at the top and bottom of the columns in either test. The curvature in these regions was less than 0.0002 radians for the entire duration of the tests. This is in agreement with the observed cracking patterns of the columns and the strain gage data which suggests hinging occurred at the level of the second course of masonry.

The shear strains were also very small at the base of the columns in both frames, which was less than 0.001. The top of the columns did have larger values for shear strains, which exceeded 0.002.

6.1.4.2 Reinforcement

The strain gages placed on the flexural reinforcement at the base of the columns indicated no yielding of the bars at that location for the entire duration of both tests. By using the crack widths and spacing between flexural cracks in the columns, an estimate of the strain in the reinforcement was obtained at 0.86 and 2.4 inches (21.8 and 61.0 mm) of lateral displacement (0.717% and 2.0% drift) for Frame 1. The same type of measurement was taken at 1.8 and 2.4 inches (45.7 mm and 61.0 mm) of displacement (1.5% and 2.0% drift) in Frame 2. In both frames, the data indicated yielding began well above the foundation. In Frame 1, yielding in the column rebar began 17.25 inches (43.82 cm) above the foundation. In Frame 2, yielding began 16.5 inches (41.9 mm) above the foundation. This confirms hinging began just above the second course of masonry where the dowel bars terminated.

At the end of the tests, at 2.4 inches (61.0 mm) of lateral displacement (2.0% drift), the column rebar in Frame 1 had a maximum strain of 0.0086 at 7.5 inches (19.05 cm) above the foundation. The strains ranged from 0.0065 at 39.3 inches (99.82 cm) above the foundation to 0.002 at 11.5 inches (29.21 cm) above the foundation. The same trends were observed in Frame 2. At 2.4 inches (61.0 mm) of lateral displacement (2.0% drift), the column rebar had a maximum strain of 0.0055 at 6.5 inches (16.51 cm) above the foundation. The strains in the rebar from 14.5 to 40 inches (36.83 to 101.6 cm) above the foundation ranged from 0.004 to 0.0022.

The shear strain data at the top of the columns indicated the shear reinforcement may have yielded, as shear strains exceeded 0.002. The width of the shear cracks in the top of the columns remained very small for both tests, and yielding of the bars could not be confirmed by crack width data.

In both of the finite element models, the flexural reinforcement first yielded at the base of the columns at 0.5 inches (12.7 mm) of displacement (0.417% drift). This suggests that the effect of the dowel connections at the base of the masonry wall may be underestimated by the initial finite element models. Yielding of the vertical reinforcement propagated up the left (tensile) column to the height of the fourth course of masonry in the model of Frame 1 (See Figure 163). In the model of Frame 2, the yielding propagated slightly higher, reaching the middle of the fifth course of masonry (See Figure 164). Frame 2 also had slightly less yielding at the top of the left (tensile) column and slightly more yielding at the base of the right (compressive) column than Frame 1.

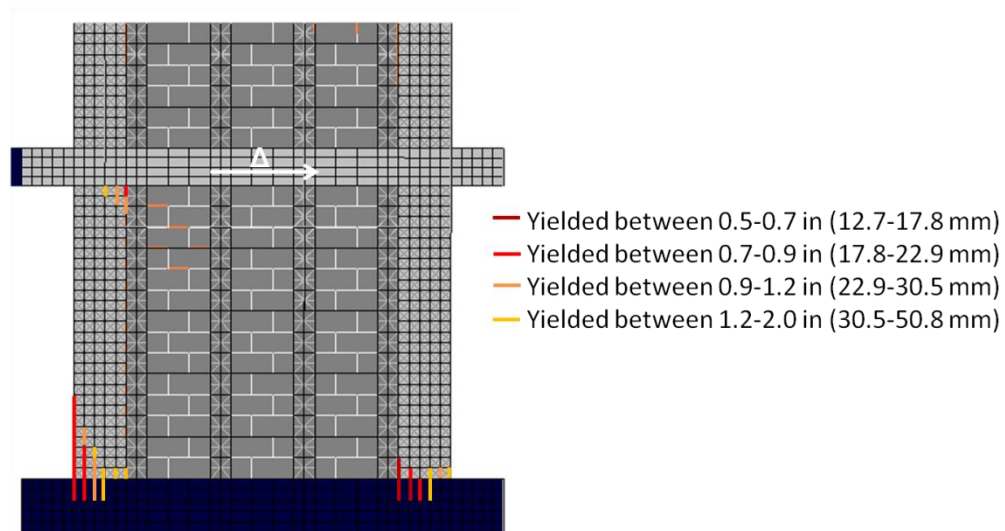


Figure 163: Strains in the flexural reinforcement of the columns in the finite element model of Frame 1 (full connection)

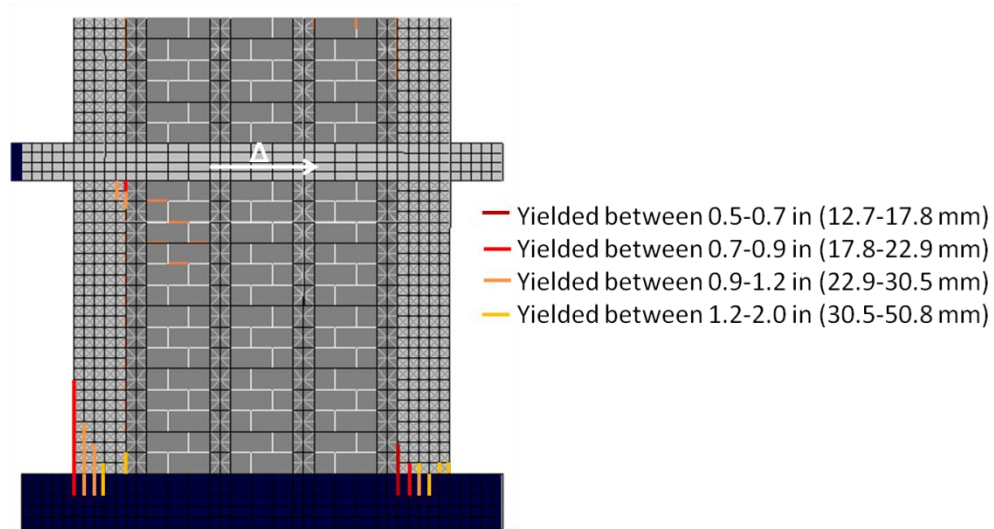


Figure 164: Strains in the flexural reinforcement of the columns in the finite model of Frame 2 (connection only at the base)

6.2 Influence of Masonry and Connections on the Behavior of the RC frame

The cracking patterns, interface slip and yielding of the reinforcement in the hybrid concrete-masonry frames suggest that the typical strut mechanism observed in unreinforced masonry infill structures was altered due to the connections from the reinforced concrete frame to the grouted cores of the masonry infill. The presence of the connection at the top of the frame was key to preventing out-of-plane failure of the masonry, but did not significantly affect the ductility or capacity of the frame. The connections from the masonry wall to the columns constrained the grouted cores at the edge of the wall to displace with the columns, but did not appear to alter the cracking patterns or force-displacement behavior of the frame. Thus, the effect of the top and side connections can be neglected when characterizing the influence of the masonry and connections on the behavior of the RC frame.

The bond between the masonry wall and the RC beam was very weak due to the gap that was left at the top of the masonry infill wall during construction and the poor cohesion properties of the 3:1 sand-cement mortar. The shear transfer at this interface can be assumed to be very limited due to the early initiation of slip observed in the experiment. The cracking patterns of the columns also indicated the bearing area for the masonry strut was primarily at the top of the RC column, centered at about one to two courses down from the top of the masonry wall (See Figure 165 a-d). The shear cracking at the top of the column in Frame 2 propagated through a zone equivalent to 36% of the total column height.

The presence of the connections at the base of the masonry wall in both frames had significant influence on the behavior of the RC frame. This boundary slipped last, providing a zone to transfer shear forces. In both frames, the initial shear bearing area for the compression was through the stiffened zone at the base of the masonry wall through the height of the cast-in-place dowel connections (See Figure 165 a and b). This was more apparent in Frame 1 than Frame 2. As the tests progressed, the crack patterns of the frames both indicate the masonry strut was supported on the column at the mid-height of the stiffened zone at the base of the wall. By drawing the masonry struts in a manner consistent with the cracking observed in the experiments (See Figure 165 c and d), the shear critical zone for the columns is moved up compared to what would be assumed in a typical strut and tie analysis.

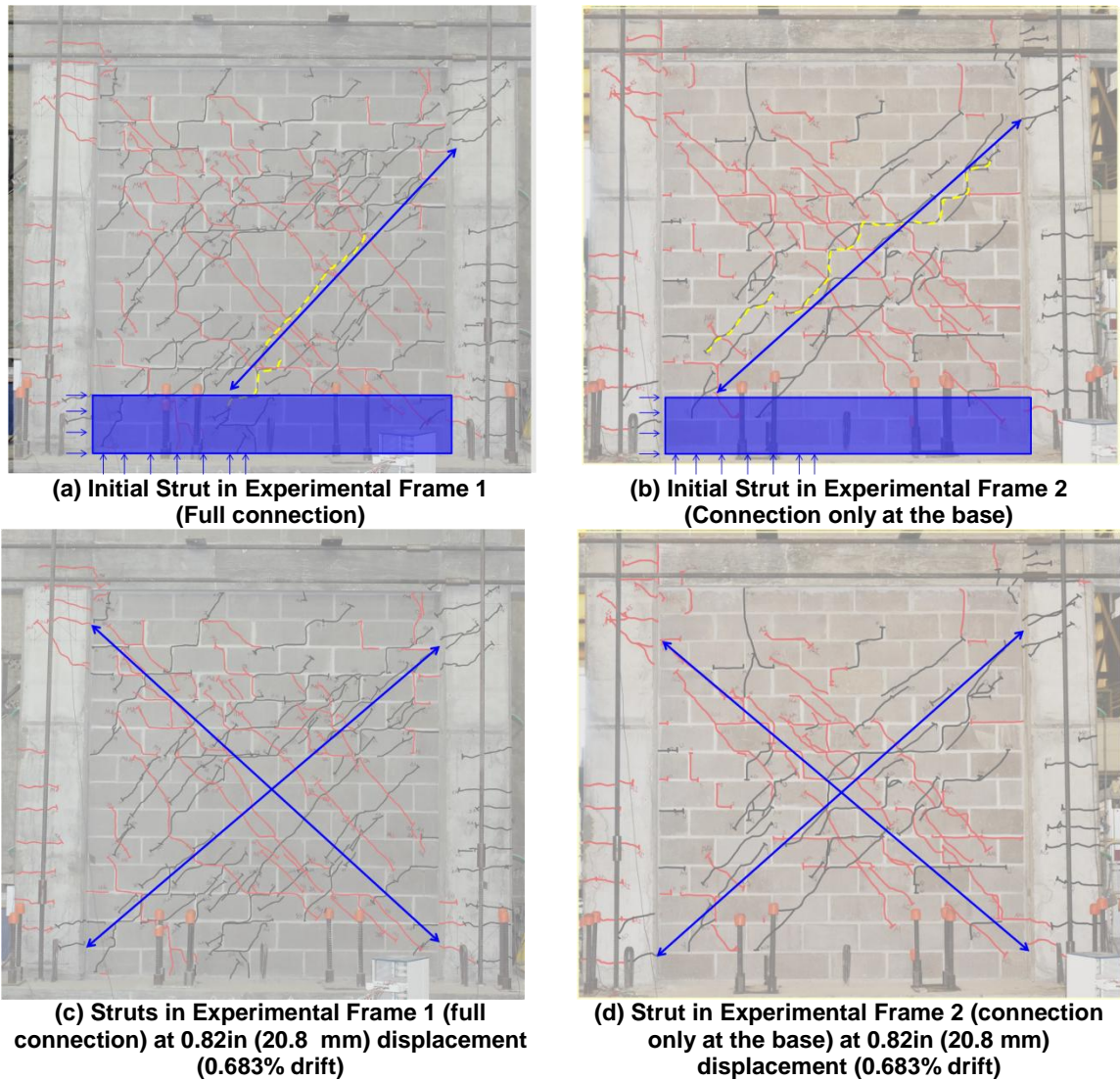


Figure 165: Strut mechanisms observed during the experiments

6.3 Improvement of Finite Element Models Based on Experimental Observations

Although the initial finite element models gave very close predictions for the peak strengths of the frames and predicted the same general failure mechanisms as were observed in the experiments, several improvements can be made.

6.3.1 Masonry Modeling and Material Properties

In general, the mortar joints in the finite element models cracked at much lower displacements than was observed in the experiments. In the revised model, interface element failure surface, representing the mortar was changed to match the upper bound of the triplet test data, rather than the average. Also, the shear cracks which were observed in the ungrouted cells of the experimental frames were not captured by the initial finite element models. Prior to the experiment, it was thought that the ungrouted units would primarily crush and would not exhibit shear cracking. Thus, they were modeled with a single smeared crack element for simplicity even though it is well known that smeared crack elements can overestimate shear capacity. In the revised finite element models, the ungrouted units have been modeled using the same eight element module as was used for the grouted cores in order to capture shear cracking.

In the initial model, it was assumed that the grouted cores would act in unison with the masonry face shells. However, many of the shear cracks which initially spread across the grouted cores of the experimental frames were through the face shells alone. Very few shear cracks were observed in the grouted cores once the face shells had fallen off. The initial finite element models do not capture any shear cracks across the grouted cells, as the stresses are not high enough to cause the entire core to crack. As a result, the grouted cells in the revised model were represented with two layers of 8 element modules with shared nodes to permit shear cracking to spread over the face shells of the grouted shells. One layer was used to model the grout cores and the other was used to model the masonry and mortar joints. The nodes for both layers are shared so the is constrained to

displace together, but face shells are permitted to crack even when the grouted cores do not.

For the initial models, the head joints were given a bond strength equal to half the bed joint bond strength. This resulted in the head joints cracking first, instead of stair-stepped cracks like those observed in the experimental frames. In the revised models, the head joint bond strength was increased to 75% of the bed joint bond strength, which resulted in stair-stepped cracking like the experiments.

6.3.2 Interface Properties

The interfaces in the initial finite element models were given the same properties as the mortar bed joints. This resulted in the initial finite element models predicting interface cracking beginning with the column-wall interfaces, then the top beam-wall interface and finally the foundation-wall interface. The experiment showed cracking very early at the top interface, followed by the column-wall interfaces and finally the foundation-wall interface. In the revised models, the top interface was given a very high flexibility, with stiffness equal to 10% of the mortar joint stiffness. The top interface was also reduced to 50% of the mortar bed joint tensile strength, shear friction and cohesion. The column-wall and foundation-wall interfaces were kept the same as the bed joints in the rest of the masonry wall.

6.3.3 Dowel Reinforcement Modeling

The influence of the connections on the RC frame behavior appeared to be underestimated by the initial finite element models. This was evidenced by the flexural cracking of the columns in both models, which initiated at the base of the column rather than just above the second course of masonry where the splice for the dowel

reinforcement terminated. In addition, no difference between the cracking patterns of the RC frames was observed between the two initial models. However, in the experiments flexural cracking initiated earlier, and more shear cracks developed in the columns of Frame 2 than developed in the columns of Frame 1.

The influence of the dowel reinforcement was more pronounced after the following revisions to the initial finite element models. First, the grouted cores through the height of the dowel were given an increased shear stiffness and shear strength compared to the grouted cores in the rest of the wall. The elastic modulus of the grouted cores through the height of the dowels was not increased, because the truss elements used to model the vertical reinforcement already account for the normal stiffness of the reinforcement. Instead, only the shear stiffness was increased. The increased shear modulus was calculated assuming the grouted cells were a matrix with steel fibers, and resulted in an increase in shear stiffness of 10% through the height of the dowels (See Appendix C for calculations). Second, the vertical reinforcement in the grouted cores was partially distributed to the edges of the grouted unit to account for its contribution to the bending capacity of the grouted core (See Appendix C for calculations).

6.3.4 Concrete Fracture Energy

In the post-peak regime, the finite element models could be improved by exhibiting more strength degradation. By reducing the fracture energy of the concrete by 33%, the revised models exhibit more brittle behavior and degrade faster than the initial finite element models.

6.4 Results of Revised Finite Element Models

6.4.1 Damage Sequence

The initial cracking patterns of the revised model are much closer to those observed in the experiments. Table 7 shows the initial cracking patterns for both revised models. The interface elements representing the grout cores, masonry and concrete have been colored the same as the smeared crack elements for clarity. The order of interface cracking is more in tune with the experiment, as cracking begins at the beam-wall interface much earlier than the initial finite element models. Additionally, the initial cracks through the masonry correspond well to the experiments. The cracks propagate through both the units and the mortar joints instead of beginning only in the mortar joints like the initial models.

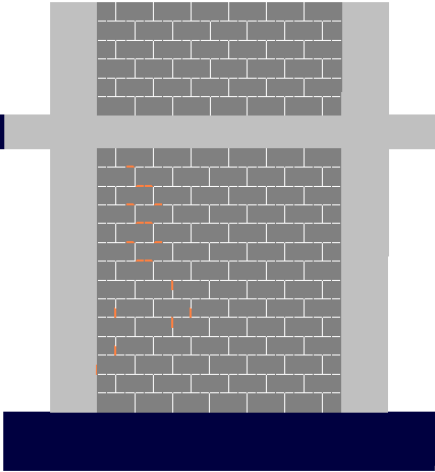
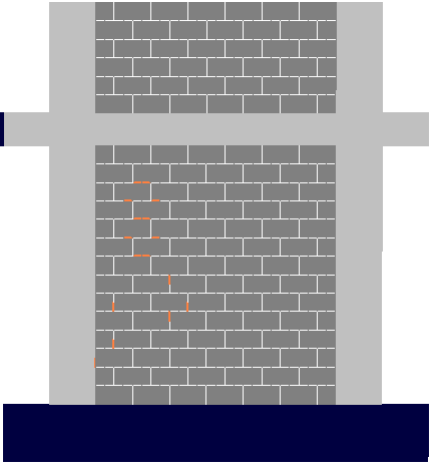
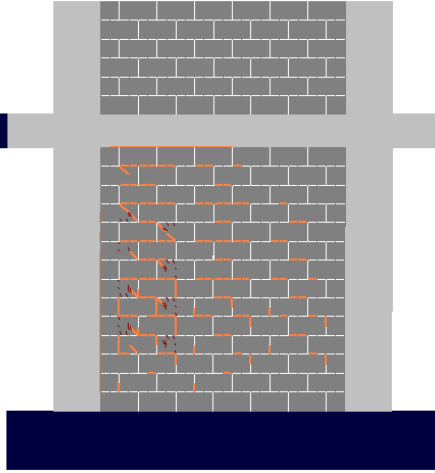
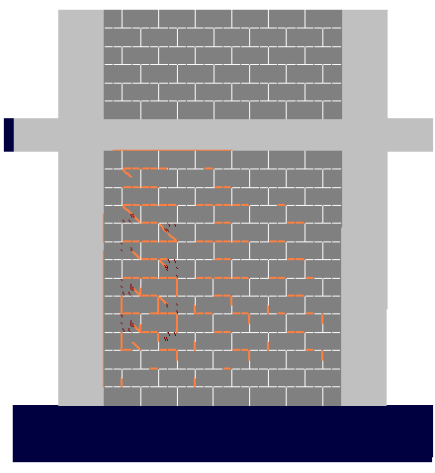
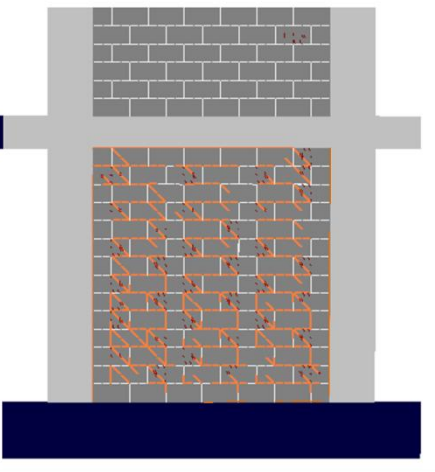
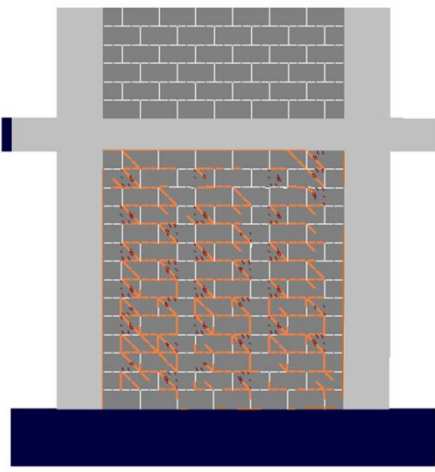
Cracking in the revised models begins much later than in the initial models, at 0.014 in (0.4 mm) of lateral displacement for both frames (0.0117% drift). This is more consistent with the experimental observations than the initial models which predicted cracking of both frames to initiate at 0.007 inches (0.2 mm) of lateral displacement (0.00583% drift). Even though cracking is still predicted at a lower displacement than what was recorded in the experiments, the load at first cracking of the masonry is very close to what was recorded in the experiments. In Frame 1, the experimentally recorded cracking load was 103.6 kips (460.84 kN) and the revised analytical model predicts masonry cracking at 37.3 kips (165.92 kN) of load. Although the model predicts cracking too early, it does predict a larger cracking load for this frame than the frame with connections only at the base, a trend which was not captured by the initial models. In the Frame 2, the revised analytical model predicts masonry cracking at 33.06 kips (147.06

kN) of load which is within 8% of the experimentally recorded cracking load, 30.8 kips (137 kN). This is a significant improvement over the initial model prediction which was 54% below the actual cracking load.

It is also important to note that cracking propagates faster in the model of Frame 2 than in the model of Frame 1 (See Table 7 0.025in (0.6 mm), 0.00208% drift). This is consistent with experimental observations and was not captured by the initial finite element models. In the revised models, the cracking propagates into the face shells of the grouted shells by 0.05 in (1.27mm) of displacement (0.0417% drift).

(space left blank intentionally)

Table 7: Initial cracking patterns of revised finite element models

<p align="center">FE Model 1 (Full connection)</p>	<p align="center">FE Model 2 (Connection only at the base)</p>
 <p align="center">Initial Cracking- 0.014 in (0.36 mm), 0.0117% drift</p>	 <p align="center">Initial Cracking- 0.014 in (0.36 mm), 0.0117% drift</p>
 <p align="center">0.025 in (0.64 mm), 0.0208% drift</p>	 <p align="center">0.025 in (0.64 mm), 0.0208% drift</p>
 <p align="center">0.05 in (1.3 mm), 0.417% drift</p>	 <p align="center">0.05 in (1.3 mm), 0.417% drift</p>

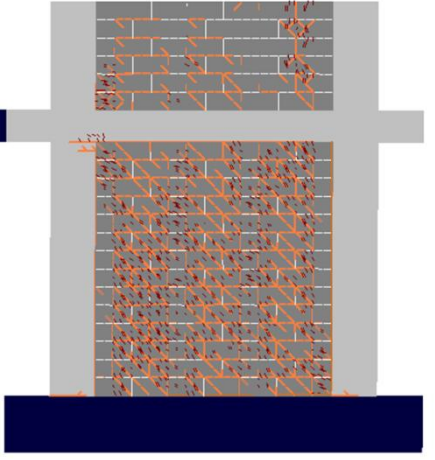
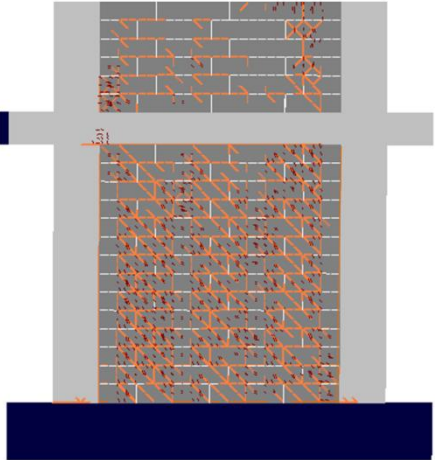
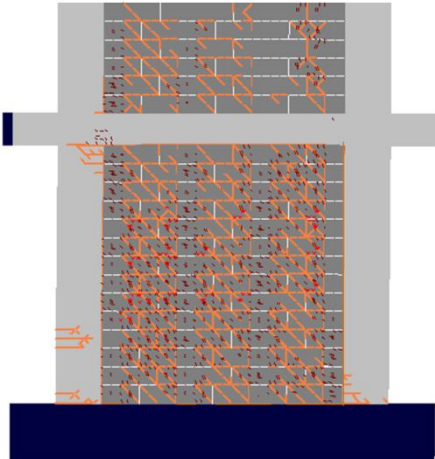
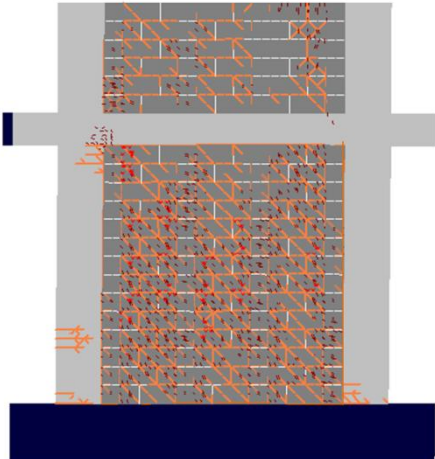
The timing of damage and the cracking patterns in the RC frames are also improved in the revised models. Both the initial and revised models correctly predict the first damage to the columns as hairline cracks at the foundation (See Figure 138 and Table 8 0.15 inches (3.8 mm), 0.125% drift). The revised models correctly predict the next crack to occur just above the location where the dowel bars terminate, whereas the initial models predicted the cracking to spread upwards from the foundation (See Figure 139 and Table 8 0.3 inches (7.6 mm), 0.25% drift). This crack occurs at the same displacement in both models, even though experimental Frame 2 cracked slightly earlier than experimental Frame 1.

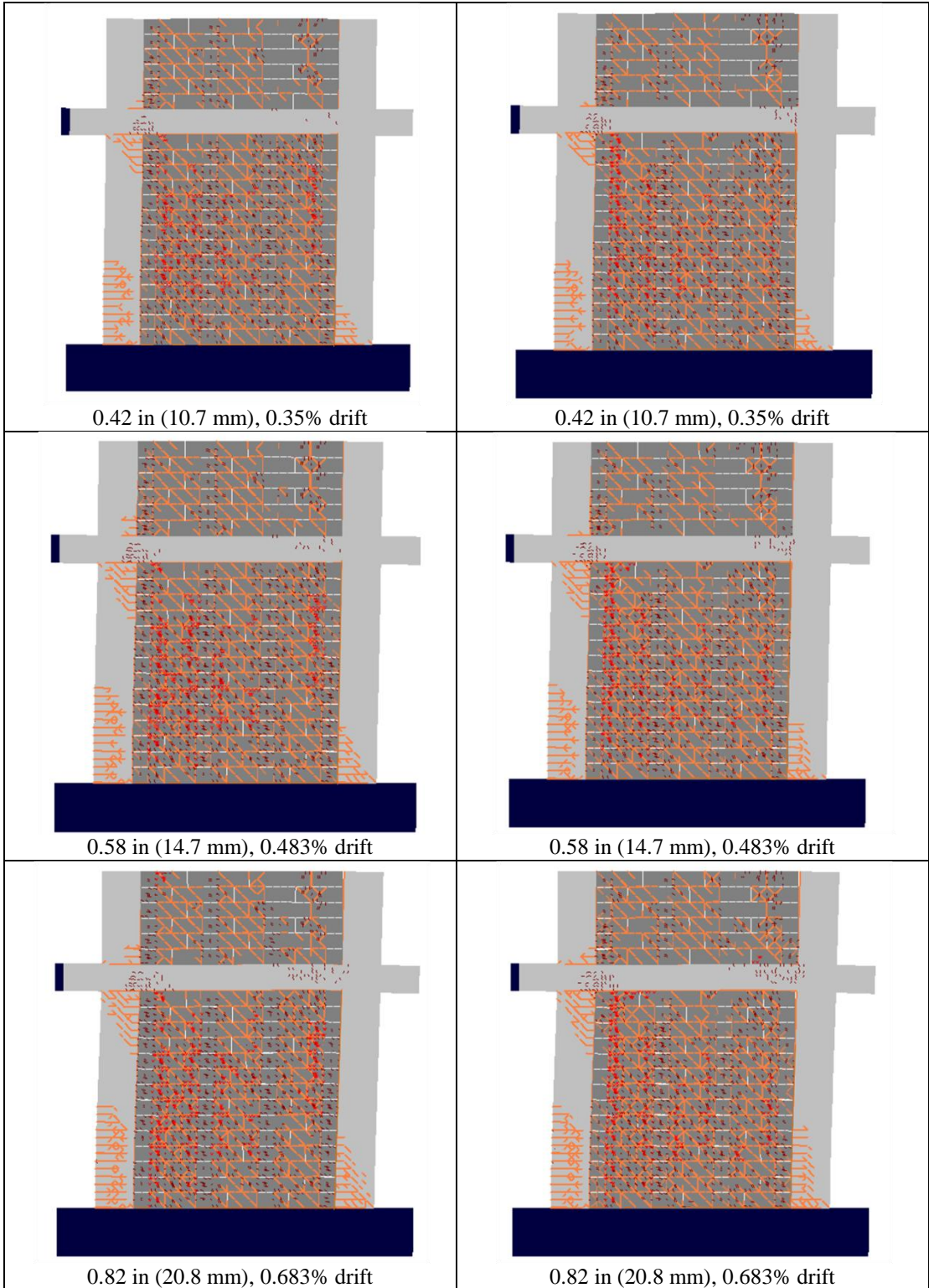
Shear cracking at the top of the columns occurs in both revised models (See Table 8 0.3 inches (7.6 mm), 0.25% drift). The cracks at the top left and bottom right of the frames are more clearly combined shear and flexural cracks, where the initial models had primarily shear cracking in these locations. Beyond 0.82 inches (20.8 mm) of displacement (0.683% drift), slight differences between the two frames can be detected. The Frame 2 model has slightly more damage to the top left column and flexural cracks extend higher up in the right column than the Frame 1 model. In the experiments, more damage was observed in Frame 2 than Frame 1, and this difference was not captured by the initial models.

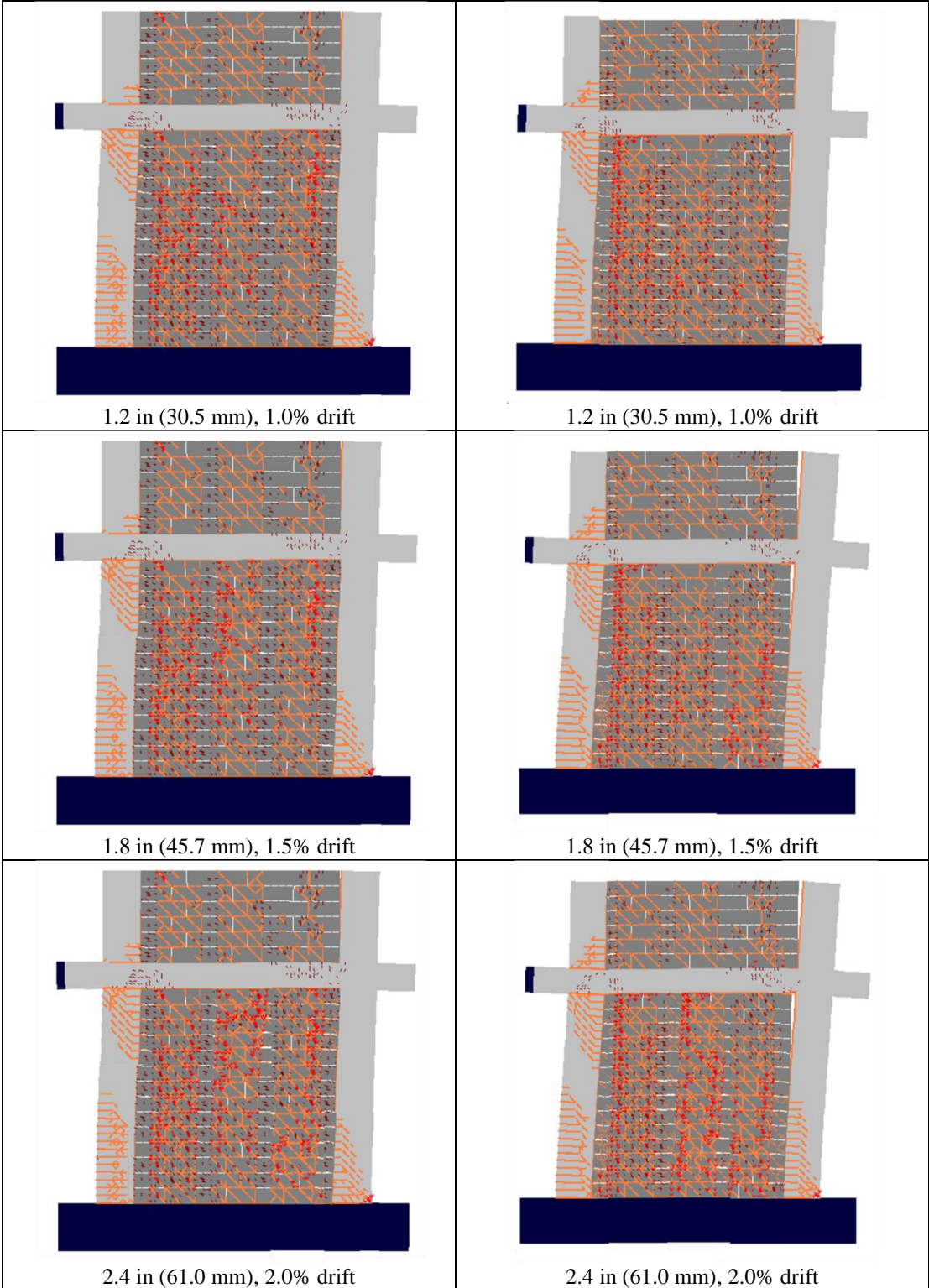
Crushing of the masonry initiates in both revised models at about 0.25 inches (6.4 mm) lateral displacement (0.208% drift), about the same as the initial finite element models. In the Frame 1 model, crushing primarily stays below the top courses where the dowel bars are located, until very late in the simulation. In the Frame 2 model, crushing spreads to the top courses of masonry much earlier than the in the Frame 1 model. This is

consistent with the experimental observations. The initial models had predicted the same crushing damage pattern for both walls

Table 8: Damage sequence for revised finite element models

FE Model 1 (Full connection)	FE Model 2 (Connection only at the base)
 <p data-bbox="386 915 721 945">0.15 in (3.8 mm), 0.125% drift</p>	 <p data-bbox="938 915 1273 945">0.15 in (3.8 mm), 0.125% drift</p>
 <p data-bbox="402 1423 704 1453">0.3 in (7.6 mm), 0.25% drift</p>	 <p data-bbox="954 1423 1256 1453">0.3 in (7.6 mm), 0.25% drift</p>





6.4.2 Force-Displacement Behavior

There does not seem to be any significant improvements in the representation of the force-displacement behavior from the initial to the revised models. The capacity predictions of the initial models were very close to the experimental values. The revised models have peak strengths which occur at a slightly larger displacement than in the initial models, but the error on the capacity prediction is about the same as the previous models. The peak capacity of the revised model for Frame 1 was 205.15 kips (912.55 kN) at 1.07 inches (27.2 mm) of displacement (0.892% drift). This is within 5% of the capacity and 25% of the displacement at peak strength of Frame 1, which achieved a peak strength of 197.16 kips (877.01 kN) at 0.86 inches (21.8 mm) of displacement (0.717% drift). The peak capacity of the revised model of Frame 2 was 189.03 kips (840.85 kN) at 1.4 inches (35.6 mm) of displacement (1.167% drift). Experimental Frame 2 had a peak strength of 193.4 kips (860.29 kN) at 1.1 inches (27.9 mm) of displacement (0.917% drift). The predictions of the revised model are within 3% of the capacity and 28% of the displacement at peak strength of experimental Frame 2, and closer than the prediction of the initial model of Frame 2.

The force-displacement plots for the initial and revised models as well as the experiments are shown in Figures 166 and 167. It is clear that the initial and revised force displacement curves for the models are almost indistinguishable. The revised models have a slightly more defined peak and degrade slightly more than the initial models. Additionally, the revised models are slightly more brittle because of the reduced fracture energy in the concrete which causes the sudden drop in capacity when a large shear crack forms in the frame with connections only at the base.

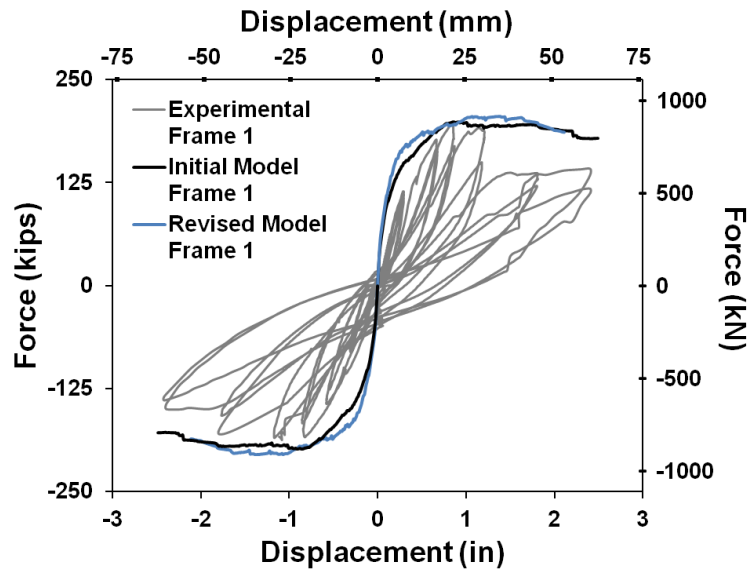


Figure 166: Force-displacement plot of the experimental and analytical Frame 1 (full connection)

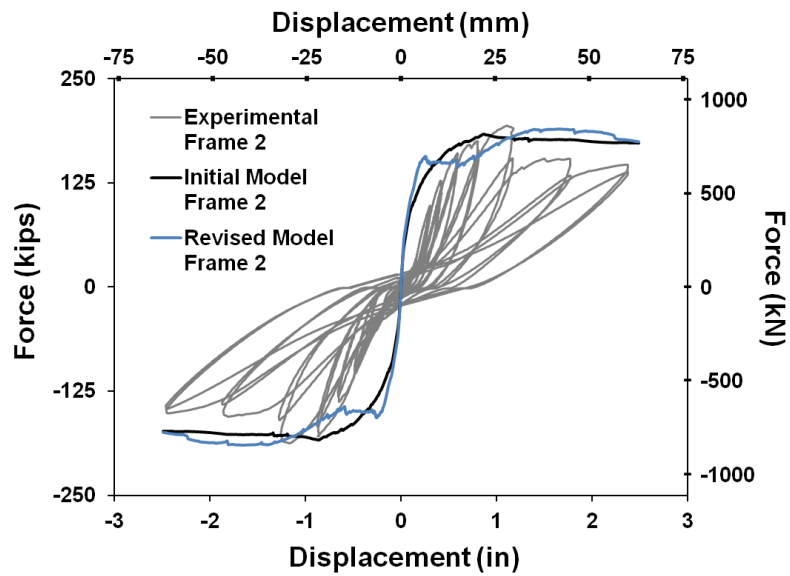


Figure 167: Force-displacement plot of the experimental and analytical Frame 2 (connection only at the base)

If the only goal of the finite element models were to predict the capacity of reinforced concrete-masonry hybrid frames, it may be more desirable to use the simpler modeling methodology from the initial models because the initial models are more

numerically stable than the revised models with the overlay elements. However, since the models are used for parametric studies to characterize how design changes to the masonry detailing effect the behavior of the frame, the model which most accurately captures the damage patterns is desired. Thus, the revised models are used for the remainder of this work even though they are more complex than the initial models.

6.4.3 Yielding of Reinforcement

The strain in the reinforcement of the revised models is shown in Figures 168 and 169. The displacement at first yield of the column bars is very similar to the initial models, but the yielding correctly initiates just above course two rather than at the base of the columns. This effect is more pronounced in the model of Frame 1 than in Frame 2. Additionally, the yielding of the bars in the masonry walls of both revised models is slightly delayed compared to the initial models, starting at 0.75 inches (19.1 mm) instead of 0.5 inches (12.7 mm). There is less yielding in the masonry reinforcement in Frame 2 than that in Frame 1. This is consistent with the experimental observations that the fully connected infill wall of Frame 1 had greater shear strains than the infill wall in Frame 2.

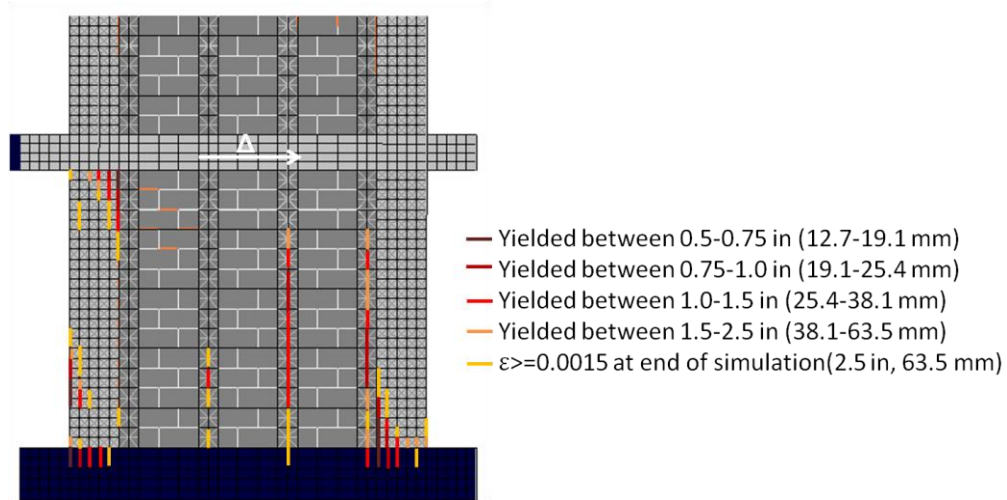


Figure 168: Strains in the reinforcement of the revised finite element model of Frame 1 (full connection)

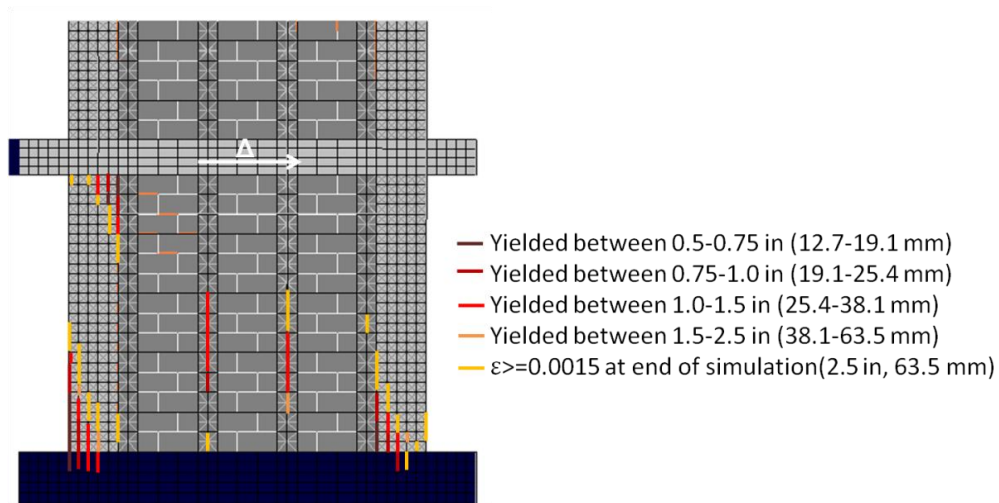


Figure 169: Strains in reinforcement of the revised finite element model of Frame 2 (connection only at the base)

6.5 Chapter Summary

The experimental program consisted of two Caribbean-style hybrid concrete-masonry structures, one which had cast-in-place connections on all edges of the partially grouted infill wall, and one which had connections only at the base. Both frames failed at

similar loads and drift levels, exhibiting a compression strut mechanism and combined flexural and shear cracking in the columns of the bounding frame.

Cast-in-place connections at the base of the masonry wall were present in both frames and permitted shear transfer into the foundation. The dowel connections at the base of both masonry walls also significantly stiffened the courses of masonry through the height of the dowels and shifted the hinging of the columns up to the location at which the dowels were terminated.

Connections from the reinforced concrete beam to the top of the masonry infill wall were crucial to preventing out-of-plane failure of the masonry in Frame 1. During the cyclic test of Frame 2, which did not have these connections, the masonry shifted out of plane several inches and would have likely fallen out in a dynamic test. It is also likely that the connection at the top of the masonry wall to the reinforced concrete beam provided some additional shear transfer as the shear cracking at the top of the columns in the frame with connections was not as severe as the frame without connections. The primary bearing zone for the masonry compression strut for both frames was at the top of the columns rather than shared between the column and beam. This was because the bond between the top course of masonry and the reinforced concrete beam was very weak.

Connections from the reinforced concrete columns into the bed joints of the masonry had little to no influence in delaying the cracking of the interfaces between the masonry wall and the reinforced concrete columns. However, interface cracking was delayed in the stiffened zones within the height of the vertical dowel connections. Delayed interface cracking was observed at the bottom two courses of both walls and the

top two courses of the wall with connections around the entire perimeter of the infill wall (Frame 1).

The results suggest that partially grouting and reinforcing weak masonry infill and providing connections at the top and bottom of the wall may minimize out-of-plane failure of the masonry and alter the strut mechanism typically observed in RC frames with unreinforced infill. The shear critical zone in the RC columns appears to be larger than what is expected in a seismically designed moment frame.

The finite element models used to predict the behavior of the hybrid concrete-masonry frames gave very close predictions for peak strength and the displacement at peak strength, which were within 10% of the experimental capacity and 21% of the displacement values for both frames. The progression of failure closely matched the experiments for both models, but damage generally occurred earlier in the finite element models than the experiments, and the hinging zone was predicted to be at the base of the columns rather than just above the height of the dowel bars from the foundation. The timing of damage was nearly identical between the two models and very close to the timing of damage in experimental Frame 2, which had connections only at the base of the infill.

The underestimation of the dowel connections' effect was determined to be the underlying cause of the deficiencies in the initial model. The finite element models were revised to account for the increased stiffness in the masonry in the localized cells with cast-in-place dowel connections. The grouted cells were also modeled as two separate layers, one for the face shells and one for the grout. This was done to permit the face shells to crack while the grouted cores remained intact, consistent with experimental

observations. The ungrouted cells were modeled with an 8-element module to better capture the shear cracking observed in the experiments. The top interface between the masonry wall and the RC beam was also modeled with increased flexibility and lower tensile strength to better represent the poor bond at the top of the infill wall. Finally, fracture energy of the concrete was slightly reduced to lower the residual strength of the models. A better match to the cracking patterns in the masonry walls, the cracking order of the interfaces and the location of yielding in the reinforcement was achieved with the revised models.

CHAPTER 7

APPLICATIONS FOR ENGINEERING PRACTICE

A high degree of confidence can be placed in the finite element models because they exhibited a close match to the cracking patterns and capacities of the experimental frames. The finite element models are used to conduct several analytical studies to obtain information which will be useful to practicing engineers. In addition, the results of the finite element models are compared to several proposed simplified models which may be more practical for design purposes.

First, the finite element model is used to explore several changes to the design of hybrid concrete-masonry structures. This includes different types of connections which were observed in the Caribbean, but not tested experimentally, and proposed improvements based on observations from the experiments. Second, a parametric study is conducted to characterize the influence of the infill properties on the seismic performance of hybrid concrete-masonry frames. The study includes the influence of masonry material properties and the influence of reinforcement details. Finally, several simplified models are presented and compared to the results of the finite element models. An elastic transformed section model is used to predict the cracking load and a cracked section model is used to predict the ultimate shear capacity of the experimental frames. A modification of the typical TMS 402 strut model is also suggested to account for the effect of the dowel connections on the geometry and behavior of the masonry diagonal strut in hybrid concrete-masonry structures.

7.1 Analytical Study on Design Changes

Alternative methods to connect the partially grouted infill wall to the bounding reinforced concrete frame are explored with analytical models. Two new models were created with the same material properties and geometry as the models of experimental Frames 1 and 2, but each has an alternative method to connect the infill to the bounding frame. One model has no connections to the bounding RC frame and one wall has only vertical connections from the infill to the foundation and the RC beam.

Next, an analytical study on a possible improvement in the design of the reinforced concrete frame is presented. Observations from the experiments led to the suggestion to increase the length of the zone of closely spaced ties in the RC columns in order to improve the seismic performance of the hybrid concrete-masonry wall. Two additional models were created from the validated finite element models of Frame 1 and Frame 2 by increasing the region of the closely spaced ties in the RC columns of each model. The size of the close tie spacing region was selected so that it bounds the region in which shear cracks were observed in the test specimens. The results of these models are compared to the results from the finite element models of the experimental frames to determine if the suggested change improves the seismic performance.

7.1.1 Alternative Connections of the Infill to the RC frame

To assess the behavior of hybrid concrete masonry frames with alternative connections to the bounding frame, two additional finite element models were created. Each model utilized the same geometry and material properties as the experimentally validated finite element models, but one had no connections to the RC frame and the other had connections from the infill to the foundation and to the RC beam but not to the

columns. The results of the models are compared to the experimentally validated finite element models in Figure 170.

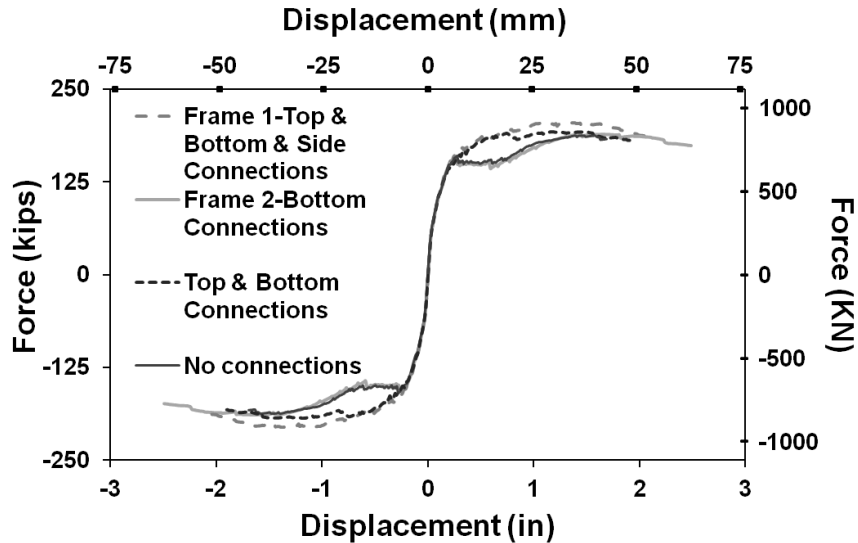


Figure 170: Force vs. displacement of the finite element models with different connections of the infill to the bounding RC frame

The results show that the model with no connections from the infill to the RC frame behaves nearly the same as the model with connections only at the base. The peak strength of the model with no connections is 185.86 kips (286.75 kN), which is only 1.7% less than the model with connections at the base. The displacement at peak strength is also almost identical between the two models, 1.4 inches (35.6 mm) and 1.41 inches (35.8 mm) for the model with no connections and the model with connections at the base, respectively (1.167% and 1.175% drift, respectively).

The study also shows that very little gain in peak strength is observed from the connections to the RC columns. The model with connections on all edges has greater peak strength than the model with connections at the top and bottom of the infill, but achieves peak strength at a lower displacement. For the model with connections on all

edges of the infill wall, the peak strength is 205.15 kips (912.55 kN) and occurs at 1.07 inches (27.2 mm) of displacement (0.892% drift). The model with connections at the top and bottom of the infill has a peak strength of 193.14 kips (859.13 kN) at 1.18 inches (30.0 mm) of displacement (0.983% drift). No significant changes in cracking patterns were observed in these models.

7.1.2 Suggested Changes Based on Experimental Observations

Both experimental Frames 1 and 2 exhibited shear cracking in the columns beyond the length of the close tie spacing zone required for seismically detailed moment frames. Increasing the shear critical zone, so that the close tie spacing bounds the zone in which shear cracks were observed experimentally, may improve the ductility of the hybrid concrete-masonry frames. Two additional models were made by increasing the span of the shear critical zone with 4 inch (10.16 cm) tie spacing from 20 inches (50.80 cm) to 40 inches (101.60 cm) in the Frame 1 and Frame 2 models.

Increasing the length of the close tie spacing zone in Frame 1 from 20 inches (50.80 mm) to 40 inches (101.60 cm) is predicted to increase the displacement at peak strength from 1.07 inches (27.18 mm) to 1.47 inches (37.34 mm). This is a 37.4% increase over the original Frame 1 model. Little change is observed in the peak strength of the Frame 1 model by increasing the length of the shear critical zone. The peak strength is 205.64 kips (914.73 kN), 0.24% greater than the original Frame 1 model. The force-displacement curve for both models is shown in Figure 171. The cracking patterns of both models are nearly the same.

For Frame 2, which only had connections at the base of the masonry infill, increasing the length of the shear critical zone is predicted to make very little difference

in the peak strength or the displacement at peak strength. The model with the increased length of the column close-tie spacing zone has a peak strength of 192.31 kips (855.44 kN), which is 3.47% greater than the original Frame 2 model. The model with the increased length of the column close-tie spacing zone has a displacement at peak strength of 1.37 inches (34.80 mm), which is only 2.84 % less than the displacement at peak strength of 1.41 inches (35.81 mm) predicted in the original Frame 2 model. The force-displacement curve for both models is shown in Figure 171. The cracking patterns between the two models are also virtually identical.

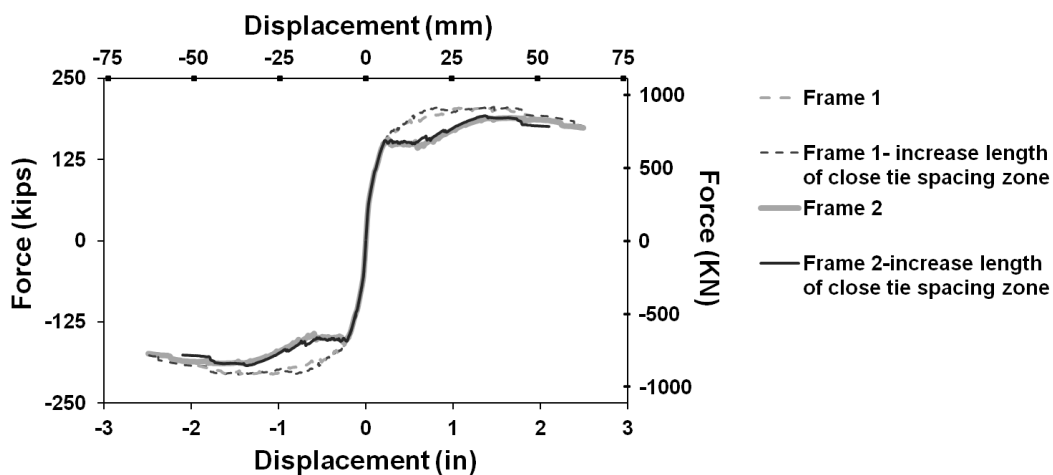


Figure 171: Influence of increasing the length of the column close tie spacing zone from 20 inches (50.8 cm) to 40 inches (101.6 cm) on the force-displacement behavior of Frames 1 and 2

7.2 Parametric Study on Infill Properties

An analytical study is presented which characterizes the sensitivity of the peak strength and displacement at peak strength of the hybrid concrete masonry walls to changes in the reinforcement detailing and properties of the masonry infill. The initial stiffness of the models are not compared, since the validated finite element models were

unable to capture the difference in initial stiffness between experimental Frames 1 and 2. If these changes significantly alter the general behavior of the frames, the cracking patterns and new failure mechanisms are also discussed.

7.2.1 Reinforcement Sizes and Spacing

In order to characterize the influence of changes to the detailing of the masonry infill on the seismic performance of hybrid concrete-masonry walls, a small parametric study was conducted. The parametric study was conducted with the revised models of Frame 1 and Frame 2 by varying each of the model parameters to a value above and below its initial value.

7.2.1.1 Methodology

The effect of changing the area of the reinforcing bars was examined first. Four models were made by first increasing the area of the vertical reinforcement in each model by a factor of two, then decreasing the area of the vertical reinforcement by a factor of two in the Frame 1 and Frame 2 models. Four more models were also created by varying the area of the horizontal reinforcement by a factor of two in each model. Yet four more models were made by increasing then decreasing the area of the vertical dowel reinforcement by a factor of two in the Frame 1 and Frame 2 models. Only Frame 1 had horizontal dowel reinforcement, so only two models were created by varying the area of the horizontal dowel reinforcement by a factor of two.

Next, the spacing of the vertical and horizontal reinforcement was varied from their initial spacing of 32 inches (81.28 cm) and 24 inches (60.96 cm) on center, respectively. The vertical reinforcement spacing was decreased to 16 inches (40.64 cm) on center and increased to 48 inches (121.92 cm) on center in the revised models of

Frame 1 and Frame 2, making four new models. Four more models were created by decreasing the horizontal reinforcement spacing to 16 inches (40.64 cm) on center then increasing the spacing to 40 inches (101.6 cm) on center in both models.

7.2.1.2 Results

The peak strength of the models was not significantly influenced by the variation in the masonry reinforcement detailing. This can be seen from the histogram in Figure 172. A consistent trend could not be found for many of the cases which were tested. However, an increase in the area of the vertical reinforcing bars resulted in an increase in peak strength for both Frame 1 and 2. Likewise, a decrease in the area of the vertical or horizontal reinforcing bars resulted in a decrease in peak strength for both frames. Most of the models have a peak strength which was within 6% of the baseline models. The exception is that for the model of Frame 1, which has connections on all edges of the infill, decreasing the spacing of the vertical reinforcement to 16 inches (40.64 cm) on center resulted in a 9.4% increase in capacity. Likewise, increasing the spacing of the vertical reinforcement to 48 inches (121.92 cm) on center resulted in a 9.8% decrease in capacity.

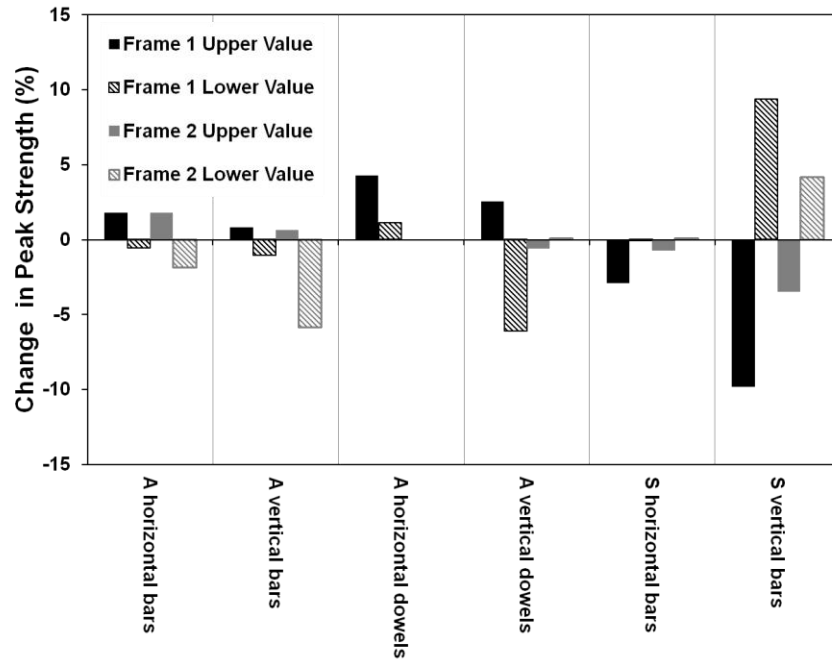


Figure 172: Percent change in peak strength for changes in masonry infill reinforcement detailing

Very few conclusions can be drawn about the influence of the masonry reinforcement on the displacement at peak strength of the hybrid concrete-masonry frames. The revised models of Frames 1 and 2 maintained a capacity very close to their peak capacities up to 0.5 inches (12.7 mm) after their peak capacity was achieved. None of the models with modified reinforcement details had a displacement at their peak capacity which was outside this bound.

The spacing of the vertical reinforcement and the area of the vertical dowel bars had a significant effect on the displacement at peak strength of the models (See Figure 173). Decreasing the spacing of the vertical reinforcement from 32 inches (81.28 cm) on center to 16 inches (40.64 cm) on center resulted in the peak strength occurring 19.6% earlier in Frame 1 and 3.7% earlier in Frame 2. Increasing the spacing of the vertical reinforcement from 32 inches (81.28 cm) on center to 48 inches (121.92 cm) on center,

resulted in an increase in the displacement at peak strength by 17% in Frame 1 and a decrease in the displacement at peak strength of 15.7% in Frame 2. Changing the area of the vertical dowel reinforcing bars had a greater influence on Frame 1 than Frame 2. Decreasing the area of the vertical dowel reinforcement resulted in a reduced displacement at peak strength for both models, but had a greater influence on Frame 1 than Frame 2.

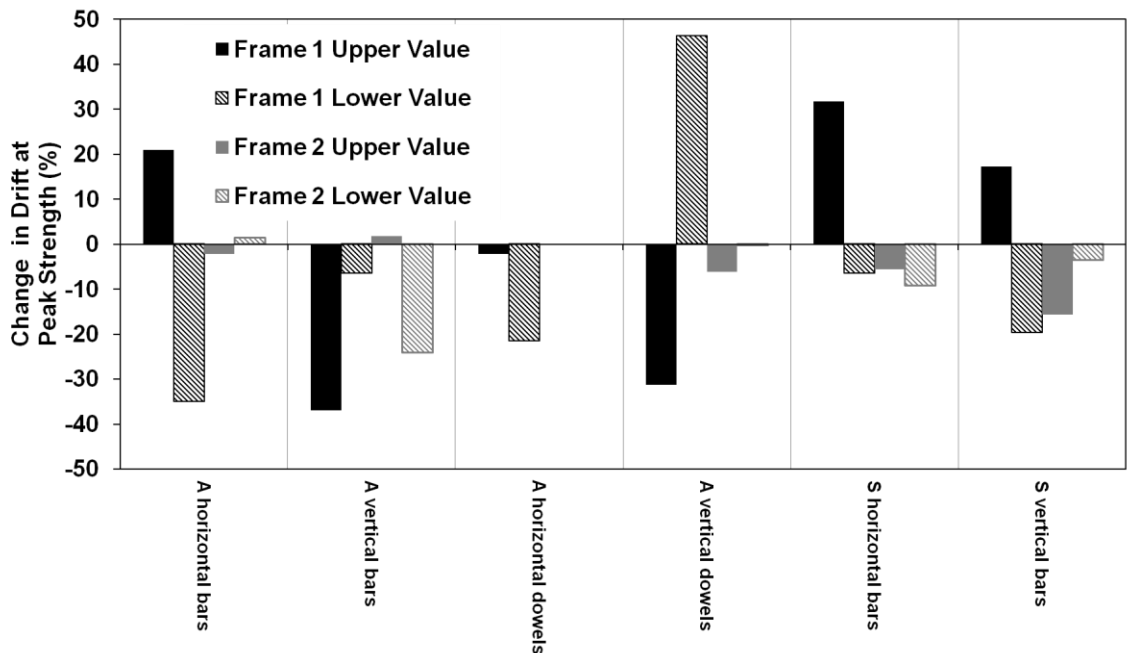


Figure 173: Percent change in displacement at peak strength for changes in masonry infill reinforcement detailing

7.2.2 Masonry Material Properties

The influence of the masonry material properties on the seismic performance of the hybrid concrete-masonry frames was also examined. Unlike the study on the reinforcement sizes and spacing, each parameter examined does not necessarily have a

higher and a lower value. The specific changes made to each model are presented in the methodology.

7.2.2.1 Methodology

The first property which was examined was the influence of the prism strength of the ungrouted masonry on the seismic behavior of the frames. The prism strength of the ungrouted masonry was increased by a factor of two. The elastic modulus, strain at peak compressive strength, strain at the transition zone, tensile strength and fracture energy were also changed in a manner consistent with the calibration method discussed in Chapter 2. The prism strength of the ungrouted masonry was decreased below that measured in the experiment because the masonry was already very weak.

Next, the influence of the compressive strength of the grout was examined. The compressive strength of the grout was increased and decreased by a factor of two in the models of Frame 1 and Frame 2. The elastic modulus, strain at peak compressive strength and strain at the transition zone were changed to keep within the range of expected values for grout. The tensile strength was kept equal to 10% of the compressive strength and the fracture energy in the model was assumed to increase proportionally to the tensile strength.

Then, two models were created by replacing the type M mortar, which is common in the Caribbean and used in Frames 1 and 2, with a type N mortar. Type N mortar contains lime and has better bond characteristics than the type M mortar used in the experimental frames. The mortar interface elements were calibrated to data from Stavridis 2007. Tables containing the material properties used in each of these models are presented in Appendix C.

Finally, the cells in the infill walls which were initially hollow were grouted. The grout strength and stress vs. strain behavior was kept the same as the baseline models and the experimental frames.

7.2.2.2 Results

Increasing the prism strength of the ungrouted masonry resulted in an increase in peak strength of about 25% for both frames (See Figure 174). Increasing the ungrouted prism strength also increased the displacement at peak strength by 67% for Frame 1, which had connections on all edges of the infill, and 9% for Frame 2, which had connections only at the base (See Figure 175). Compared to the experimentally validated finite element models, the crushing of the masonry in the models with increased ungrouted prism strength was greatly delayed. The cracking in the columns initiated a little earlier and more flexural cracks occurred than in the experimentally validated models. Table 9 shows the difference in cracking patterns of the Frame 1 model when the strength of the ungrouted prism was increased. Table 10 shows the same data for Frame 2.

Table 9: Influence of ungrouted prism strength on the damage sequence for Frame 1 (full connection)

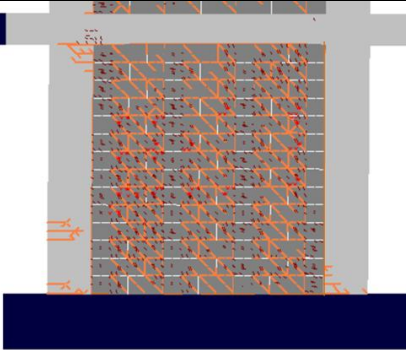
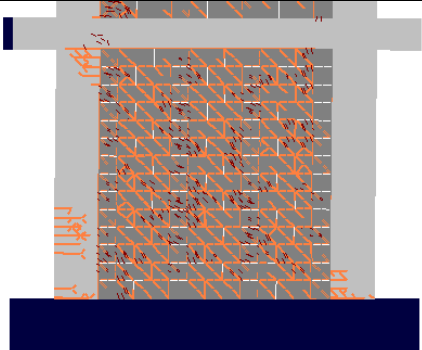
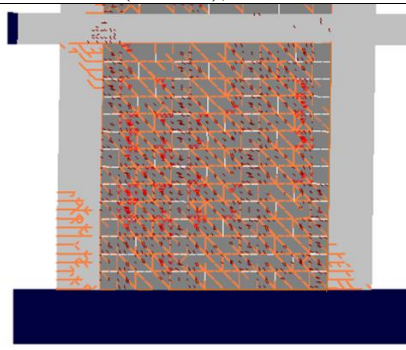
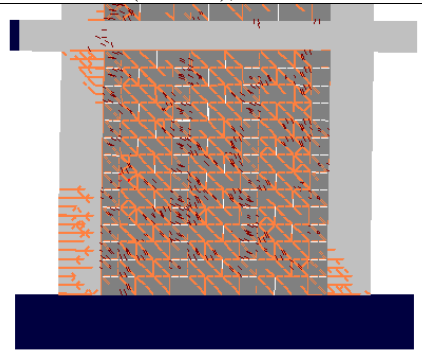
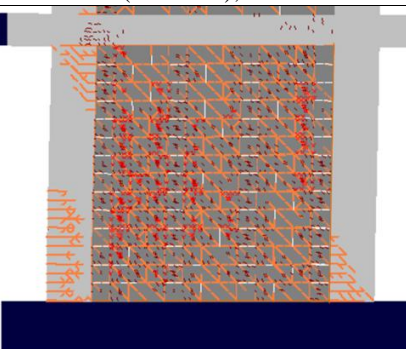
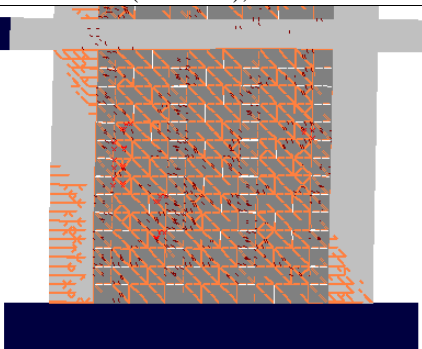
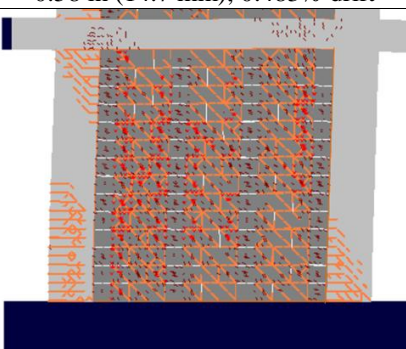
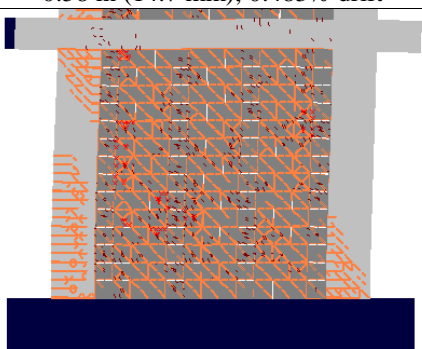
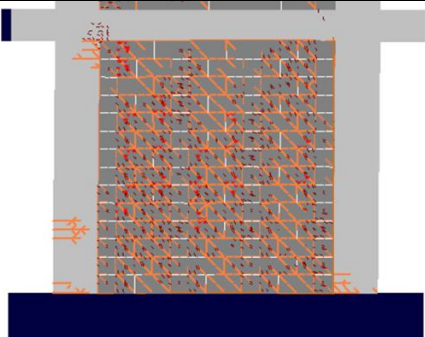
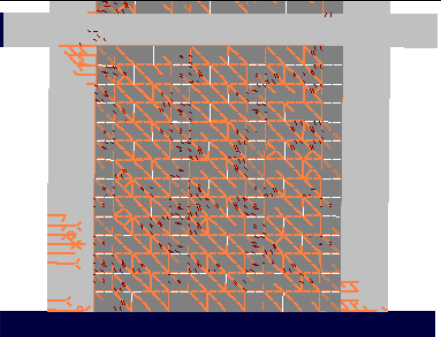
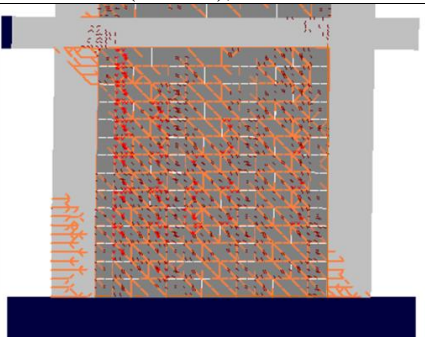
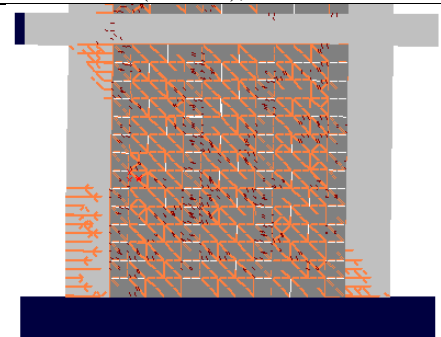
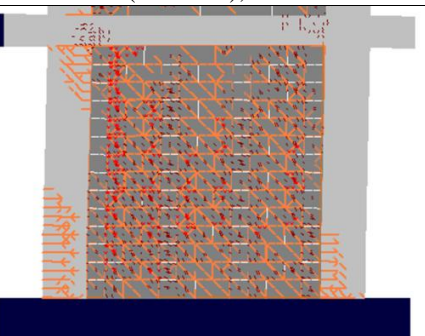
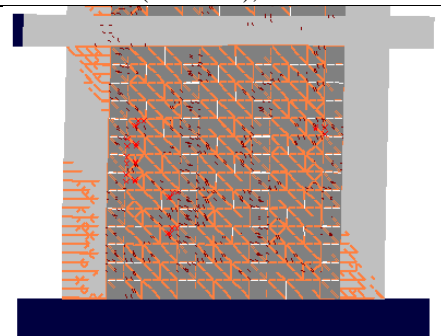
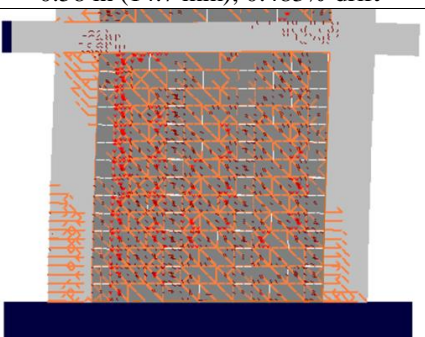
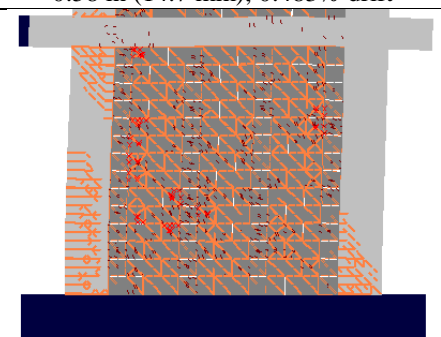
FE Model 1 (baseline)	FE Model 1 (increased ungrouted prism strength)
 <p data-bbox="418 682 724 709">0.3 in (7.6 mm), 0.25% drift</p>	 <p data-bbox="964 682 1269 709">0.3 in (7.6 mm), 0.25% drift</p>
 <p data-bbox="407 1066 735 1094">0.42 in (10.7 mm), 0.35% drift</p>	 <p data-bbox="954 1066 1282 1094">0.42 in (10.7 mm), 0.35% drift</p>
 <p data-bbox="399 1451 743 1478">0.58 in (14.7 mm), 0.483% drift</p>	 <p data-bbox="948 1451 1292 1478">0.58 in (14.7 mm), 0.483% drift</p>
 <p data-bbox="399 1833 743 1860">0.82 in (20.8 mm), 0.683% drift</p>	 <p data-bbox="948 1833 1292 1860">0.82 in (20.8 mm), 0.683% drift</p>

Table 10: Influence of ungrouted prism strength on the damage sequence for Frame 2 (connection only at the base)

FE Model 2 (baseline)	FE Model 2 (increased ungrouted prism strength)
 <p data-bbox="418 682 734 709">0.3 in (7.6 mm), 0.25% drift</p>	 <p data-bbox="971 682 1286 709">0.3 in (7.6 mm), 0.25% drift</p>
 <p data-bbox="418 1064 734 1092">0.42 in (10.7 mm), 0.35% drift</p>	 <p data-bbox="971 1064 1286 1092">0.42 in (10.7 mm), 0.35% drift</p>
 <p data-bbox="418 1446 734 1474">0.58 in (14.7 mm), 0.483% drift</p>	 <p data-bbox="971 1446 1286 1474">0.58 in (14.7 mm), 0.483% drift</p>
 <p data-bbox="418 1829 734 1856">0.82 in (20.8 mm), 0.683% drift</p>	 <p data-bbox="971 1829 1286 1856">0.82 in (20.8 mm), 0.683% drift</p>

Increasing and decreasing the strength of the grout had little effect on the peak strength of Frame 1 or 2 (See Figure 174). The displacement at peak strength for Frame 1, which had connections on all edges of the infill, was increased 38% by doubling the compressive strength of the grout. Reducing the grout compressive strength by one-half resulted in a reduction of the displacement at peak strength of 35% for Frame 1 (See Figure 175). The displacement at peak strength of Frame 2 was hardly influenced by increasing or decreasing the grout compressive strength (<7.5% change). The cracking patterns of the models with different grout strengths were nearly the same as the experimentally validated finite element models.

Changing the mortar in the models from a type M mortar to a type N mortar changed the peak strength by less than 2.5% in either frame (See Figure 174). The displacement at peak strength was greatly increased for Frame 1, increasing 66.8% (See Figure 175). The displacement at peak strength of Frame 2 increased by only 8.6% (See Figure 175). Changing the mortar from a type M to a type N delayed the initial cracking of the masonry for both frames. Ultimately, the delay in initial damage did not significantly influence the behavior of the frames later in the simulation.

Fully grouting the wall lead to a significant increase in peak strength of both models. The capacity of Frame 1 increased by 57.7% and the capacity of Frame 2 increased by 60.8% (See Figure 174). Fully grouting the wall decreased the displacement at peak strength of Frame 1 by 35.5% and decreased the displacement at peak strength of Frame 2 by 33.6% (See Figure 174). Compared to the baseline models, the cracking of the frame occurred much earlier and the column cracking was much more extensive. The infill exhibited very little crushing compared to the baseline models. These trends can be

seen from Tables 11 and 12. However, the increased stiffness of the infill walls did not lead to a brittle failure of the frames. The columns in the models with fully grouted infills still exhibited combined flexural and shear cracking.

(space left blank intentionally)

Table 11: Influence of fully grouting infill wall on the damage sequence for Frame 1 (full connection)

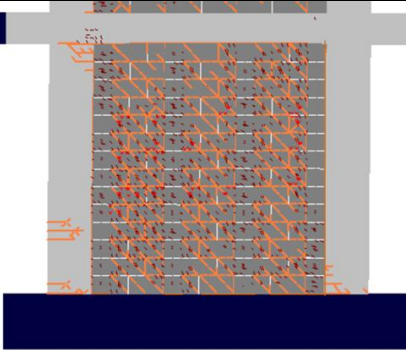
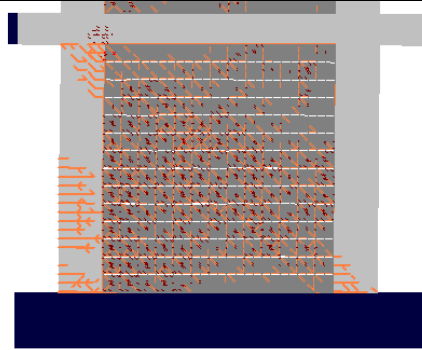
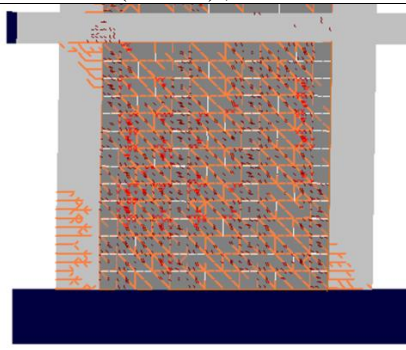
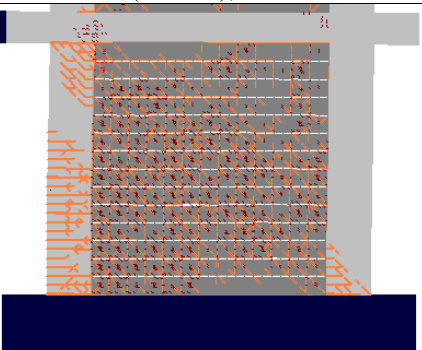
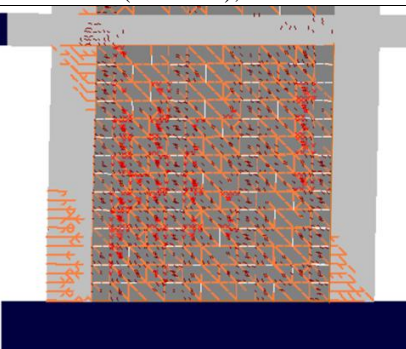
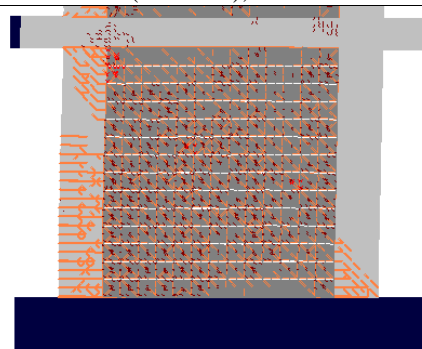
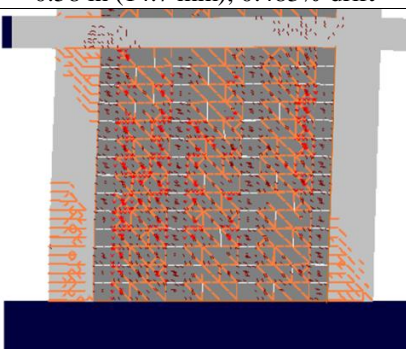
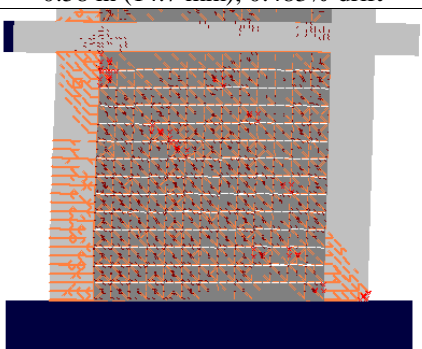
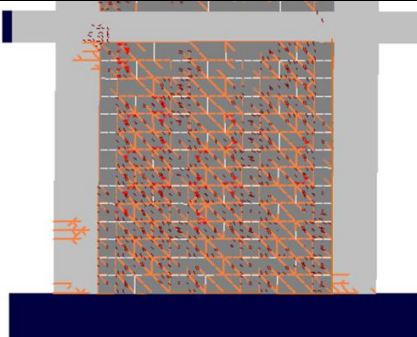
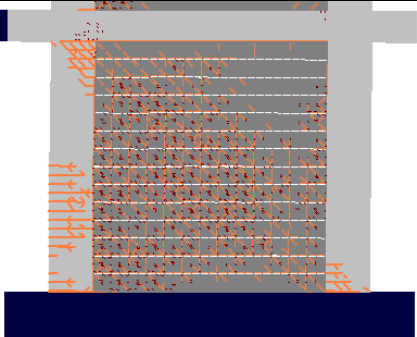
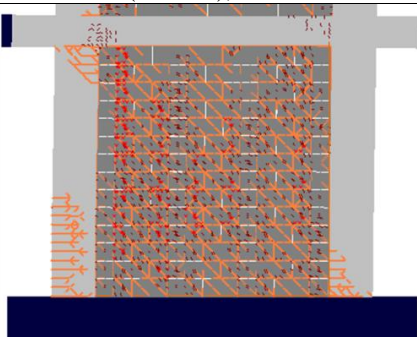
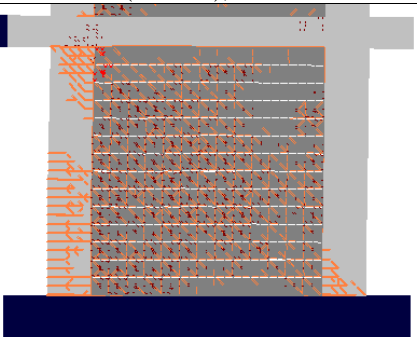
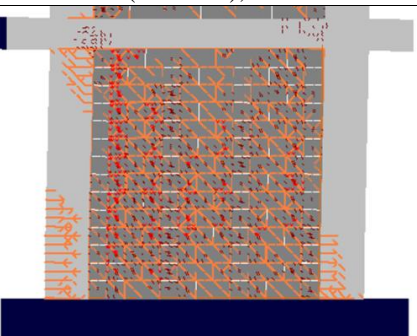
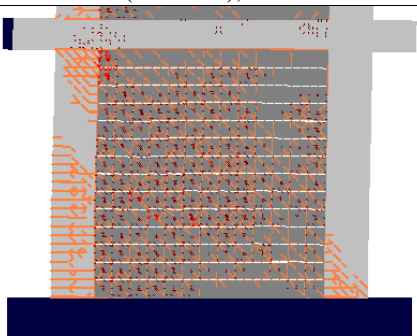
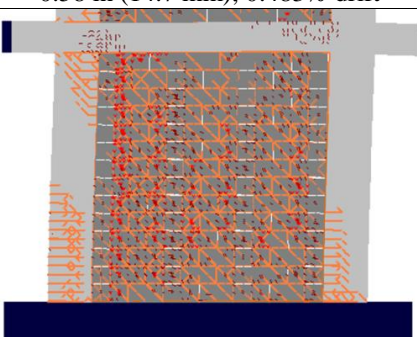
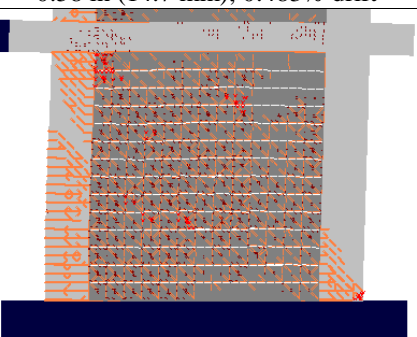
FE Model 1 (baseline)	FE Model 1 (fully grouted infill wall)
 <p data-bbox="418 682 724 709">0.3 in (7.6 mm), 0.25% drift</p>	 <p data-bbox="964 682 1269 709">0.3 in (7.6 mm), 0.25% drift</p>
 <p data-bbox="407 1066 735 1094">0.42 in (10.7 mm), 0.35% drift</p>	 <p data-bbox="954 1066 1282 1094">0.42 in (10.7 mm), 0.35% drift</p>
 <p data-bbox="402 1451 743 1478">0.58 in (14.7 mm), 0.483% drift</p>	 <p data-bbox="950 1451 1291 1478">0.58 in (14.7 mm), 0.483% drift</p>
 <p data-bbox="402 1833 743 1860">0.82 in (20.8 mm), 0.683% drift</p>	 <p data-bbox="950 1833 1291 1860">0.82 in (20.8 mm), 0.683% drift</p>

Table 12: Influence of fully grouting infill wall on the damage sequence for Frame 2 (connection only at the base)

FE Model 2 (baseline)	FE Model 2 (increased ungrouted prism strength)
 <p data-bbox="418 682 722 709">0.3 in (7.6 mm), 0.25% drift</p>	 <p data-bbox="971 682 1274 709">0.3 in (7.6 mm), 0.25% drift</p>
 <p data-bbox="406 1064 747 1092">0.42 in (10.7 mm), 0.35% drift</p>	 <p data-bbox="950 1064 1291 1092">0.42 in (10.7 mm), 0.35% drift</p>
 <p data-bbox="397 1446 738 1474">0.58 in (14.7 mm), 0.483% drift</p>	 <p data-bbox="950 1446 1291 1474">0.58 in (14.7 mm), 0.483% drift</p>
 <p data-bbox="397 1829 738 1856">0.82 in (20.8 mm), 0.683% drift</p>	 <p data-bbox="950 1829 1291 1856">0.82 in (20.8 mm), 0.683% drift</p>

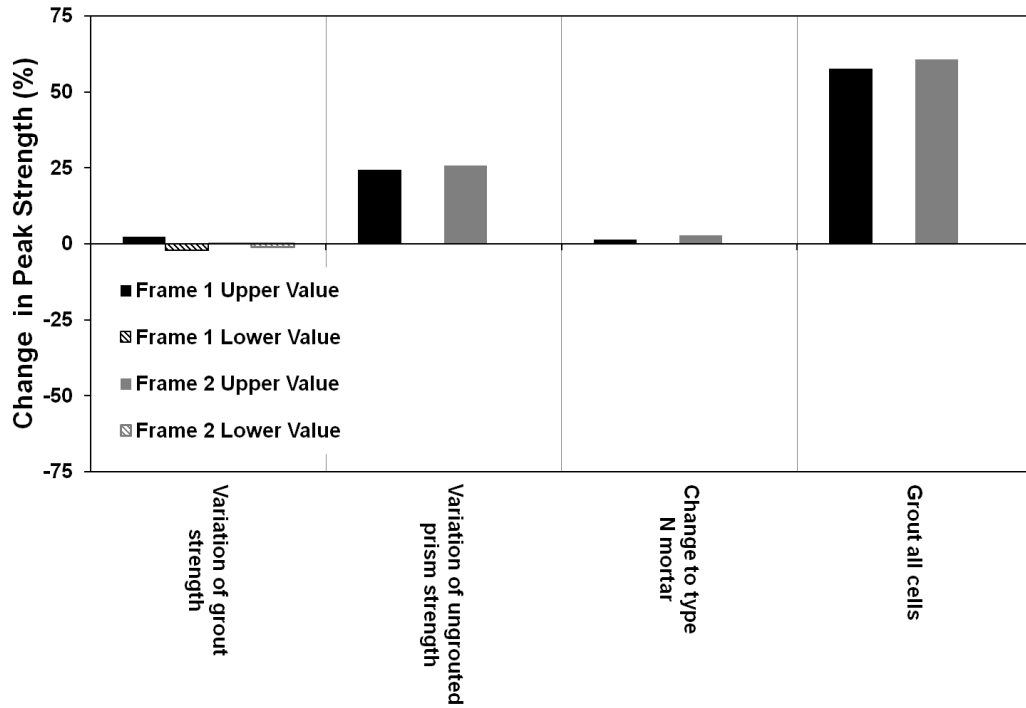


Figure 174: Percent change in peak strength for changes in masonry infill properties

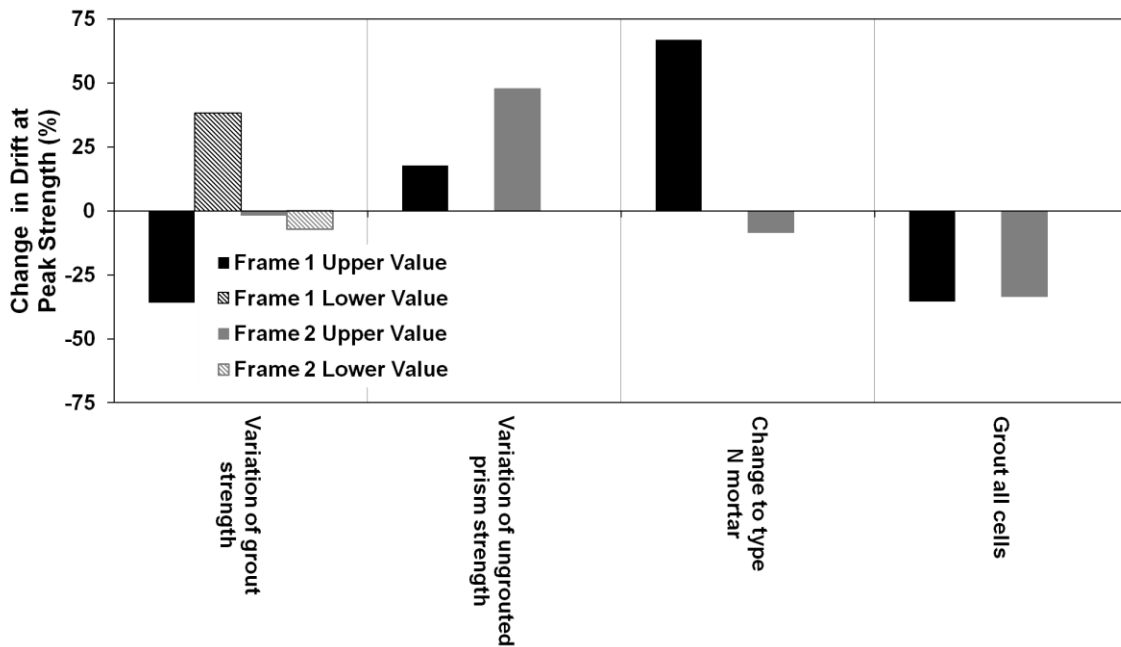


Figure 175: Percent change in displacement at peak strength for changes in masonry infill properties

7.2.3 Discussion

It is evident that most of the infill properties do not greatly influence the peak strength of the hybrid concrete masonry frames. However, increasing the ungrouted prism strength by a factor of two resulted in a 25% gain in strength for both frames, and fully grouting the infill wall resulted in an increase in strength of 57.7% for Frame 1 and 60.75% for Frame 2. Changing the spacing of the vertical reinforcement also had a noticeable effect on Frame 1, but not on Frame 2. Reducing the spacing of the vertical reinforcement from 32 inches (81.28 cm) to 16 inches (40.64 cm) increased the peak strength of Frame 1 by almost 10%, and increasing the spacing to 48 inches (121.92 cm) reduced the strength of Frame 1 by nearly 10%.

Most of the infill properties did not consistently influence the displacement at peak strength of the models. However, increasing the ungrouted prism strength and fully grouting the infill wall consistently changed the displacement at peak strength for both models. Doubling the ungrouted prism strength led to an increase in displacement at peak strength of 67% for Frame 1 and 9% for Frame 2. The displacement of Frames 1 and 2 were affected by the spacing of the vertical reinforcement which led to a variation of up to 20% in the displacement at peak strength. However, increasing the vertical reinforcement spacing led to an increase in displacement at peak strength for Frame 1 and a decrease in displacement at peak strength for Frame 2. Frame 1, which had connections on all edges of the infill, was also influenced by the area of the vertical dowel reinforcement, the grout strength, and changing the mortar to a type N. These changes had minimal influence on the displacement at peak strength for Frame 2.

These results are useful to determine which individual parameters most influence the seismic behavior of the concrete masonry frames. This study could be expanded to look at the effect of coupling several of the changes examined in this study and determine if coupling results in different behavior than varying the individual parameters.

7.3 Simplified Models

7.3.1 Elastic Transformed Section Model

In order to predict the cracking load for hybrid concrete-masonry walls, an elastic transformed section model was proposed.

First, the boundary columns are transformed into an equivalent area of masonry. The grout within the cores having reinforcement is neglected, such that the entire infill wall is taken as the same thickness (See Figure 176). Then, the shear stress in the section is defined by Equation 22, where V is the applied shear force, I_{trans} is the moment of inertia of the transformed section, Q is the static moment of inertia of the section considered, and t is the thickness through that section.

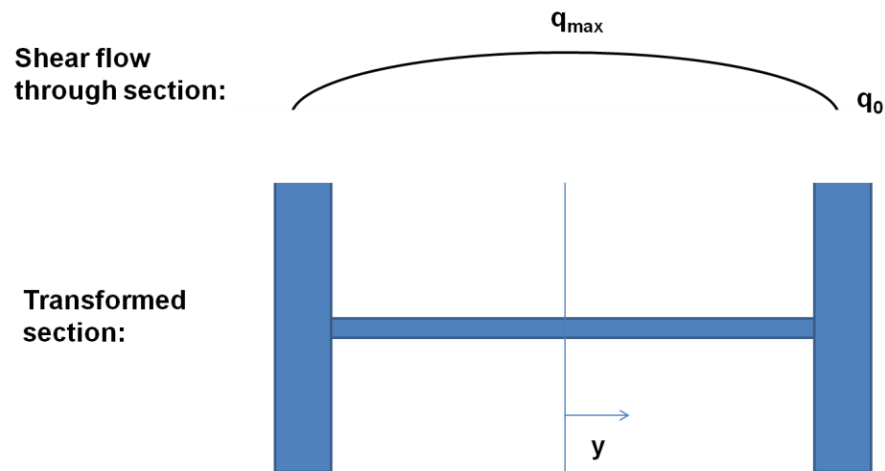


Figure 176: Schematic of the transformed section and shear flow for the test frames

$$\tau = \frac{VQ}{I_{trans}t} \quad (22)$$

Taking maximum shear flow to be at the center of the wall, the cracking load $V_{cracking}$ can be solved for by Equation 23. The normal shear stress in the masonry, f_{vn} , is taken as the allowable in-plane shear stress for unreinforced masonry from TMS 402-13 Section 3.2.4. The net area, A_n , is the transformed section area and N_v is the dead load.

$$V_{cracking} = \frac{f_{vn}I_{trans}t}{Q} \quad (23)$$

$$f_{vn} = \min\left(3.8\sqrt{f'_m}, 300\text{psi}(2068\text{ kPa}), 56\text{psi}(386\text{ kPa}) + 0.45\frac{N_v}{A_n}\right) \quad (24)$$

This calculation was carried out for the experimental frames and is given in Appendix E. The cracking load predicted by the transformed section model was 22.27 kips (99.06 kN). The cracking load prediction was the same for both Frame 1 and Frame 2 because this method does not account for the influence of different connection types. The cracking load predicted by the elastic transformed section method was lower than the cracking load the finite element models predicted. The Frame 1 finite element model, which had dowel connections on all edges of the infill, predicted cracking of the infill to occur at 37.30 kips (165.92 kN) of lateral load. The Frame 2 finite element model, which had dowel connections only at the base of the infill, predicted the cracking load to be 33.06 kips (147.06 kN). In the experiments, the infill of Frame 1 first cracked at 103.6 kips (460.8 kN) of lateral load and the infill of Frame 2 cracked at 30.8 kips (137.0 kN) of lateral load.

7.3.2 Cracked Section Model

Although the experiments showed that the hybrid concrete-masonry frames failed from combined shear and flexural forces, it is useful to explore if the shear strength of a simple cracked section model would yield adequate predictions for capacity.

The model is constructed by first transforming the columns to an equivalent width of masonry, as was done for the elastic transformed section model. Then, the shear capacity of the system is calculated by Equation 25. In Equation 25, d is the distance from the edge of the frame to the centroid of the reinforcement in the opposite column (See Figure 177). The nominal shear strength of the masonry is given by Equation 24. The variable b could either be taken as the minimum thickness of the transformed section, 2.5 inches (63.5 mm), or the average thickness, 18.14 inches (46.07 cm).

$$V_{ultimate} = f_{vn}bd \quad (25)$$

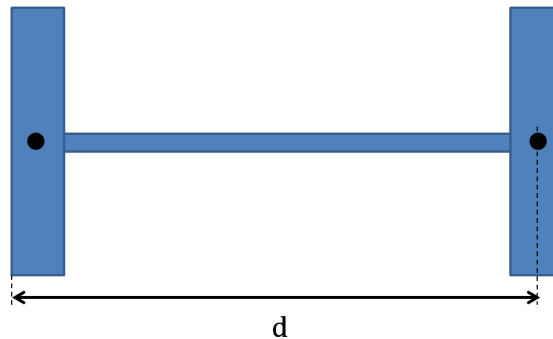


Figure 177: Schematic of cracked section model

This calculation was carried out for the experimental frames and is given in Appendix E. Taking b equal to the minimum thickness of the transformed section resulted in a predicted ultimate strength of 25.22 kips (112.18 kN) which is well below the capacity of either experimental frame. If b was taken as the average thickness of the transformed section, the predicted shear capacity was 182.95 kips (813.8 kN) which is

7.2% less than the capacity of Frame 1 and 3.2% less than the capacity of Frame 2. The cracked section model may be an appropriate model for predicting the peak capacity of hybrid concrete-masonry structures provided b is taken as the average thickness of the transformed section.

7.3.3 Modification of TMS 402 Strut Model for Infills with Connections

A modification to the TMS 402 strut procedure for partially grouted reinforced infill with cast-in-place connections was proposed in order to capture the mechanisms observed during the experiments.

To construct the model, the bottom node of the compression strut is assumed to be attached to the column at the mid height of the dowel splice at the base of the masonry wall. The strut is assumed to only bear on the column, at a distance equal to $\frac{w_{inf} \cos \theta_{strut}}{2}$. The angle and dimension of the strut are solved for iteratively, using Equations B-1 and B-2 in the TMS 402-13 code, assuming the ungrouted masonry properties for E_m and $t_{net inf}$.

For the frames tested, this yielded an equivalent strut width of 23.74 inches (60.3 cm) and a strut angle of 42.48° . The calculated strut is shown over the cracking patterns of the frames at the 0.82 inch (20.8 mm) amplitude cycles in Figure 178.

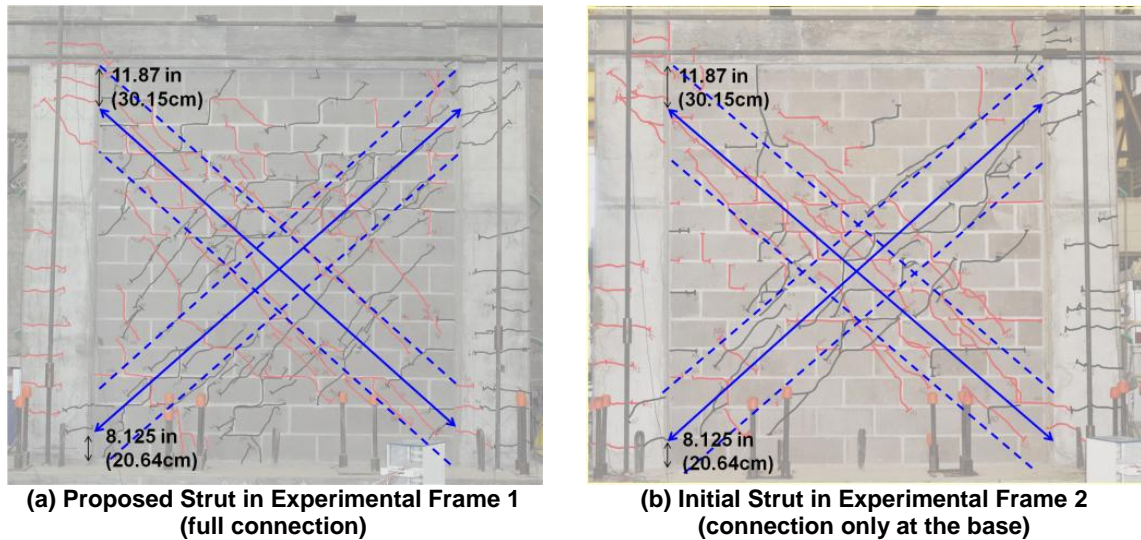


Figure 178: Proposed strut overlaid on experimental frames at 0.82in (20.8 mm) lateral displacement (0.683% drift)

Using the proposed methodology, the bounding column is now divided into three separate members: the shear critical region above the strut node, the shear critical region below the strut node, and the middle region. TMS 402-13 Appendix B requires that the columns and beams of the bounding frame be designed for 1.1 times the forces resulting from an elastic analysis with the equivalent struts. In addition, the shear in the columns and the beams must be augmented by the horizontal and vertical components of the compression force in the masonry strut. With the proposed methodology, the shear forces in top and bottom segments of the columns already include the horizontal component of the masonry compression strut, and only need to be amplified by the design factor of 1.1. The middle segment of the column and the beam must be amplified by the suggested 1.1 factor and augmented with the components of the force in the masonry strut. It is suggested that the segments of the columns be detailed as three separate members, following the seismic detailing ACI 318. Such detailing would ensure close tie spacing

within a distance l_0 on either side of the node where the compression strut is assumed to bear on the column.

The stiffness prediction for the experimental frames using a traditional elastic strut analysis with ungrouted masonry properties and the newly proposed strut analysis were very similar. The model using the proposed methodology had a stiffness that was approximately 8% lower than the traditional strut and tie analysis. Both models were very close to the initial stiffness of Frame 1, which had connections on all edges of the masonry wall. The newly proposed model was within 30% of the initial stiffness and the traditional model was within 40%. The newly proposed model overestimated the stiffness of Frame 2, which had connections only at the base, by 96% and the traditional strut model overestimated initial stiffness of Frame 2 by 112%. Both strut models were closer to the initial stiffness of the frames than the finite element models, which overestimated initial stiffness by 113 % for Frame 1 and 214% for Frame 2. However, the finite element models are still useful, since the strut models are elastic and cannot give predictions for peak strength or displacement at peak strength, which were very closely predicted by the finite element models.

The major difference between the traditional strut model and the proposed modification was the force distribution on the columns. The shear forces on the columns and beams as well as the compression force in the masonry strut of both models are shown in Figure 179a and b for a 100 kip lateral load. Once the shear forces are amplified by the 1.1 design factor and augmented by the components of the compression strut, the design forces are essentially the same between the two models (See Figure 179 c and d). However, treating the column as three separate members as suggested in the proposed

methodology required that the zones for close tie spacing be extended 28 inches (71.12 cm) up from the base of the columns and approximately 40 inches (101.6 cm) down from the tops of the columns in a seismic design category D. For the same seismic design category, using the traditional strut and tie analysis required closely spaced stirrups 20 inches (50.8 cm) from the base and top of the columns. The closely spaced tie zone resulting from the newly proposed method better encompasses the zone in which shear cracking of the columns was observed in the tests. Thus, better seismic performance of the RC frames may be achieved by designing the frames using the newly proposed methodology as compared to a traditional strut and tie analysis. The procedure for the newly proposed strut model is found in Appendix F and utilizes the same format and language as the current TMS 402 Appendix B procedure.

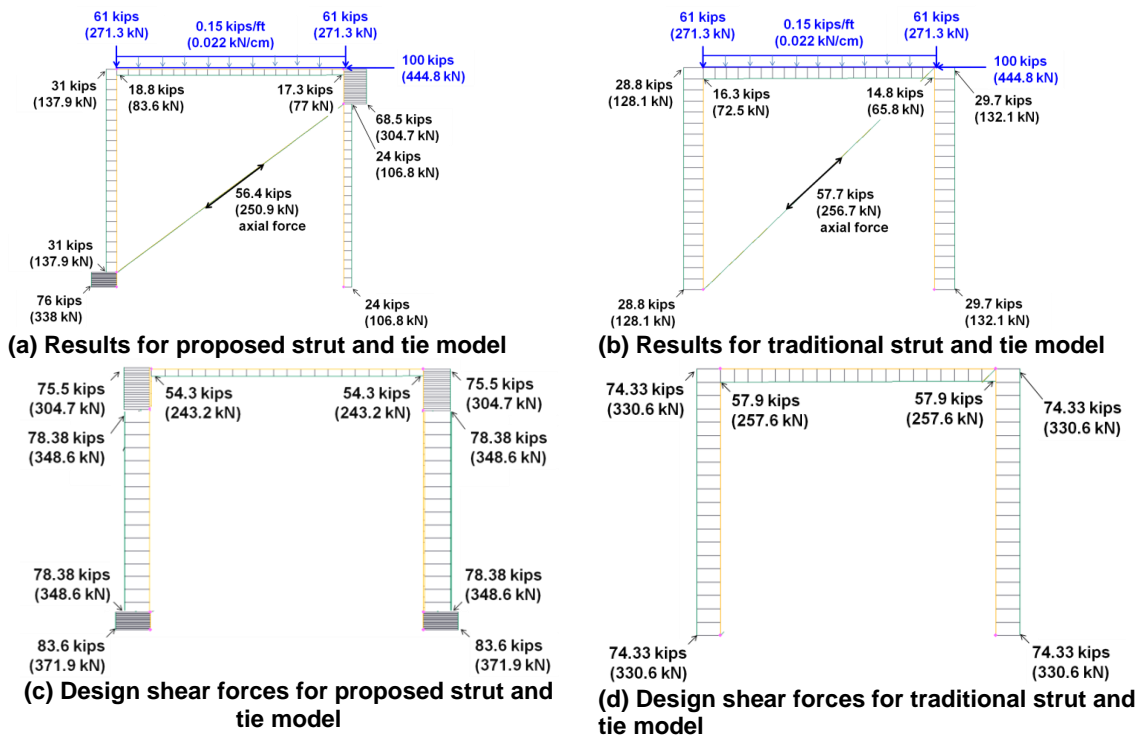


Figure 179: Resultant forces and forces for design from strut and tie models. Applied forces are labeled in blue, resultant forces are labeled in black and are shear forces, u.n.o.

7.4 Chapter Summary

The analytical studies using the experimentally validated finite element models revealed several important characteristics of hybrid concrete masonry structures. First, the force-displacement behavior of hybrid concrete-masonry frames with infill walls connected on all edges appear to behave the same as frames with infills connected to the RC frame at the top and bottom only. This analytical result reinforces the experimentally obtained conclusion that the horizontal dowel reinforcement has little influence over the global behavior of the frame and is consistent with other studies in the literature on dowel connections for infill retrofitting schemes (Kyriakides 2011). Likewise, hybrid concrete-masonry frames with infills connected only at the base exhibit the same force-displacement behavior as frames with infill walls which are not connected to the bounding frame.

Increasing the shear critical zone in the bounding columns of the frames did not appear to have any significant influence on the force-displacement behavior. The parametric studies on changes to the infill properties revealed that only increasing the ungrouted prism strength and grouting all cells within the infill wall significantly affected the capacity of both frames. As the ungrouted prism strength was increased by a factor of 2, the strength of the frames increased by 25%. Fully grouting the infill wall while maintaining the same grout strength as the experimental frames led to an increase in capacity of around 60% for both frames. Most of the infill properties did not consistently influence the displacement at peak strength of the models. However, doubling the ungrouted prism strength increased the displacement at peak strength by 17.8% for Frame 1 and 47.9% for Frame 2. Fully grouting the infill wall while maintaining the same grout

strength as the experimental frames led to a decrease in the displacement at peak strength of 35.5% for Frame 1 and 33.6% for Frame 2.

The Frame 1 model, which had connections on all edges of the infill, appeared more sensitive to changes in the infill properties than Frame 2, which only had connections at the base. An increase of about 10% lateral capacity was observed in Frame 1 by decreasing the spacing of the vertical masonry reinforcement. The displacement of Frame 1 was also influenced by the area of the vertical dowel reinforcement, the grout strength, and changing the mortar to a type N.

It is important to note that the models used for the experimental studies are 2D and do not capture out-of-plane effects. The experiments demonstrated the advantage of connections at the top of the masonry infill to prevent out-of-plane failure of the infill. It is also important to note that the parametric studies looked at the influence of single parameter variation on the behavior of the models. Future work may include expanding the study to look at the influence of parameters as they are coupled. For example, fully grouting the infill wall did not lead to brittle failure of Frame 1 or 2, but fully grouting the infill wall while increasing the grout strength may lead to brittle failure.

Several simplified approaches were presented for modeling hybrid concrete masonry walls. The elastic transformed section method predicted initial cracking loads which were lower than the finite element model predictions and the experimental data. As a result, it may be a useful design tool because the approach is conservative. The elastic transformed section model predicted a cracking load which was 40% less than the cracking load of the Frame 1 finite element model and 78% lower than experimental Frame 1. The predicted cracking load from the elastic transformed section model was

33% lower than the Frame 2 finite element model and 28% lower than the experimentally recorded value. The elastic transformed section method could be improved by incorporating the delay in cracking due to the connections of the infill to the bounding frame.

The cracked section model resulted in very close predictions for the peak capacities of the experimental frames, provided that the width b was taken as the average of the width of the hybrid-concrete masonry wall (See Section 7.3.2). The prediction for peak strength was conservative and within 8% of the experimentally recorded strengths for both frames. However, given the small margin on this prediction, more experimental studies should be conducted to determine rather this equation is adequate.

Most importantly, the proposed modification to the TMS 402 strut model for hybrid concrete-masonry frames gave a closer match to the initial stiffness of the frames than the finite element models. Compared to a traditional TMS 402 strut model, the design forces in the proposed model were nearly identical, but the predictions for initial stiffness were slightly lower. In addition, the new methodology ensures close tie spacing within a distance l_0 on either side of the node where the compression strut is assumed to bear on the column.

CHAPTER 8

SUMMARY, CONCLUSIONS, AND RECCOMENDATIONS

The focus of this study was the seismic performance, analysis and design of Caribbean hybrid concrete-masonry structures. Although few studies have been done on reinforced masonry infill, hybrid concrete-masonry structures are unique because the masonry is only partially grouted and reinforced because the masonry infill contains various types of connections to the reinforced concrete frame.

The aim of the experimental study was to conduct full-scale tests which would give insight into the seismic performance of hybrid concrete-masonry and provide validation for finite element models. The purpose of the analytical work was to develop high-fidelity finite element models which could be used to assess the effect of design changes to the masonry infill. Several simplified models also were proposed as part of the analytical work which could be incorporated into engineering models for design. Both the proposed calibration method for the shear and tensile behavior of mortared bed joints of concrete masonry units with grouted cells and the proposed modification of the TMS 402 equivalent strut equation for infills with connections have significant applications beyond Caribbean structures.

In this section, a brief summary of the experimental and analytical work is presented along with the major conclusions which resulted from this research. Recommendations on the construction and design of hybrid concrete masonry are given based on the experimental and analytical results; and the significance of the findings is presented. Areas for future work are identified.

8.1 Summary of Experimental Work

Two full-scale test specimens were constructed to model frames of the exterior, bottom floor of a five-story office building in Trinidad. The RC frames were seismically detailed and had partially grouted and reinforced masonry infill. Frame 1 had cast-in-place dowel connections extending from the foundation into the grouted cells, from the columns into the reinforced bed joints and from the beam extending down into grouted cells. Frame 2 only had dowel connections extending from the foundation into the grouted cells of the infill wall. The material properties for the concrete in the RC frame, reinforcement, masonry units, mortar and weak concrete for the grouted cells were kept within typical ranges based on responses from engineers in the Caribbean. The seismic performance of the two frames was assessed with cyclic testing. Both frames failed at similar loads and drift levels, exhibiting a compression strut mechanism in the masonry and combined flexural and shear cracking in the columns of the bounding frame.

8.2 Conclusions from the Experimental work

Several major conclusions resulted from the experimental program:

- The failure mechanism, peak strength and displacement at peak strength were very similar between the two test frames, even though they had different connections from the infill to the RC frame. However, the connections at the top of the infill in Frame 1 prevented the out-of-plane failure of the masonry which was evident in Frame 2 at drift levels over 1.5%. (See Section 6.1.1 and 6.1.2).
- The experimental test frames achieved about twice the analytically predicted peak strength of a seismically-detailed RC frame, but the infilled frames achieved peak

strength at a drift level which was about one-half that of the plain moment frame. (See Section 6.1.1).

- The cracking patterns, strain gage data and shear deformations in the infills and the RC frame indicated the typical strut mechanism observed in unreinforced masonry infill structures was altered due to the vertical connections from the reinforced concrete frame to the grouted cores of the masonry infill. In both frames, the initial shear/bearing area for the wall onto the frame was through the stiffened zone at the base of the masonry wall through the height of the cast-in-place dowels. As the tests progressed, the node for the masonry strut was on the column at a height approximately one course up from the bottom of the wall. (See Section 6.2).

8.3 Summary of Analytical Work

The work proposed a meshing scheme for hybrid concrete masonry structures which has the flexibility to model truss and bond beam reinforcement and explicitly accounts for the contribution of vertical reinforcement to the shear capacity of mortared bed joints with grouted cores. Because many of the materials tests needed to calibrate the model are difficult to conduct, an alternative calibration method was proposed to calculate shear and tensile properties of bed joints with grouted cores as a function of the compressive strength of the grout core (f_g). The triplet tests and bond wrench tests conducted on samples of grouted masonry validate the proposed methodology for calculating shear and tensile properties of the bed joints with grouted cores as a function of the grout compressive strength (f_g).

The finite element models utilized the proposed modeling scheme and predicted the behavior of the hybrid concrete-masonry frames. The models gave very close predictions for peak strength and the displacement at peak strength, which were within 10% of the experimental capacity and 21% of the displacement values for both frames. The finite element models were then refined, based on the experiments to give more precise cracking patterns in the masonry infill and to improve the match between the drift levels predicted by the models and the drift of the experimental frames when the masonry wall-to-RC frame interfaces cracked. The refined finite element models were then used to conduct analytical studies on the effect of changing the detailing of the RC frame, the connections of the infill to the RC frame, and the properties of the masonry infill and masonry reinforcement.

Three different simplified models were proposed to determine the cracking load, peak strength and elastic force-displacement behavior of the hybrid concrete-masonry frames. The cracking load is determined based on an elastic transformed section model. The peak strength was determined using a cracked section model. Finally, a modification of the TMS 402 equivalent strut model was proposed for masonry infills with connections to the RC frame. This model gave a better match to the initial stiffness of the frames than the finite element models.

8.4 Conclusions from the Analytical Work

Several major conclusions resulted from the analytical work:

- The proposed methodology to predict the bond strength, shear friction factor, and cohesion of bed joints with grouted cores as a function of the compressive

strength of the components was validated with triplet tests and bond wrench tests. (See Section 4.2.2).

- The constitutive finite element model was shown to neglect the shear contribution of the vertical reinforcement across the bed joint via dowel action. This effect was accounted for in the newly proposed model by using a pair of discrete truss elements. (See Section 4.2.4).
- A high degree of confidence can be placed in the finite element models, since they were able to predict the cracking patterns observed in the experiments and predict the peak force within 2% of the experimentally recorded strength for Frame 1 and within 10% of Frame 2. The drift at peak strength of the model of Frame 1 was within 2% of the drift at peak strength of experimental Frame 1 and the drift at peak strength of the model of Frame 2 was within 20% of the experimentally recorded drift. (See Section 6.1.1.3).
- Analytical studies varying the type of connection of the infill to the RC frame showed that frames with no connections and frames with connections only at the base have very similar force-displacement behavior. Likewise, frames with connections on all edges and frames with connections only at the top and bottom of the masonry wall behave the same. (See Section 7.1.1).
- The parametric study on infill properties revealed that only increasing the strength of the ungrouted masonry units and fully grouting the infill walls significantly influenced the peak strength and displacement at peak strength for both frames. When the ungrouted prism strength was doubled, the peak strength increased by approximately 25% for both Frame 1 and Frame 2. Doubling the ungrouted prism

strength also increased the drift at peak strength for both frames (67% increase for Frame 1 and 9% increase for Frame 2). When the infill wall was fully grouted, the capacity of Frame 1 increased by 57.7% and the capacity of Frame 2 increased by 60.8%. Fully grouting the infill wall decreased the displacement at peak strength of Frame 1 by 35.5% and decreased the displacement at peak strength of Frame 2 by 33.6%. (See Section 7.2).

- The parametric study revealed that Frame 1 with connections on all edges of the masonry was much more sensitive to changes in the masonry infill properties than Frame 2, which had connections only at the base. Decreasing the spacing of the vertical reinforcement by half increases the peak strength of Frame 1 by almost 10%. All other changes to the infill properties resulted in a change in the peak strength of less than 10%. The displacement at peak strength for Frame 1 was reduced by the decreasing the spacing of the vertical reinforcement, increased by increasing the area of the vertical dowel reinforcement, decreased by increasing the grout strength, and increased by changing the mortar to a type N. (See Section 7.2).
- The elastic transformed section model yielded predictions for cracking loads which were less than the cracking loads in both experiments and the predictions of the finite element models. However, it may still be a useful design tool because the approach is simple and conservative. (See Section 7.3.1).
- The cracked section model resulted in very close predictions for the peak capacities of the experimental frames, provided that the width b is taken as the average of the width of the hybrid-concrete masonry wall. (See Section 7.3.2).

- The proposed modification of the TMS 402 strut model for hybrid concrete-masonry frames gives a closer match to the initial stiffness of the frames than the finite element models. Compared to a traditional TMS 402 strut model, the design forces in the proposed model are nearly identical, but the predictions for initial stiffness are slightly lower. In addition, the new methodology ensures close tie spacing within a distance l_0 on either side of the node where the compression strut is assumed to bear on the column. (See Section 7.3.3).

8.5 Recommendations

The conclusions from the experimental and analytical work lead to recommendations for the design and detailing of Caribbean-style hybrid concrete-masonry frames. Caution should be used against extending these conclusions to masonry infill with ungrouted prism strengths greater than 1400 psi (9.65 MPa) or infills with heavy reinforcement, as stronger infills may lead to more brittle behavior and higher shear stresses in the columns of the bounding frames. Parametric studies were performed which indicate that the behavior of the frames remained somewhat ductile, failing in combined flexure and shear when changes in any one of the relevant parameters (reinforcement areas, spacing and the strength of the masonry) occur. However, these results have not been validated with experiments, and combining several changes to the infill design may lead to a more brittle and undesirable failure mechanism.

The most efficient use of steel for hybrid concrete-masonry structures with seismically detailed RC frames is to partially reinforce the wall only in the vertical direction and to connect the masonry infill to the foundation and the beam with cast-in-place dowel reinforcement. Lightly reinforced, partially grouted masonry with

connections at the top and bottom of the masonry wall have increased capacity compared to infills without connections. They also prevent out-of-plane collapse of the wall and do not significantly influence the ductility of the frame. In these experiments, the horizontal reinforcement placed down the center of the bed joint had little effect on the behavior of the frame.

The partially grouted reinforced infill connected to the bounding frame may be accounted for in engineering models using the proposed modification of the strut model for infill frames TMS 402. This procedure will lead to close tie spacing within a distance l_0 on either side of the node where the compression strut is assumed to bear on the column. Close tie spacing near the bearing zone of the compression strut reduces the chances of shear failures in these zones.

The experimental work also leads to several recommendations specific to Caribbean construction practices. First, the aggregate in the concrete of the grouted cores may lead to voids in the cores if they are not consolidated properly. No issues with voids or settlement were observed in the experimental frames which were filled with concrete and tamped with a rod every three courses. Using a standard grout with aggregate size less than $\frac{3}{8}$ -in. (10 mm) would reduce the possibility of voids in the grouted cores. Second, poor bond strength was observed between the Caribbean-style mortar (3 parts sand to 1 part Portland cement) and the concrete masonry units (See Appendix B). Using a Type N mortar, which contains lime, would increase the bond strength of the bed joints. Third, the single # 3 bar placed in the center of the masonry bed joint led to splitting of the unit and did not significantly contribute to the lateral capacity of the infill wall (p. 215, Section 6.1.3.2). Using wire ladder joint reinforcement or deformed wired placed in

the mortar along the face shell of the masonry unit will prevent the bar from splitting the unit as it is compressed. Smaller reinforcement placed in the mortar is also more likely to contribute to the lateral capacity of the infill as the reinforcement is continuously bonded to the masonry.

The analytical models for the shear and tensile capacity of mortared bed joints with grouted cores and the results of the small tests on masonry assemblies led to several recommendations for modeling grouted masonry. The shear friction factor and tensile bond strength of grouted masonry appear to be significantly greater than ungrouted masonry. The cohesion of grouted masonry is only marginally greater than ungrouted masonry. These trends were confirmed by the assembly tests (Section 4.4.3) and data from the literature (Section 4.2.3.2). The equations proposed in Section 4.2.3.2 can be used to approximate these properties based on the compressive strength of the grout core.

8.6 Significance

This work contained several significant contributions. First, the experimental program characterized the seismic behavior of hybrid concrete-masonry frames and showed they do not exhibit the typical strut mechanism observed in unreinforced masonry infill structures. Second, a detailed finite element modeling scheme and calibration methodology was developed for modeling partially grouted masonry. This model includes a novel calibration method to account for the difference in the shear and tensile behavior of mortared bed joints with and without grouted cores, and a method to account for the contribution of vertical reinforcement to the shear capacity of the bed joints with grouted cores. Neither phenomenon was incorporated into previous finite element modeling schemes. Third, simplified models were proposed for use in

engineering design. The modification of the TMS 402 strut model for hybrid concrete-masonry could be used in large models to incorporate the effects of the masonry infill and connections. This was identified as one of the primary desires of engineers in the Caribbean, who struggled to reconcile their local construction methods with typical seismic design code procedures

This work clearly has significance to the local engineers in the Caribbean, who can use the results of the experimental and analytical studies, recommendations for seismic detailing, and simplified models to expand upon their existing design methods. However, the work also lends itself to several applications beyond Caribbean-style hybrid concrete-masonry structures. First, the data from the grouted masonry triplets and bond wrench specimens indicate shear friction factor and tensile strength of bed joints with grouted cores are significantly greater than ungrouted masonry, while cohesion of bed joints with grouted cores are only marginally greater than ungrouted masonry. Equations to determine the shear friction, cohesion and bond strength of masonry bed joints with grouted cores were also developed. If the proposed equations were incorporated in the TMS 402 code, their use could lead to a reduction in the shear reinforcement required in reinforced masonry walls. Second, the proposed modification of the TMS 402 strut model for infill frames with connections would encourage the use of such connections. The experiments verified that the connections improved the out-of-plane behavior of the masonry infill. The current TMS 402 code allows for out-of-plane restraints, but they must be designed to avoid the transfer of in plane loads. An modification of the TMS 402 code like the one suggested in this research would allow for simple out-of-plane restraints which do not have to be designed to prevent in-plane load transfer.

8.7 Future Work

The following areas are identified which could build upon the results of this study:

- More experimental tests of grouted masonry triplets and bond wrench specimens with varying grout mixes and unit strengths could be conducted to refine the formulas proposed in Chapter 5 for possible adaptation into the TMS 402 code.
- More extensive parametric studies on the seismic performance of hybrid concrete-masonry structures, examining the effect of simultaneously combining several design changes to the masonry infill and connections could be conducted. It is possible that the trends of the variation in individual parameters compound when multiple changes are considered, or some combination may lead to a significantly different failure mechanism than observed in the experiment.
- Additional experiments on masonry infill structures with cast-in-place dowel connections to the RC frames would be useful to validate or refine the proposed modification of the TMS 402 strut model. If the finite element modeling scheme and material calibration proposed in this work gives close predictions for the seismic performance of other experimental frames, the models can be used to generate many different frames to validate the simplified model.

APPENDIX A

NOTES FROM SITE VISITS TO THE CARIBBEAN

Table 13: Material and construction data gathered from site visits to the Caribbean

COMPANY INFORMATION			MATERIAL DATA					ADDITIONAL NOTES REGARDING CONSTRUCTION PRACTICES
Company Number*	Company Location	Company Type	Concrete	Concrete Masonry Units (CMU)	Grout	Mortar	Rebar	
1	Belize	Construction	w/c ratios of 0.4 to 0.6 Course aggregate: limestone Fines: natural sand remove anything less than 200mm MSA: 3/4in and larger is used	28 day strength: 3500psi 1 day strength: 650psi standard 8in units	-	-	-	-
2	Belize	Construction	Limestone aggregate 3/4in MSA	-	-	-	-	-
3	Belize	Design	3500psi compressive strength typical. 3/8in MSA	1000psi specified minimum compressive strength	2000psi compressive strength specified by cylinder testing (but not always done) "Grout" is actually weak concrete, 3/8in MSA	Face shells and webs are mortared 1:3 Portland cement to sand no lime	Masonry horizontal rebar is one number 3 bar just placed in mortar, straight connections into the columns Masonry vertical rebar is one number 5 bar placed in a grouted cell, 2' on center. The vertical bars typically have a "starter" bar with a splice length of	CMU blocks are laid first with rebar protruding into the spaces where columns and beams are poured. Grout is poured in after about the fifth or sixth course. Vibrators are usually not used in grout, but a piece of rebar is used to "rod" it down.

							~20-30in then the bar is continuous for the wall height	
4	Jamaica	Concrete and Ready Mix	Type 1 and 1P (p=local local pozzolanic volcanic ash) MSA:3/4in(most popular), 3/8in also produced Use masonry sand and construction sand (ASTM) 3000psi cylinder strength	-	-	-	-	7day removal of forms for 1P cement Cement may often be too hot when poured as warm weather pours are typical
5	Jamaica	Design	limestone aggregate 3000psi 28 day strength	6in hollow units 1000-1200 psi compressive strength	concrete used as grout 2500-2600 psi compressive strength, 4in slump	Face shells and webs are mortared 1:3 Portland cement to sand no lime	Masonry reinforcement: 1/2in rebar at 18in crs vertically and 3/8in rebar every three block height horizontally placed at center. Vertical and horizontal bars are doweled into the frame (see construction practices) Splice lengths are usually taken from ACI 318 or about 30*bar diameter Usually limit to one or two splices per wall. All reinforcement: deformed bars 60 and 40 ksi is common	The vertical and horizontal bars are doweled about 4 to 6 inches into the column and beam frame. Cast-in-place with a 90 degree bend. (or in some cases drilled and epoxied into the frame) In some instances a rubberized sealant is placed to create a joint. In other instances it butts against the frame and filled with mortar. (splices within the wall are typically 30*db) Not typically vibrated they are usually just rodded, but more contractors are now using the vibrators. At the top of the wall, the face shell of the masonry must be knocked out in order to place over the dowel bar and permit grouting.
6	Jamaica	Design	-	-	-	-	block masonry every other core filled with rebar	-
7	Trinidad	Concrete and Ready Mix	Compression Strength (2ksi)	-	-	-	-	-

			residential, 30MPa 3-7story (4.35ksi) MSA: 10mm or 20mm depending on design FM: 2.8-3.1 w/c: 0.36-0.59 with plasticizer, 0.59- 0.7 without Type IP cement quartz or mix of limestone and quartz (25% pozzolans) 2% air content					
8	Trinidad	CMU producer		190x190x390mm (8in block equivalent) mortar grooves 1 day strength=6MPa, 7day strength= 13MPa				
9	Trinidad	CMU producer		standard 8in,6in and 4in block (8x8x16 most common) mortar grooves f _c =11.7MPa		3:1 sand cement, no lime		common to use castor bars, and fill with grout every 3-5 blocks
10	Trinidad	Design	30MPa compressive strength most common MSA 30mm, but 20 or 10 have been specified for some projects	15MPa compressive strength	Grout with same concrete as frame (watered down)	Use a powder product (CEMEX 100 is common throughout the island), it is Portland cement based, often just mixed "by eye"	Masonry Rebar: first placed in foundation and in columns (cast-in-place connections) Follow ACI 318 for splice lengths Vertical rebar is one T12 bar every other core (grouted) Horizontal rebar is one 10mm bar at the center of	Only shear walls are connected both to the columns and the beams. Construction sequence: pour frame, wait 12 hours, take off form work and begin constructing wall. The shear walls are grouted every 4 courses (wait 1 day between lifts)

							the course. All Rebar: Use deformed high strength (410N/mm ²) deformed, ribbed bars for the main structural steel with smooth mild steel (250N/mm ²) for stirrups as ties.	
11	Trinidad	Design	31MPa 28 day strength 20mm MSA		MSA: 10mm Strength: 17MPa at 7 days Slump: approx. 10in	They specify 1 cement: 1/4 lime: 3 sand, but lime is not widely used in Trinidad Bed joints at 1/2in to accommodate reinforcement, head joints are 3/8in Face shells and webs are mortared	Masonry Rebar: Vertical rebar is anchored to the slab or beam below using epoxy Splices in the masonry wall are approximately every 4ft with lap splices of 18in For non-loading block walls, vertical bars (T12 or T16) would be typically at 32 in cc. For load bearing external block walls, 16 cc. Horizontal rebar is typically two T10 bars, one placed in each face shell placed every third course. All Rebar: use deformed bars for everything over 3/8in and a strength of 60ksi	Frame is usually constructed first, then infill block walls. In some cases, the wall is separated from the column by using "flex cell". But there are often architectural concerns that will limit the structural separation that the architect will accept. In some cases, the vertical bars are anchored into the slab. In other cases, angles/ plates are used to tie the walls to the slabs or beams. CMU block are grouted by simply pouring grout in vertically after 2-3 block lifts. Quality control is almost always an issue. In some cases the block faces are cut near the top of the wall to get the grout in.

* Specific firms will remain anonymous

Table 14: Notes regarding Caribbean design practices

COMPANY INFORMATION			NOTES REGARDING DESIGN PRACTICES
Company Number*	Company Location	Company Type	
3	Belize	Design	<p>The predominate feeling in Belize is that most of their buildings are short (5 or fewer stories) and regular in plan and elevation, so earthquake design is not taken into account at all, but seismic details are included. They do not have seismic maps of their own, and when the building is irregular or the customer asks specifically for seismic design they use spectral maps from Florida or Guatemala.</p> <p>When earthquake forces are considered, there is uncertainty about the percent of lateral forces taken by the frame system and the masonry wall. Common design practice is to model the RC frame and apply some % of lateral forces then design the wall for the rest. The R values selected for earthquake design (when it is considered) are those for moment frames.</p> <p>The types of models used for design are typically 2D and do not include P-delta effects or eccentricity. The masonry is accounted for as a cladding load.</p> <p>Soils are highly variable and there is no formal soil testing in Belize. As a consequence, foundation piles are sometimes driven which literally disappear, and a second is placed down on top. Foundations are sized for the building without account for the expected friction of the soil and engineers do not have the design parameters needed to do a proper foundation design.</p>
5	Jamaica	Design	<p>Steel structures are rarely used, only sometimes for commercial facilities. The foundations mainly consist of strip foundation. 3D models are to analyze their structures. For earthquake design, two directional forces are taken. A shear wall design is done with STAAD to account for the masonry infill. The lateral pressure on the reinforced masonry and a torsion check are done by hand calculations.</p>

10	Trinidad	Design	For shear wall type systems (where the masonry is connected to the frame) the frame is designed for lateral earthquake forces and the walls are designed to resist gravity loads and wind pressures. For non-shear wall systems, external block work walls are usually only accounted for in the mathematical model as a partition load with no other provision made for its stiffness effect on the frame. The frame is expected to carry all the loading. For commercial construction external block work may be filled every other core with tying into the frame using cast-in-place connections (horizontal and vertical). This connection is not accounted for in the model.
11	Trinidad	Design	The RC frame is designed for both gravity and earthquake loads and utilize the wall only to resist wind pressures. In either case, the wall is connected vertically with rebar into the slab above and below to prevent it from falling out in a seismic event. The wall contains both horizontal and vertical rebar, but the horizontal is discontinued at the end of the wall and a movement joint is left to assure that the wall does not attribute to the lateral stiffness of the system in an earthquake and thus attract large forces into the stiff wall. The masonry is accounted for as a cladding load in engineering models.

APPENDIX B

MATERIAL DATA

Concrete Mix Design(s)
Please use mix code numbers for ordering concrete.

MIX CODE	30367-3
STRENGTH(PSI)	3000
MAX COARSE (in.)	0.75
AIR% : LOWER %	3.0
UPPER %	6.0
SLUMP (in.)	4-6
BAG FACTOR	5.50
CEMENT(LBS) TYPE I	517
SAND 1(LBS) Wash Gray	1051
SAND 2(LBS) Natural	259
STONE(LBS) 67	1798
ADMIX 1(OZ) Water Reducing	***
ADMIX 2(OZ) Air Entraining	as req
WATER(GAL)	34.0
WATER/CMT.	0.55
LOCATION	EXPOSED #67 STONE

Figure 180: Concrete mix design for RC frame

Table 15: Concrete compressive strength

	Compressive Strength ksi (MPa)		
	7-day	28-day	Day of Test*
Foundation Pour 1 -truck 1	6.29 (43.37)	7.39 (50.95)	11.13 (76.74)
	5.99 (41.30)	-	10.78 (74.33)
Foundation Pour 1 -truck 2	4.61 (31.78)	5.30 (36.54)	7.69 (53.02)
	4.97 (34.27)	5.60 (38.61)	8.38 (57.78)
Foundation Pour 2	4.98 (34.34)	6.83 (47.09)	9.27 (63.91)
	5.47 (37.71)	5.63 (38.82)	7.82 (53.92)
Foundation-Average	5.35 (36.89)	6.33 (43.64)	9.02 (62.19)
Column Pour	2.82 (19.44)	3.91 (26.96)	5.04 (34.75)
	3.07 (21.17)	4.02 (27.72)	4.50 (31.03)
Beam Pour	3.00 (20.68)	3.85 (26.54)	5.88 (40.54)
	3.12 (21.51)	4.16 (28.68)	5.44 (37.51)
Top 1/2 Column Pour	3.17 (21.86)	3.61 (24.89)	6.26 (43.16)
	3.09 (21.30)	4.79 (33.03)	6.01 (41.44)
Frame-Average	3.05 (21.03)	4.05 (27.92)	5.52 (38.06)

* Day of Test Data was collected the week following the second test. The two tests were conducted 6 weeks apart and the age of the concrete ranged from 147 to 249 days

Table 16: Concrete tensile strength from split cylinders

	Tensile Strength ksi (MPa)
Column Pour	0.57 (3.93)
	0.52 (3.59)
Beam Pour	0.62 (4.27)
	0.66 (4.55)
	0.63 (4.34)
Top 1/2 Column Pour	0.63 (4.34)
	0.66 (4.55)
	0.65 (4.48)
Average	0.61 (4.21)

Table 17: Concrete elastic modulus

	Elastic Modulus* ksi (MPa)
Column Pour	3220 (22200)
Beam Pour	3570 (24600)
Top 1/2 Column Pour	3540 (24400)
Average	3440 (23700)

*Calculated from the best fit line to stress vs. strain data collected from 5 tests (See Figure 181)



Figure 181: Test set up to determine the Elastic Modulus of concrete

Table 18: Rebar properties

	Specimen No.	Yield Stress ksi (MPa)
# 5	1	81.3 (560.5)
	2	78.9 (544.0)
	3	80.3 (553.6)
	Average	80.2 (553.0)
# 7	1	77.6 (535.0)
	2	77.9 (537.1)
	3	78.8 (543.3)
	Average	78.1 (538.5)
# 8	1	78.8 (543.3)
	2	76.1 (524.7)
	3	76.9 (530.2)
	Average	77.3 (533.0)
	Average (all bars)	78.5 (541.2)

*The No 3 bars were too small for the grips of the tensile testing machine

Table 19: Masonry prism compressive strength

	Compressive Strength ksi (MPa) and Failure Type			
	7-day		28-day	
	UngROUTED Prisms	1.44 (9.95)	Face shell separation	1.65 (11.40)
9.50 (6.55)		Face shell separation and crushing	1.22 (8.43)	Face shell separation and shear
1.63 (11.25)		Cone and shear	1.42 (9.81)	Face shell separation and shear
Average	1.34(9.25)		1.43(9.88)	
Coefficient of Variation	0.26		0.15	
Grouted Prisms	2.50 (17.16)	Face shell separation and shear	2.72 (18.76)	Face shell separation and shear
	2.26 (15.61)	Face shell separation and shear	2.61 (18.02)	Shear and crushing
	2.54 (17.53)	Face shell separation	2.38 (16.42)	Face shell separation and shear
Average	2.43 (16.77)		2.57(17.73)	
Coefficient of Variation	0.06		0.07	



Figure 182: Preparation of prisms



Figure 183: Prisms bagged for curing at ambient temperature



Figure 184: Gypsum plaster capping applied to all prisms



Figure 185: Test set up for compressive strength of masonry prisms

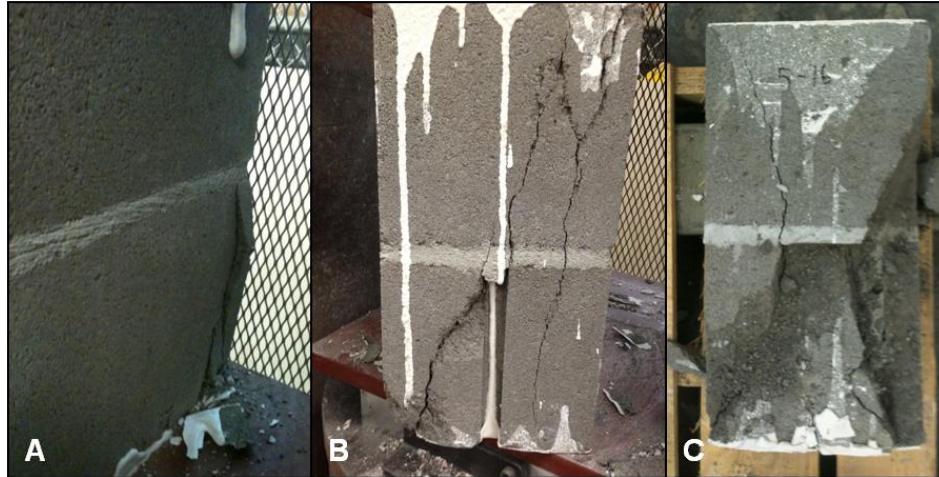


Figure 186: Failure patterns for ungrouted prisms: (a) face shell separation and crushing, (b) face shell separation and shear, and (c) cone and shear

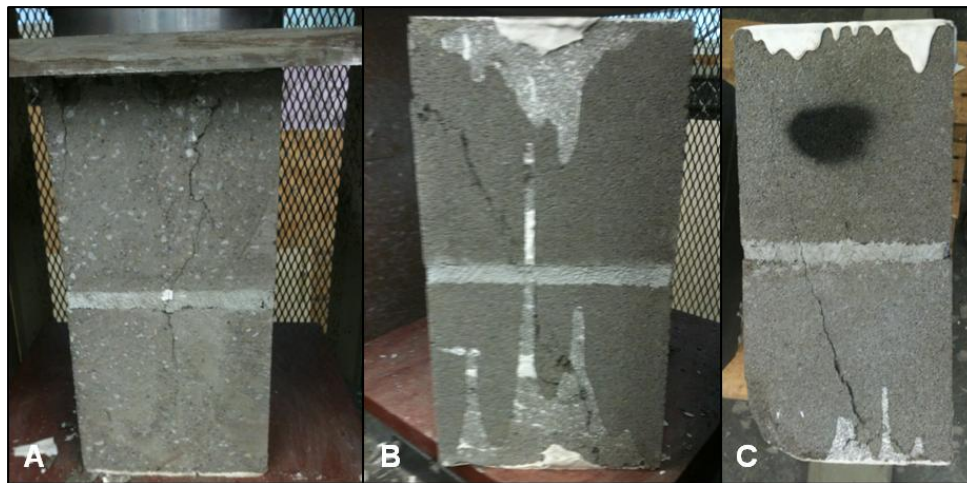


Figure 187: Failure patterns for grouted prisms: (a) face shell separation, (b) face shell separation and shear, (c) shear and crushing

Table 20: Prism elastic modulus

	Elastic Modulus* ksi (MPa)
UngROUTED Prisms	6114 (42150)**
	2871 (19790)
	1544 (10650)
Average	2207 (15220)
Coefficient of Variation	0.42
Grouted Prisms	3714 (25610)
	3118 (21500)
	2232 (15390)
Average	3022 (20840)
Coefficient of Variation	0.25

*Calculated from the best fit line to stress vs. strain data collected from tests (See Figure 188)

** gage appeared to malfunction and was swapped out for other specimens, this trial was neglected

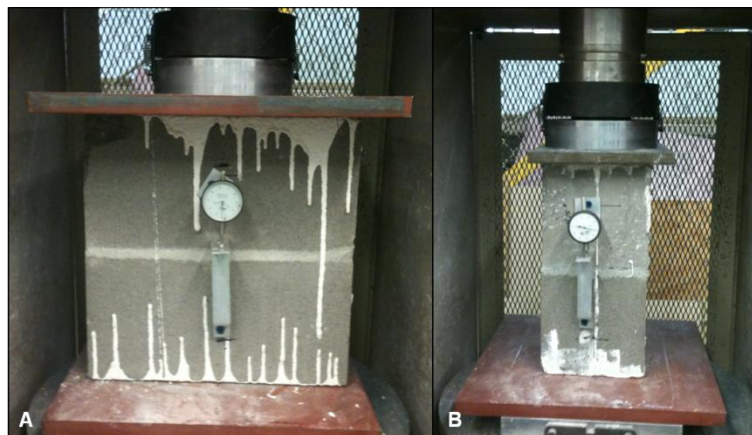


Figure 188: Test set up for Elastic Modulus of (a) ungrouted and (b) grouted prisms

Table 21: Concrete used for grouted cells-compressive strength

	Compressive Strength ksi (MPa)
Grout Cubes (ASTM C1019)	2.97 (20.48)
	3.50 (24.13)
	1.81 (12.48)*
	2.68 (18.48)
Average	3.05 (21.03)
Coeff. of Var.	0.13
Grout Cylinders**	2.22 (15.31)
	2.72 (18.75)
	3.13 (21.58)
	2.93 (20.20)
	2.95 (20.34)
	2.92 (20.13)
	2.46 (16.96)
Average	2.76 (19.03)
Coefficient of Variation	0.11

*thrown out as cube had a lot of air voids

**In the Caribbean, the concrete for grout is often specified by cylinder strength



Figure 189: Grout cube mold as specified by ASTM 1019

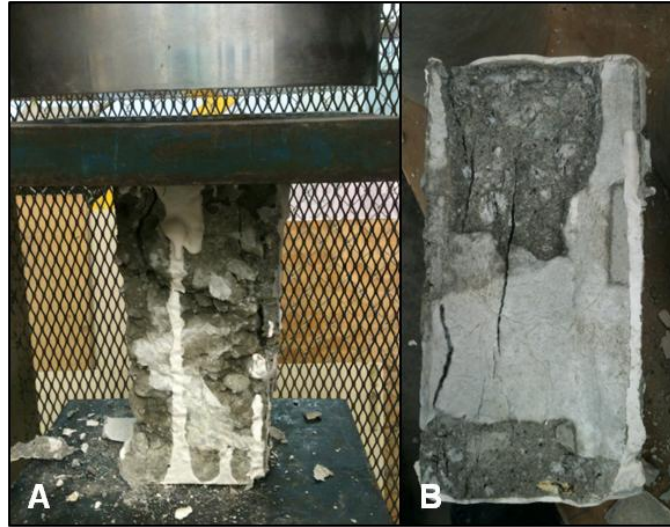


Figure 190: Grout cube (a) testing and (b) failure

Table 22: Mortar compressive strength

	Compressive Strength ksi (MPa)
Mortar Cubes (ASTM C109)	3.67 (25.30)
	3.06 (21.1)
	5.46 (37.65)
	5.28 (36.40)
	3.53 (24.34)
	4.86 (33.51)
	5.14 (35.44)
	5.48 (37.78)
	5.53 (38.13)
	4.99 (34.40)
	5.07 (34.96)
	2.50 (17.24)
	5.23 (36.06)
	4.00 (27.58)
	2.68 (18.48)
Average	4.43 (30.54)
Coefficient of Variation	0.24

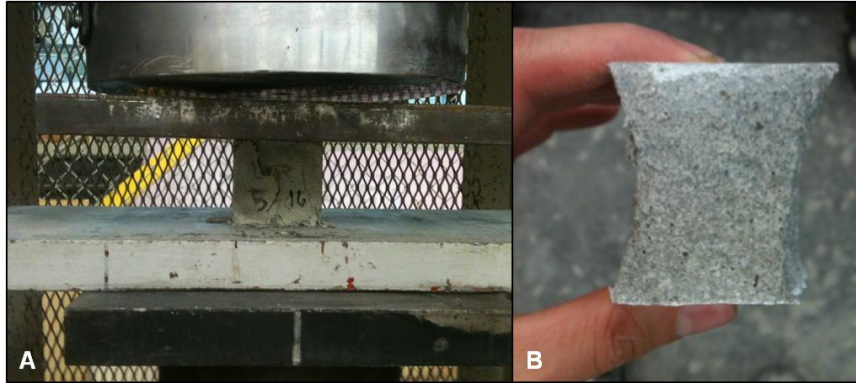


Figure 191: Mortar cube (a) testing and (b) failure

Table 23: Tensile bond strength from bond wrench tests

	Tensile Bond Strength psi (MPa)
UngROUTED Bed Joints	37.27 (0.26)
	30.09 (0.21)
	27.36 (0.19)
	56.03 (0.39)
	58.80 (0.41)
Average	41.91 (0.29)
Coeff. of Var.	0.35
Grouted Bed Joints	230.96 (1.59)
	231.53 (1.60)
	213.05 (1.47)
	219.67 (1.51)
	201.06 (1.39)
Average	219.25 (1.51)
Coefficient of Variation	0.06



Figure 192: Bond wrench test set up



Figure 193: Failures of ungrouted bed joints



Figure 194: Failures of grouted bed joints

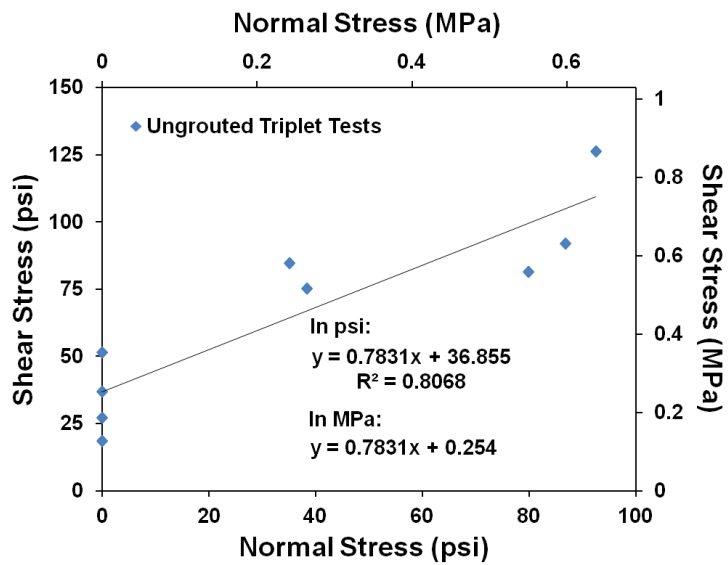


Figure 195: Shear stress vs. normal stress plot of ungrouted triplet tests

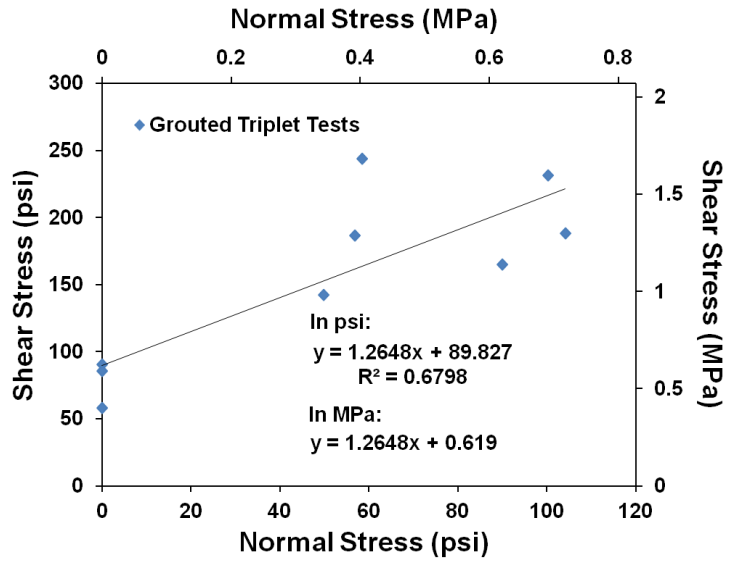


Figure 196: Shear stress vs. normal stress data from grouted triplet tests



(a) Precompression of triplet



(b) Testing of triplet

Figure 197: Triplet test set up



Figure 198: Failure of ungrouted triplet

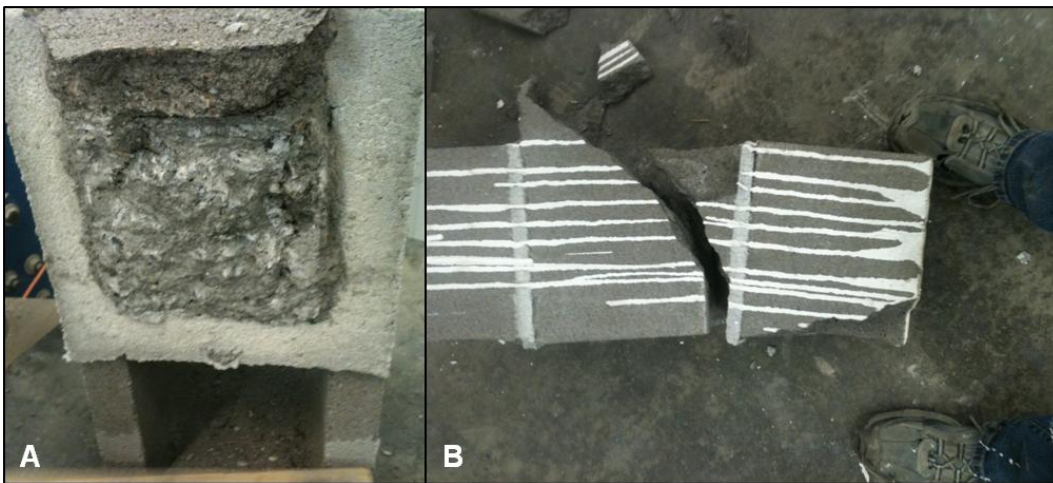


Figure 199: Failure of grouted triplet (a) while still on the testing platform and (b) removed from the testing machine

*the ungrouted portions of the triplets broke off very easily when they were removed from the testing machine

APPENDIX C

SUPPLEMENTAL DATA FOR FINITE ELEMENT MODELS

Table 24: Mortar interface element parameters for study on the influence of masonry head joint bond strength on seismic performance of URM walls*

Mortar from Magenes and Calvi (1992)									
		Baseline $S_{0\ Head} = S_{0\ Bed}$		$S_{0\ Head} / S_{0\ Bed}$ = 0.10		$S_{0\ Head} / S_{0\ Bed}$ = 0.50		$S_{0\ Head} / S_{0\ Bed}$ = 0.90	
Variables		Bed Joint	Head Joint	Bed Joint	Head Joint	Bed Joint	Head Joint	Bed Joint	Head Joint
S_0	ksi (MPa)	0.009 (0.062)	0.009 (0.062)	0.009 (0.062)	0.0009 (0.0062)	0.009 (0.062)	0.0045 (0.031)	0.009 (0.062)	0.0081 (0.056)
μ_0		0.50	0.50	0.50	0.50	0.50	0.50	0.50	0.50
μ_r		0.40	0.40	0.40	0.40	0.40	0.40	0.40	0.40
r_0	ksi (MPa)	0.01 (0.069)	0.01 (0.069)	0.01 (0.069)	0.01 (0.069)	0.01 (0.069)	0.01 (0.069)	0.01 (0.069)	0.01 (0.069)
r_r	ksi (MPa)	0.005 (0.034)	0.005 (0.034)	0.005 (0.034)	0.005 (0.034)	0.005 (0.034)	0.005 (0.034)	0.005 (0.034)	0.005 (0.034)
Mortar with 2x Bond Strength and Cohesion									
		Baseline $S_{0\ Head} = S_{0\ Bed}$		$S_{0\ Head} / S_{0\ Bed}$ = 0.10		$S_{0\ Head} / S_{0\ Bed}$ = 0.50		$S_{0\ Head} / S_{0\ Bed}$ = 0.90	
Variables		Bed Joint	Head Joint	Bed Joint	Head Joint	Bed Joint	Head Joint	Bed Joint	Head Joint
S_0	ksi (MPa)	0.02 (0.138)	0.02 (0.138)	0.02 (0.138)	0.002 (0.0138)	0.02 (0.138)	0.01 (0.069)	0.02 (0.138)	0.018 (0.124)
μ_0		0.50	0.50	0.50	0.50	0.50	0.50	0.50	0.50
μ_r		0.40	0.40	0.40	0.40	0.40	0.40	0.40	0.40
r_0	ksi (MPa)	0.02 (0.138)	0.02 (0.138)	0.02 (0.138)	0.02 (0.138)	0.02 (0.138)	0.02 (0.138)	0.02 (0.138)	0.02 (0.138)
r_r	ksi (MPa)	0.005 (0.034)	0.005 (0.034)	0.005 (0.034)	0.005 (0.034)	0.005 (0.034)	0.005 (0.034)	0.005 (0.034)	0.005 (0.034)

*all other model parameters were taken from the URM wall models for tests by Magenes and Calvi (1992)-See Table 32

Table 25: Head joint bond strength study: initial and final cracking patterns for URM wall MI1 4.92f t x 6.56ft (1.5m x 2m), 174psi (1.2 MPa)

	Mortar from Magenes and Calvi (1992)		Mortar with 2x Bond Strength and 2x Cohesion	
	Initial Cracks	Final Cracks	Initial Cracks	Final Cracks
$\frac{S_{0\ Head}}{S_{0\ Bed}} =$ $S_{0\ Bed}$				
$\frac{S_{0\ Head}}{S_{0\ Bed}} =$ 0.10				
$\frac{S_{0\ Head}}{S_{0\ Bed}} =$ 0.50				
$\frac{S_{0\ Head}}{S_{0\ Bed}} =$ 0.90				

Table 26: Head joint bond strength study: initial and final cracking patterns for URM wall MI2 4.92ft x 6.56ft (1.5m x 2m), 58psi (0.4MPa)

	Mortar from Magenes and Calvi (1992)		Mortar with 2x Bond Strength and 2x Cohesion	
	Initial Cracks	Final Cracks	Initial Cracks	Final Cracks
$\frac{S_{0\ Head}}{S_{0\ Bed}} =$ Baseline				
$\frac{S_{0\ Head}}{S_{0\ Bed}} =$ 0.10				
$\frac{S_{0\ Head}}{S_{0\ Bed}} =$ 0.50				
$\frac{S_{0\ Head}}{S_{0\ Bed}} =$ 0.90				

Table 27: Head joint bond strength study: initial and final cracking patterns for URM wall MI3 4.92ft x 9.84ft (1.5m x 3m), 174psi (1.2 MPa)

	Mortar from Magenes and Calvi (1992)		Mortar with 2x Bond Strength and 2x Cohesion	
	Initial Cracks	Final Cracks	Initial Cracks	Final Cracks
$\frac{S_{0\ Head}}{S_{0\ Bed}} =$ Baseline				
$\frac{S_{0\ Head}}{S_{0\ Bed}} =$ 0.10				
$\frac{S_{0\ Head}}{S_{0\ Bed}} =$ 0.50				
$\frac{S_{0\ Head}}{S_{0\ Bed}} =$ 0.90				

Table 28: Head joint bond strength study: initial and final cracking patterns for URM wall MI4 4.92ft x 9.84ft (1.5m x 3m), 58psi (0.4MPa)

	Mortar from Magenes and Calvi (1992)		Mortar with 2x Bond Strength and 2x Cohesion	
	Initial Cracks	Final Cracks	Initial Cracks	Final Cracks
Baseline $S_{0\ Head} = S_{0\ Bed}$				
$S_{0\ Head} / S_{0\ Bed} = 0.10$				
$S_{0\ Head} / S_{0\ Bed} = 0.50$				
$S_{0\ Head} / S_{0\ Bed} = 0.90$				

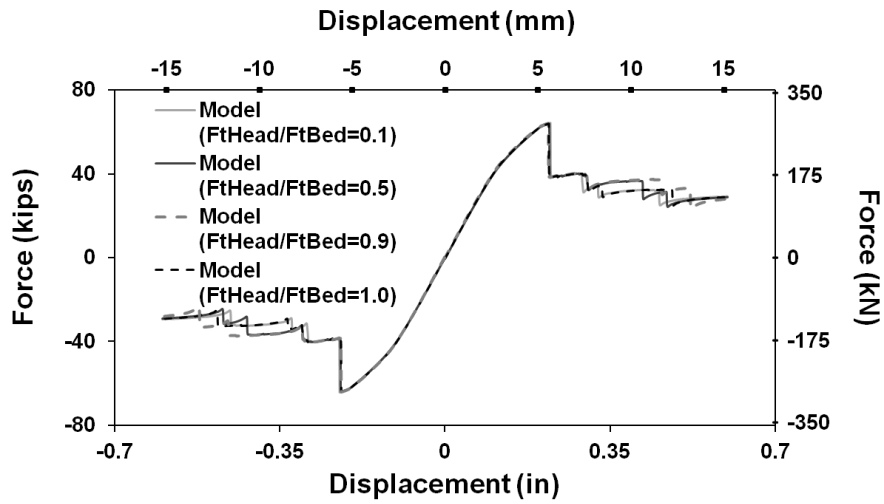


Figure 200: Influence of head joint bond strength on wall MI1 [4.92f t x 6.56ft (1.5m x 2m), 174psi (1.2 MPa) compression] *mortar properties from Table 24, Magenes and Calvi (1992)

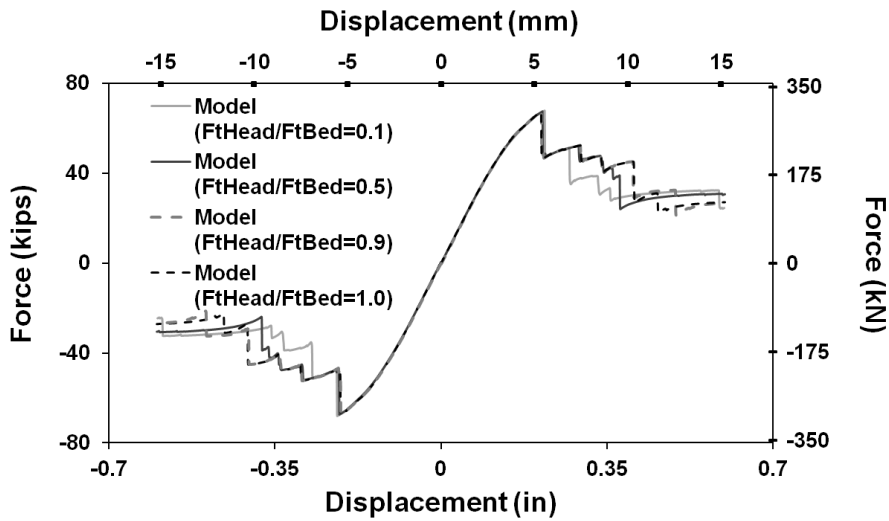


Figure 201: Influence of head joint bond strength on wall MI1 [4.92f t x 6.56ft (1.5m x 2m), 174psi (1.2 MPa) compression] *mortar properties from Table 24, Mortar with 2x Bond Strength and Cohesion

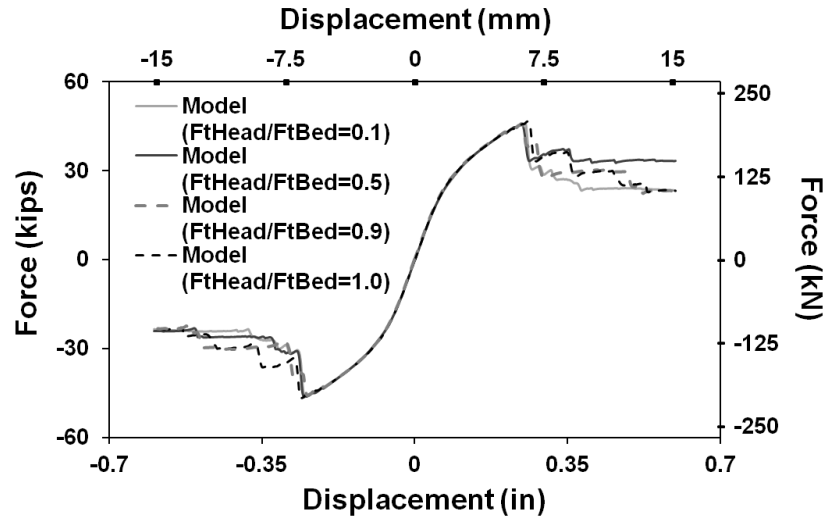


Figure 202: Influence of head joint bond strength on wall MI2 [4.92f t x 6.56ft (1.5m x 2m), 58psi (0.4MPa) compression] *mortar properties from Table 24, Magenes and Calvi (1992)

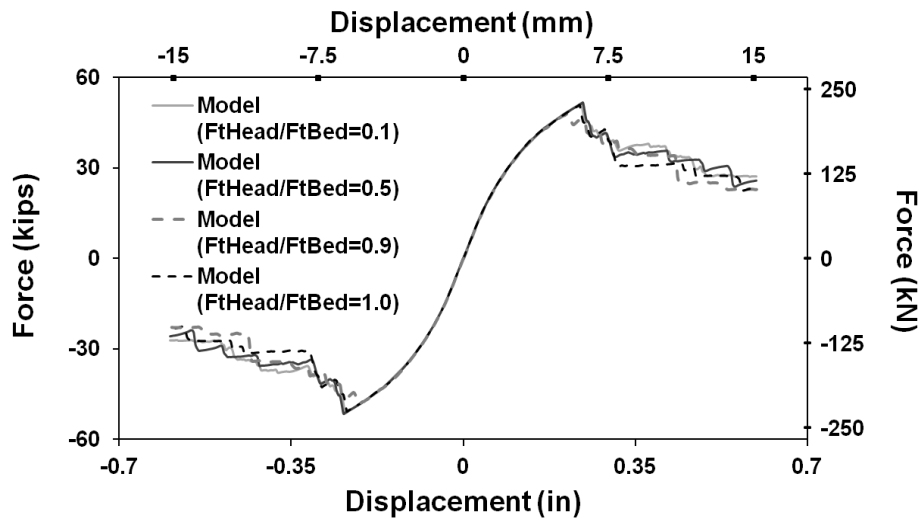


Figure 203: Influence of head joint bond strength on wall MI2 [4.92f t x 6.56ft (1.5m x 2m), 58psi (0.4MPa) compression] *mortar properties from Table 24, Mortar with 2x Bond Strength and Cohesion

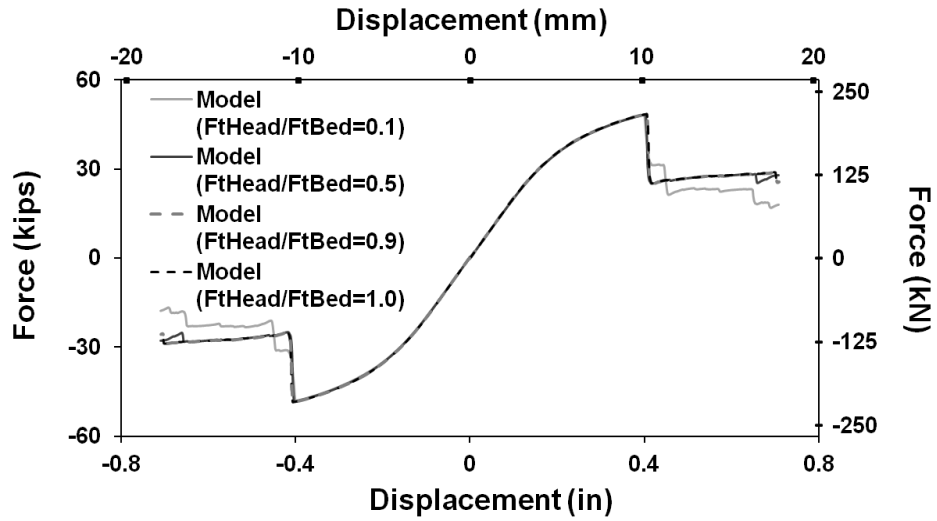


Figure 204: Influence of head joint bond strength on wall MI3 [4.92ft x 9.84ft (1.5m x 3m), 174psi (1.2 MPa) compression] *mortar properties from Table 24, Magenes and Calvi (1992)

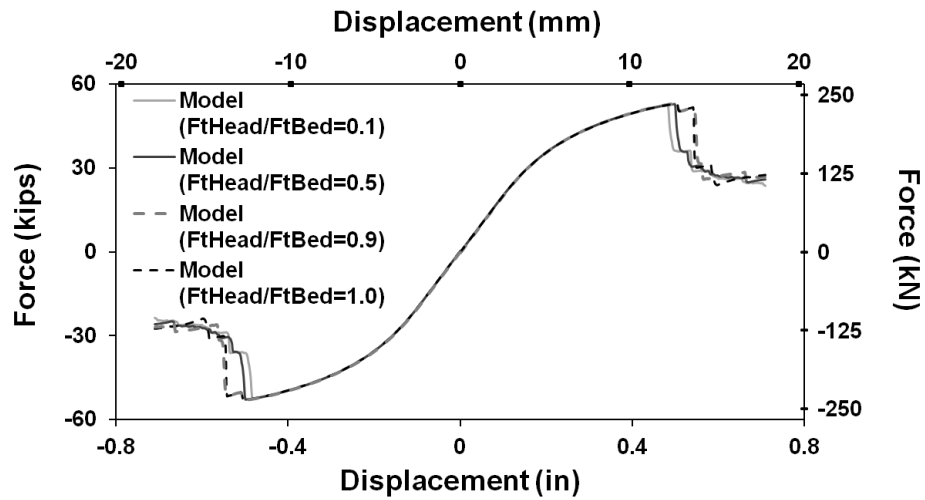


Figure 205: Influence of head joint bond strength on wall MI3 [4.92ft x 9.84ft (1.5m x 3m), 174psi (1.2 MPa) compression] *mortar properties from Table 24, Mortar with 2x Bond Strength and Cohesion

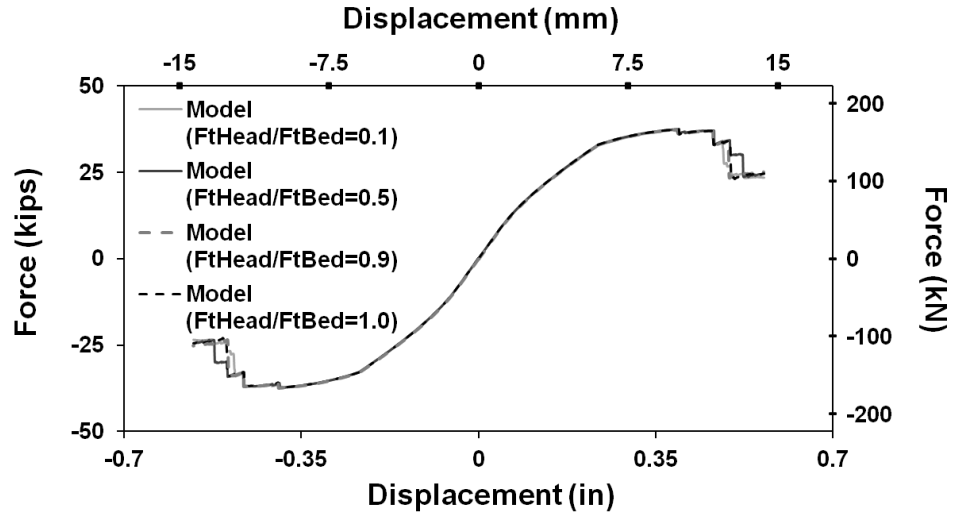


Figure 206: Influence of head joint bond strength on wall MI4 [4.92ft x 9.84ft (1.5m x 3m), 58psi (0.4MPa) compression] *mortar properties from Table 24, Magenes and Calvi (1992)

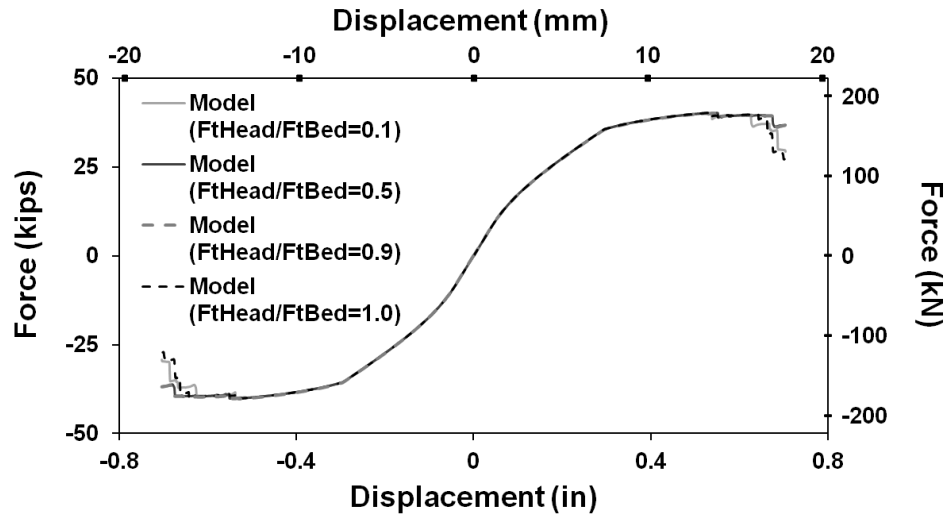


Figure 207: Influence of head joint bond strength on wall MI4 [4.92ft x 9.84ft (1.5m x 3m), 58psi (0.4MPa) compression] *mortar properties from Table 24, Mortar with 2x Bond Strength and Cohesion

Table 29: Material properties for FE models of column test (Nosho et. al. 1996)

	COMBINED SMEARED CRACK AND INTERFACE ELEMENT MODEL		SMEARED CRACK ELEMENTS ONLY (coarse mesh)	SMEARED CRACK ELEMENTS ONLY (fine mesh)
	Smeared Crack Element	Interface Element	Smeared Crack Element	Smeared Crack Element.
f'_c ksi (MPa)	5.57 (38.4)	-	5.57 (38.4)	5.57 (38.4)
f_t ksi (MPa)	0.557 (3.84)	0.557 (3.84)	0.557 (3.84)	0.557 (3.84)
G_n kip/in (N/mm)	-	0.001 (0.175)	-	-
G_{t2} kip/in (N/mm)	-	0.01 (1.75)	-	-
E ksi (MPa)	3800 (26200)	-	3100 (21374)	3100 (21374)
K_{nn} Kip/in ³ (N/mm ³)	-	5000 (1357)	-	-
μ_0	-	0.9	-	-
μ_r	-	0.7	-	-
r_0 ksi (MPa)	-	0.034 (0.234)	-	-
r_r ksi (MPa)	-	0.0013 (0.009)	-	-

Table 30: Material properties for FE models of column test (Lynn et. al. 1998)

	COMBINED SMEARED CRACK AND INTERFACE ELEMENT MODEL		SMEARED CRACK ELEMENTS ONLY
	Smeared Crack Element	Interface Element	Smeared Crack Element
f_c ksi (MPa)	3.6 (24.8)	-	3.6 (24.8)
f_t ksi (MPa)	0.36 (2.48)	0.36 (2.48)	0.36 (2.48)
G_{f1} kip/in (N/mm)	-	0.0014 (0.245)	-
G_{f2} kip/in (N/mm)	-	0.014 (2.45)	-
E ksi (MPa)	2500 (17237)	-	1900 (13100)
K_{nn} Kip/in ³ (N/mm ³)	-	2500 (679)	-
μ_0	-	0.8	
μ_r	-	0.7	
r_0 ksi (MPa)	-	0.034 (0.234)	-
r_r ksi (MPa)	-	0.0013 (0.009)	-

Table 31: Model properties for cyclic test of RC frame (Teymur et al. 2012)

	COMBINED SMEARED CRACK AND INTERFACE ELEMENT MODEL	
	Smeared Crack Element	Interface Element
f'_c ksi (MPa)	2.5 (17.2)	-
f_t ksi (MPa)	0.3 (2.07)	0.3 (2.07)
G_{r1} kip/in (N/mm)	-	0.0008 (0.14)
G_{r2} kip/in (N/mm)	-	0.008 (1.4)
E ksi (MPa)	2000 (13790)	-
K_{nn} Kip/in ³ (N/mm ³)	-	3000 (814)
μ_0	-	0.9
μ_r	-	0.7
r_0 ksi (MPa)	-	0.02 (0.14)
r_r ksi (MPa)	-	0.001 (0.007)

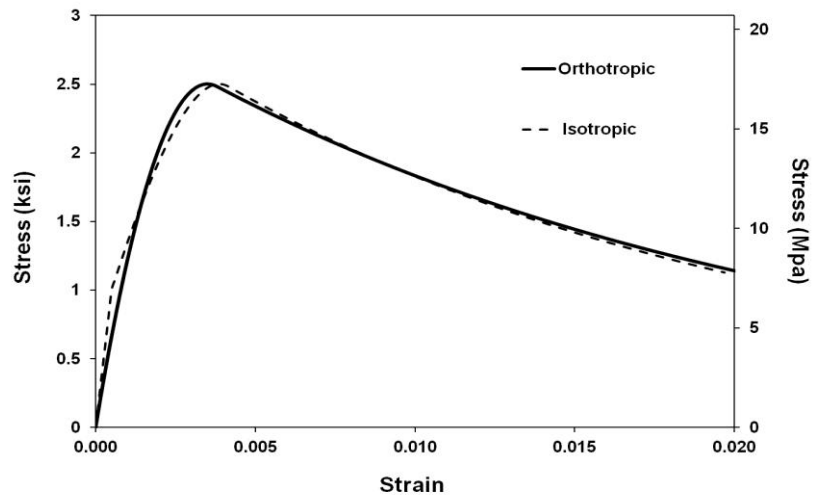


Figure 208: Concrete compressive stress vs. strain curve for finite element model of bare RC frame

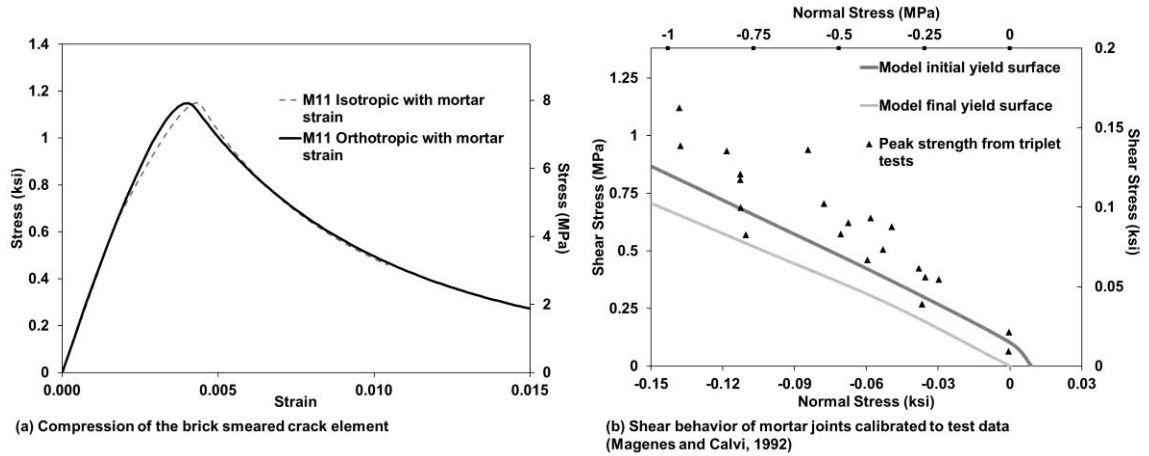


Figure 209: Masonry material calibration for models of URM walls (Magenes and Calvi 1992)

Table 32: Parameters for calibration to URM walls (Magenes and Calvi 1992)

SMEARED CRACK ELEMENTS		Brick	Mortar
E	ksi (MPa)	900 (6205)	Not Applicable
ε_1 (isotropic)	-	0.0012	
ε_2 (isotropic)	-	0.00139	
f_0	ksi (MPa)	0.63 (4.34)	
f_m^I	ksi (MPa)	1.15 (7.93)	
f_t^I	ksi (MPa)	0.175 (1.21)	
INTERFACE ELEMENTS			
D_n	kip/in (kN/mm)	5000 (876)	128.33 (22.47)
s_0	ksi (MPa)	0.175 (1.21)	0.009 (0.062)
G_f^I	kip/in* 10^{-6} (N/mm* 10^{-3})	135 (23.6)	4.25 (0.744)
G_f^{II}	kip/in* 10^{-6} (N/mm* 10^{-3})	135000 (236)	042.5 (7.44)
μ_0	-	0.85	0.5
μ_r	-	0.75	0.4
r_0	ksi (MPa)	0.04 (0.276)	0.01 (0.069)
r_r	ksi (MPa)	0.005 (0.034)	0.005 (0.034)

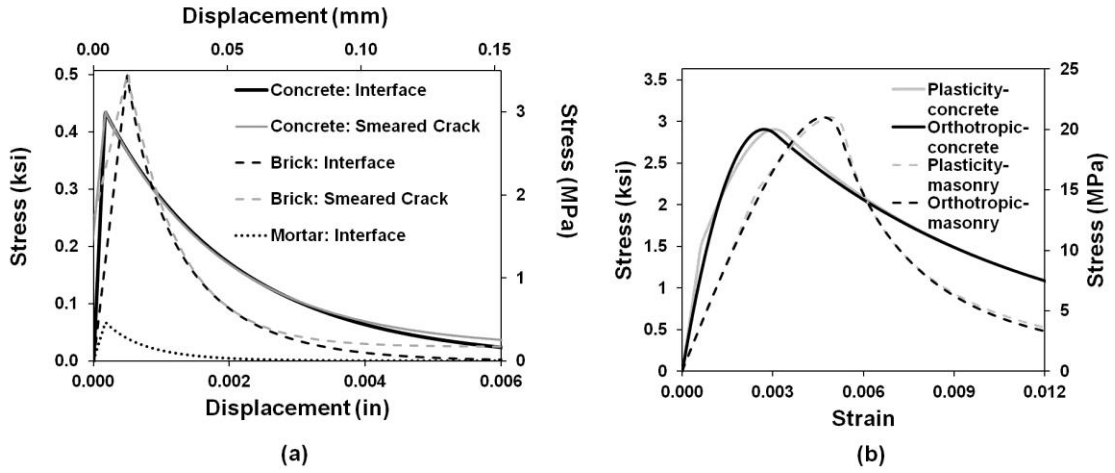


Figure 210: Concrete, brick and mortar material calibrations for (a) tension and (b) compression in the model of the 3-story 3-bay RC frame with HCT infills

Table 33: Summary of material properties and model parameters for the 3-story 3-bay RC frame with HCT infills

	CONCRETE			BRICK			MORTAR		
	Smeared Crack Element	Interface Element	Measured Prop.	Smeared Crack Element	Interface Element	Measured Prop.	Bed Joint Interface Element	Head Joint Interface Element	Measured Prop.
f'_c ksi (MPa)	2.9 (20)	-	2.9 (20)	3.05 (21)	-	3.7 (25.5) unit strength	-	-	0.7- (4.7)
f_t ksi (MPa)	0.44 (3)	0.44 (3)	-	0.46 (3.15)	0.46 (3.15)	-	0.068 (0.47)	0.068 (0.47)	-
G_n kip/in (N/mm)	-	0.001 (0.175)	-	-	0.0006 (0.099)	-	0.00005 (0.0087)	0.00005 (0.0087)	-
G_r kip/in (N/mm)	-	0.01 (1.75)	-	-	0.006 (0.99)	-	0.0005 (0.087)	0.0005 (0.087)	-
E ksi (MPa)	3050 (21000)	-	-	2030 (14000)	-	-	-	-	-
K_{nn} Kip/in ³ (N/mm ³)	-	2578 (700)	-	-	1013 (275)	-	387 (105)	387 (105)	-
μ_0	-	1.0	-	-	0.9	-	0.9	0.9	-
μ_r	-	0.9	-	-	0.8	-	0.8	0.8	-
r_0 ksi (MPa)	-	0.049 (0.34)	-	-	0.049 (0.34)	-	0.078 (0.54)	0.049 (0.34)	-
r_r ksi (MPa)	-	0.01 (0.07)	-	-	0.001 (0.007)	-	0.007 (0.05)	0.007 (0.05)	-

Table 34: Summary of material properties and model parameters for the initial models of the hybrid concrete-masonry test frames

	CONCRETE			UNGROUTED CMU			GROUTED CMU			MORTAR JOINTS			GROUT AND MORTAR JOINTS	
	Smeared Crack Element	Interface Element	Measured Prop.	Smeared Crack Element	Interface Element	Measured Prop.	Smeared Crack Element	Interface Element	Measured Prop.	Bed Joint Interface Element	Head Joint Interface Element	Measured Prop.	Bed Joint Interface Element	Measured Prop.
f'_c ksi (MPa)	4.0 (27.6)	-	4.0 (27.6)	1.4 (9.65)	-	1.4 (9.65)	2.6 (17.9)	-	2.6 (17.9)	-	-	-	-	-
f'_{c0} ksi (MPa)	2.4 (16.6)	-	-	1.0 (6.85)	-	-	1.5 (10.3)	-	-	-	-	-	-	-
f_t ksi (MPa)	0.61 (4.21)	0.61 (4.21)	0.61 (4.21)	0.17 (1.17)	0.17 (1.17)	-	0.3 (2.07)	0.3 (2.07)	-	0.042 (0.29)	0.021 (0.145)	0.042 (0.29)	0.216 (1.49)	0.216 (1.49)
G_1 kip/in (N/mm)	-	0.0015 (0.263)	-	-	0.0005 (0.088)	-	-	0.0006 (0.105)	-	0.0001 (0.018)	0.0001 (0.018)	-	0.0003 (0.053)	-
G_2 kip/in (N/mm)	-	0.015 (2.63)	-	-	0.005 (0.88)	-	-	0.006 (1.05)	-	0.001 (0.18)	0.001 (0.18)	-	0.003 (0.53)	-
E ksi (MPa)	3440 (23700)	-	3440 (23700)	4200 (28900)	-	*	3000 (20700)	-	*	-	-	-	-	-
K_{nn} Kip/in ³ (N/mm ³)	-	7000 (1900)	-	-	3000 (814)	-	-	3000 (814)	-	575 (156)	575 (156)	-	1600	-
μ_0	-	0.9	-	-	0.9	-	-	0.9	-	0.75	0.75	*	0.56	*
μ_r	-	0.7	-	-	0.7	-	-	0.7	-	0.6	0.6	*	0.56	*
r_0 ksi (MPa)	-	0.02 (0.138)	-	-	0.02 (0.138)	-	-	0.02 (0.138)	-	0.0025 (0.017)	0.0025 (0.017)	*	0.00001 (0.00007)	*
r_r ksi (MPa)	-	0.005 (0.034)	-	-	0.005 (0.034)	-	-	0.005 (0.034)	-	0.00001 (0.00007)	0.00001 (0.00007)	*	0.00001 (0.00007)	*

*these properties were calibrated from curve fits to test data, see Chapter 5

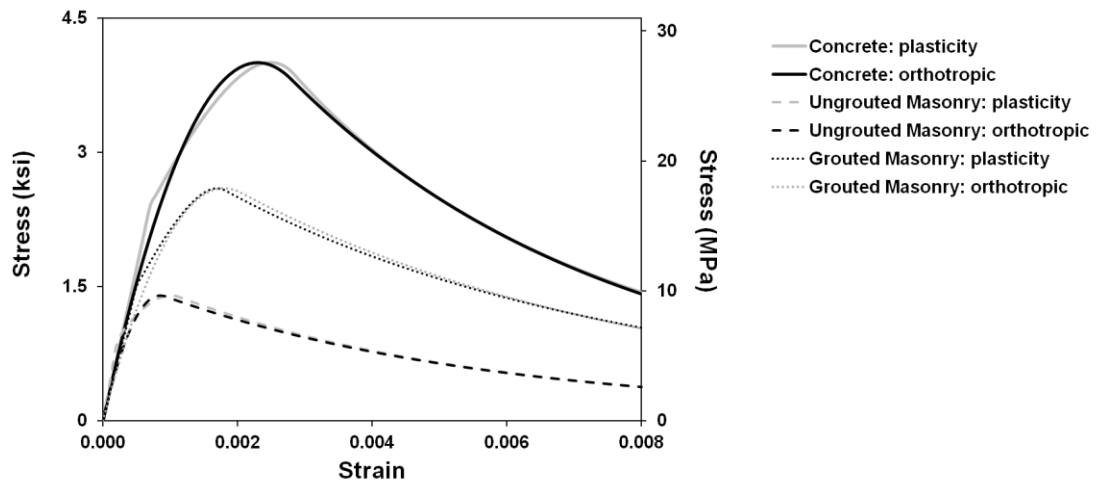


Figure 211: Compressive stress vs. strain for concrete, grouted masonry, and ungrouted masonry in the initial finite element models of the hybrid concrete-masonry test frames

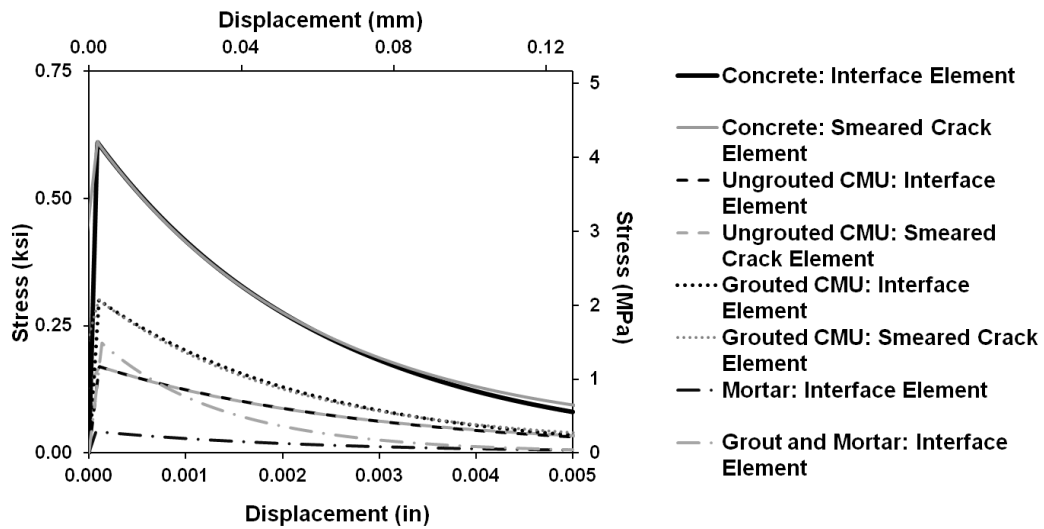


Figure 212: Tensile stress vs. strain for concrete, grouted CMU, ungrouted CMU, mortar and bed joints in grouted cells* in the initial finite element models of the hybrid concrete-masonry test frames *bed joints in grouted cells are the grout and mortar interface

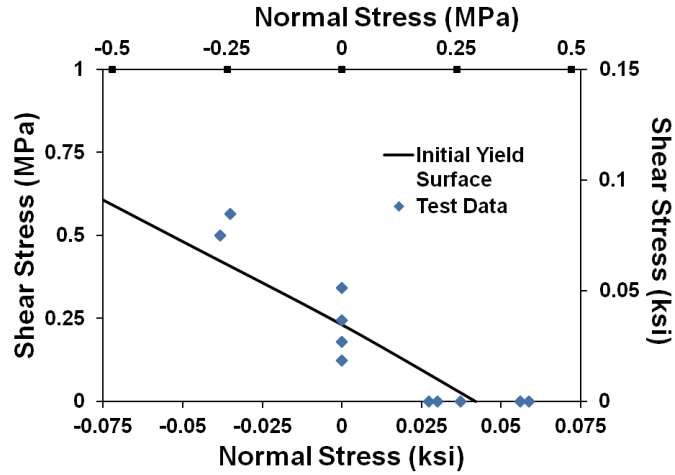


Figure 213: Ungrouted bed joint interface element failure surface in initial finite element models of hybrid concrete-masonry test frames and test data from bond wrench tests and triplet tests

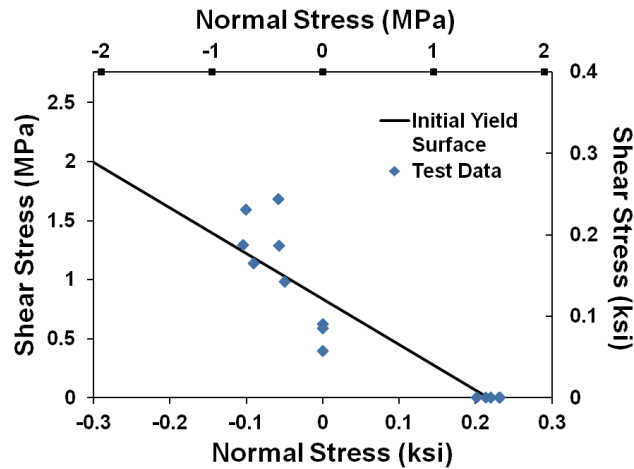


Figure 214: Grouted bed joint interface element failure surface in initial finite element models of hybrid concrete-masonry test frames and test data from bond wrench tests and triplet tests

Table 35: Summary of material properties and model parameters for revised models of the hybrid concrete-masonry test frames

	CONCRETE		UNGROUTED CMU		GROUT CORES		MORTAR JOINTS		
	Smeared Crack Element	Interface Element	Smeared Crack Element	Interface Element	Smeared Crack Element	Interface Element	Bed Joint Interface Element	Head Joint Interface Element	Beam-Wall Interface Element
f'_c ksi (MPa)	4.77 (32.89)	-	1.4 (9.65)	-	3.0 (20.68)	-	-	-	-
f'_{c0} ksi (MPa)	2.9 (20.00)	-	1.0 (6.85)	-	1.8 (12.41)	-	-	-	-
f_t ksi (MPa)	0.73 (5.03)	0.73 (5.03)	0.17 (1.17)	0.17 (1.17)	0.3 (2.07)	0.3 (2.07)	0.056 (0.386)	0.042 (0.290)	0.028 (0.193)
G_{11} kip/in (N/mm)	-	0.001 (0.18)	-	0.0005 (0.088)	-	0.0006 (0.105)	0.0001 (0.018)	0.0001 (0.018)	0.0001 (0.018)
G_{12} kip/in (N/mm)	-	0.01 (1.8)	-	0.005 (0.88)	-	0.006 (1.05)	0.001 (0.18)	0.001 (0.18)	0.001 (0.18)
E ksi (MPa)	3760 (25900)	-	4200 (28900)	-	3120 (21500)	-	-	-	-
K_{nn} Kip/in ³ (N/mm ³)	-	5000 (1360)	-	3000 (814)	-	3000 (814)	575 (156)	575 (156)	50 (13.57)
μ_0	-	1.0	-	0.9	-	0.8	0.8	0.8	0.8
μ_r	-	0.8	-	0.8	-	0.7	0.7	0.7	0.7
r_0 ksi (MPa)	-	0.02 (0.138)	-	0.02 (0.138)	-	0.02 (0.138)	0.007 (0.048)	0.007 (0.048)	0.005 (0.034)
r_r ksi (MPa)	-	0.005 (0.034)	-	0.005 (0.034)	-	0.005 (0.034)	0.00001 (0.00007)	0.00001 (0.00007)	0.00001 (0.00007)

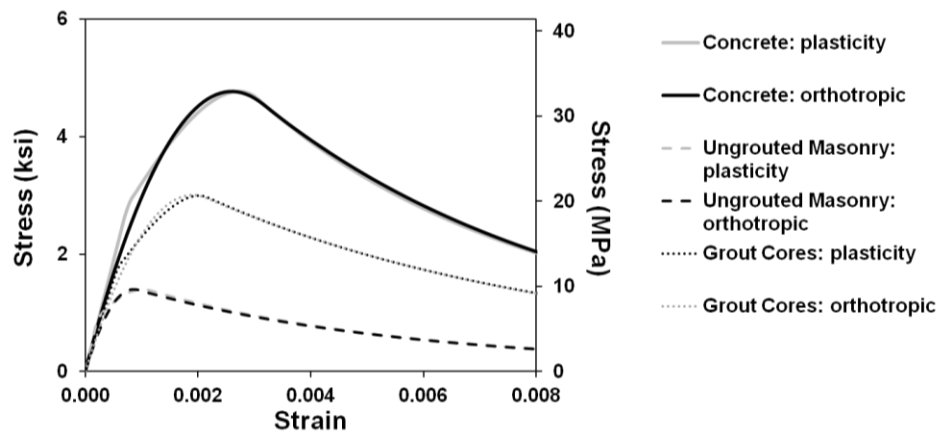


Figure 215: Compressive stress vs. strain for concrete, grouted masonry, and ungrouted masonry in the revised finite element models of the hybrid concrete-masonry test frames

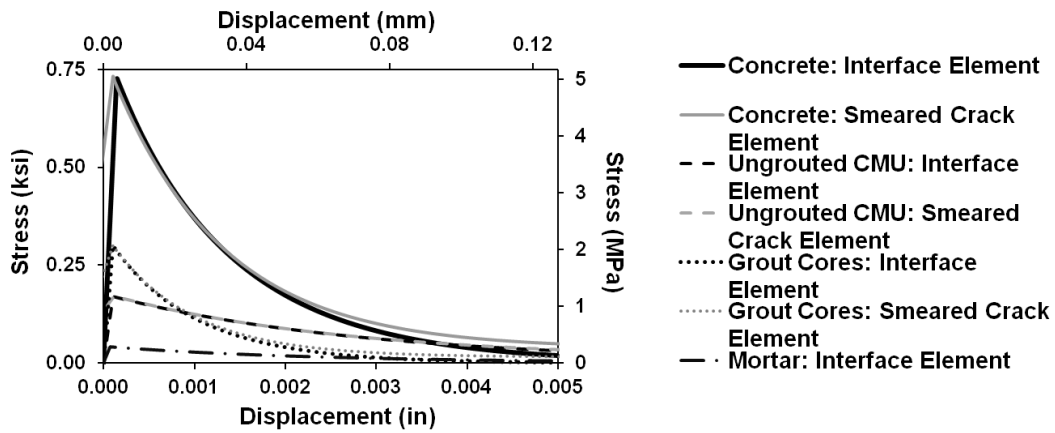


Figure 216: Tensile stress vs. strain for concrete, ungrouted CMU, grout cores and mortar in the revised finite element models of the hybrid concrete-masonry test frames

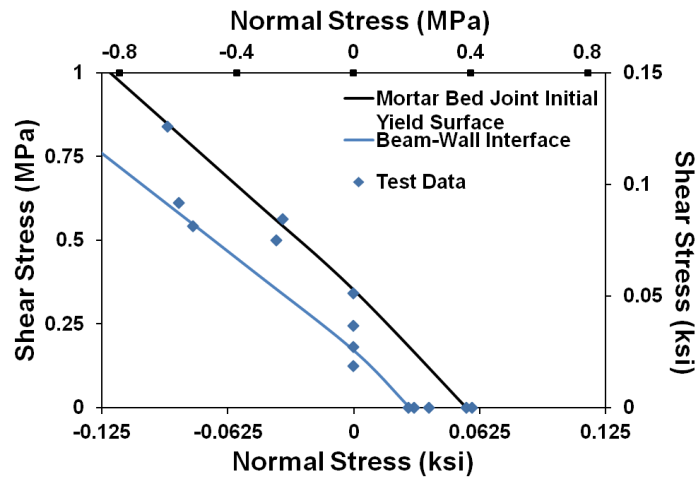


Figure 217: UngROUTed bed joint interface element failure surface in revised finite element models of hybrid concrete-masonry test frames and test data from bond wrench tests and triplet tests

Calculation to Account for Additional Shear Stiffness in the Grouted Masonry Cells through the Splice Region of Dowel Connections:

Grout Shear Modulus, G_g

Steel Shear Modulus, G_s

"Fiber Volume" of Steel Reinforcement, 2 #5 bars:

$$V_f = \frac{2 \cdot 0.31 \text{ in}^2}{A_g} = 0.01 \text{ where } A_g \text{ is the area of the grouted core}$$

Composite Shear Modulus:

$$G_{comp} = \frac{G_g}{\left[1 - \sqrt{V_f} \left(1 - \frac{G_g}{G_s}\right)\right]}$$

$$\frac{G_{comp}}{G_g} = 1.098$$

assumed 10% increase in shear stiffness due to presence of splice.

Local Bending Contribution of Vertical Masonry Reinforcement:

Bending capacity of single #5 bar

$$d_{\#5bar} = 0.625 \text{ in}$$

$$I_{\#5bar} = \frac{\pi}{4} \left(\frac{d_{\#5bar}}{2}\right)^4$$

$$y_{\#5bar} = \frac{d_{\#5bar}}{2}$$

$$F_y = 60 \text{ ksi}$$

$$M_{\#5bar} = \frac{F_y I_{\#5bar}}{y_{\#5bar}} = 1.88 \text{ kip} \cdot \text{in}$$

Distribute a portion of the steel to the edges of the grouted unit to model this local bending capacity using truss elements:

$$A_{outer} = \frac{M_{\#5bar}}{w_{cell} * F_y} = 0.003 in^2 \text{ (~1\% of steel to outer edge)}$$

Repeat the calculation for the splice regions:

$$A_{outer2} = \frac{2M_{\#5bar}}{w_{cell} * F_y} = 0.006 in^2 \text{ (~1\% of steel to outer edge)}$$

Table 36: Summary of material properties and model parameters for parametric study on masonry material properties-increased grout strength (x2)

	CONCRETE		UNGROUTED CMU		GROUT CORES		MORTAR JOINTS		
	Smearred Crack Element	Interface Element	Smearred Crack Element	Interface Element	Smearred Crack Element	Interface Element	Bed Joint Interface Element	Head Joint Interface Element	Beam-Wall Interface Element
f'_c ksi (MPa)	4.77 (32.89)	-	1.4 (9.65)	-	6.0 (41.37)	-	-	-	-
f'_{c0} ksi (MPa)	2.9 (20.00)	-	1.0 (6.85)	-	3.6 (24.82)	-	-	-	-
f_t ksi (MPa)	0.73 (5.03)	0.73 (5.03)	0.17 (1.17)	0.17 (1.17)	0.6 (4.14)	0.6 (4.14)	0.056 (0.386)	0.042 (0.290)	0.028 (0.193)
G_{n1} kip/in (N/mm)	-	0.001 (0.18)	-	0.0005 (0.088)	-	0.0012 (0.21)	0.0001 (0.018)	0.0001 (0.018)	0.0001 (0.018)
G_{n2} kip/in (N/mm)	-	0.01 (1.8)	-	0.005 (0.88)	-	0.012 (2.1)	0.001 (0.18)	0.001 (0.18)	0.001 (0.18)
E ksi (MPa)	3760 (25900)	-	4200 (28900)	-	4415 (30440)	-	-	-	-
K_{nn} Kip/in ³ (N/mm ³)	-	5000 (1360)	-	3000 (814)	-	3000 (814)	575 (156)	575 (156)	50 (13.57)
μ_0	-	1.0	-	0.9	-	0.8	0.8	0.8	0.8
μ_r	-	0.8	-	0.8	-	0.7	0.7	0.7	0.7
r_0 ksi (MPa)	-	0.02 (0.138)	-	0.02 (0.138)	-	0.02 (0.138)	0.007 (0.048)	0.007 (0.048)	0.005 (0.034)
r_r ksi (MPa)	-	0.005 (0.034)	-	0.005 (0.034)	-	0.005 (0.034)	0.00001 (0.00007)	0.00001 (0.00007)	0.00001 (0.00007)

Table 37: Summary of material properties and model parameters for parametric study on masonry material properties-decreased grout strength ($\div 2$)

	CONCRETE		UNGROUTED CMU		GROUT CORES		MORTAR JOINTS		
	Smeared Crack Element	Interface Element	Smeared Crack Element	Interface Element	Smeared Crack Element	Interface Element	Bed Joint Interface Element	Head Joint Interface Element	Beam-Wall Interface Element
f'_c ksi (MPa)	4.77 (32.89)	-	1.4 (9.65)	-	1.5 (10.34)	-	-	-	-
f'_{c0} ksi (MPa)	2.9 (20.00)	-	1.0 (6.85)	-	0.9 (6.21)	-	-	-	-
f_t ksi (MPa)	0.73 (5.03)	0.73 (5.03)	0.17 (1.17)	0.17 (1.17)	0.15 (1.03)	0.15 (1.03)	0.056 (0.386)	0.042 (0.290)	0.028 (0.193)
G_{11} kip/in (N/mm)	-	0.001 (0.18)	-	0.0005 (0.088)	-	0.0003 (0.053)	0.0001 (0.018)	0.0001 (0.018)	0.0001 (0.018)
G_{12} kip/in (N/mm)	-	0.01 (1.8)	-	0.005 (0.88)	-	0.003 (0.53)	0.001 (0.18)	0.001 (0.18)	0.001 (0.18)
E ksi (MPa)	3760 (25900)	-	4200 (28900)	-	2210 (15200)	-	-	-	-
K_{nn} Kip/in ³ (N/mm ³)	-	5000 (1360)	-	3000 (814)	-	3000 (814)	575 (156)	575 (156)	50 (13.57)
μ_0	-	1.0	-	0.9	-	0.8	0.8	0.8	0.8
μ_r	-	0.8	-	0.8	-	0.7	0.7	0.7	0.7
r_0 ksi (MPa)	-	0.02 (0.138)	-	0.02 (0.138)	-	0.02 (0.138)	0.007 (0.048)	0.007 (0.048)	0.005 (0.034)
r_r ksi (MPa)	-	0.005 (0.034)	-	0.005 (0.034)	-	0.005 (0.034)	0.00001 (0.00007)	0.00001 (0.00007)	0.00001 (0.00007)

Table 38: Summary of material properties and model parameters for parametric study on masonry material properties-increased ungrouted prism strength (x2)

	CONCRETE		UNGROUTED CMU		GROUT CORES		MORTAR JOINTS		
	Smeared Crack Element	Interface Element	Smeared Crack Element	Interface Element	Smeared Crack Element	Interface Element	Bed Joint Interface Element	Head Joint Interface Element	Beam-Wall Interface Element
f'_c ksi (MPa)	4.77 (32.89)	-	2.8 (19.31)	-	3.0 (20.68)	-	-	-	-
f'_{c0} ksi (MPa)	2.9 (20.00)	-	1.96 (13.51)	-	1.8 (12.41)	-	-	-	-
f_t ksi (MPa)	0.73 (5.03)	0.73 (5.03)	0.17 (1.17)	0.17 (1.17)	0.3 (2.07)	0.3 (2.07)	0.056 (0.386)	0.042 (0.290)	0.028 (0.193)
G_{11} kip/in (N/mm)	-	0.001 (0.18)	-	0.0005 (0.088)	-	0.0006 (0.105)	0.0001 (0.018)	0.0001 (0.018)	0.0001 (0.018)
G_{12} kip/in (N/mm)	-	0.01 (1.8)	-	0.005 (0.88)	-	0.006 (1.05)	0.001 (0.18)	0.001 (0.18)	0.001 (0.18)
E ksi (MPa)	3760 (25900)	-	4200 (28900)	-	3120 (21500)	-	-	-	-
K_{nn} Kip/in ³ (N/mm ³)	-	5000 (1360)	-	3000 (814)	-	3000 (814)	575 (156)	575 (156)	50 (13.57)
μ_0	-	1.0	-	0.9	-	0.8	0.8	0.8	0.8
μ_r	-	0.8	-	0.8	-	0.7	0.7	0.7	0.7
r_0 ksi (MPa)	-	0.02 (0.138)	-	0.02 (0.138)	-	0.02 (0.138)	0.007 (0.048)	0.007 (0.048)	0.005 (0.034)
r_r ksi (MPa)	-	0.005 (0.034)	-	0.005 (0.034)	-	0.005 (0.034)	0.00001 (0.00007)	0.00001 (0.00007)	0.00001 (0.00007)

Table 39: Summary of material properties and model parameters for parametric study on masonry material properties-type N mortar

	CONCRETE		UNGROUTED CMU		GROUT CORES		MORTAR JOINTS		
	Smeared Crack Element	Interface Element	Smeared Crack Element	Interface Element	Smeared Crack Element	Interface Element	Bed Joint Interface Element	Head Joint Interface Element	Beam-Wall Interface Element
f'_c ksi (MPa)	4.77 (32.89)	-	1.4 (9.65)	-	3.0 (20.68)	-	-	-	-
f'_{c0} ksi (MPa)	2.9 (20.00)	-	1.0 (6.85)	-	1.8 (12.41)	-	-	-	-
f_t ksi (MPa)	0.73 (5.03)	0.73 (5.03)	0.17 (1.17)	0.17 (1.17)	0.3 (2.07)	0.3 (2.07)	0.072 (0.50)	0.054 (0.37)	0.036 (0.25)
G_{11} kip/in (N/mm)	-	0.001 (0.18)	-	0.0005 (0.088)	-	0.0006 (0.105)	0.0002 (0.035)	0.0002 (0.035)	0.0001 (0.018)
G_{12} kip/in (N/mm)	-	0.01 (1.8)	-	0.005 (0.88)	-	0.006 (1.05)	0.002 (0.35)	0.002 (0.35)	0.001 (0.18)
E ksi (MPa)	3760 (25900)	-	4200 (28900)	-	3120 (21500)	-	-	-	-
K_{nn} Kip/in ³ (N/mm ³)	-	5000 (1360)	-	3000 (814)	-	3000 (814)	575 (156)	575 (156)	50 (13.57)
μ_0	-	1.0	-	0.9	-	0.8	0.75	0.75	0.75
μ_r	-	0.8	-	0.8	-	0.7	0.65	0.65	0.65
r_0 ksi (MPa)	-	0.02 (0.138)	-	0.02 (0.138)	-	0.02 (0.138)	0.02 (0.138)	0.02 (0.138)	0.01 (0.07)
r_r ksi (MPa)	-	0.005 (0.034)	-	0.005 (0.034)	-	0.005 (0.034)	0.005 (0.034)	0.005 (0.034)	0.005 (0.034)

APPENDIX D
SUPPLEMENTAL DATA AND EXAMPLE CALCULATIONS FROM
EXPERIMENTS

Post-Tensioned Loads on the Columns:

Tributary Area

$$A_{trib} = 5ft * 10ft = 50ft^2 (4.65 m^2)$$

Dead Load

$$w_{slab} = A_{trib} 0.5ft * 150 \frac{lb}{ft^3}$$

$$w_{SDL} = A_{trib} 20 \frac{lb}{ft^2}$$

$$w_{CMU} = 23.625lb/ft$$

$$w_{core} = \frac{8in * 4.85in * 5.5in}{1728in^3} ft^3 * 150 \frac{lb}{ft^3}$$

$$w_{course} = 6.5w_{CMU} + 4w_{core}$$

$$w_{wall} = 14w_{course}$$

$$w_{beam} = 1ft * 1.167ft * 10ft * 150 \frac{lb}{ft^3}$$

$$w_{col} = 1.667ft * 1.667ft * 10ft * 150 \frac{lb}{ft^3}$$

$$L_D = 5w_{slab} + 5w_{SDL} + 3w_{wall} + 11w_{course} + 4w_{beam} + 4w_{col} = 61.08 \text{ kips (271.7 kN)}$$

*1 courses are missing from the half wall built, 3 courses to each column

Force in bars due to stretching during the test

$$L_{undeformed} = 120in (304.8 cm)$$

$$L_{deformed} = \sqrt{L_{undeformed}^2 + (2in)^2}$$

$$\epsilon_{bar} = \frac{L_{deformed} - L_{undeformed}}{L_{undeformed}} = 0.000142$$

$$A_{bar} = 1.25in^2$$

$$F_{bar} = 29700ksi * \epsilon_{bar} * A_{bar} = 5.26kips (23.4 kN)$$

*anticipated max displacement was approximately 4in. Designed for 2in. average displacement.

Post-tensioning load in each column

$$L_p = \frac{L_D}{2} - F_{bar} = 25.28kip (112.5 kN)$$

Moment Capacity of a Bare RC Frame with the Same Reinforcement as the Experimental Frames:

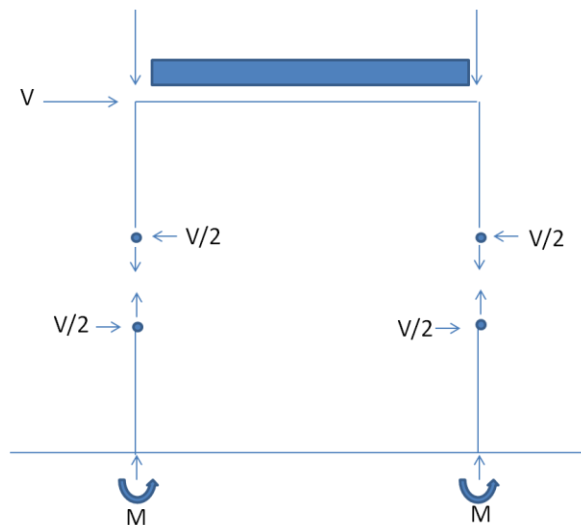


Figure 218: Portal frame

From ACI 318

$$M_{col} = 228 \text{ kip} * \text{ft} (309.1 \text{ kN} * \text{m})$$

From Portal Method

$$V_{Capacity} = \frac{M_{col} * 2}{L_{col}/2} = 91.2 \text{ kip} (405.7 \text{ kN})$$

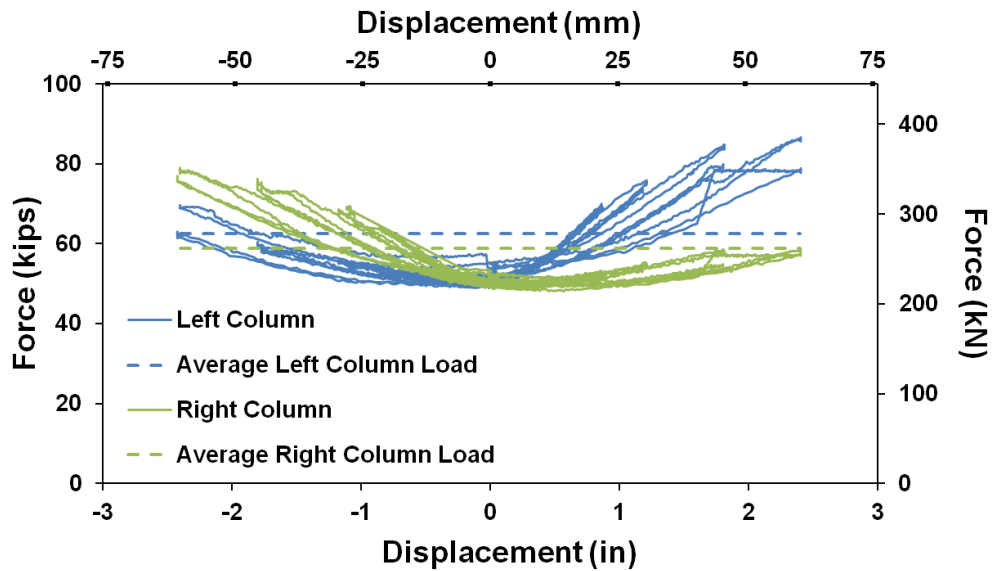


Figure 219: Frame 1 column loads

Left column in tension for positive (push) cycles. Right column in compression for positive (push) cycles.

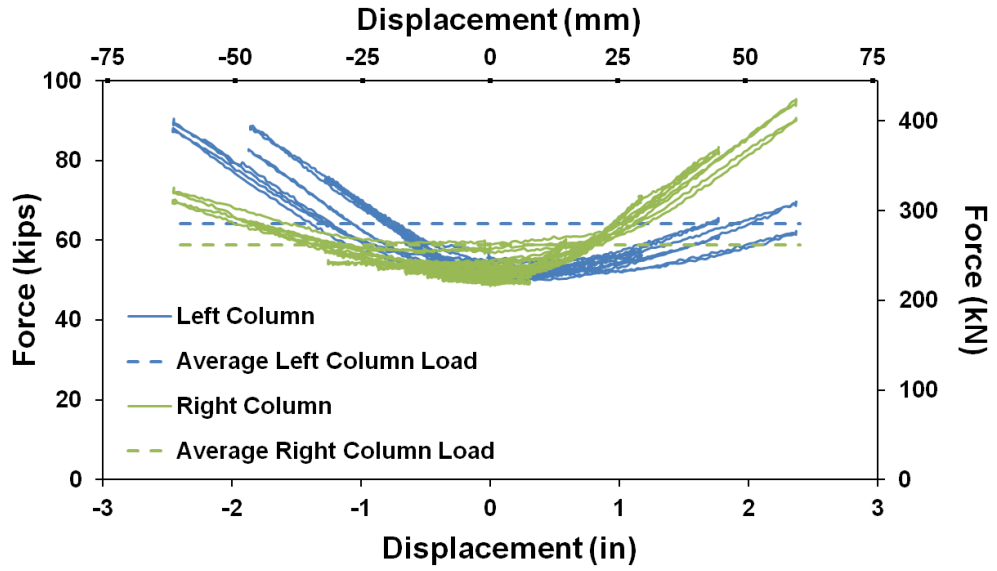


Figure 220: Frame 2 column loads

Left column in compression for positive (push) cycles. Right column in tension for positive (push) cycles.

(space left blank intentionally)

Calculation for Shear and Flexural Deformations in the RC columns and the Masonry Infill:

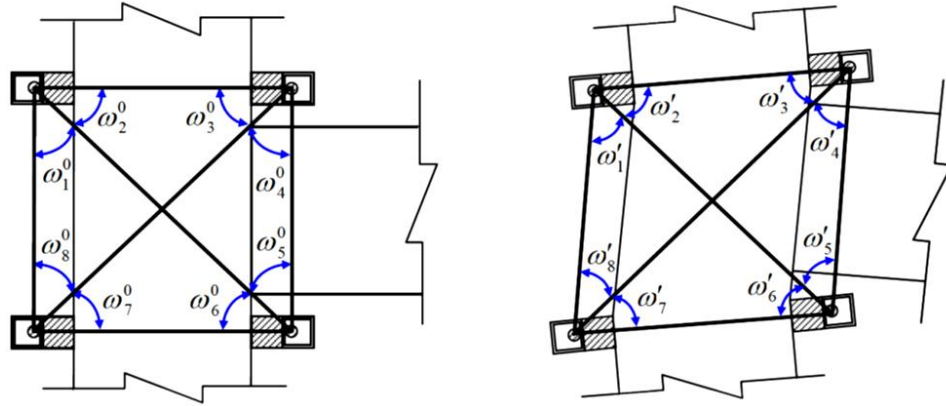


Figure 221: Shear deformation schematic

Shear Strain

$$\gamma_{xy} = \frac{1}{4} \left[\sum_{i=1,2,5,6} (\omega'_i - \omega_i^0) - \sum_{i=3,4,7,8} (\omega'_i - \omega_i^0) \right]$$

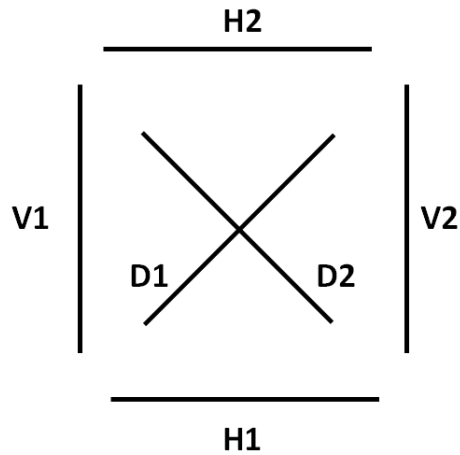


Figure 222: Gage length diagram

Curvature

for small deformations curvature can be approximated as

$$\theta = \frac{\Delta V1 - \Delta V2}{H1}$$

Table 40: Crack data Frame 1, column in tension during positive (push) cycles

0.86 inches (20.85 mm) Lateral Displacement				
Topmost crack →Bottom crack	Crack width in (mm)	Distance from last crack* in (cm)	Gage length in (cm)	Strain in bar
	0.016 (0.406)	13 (33.02)		
	0.013 (0.330)	4.25 (10.80)	8.625 (21.91)	0.0015
	0.005 (0.127)	6.25 (15.98)	5.25 (13.34)	0.00095
	0.01 (0.254)	6 (15.24)	6.125 (15.56)	0.0016
	0.01 (0.254)	4.75 (12.07)	5.375 (13.65)	0.0019
	0.003 (0.076)	12.5 (31.75)	8.625 (21.91)	0.00024
2.4 inches (60.96 mm) Lateral Displacement				
Topmost crack →Bottom crack	Crack width in (mm)	Distance from last crack* in (cm)	Gage length in (cm)	Strain in bar
	0.005 (0.127)	12.5 (31.75)		
	0.005 (0.127)	4.5 (11.43)	8.5 (21.59)	0.00059
	0.005 (0.127)	6.5 (16.51)	5.5 (13.97)	0.00091
	0.007 (0.178)	5.5 (13.97)	6 (15.24)	0.0012
	0.016 (0.406)	4.5 (11.43)	5 (12.7)	0.0032
	0.016 (0.406)	12.25 (31.11)	8.375 (21.27)	0.0019
	0.025(0.635)	5.8 (14.73)	9.025 (22.92)	0.0028
	0.025 (0.635)	5.25 (13.34)	5.525 (14.03)	0.0045
	0.03 (0.762)	4 (10.16)	4.625 (11.74)	0.0065
0.05 (1.270)	7.5 (19.05)	5.75 (14.61)	0.0087	

*for the bottom crack, this is the distance from the foundation

Table 41: Crack data Frame 2, column in tension during positive (push) cycles

1.8 inches (45.72 mm) Lateral Displacement				
Topmost crack →Bottom crack	Crack width in (mm)	Distance from last crack* in (cm)	Gage length in (cm)	Strain in bar
	0.005 (0.127)	6 (15.24)		
	0.007(0.178)	4.5 (11.43)	5.25 (13.34)	0.0013
	0.005 (0.127)	5 (12.70)	4.75 (12.07)	0.0011
	0.01 (0.254)	12.5 (31.75)	8.75 (22.22)	0.0011
	0.025 (0.635)	10.5 (26.67)	11.5 (29.21)	0.0022
	0.025 (0.635)	11 (27.94)	10.75 (27.31)	0.0023
	0.009 (0.229)	5.5 (13.97)	8.25 (20.96)	0.0011
2.4 inches (60.96 mm) Lateral Displacement				
Topmost crack →Bottom crack	Crack width in (mm)	Distance from last crack* in (cm)	Gage length in (cm)	Strain in bar
	0.005 (0.127)	6 (15.24)		
	0.007(0.178)	4.5 (11.43)	5.25 (13.34)	0.0013
	0.005 (0.127)	5 (12.70)	4.75 (12.07)	0.0011
	0.016 (0.406)	12.5 (31.75)	8.75 (22.22)	0.0018
	0.035 (0.889)	10.5 (26.67)	11.5 (29.21)	0.0030
	0.035 (0.889)	11 (27.94)	10.75 (27.31)	0.0033
	0.04 (1.016)	5.5 (13.97)	8.25 (20.96)	0.0048

*for the bottom crack, this is the distance from the foundation

Table 42: Crack data frame 2, column in compression during positive (push) cycles

1.8 inches (45.72 mm) Lateral Displacement				
crack Topmost crack →Bottom	Crack width in (mm)	Distance from last crack* in (cm)	Gage length in (cm)	Strain in bar
	0.007(0.178)	10.5 (26.67)		
	0.016 (0.406)	4 (10.16)	7.25 (18.42)	0.0022
	0.01 (0.254)	5 (12.70)	4.5 (11.43)	0.0022
	0.013 (0.330)	3.5 (8.89)	4.25 (10.80)	0.0031
	0.015 (0.381)	9 (22.86)	6.25 (15.88)	0.0024
	0.02 (0.508)	3.5 (8.89)	6.25 (15.88)	0.0032
	0.02 (0.508)	8 (20.32)	5.75 (14.61)	0.0035
	0.035(0.889)	7 (17.78)	7.5 (19.05)	0.0047
2.4 inches (60.96 mm) Lateral Displacement				
crack Topmost crack →Bottom	Crack width in (mm)	Distance from last crack* in (cm)	Gage length in (cm)	Strain in bar
	0.007(0.178)	10.5 (26.67)		
	0.016 (0.406)	4 (10.16)	7.25 (18.42)	0.0022
	0.016 (0.406)	5 (12.7)	4.5 (11.43)	0.0036
	0.013 (0.330)	3.5 (8.89)	4.25 (10.80)	0.0031
	0.02 (0.508)	9 (22.86)	6.25 (15.88)	0.0032
	0.025 (0.635)	3.5 (8.89)	6.25 (15.88)	0.004
	0.02 (0.508)	8 (20.32)	5.75 (14.61)	0.0035
	0.04 (1.016)	7 (17.78)	7.5 (19.05)	0.0053

*for the bottom crack, this is the distance from the foundation

Calculation for Strains in the Vertical Column Reinforcement as a Function of Crack Width and Location:

Gage length

$$L_{gage} = \frac{d_{last} + d_{next}}{2}$$

where d_{last} is the distance to crack under consideration from crack below and d_{next} is the distance to crack under consideration from crack above.

$$\epsilon_{bar} = \frac{w_{crack}}{L_{gage}}$$

where w_{crack} is the crack width

Calculation for Adjusting Amplitude of Negative (Pull) Cycles for Bar Stretching:

1. Record force required to reach displacement Δ_i

$$F_{\Delta i}$$

2. Calculate the stress in the DYWIDAG bars if the same force was applied in the negative cycle:

$$\sigma_b = \frac{F_{\Delta i}}{4A_b}$$

3. Calculate the strain in the bars

$$\varepsilon_b = \frac{\sigma_b}{E_b}$$

4. Calculate the displacement of the loading plate due to stretching of the bars

$$\Delta_b = l_b \varepsilon_b$$

5. Calculate the displacement to pull the structure in the negative cycle

$$\Delta_{-i} = \Delta_i + \Delta_b$$

The same stretching was subtracted from the recorded displacement at the actuator head:

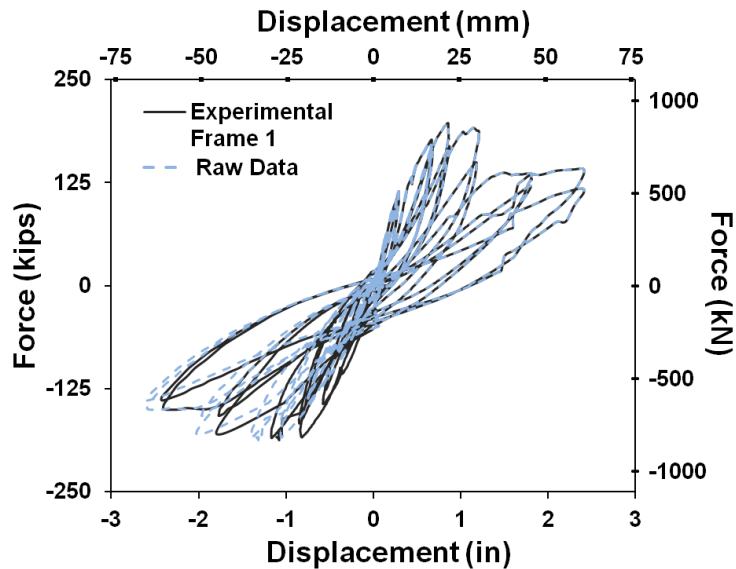


Figure 223: Processed and raw force-displacement data for Frame 1 with dowel connections on all edges of the masonry infill

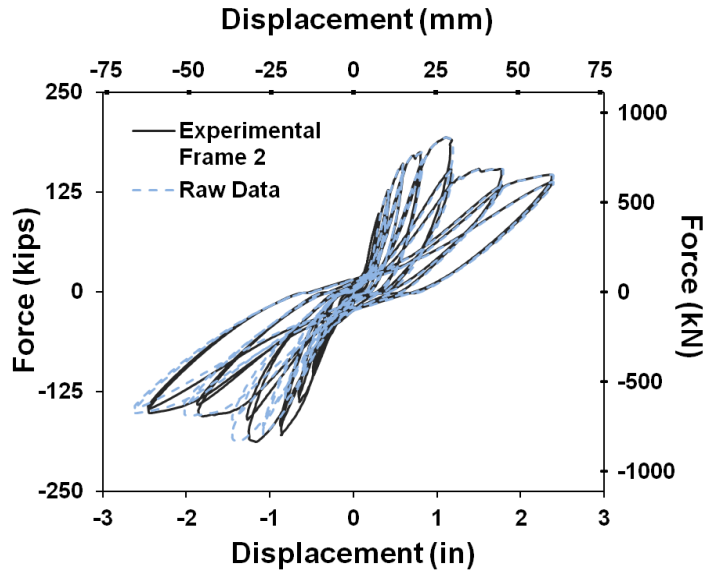


Figure 224: Processed and raw force-displacement data for Frame 2 with dowel connections only at the base of the masonry infill

APPENDIX E

CALCULATIONS FOR SIMPLIFIED MODELS

Elastic Transformed Section Model:

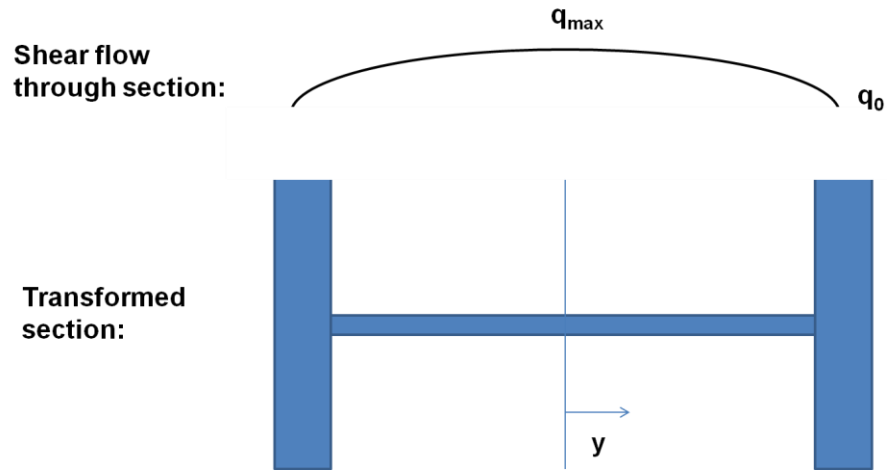


Figure 225: Shear flow through transformed section

$$f_m = 1400 \text{psi} (9.65 \text{MPa})$$

$$E_m = 900 f_m$$

$$f_c = 4000 \text{psi} (27.58 \text{MPa})$$

$$E_c = 57000 \text{psi} \sqrt{f_c} = 3605000 \text{psi} (24856 \text{MPa})$$

$$l_{col} = w_{col} = 20 \text{in} (50.8 \text{cm})$$

$$A_{col} = 400 \text{in}^2 (2581 \text{cm}^2)$$

$$A_{col_masonry} = \frac{E_c}{E_m} A_{col} = 11444 \text{in}^2 (73832 \text{cm}^2)$$

$$t_{col_masonry} = \frac{A_{col_masonry}}{l_{col}} = 57.2 \text{in} (145.3 \text{cm})$$

$$t_{infill} = 2.5 \text{in} (6.35 \text{cm})$$

$$l_{infill} = 100 \text{in} (254 \text{cm})$$

$$I_{trans} = \frac{t_{infill} l_{infill}^3}{12} + 2 \frac{t_{col_masonry} l_{column}^3}{12} + 2 t_{col_masonry} l_{col} \left(\frac{l_{infill} + l_{col}}{2} \right)^2$$

$$= 8240204 in^4 (342983186 cm^4)$$

$$Q_{max} = t_{col_masonry} l_{col} \left(\frac{l_{infill} + l_{col}}{2} \right) + t_{masonry} \frac{l_{infill}}{2} \frac{l_{infill}}{4}$$

$$= 71792 in^3 (117643 cm^3)$$

$$N_v = 122 kips (542.7 kN)$$

$$A_n = l_{infill} t_{infill} + 2 l_{col} b_{col_masonry} = 2538 in^2 (16323 cm^2)$$

$$f_{vn} = \min \left(3.8 \sqrt{f'_m}, 300 psi (2068 kPa), 56 psi (386 kPa) + 0.45 \frac{N_v}{A_n} \right)$$

$$= 77.6 psi (0.535 MPa)$$

$$V_{cracking} = \frac{f_{vn} I_{trans} t_{infill}}{Q_{max}} = 22.27 kips (99.1 kN)$$

Cracked Section Model:

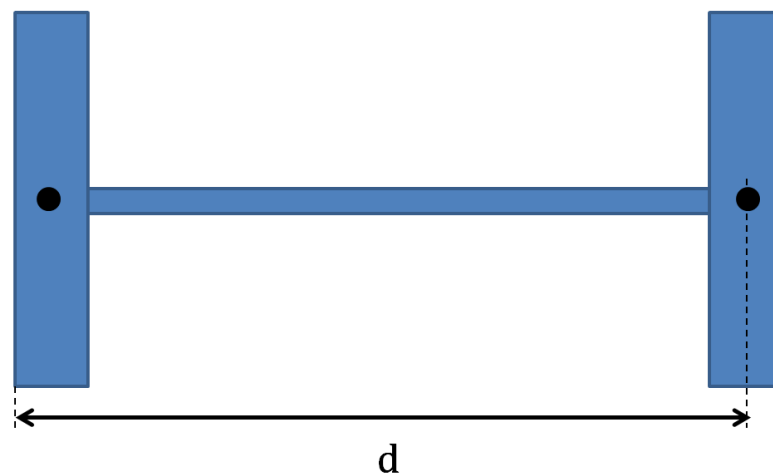


Figure 226: Schematic of cracked section model

$$d = l_{infill} + \frac{3}{2}l_{col} = 130in (330.2cm)$$

$$b_{min} = 2.5in(6.35cm)$$

$$b_{smeared} = \frac{t_{infill}l_{infill} + 2t_{col_masonry}l_{col}}{l_{infill} + 2l_{col}} = 18.14in(46.1cm)$$

$$V_{ultimate1} = f_{vn}b_{min}d = 25.22kip (112.2kN)$$

$$V_{ultimate2} = f_{vn}b_{smeared}d = 182.95kip (813.8kN)$$

Strut Model:

Transformed section to determine bounding column moment of inertia:

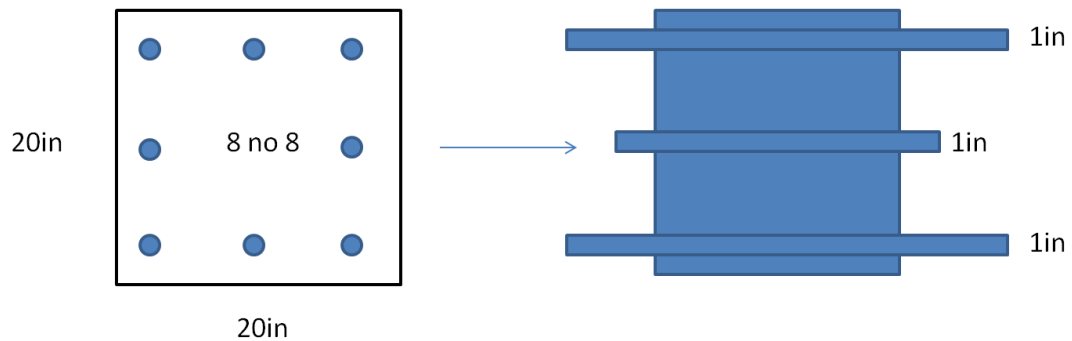


Figure 227: Transformed section of bounding column from test frames

Bottom and top reinforcement transformed area

$$A_1 = \frac{E_s}{E_c} 3A_{col_bar} + (l_{col}d_{col_bar} - 3A_{col_bar}) = 36.70in^2(236.8cm^2)$$

Middle reinforcement area

$$A_2 = \frac{E_s}{E_c} 2A_{col_bar} + (l_{col}d_{col_bar} - 2A_{col_bar}) = 31.13in^2(200.8cm^2)$$

$$cover = 1.5in(3.81cm)$$

$$d_{hoop} = 0.375in(0.95cm)$$

Calculate moment of inertias of respective sections

$$I_b = \frac{l_{col}(cover + d_{hoop})^3}{12} + l_{col}(cover + d_{hoop}) \left(\frac{l_{col}}{2} - \frac{cover + d_{hoop}}{2} \right)^2$$

$$= 3090.8in^4(128648.8cm^4)$$

$$I_{A1} = \frac{\frac{A_1}{d_{col_bar}} d_{col_bar}^3}{12} + A_1 \left(\frac{l_{col}}{2} - cover - d_{hoop} - \frac{d_{col_bar}}{2} \right)^2 =$$

$$2136.5in^4(88927.8cm^4)_{col}$$

$$I_{mid} = \frac{l_{col} \left(\frac{l_{col}}{2} - cover - d_{hoop} - \frac{3}{2}d_{col_bar} \right)^3}{12}$$

$$+ l_{col} \left(\frac{l_{col}}{2} - cover - d_{hoop} - \frac{3}{2}d_{col_bar} \right) \left(\frac{\left(\frac{l_{col}}{2} - cover - d_{hoop} - \frac{3}{2}d_{col_bar} \right)}{2} + \frac{d_{bar}}{2} \right)^2$$

$$= 2410.5in^4(100332.6cm^4)$$

$$I_{A2} = \frac{\frac{A_2}{d_{col_bar}} d_{col_bar}^3}{12} = 2.594in^4(108cm^4)$$

$$I_{bc} = 2(I_b + I_{A1} + I_{mid}) + I_{A2} = 15278.4in^4(635935cm^4)$$

$$E_{bc} = E_c = 3605000psi(24856MPa)$$

guess the width of the strut and strut angle

$$w_{guess} = 24in (60.96cm)$$

$$\theta_{guess} = 45^{\circ}$$

$$h = h_{infill} - \frac{w_{guess}}{2} \cos(\theta_{guess}) = 95.5in (242.6cm)$$

$$\theta_{strut} = \tan^{-1}\left(\frac{h}{l_{infill}}\right) = 42.46^{\circ}$$

guess θ_{strut} until $\theta_{guess} = \theta_{strut}$

$$w_{guess} = 24in (60.96cm)$$

$$\theta_{guess} = 42.45^{\circ}$$

$$h = h_{infill} - \frac{w_{guess}}{2} \cos(\theta_{guess}) = 95.5in (242.6cm)$$

$$\theta_{strut} = \tan^{-1}\left(\frac{h}{l_{infill}}\right) = 42.45^{\circ}$$

$$\lambda_{strut} = \sqrt[4]{\frac{E_m t_{infill} \sin(\theta_{strut})}{4E_{bc} I_{bc} h_{infill}}} = 0.017 \frac{1}{in} \left(0.007 \frac{1}{cm}\right)$$

$$w_{infill} = \frac{0.3}{\lambda_{strut} \cos(\theta_{strut})} = 23.76in (60.35cm)$$

Repeat process taking $w_{guess} = 23.76in (60.35cm)$

At end,

$$w_{infill} = \frac{0.3}{\lambda_{strut} \cos(\theta_{strut})} = 23.78in (60.4cm)$$

APPENDIX F

PROPOSED MODIFICATION OF THE TMS 402 STRUT MODEL

FOR PARTICIPATING INFILLS

The following section presents a draft of the proposed modification of the TMS 402 strut model incorporated into appendix B of the TMS 402 code. These changes have been proposed for Sections B.3.2, B.3.4, and B.3.5. If out-of-plane tests were conducted on partially grouted and reinforced infills with cast-in-place dowel connections, further suggestions could be made for Sections B.3.3 and B.3.6.

B.3.2 In-plane connection requirements for participating infills

Mechanical connections between the infill and the bounding frame shall be permitted.

B.3.2.1 If these connections do not transfer in-plane forces between the infill and the bounding frame, the participating infill may be designed using the procedure outlined in Sections B.3.4.1.1, B.3.4.2, and B.3.4.3.

B.3.2.2 If the infill is composed of concrete masonry units connected to the bounding frame with cast-in-place dowel reinforcement conforming to Sections B.3.2.2.1-B.3.2.2.5, the participating infill may be designed using the procedure outlined in Sections B.3.4.1.2, B.3.4.2, and B.3.4.3.

B.3.2.2.1 Infills are constructed of concrete masonry units which are partially grouted and reinforced. Reinforcement must comply with the size and lap splice requirements of Section 2.1.7 or Section 3.3.3.

B.3.2.2.2 Dowel reinforcement must be cast-in-place to the foundation or beam below the infill and the beam above the infill, such that there are connections on the top and bottom of the infill wall.

B.3.2.2.3 There must be at least 3 cast-in-place dowel connections to the bounding frame at the top and the bottom of the infill. The vertical cells adjacent to the reinforced concrete columns must be connected to the bounding top and bottom beams of the frame with cast-in-place dowel reinforcement.

B.3.2.2.4 All dowel reinforcement must extend from the bounding frame into a grouted cell with reinforcement.

B.3.2.2.5 All splices of the dowel reinforcement to the vertical reinforcement in the infill wall must comply with the requirements of Section 2.1.7 or Section 3.3.3.

B.3.4 Design of Participating Infills for In-Plane Forces

B.3.4.1 Unless the stiffness of the infill is obtained by a more comprehensive analysis, a participating infill shall be analyzed as an equivalent strut using either Section B.3.4.1.1 or B.3.4.1.2.

B.3.4.1.1 For unreinforced masonry infills without in-plane connections or in-plane connections complying with Section B.3.2.1, a participating infill shall be analyzed as an equivalent strut, capable of resisting compression only; whose width is calculated using Equation B-1; whose thickness is the specified thickness of the infill; and whose elastic modulus is the elastic modulus of the infill.

$$w_{inf} = \frac{0.3}{\lambda_{strut} \cos(\theta_{strut})} \quad (\text{Equation B-1})$$

where

$$\theta_{strut} = \tan^{-1} \left(\frac{h_{inf}}{l_{inf}} \right) \quad (\text{Equation B-2})$$

$$\lambda_{inf} = \sqrt[4]{\frac{E_m t_{net\ inf} \sin(2\theta_{strut})}{4E_{bc} I_{bc} h_{inf}}} \quad (\text{Equation B-3})$$

B.3.4.1.2 For partially grouted reinforced masonry infills with cast-in-place connections complying with Section B.3.2.2, a participating infill shall be analyzed as an equivalent strut, capable of resisting compression only; whose width is determined using the procedure below; whose thickness is equal to two face shell thicknesses; and whose elastic modulus is the elastic modulus of the ungrouted prism.

Iteratively determine the width of the compression strut and the angle of the strut subject to the following constraints:

$$w_{inf} = \frac{0.3}{\lambda_{strut} \cos(\theta_{strut})} \quad (\text{Equation B-4})$$

where

$$\theta_{strut} = \tan^{-1} \left(\frac{h_{inf} - (h_{node\ B} + h_{node\ T})}{l_{inf}} \right) \quad (\text{Equation B-5})$$

$$\lambda_{inf} = \sqrt[4]{\frac{E_m t_{net\ inf} \sin(2\theta_{strut})}{4E_{bc} I_{bc} h_{inf}}} \quad (\text{Equation B-6})$$

and

The bottom node of the compression strut attached to the column at the mid height of the dowel splice at the base of the masonry wall:

$$h_{node\ B} = \frac{l_{d\ dowel}}{2} \quad (\text{Equation B-7})$$

The top node of the compression strut must be attached to the column such that the bearing area for the strut begins at the top of the column:

$$h_{node T} = \frac{w_{inf}}{2} \cos \theta_{strut} \quad (\text{Equation B-8})$$

B.3.4.2 Design forces in equivalent struts as defined in Section B.3.4.1.1 or Section B.3.4.1.2, shall be determined from an elastic analysis of a braced frame including such equivalent struts.

B.3.5 Design of Frame Elements with Participating Infills for In-Plane Loads

B.3.5.1 Design each frame member not in contact with an infill for shear, moment, and axial force not less than the results from the equivalent strut frame analysis.

B.3.5.2 Design each bounding column in contact with an infill for shear and moment equal to not less than 1.1 times the results from the equivalent strut frame analysis, and for axial force not less than the results from that analysis. In addition, follow the applicable procedure of Sections B.3.5.2.1 or B.3.5.2.2.

B.3.5.2.1 For unreinforced masonry infills without in-plane connections or in-plane connections complying with Section B.3.2.1, augment the design shear at the end of the column by the horizontal component of the equivalent strut force acting on that end under design loads.

B.3.5.2.2 For partially grouted reinforced masonry infills with cast-in-place connections complying with Section B.3.2.2, treat the bounding columns as three separate members, a member above the top node of the compression strut, a member below the bottom node of the compression strut, and a member for the middle segment. Augment the design shear at the ends of the middle segment of the column by the horizontal component of the equivalent strut force acting on that end under design loads.

When prescribing the reinforcement for the column, treat the column as three separate members with their own close tie-spacing region l_0 such that close tie spacing is ensured on either side of the node where the compression strut is assumed to bear on the column.

B.3.5.3 Design each beam in contact with an infill for shear and moment equal to not less than 1.1 times the results from the equivalent strut frame analysis, and for axial force not less than the results from that analysis. In addition, augment the design shear at each end by the vertical component of the equivalent strut force acting on that end under design loads.

REFERENCES

- Abrams, D. (2011). *Hybrid Masonry Seismic Structural Systems*. Paper presented at the NEES and MCEER Quake Summit, Buffalo, NY.
- Abrams, D., Fahnestock, L., and Eidini, M. (2010). *Basic Mechanisms for Hybrid Masonry Structures*. Paper presented at the ASCE Structures Congress.
- Alaluf, R. et. al. (2011). The M 7.1 Ercis-Van, Turkey Earthquake of October 23, 2011 *EERI Special Earthquake Report*: Earthquake Engineering Research Institute.
- Alcocer, S., Klinger, R., Greene, M., Nathe, S., Austin, V., and Gilland, E. (2006). The Tecoman Mexico Earthquake January 21, 2003: EERI and SMIS.
- Amadei, B., Strure, S., and Saeb, S. (1989). An Evaluation of Masonry Joint Shear Strength in Existing Buildings. Report for the National Science Foundation. University of Colorado at Boulder. Boulder, CO.
- Angel, R., Abrams, D., Shapiro, D., Uzarski, J., and Webster, M. (1994). Behavior of Reinforced Concrete Frames with Masonry Infills. Report for the National Science Foundation. University of Illinois. Urbana-Champaign, IL.
- ASCE. (2000). *FEMA 356: Seismic Rehabilitation of Buildings*.
- ASCE. (2006). *ASCE 41-06 Seismic Rehabilitation of Existing Buildings*. Reston, VA.
- Atkinson, R., and Yan, G. (1990). A Statistical Study of Masonry Deformability, *Development of a Database for Compressive Stress-Strain Behavior of Masonry*. University of California Earthquake Engineering Research Center. Richmond, CA.
- Ayoub, A., and Filippou, F. (1998). Nonlinear Finite Element Analysis of RC Shear Panels and Walls. *Journal of Structural Engineering*, March, 298-308.
- Barzegar-Jamshidi, F., and Schnobrich, W. (1986). Nonlinear Finite Element Analysis of Reinforced Concrete under Short Term Monotonic Loading. University of Illinois. Urbana-Champaign, IL.
- Bayhan, B., and Gülkan, P. (2011). Buildings Subjected to Recurring Earthquakes: A Tale of Three Cities. *Earthquake Spectra*, 27(3), 635-659.
- Bazant, Z. P. (1984). Size Effect in Blunt Fracture: Concrete, Rock, Metal. *Journal of Engineering Mechanics*, 110, 518-535.
- Bazant, Z. P. (1986). Mechanics of Distributed Cracking. *Applied Mechanics Rev*, 39(5).

- Bazant, Z. P., and Becq-Giraudon, E. (2002). Statistical Prediction of Fracture Parameters of Concrete and Implications for Choice of Testing Standard. *Cement and Concrete Research*, 32, 529-556.
- Bazant, Z. P., and Cedolin, L. (1979). Blunt Crack Band Propagation in Finite Element Analysis. *Journal of the Engineering Mechanics Division*, 105(2), 297-315.
- Bazant, Z. P., and Cedolin, L. (1980). Effect of Finite Element Choice in Blunt Crack Band Analysis. *Computer Methods in Applied Mechanics and Engineering*, 24, 305-316.
- Bazant, Z. P., and Gambarova, P. (1984). Crack Shear in Concrete: Crack Band Microplane Model. *Journal of Engineering Mechanics*, 110, 2015-2035.
- Bazant, Z. P., and Oh, B. (1983). Crack Band Theory for Fracture of Concrete. *Materials and Structures*, 93(16), 155-177.
- Bazant, Z. P., and Pijaudier-Cabot, G. (1989). Measurement of Characteristic Length of Nonlocal Continuum. *Journal of Engineering Mechanics*, 115, 755-767.
- Bazant, Z. P., and Prat, P. (1988). Microplane Model for Brittle-Plastic Material Part I. *Journal of Engineering Mechanics*, 114, 1672-1702.
- Belytschko, T., Fish, J., and Engelmann, B. (1988). Finite Element with Embedded Localization Zones. *Computer Methods in Applied Mechanics and Engineering*, 70, 59-89.
- Bendimerad, F. (2004). *The 21 May 2003 Boumerdes Earthquake, Lessons Learned and Recommendations*. Paper presented at the 13th World Conference on Earthquake Engineering, Vancouver, B.C.
- Bennett, R., Flanagan, R., Adham, S., Fischer, W., and Tenbus. (1996). Evaluation and Analysis of the Performance of Masonry Infills During the Northridge Earthquake. Report for the National Science Foundation.
- Bhide, S., and Collins, M. (1989). Influence of Axial Tension on Shear Capacity of Reinforced Concrete Members. *Journal of Structural Engineering*, 86(5), 570-581.
- Biggs, D. (2007). *Hybrid Masonry Structures*. Paper presented at the 10th North American Masonry Conference, St. Lewis, MO.
- Birkeland, P., and Birkeland, H. (1966). Connections in Precast Concrete Construction. *ACI Journal*, 63(3), 345-368.
- Bocca, P. (1989). Fracture Mechanics of Brick Masonry: Size Effects and Snap-Back Analysis. *Materials and Structures*, 22, 364-373.

- Bolander, J., and Saito, S. (1998). Fracture Analyses using Spring Networks with Random Geometry. *Engineering Fracture Mechanics*, 61, 569-591.
- Borchelt, J. G. (1982). *Masonry, Materials, Properties, and Performance: A Symposium*. American Society for Testing and Materials.
- Brokken, S., and Bertero, V. (1981). Studies on Effects of Infills in Seismic Resistant RC Construction. Report for the National Science Foundation. University of California. Berkeley, CA.
- Brzev, S., Astroza, M., and Yadlin, M. (2010). Performance of Confined Masonry Buildings in the February 27, 2010 Chile Earthquake. Report for the Earthquake Engineering Research Institute.
- Buonopane, S., and White, R. (1999). Pseudodynamic Testing of Masonry Infilled Reinforced Concrete Frame. *Journal of Structural Engineering*, 578-589.
- Calvi, G., Bolognini, D., and Penna, A. (2004). *Seismic Performance of Masonry-Infilled R.C. Frames: Benefits of Slight Reinforcements*. Paper presented at the 6th Congresso Nacional de Sismologia e Engenharia. Sísmica, Italy.
- CEN. (2003). *Eurocode 8: Design of Structures for Earthquake Resistance*: European Committee for Standardization.
- Cervenka, J., and Papanikolaou, V. (2008). Three Dimensional Combined Fracture-Plastic Material Model for Concrete. *International Journal of Plasticity*, 24, 2192-2220.
- Cervera, M., Hinton, E., and Hassan, O. (1987). Nonlinear Analysis of Reinforced Concrete and Shell Structures using 20-Noded Isoparametric Brick Elements. *Computers and Structures*, 25(6), 845-869.
- Cheema, T., and Klingner, R. (1986). Compressive Strength of Concrete Masonry Prisms. *ACI Journal*, Jan.-Feb., 88-97.
- Chen, F. W. (2007). *Plasticity in Reinforced Concrete*: J Ross Publishing.
- Chen, W.-W., Yeh, Y.-K., Hwang, S.-J., Lu, C.-H., and Chen, C.-C. (2012). Out-of-Plane Seismic Behavior and CFRP Retrofitting of RC Frames Infilled with Brick Walls. *Engineering Structures*, 34, 213-224.
- Chung, W., and Ahmad, S. (1995). Analytical Model for Shear Critical Reinforced-Concrete Members. *Journal of Structural Engineering*, 121, 1023-1029.
- Cope, R., and Rao, P. (1981). Nonlinear Finite Element Strategies for Bridge Slabs. *Reports of the working commissions IABSE*, (pp. 273-288). Liverpool University. Liverpool, England.

- Cope, R., Rao, P., Clark, L., and Norris, P. (1980). Modeling of Reinforced Concrete Behavior for Finite Element Analysis of Bridge Slabs. *Numerical Methods for Nonlinear Problems* (pp. 457-470). Pineridge Press.
- Corte, G., Fiorino, L., and Mazzolani, F. (2008). Lateral-Loading Tests on a Real RC Building Including Masonry Panels with and without FRP Strengthening. *Journal of Materials in Civil Engineering*, 419-431.
- Cowan, H. (1953). The strength of Plain, Reinforced and Prestressed Concrete under the Action of Combined Stresses, with Particular Reference to the Combined Bending and Torsion of Rectangular Sections. *Magazine of Concrete Research*, 5, 75-86.
- Crisfield, M., and Wills, J. (1989). Analysis of RC Panels using Different Concrete Models. *Journal of Engineering Mechanics*, 115, 578-597.
- De Borst, R., and Nauta, P. (1985). Non-Orthogonal Cracks in a Smeared Finite Element Model. *Engineering Computations*, 2, 35-46.
- Desayi, P., and Krishnan, S. (1964). Equation for the Stress-Strain Curve of Concrete. *Journal of the American Concrete Institute*, 61, 345-350.
- DesRoches, R., Comerio, M., Eberhard, M., Mooney, W., and Rix, G. (2011). Overview of the 2010 Haiti Earthquake. *Earthquake Spectra*, 27(S1), 1-23.
- Drucker, D., and Prager, W. (1952). Soil Mechanics and Plastic Analysis for Limit Design. *Quarterly of Applied Mathematics*, 10(2), 157-165.
- Drysdale, R., Hamid, A., and Baker, L. (1994). *Masonry Structures Behavior and Design*. Prentice Hall. Eaglewood Cliffs, New Jersey.
- Eligehausen, G., Ozbolt, J., and Pampanin, S. (2009). 3D Analysis of Seismic Response of RC Beam-Column Exterior Joints Before and After Retrofit. *Concrete Repair, Rehabilitation and Retrofitting II*. Taylor and Francis Group. London.
- Ezzatfar, P., Binici, B., Kurc, O., Canbay, E., Sucuoğlu, H., and Özcebe, G. (2012). *Application of Mesh Reinforced Mortar for Performance Enhancement of Hollow Clay Tile Infill Walls*. Paper presented at the Advances in Civil Engineering Conference, Ankara, Turkey.
- Fiore, A., Netti, A., and Monaco, P. (2012). The Influence of Masonry Infill on the Seismic Behaviour of RC Frame Buildings. *Engineering Structures*, 44, 133-145.
- Flanagan, R., and Bennett, R. (1999). In-Plane Behavior of Structural Clay Tile Infilled Frames. *Journal of Structural Engineering*, 125, 590-599.
- Gallegos, H. (1994). Masonry in Peru. *Masonry in the Americas*, 307-331.

- Goodman, R. E., Taylor, R. L., and Brekke, T. L. (1968). A Model for the Mechanics of Jointed Rock. *Journal of Soil Mechanics and Foundation Div. ASCE*, 94(3), 637-659.
- Gopalaratnam, V., and Shah, S. (1985). Softening Response of Plain Concrete in Direct Tension. *ACI Journal May-June*, 310-323.
- Gostic, S., and Zarnic, R. (1999). *Cyclic Lateral Response of Masonry Infilled RC Frames and Confined Masonry Walls*. Paper presented at the 8th North American Masonry Conference, Austin, TX.
- Govindjee, S., and Hall, G. (1998). A Local Integration Method for Coupled Damage and Plasticity. Report for Earthquake Engineering Research Center. University of California, Berkeley.
- Guevara, L. T., and García, L. E. (2005). The Captive- and Short-Column Effects. *Earthquake Spectra*, 21(1), 141.
- Gupta, A., and Akbar, H. (1984). Cracking in Reinforced Concrete Analysis. *Journal of Structural Engineering*, 110(8), 1735-1746.
- Gylltoft, K. (1983). *Fracture Mechanics Models for Fatigue in Concrete Structures*. PhD dissertation, Lulea University of Technology, Lulea, Sweden.
- Hamid, A. (1978). *Behaviour Characteristics of Concrete Masonry*. PhD dissertation, McMaster University, Ontario, Canada.
- Hamid, A., Drysdale, R., and Heidebrecht, A. (1979). Shear Strength of Concrete Masonry Joints. *ACI Journal of the Structural Division*, 105(7), 1227-1240.
- Harries, K., Zeno, G., and Bahram, S. (2012). Toward an Improved Understanding of Shear-Friction Behavior. *ACI Structural Journal*, 109(6), 835-844.
- Hashemi, A., and Mosalam, K. M. (2006). Shake-Table Experiment on Reinforced Concrete Structure Containing Masonry Infill Wall. *Earthquake Engineering and Structural Dynamics*, 35(14), 1827-1852.
- Hegger, J., Sherif, A., and Wolfgang, R. (2004). Nonlinear Finite Element Analysis of Reinforced Concrete Beam-Column Connections. *ACI Structural Journal*, Sept-Oct, 604-614.
- Hillerborg, A. (1983). Concrete Fracture Energy Tests Performed by 9 Laboratories According to a Draft RILEM Recommendation. Report to RILEM. Lund. Sweden.
- Hsieh, S., Ting, C., and Chen, W. F. (1979). *An Elastic-Fracture Model for Concrete*. Paper presented at the 3rd Engineering Mechanics Division Special Conference, Austin, TX.

- Hybrid Masonry Design. (2009). Technology Brief. International Masonry Institute.
- Kahn, L., and Mitchell, A. (2002). Shear Friction Tests with High-Strength Concrete. *ACI Structural Journal*, 99(1), 98-103.
- Kakaletsis, D. (2009). Analytical Modeling of Masonry Infills with Openings. *Structural Engineering and Mechanics*, 31(4), 423-437.
- Kaufmann, W., and Marti, P. (1998). Structural Concrete: Cracked Membrane Model. *Journal of Structural Engineering*, 124, 1467-1475.
- Kaushik, H., Rai, D., and Jain, S. (2007). Stress-Strain Characteristics of Clay Brick Masonry under Uniaxial Compression. *Journal of Materials in Civil Engineering*, September, 728-739.
- Kawai, T. (1978). New Discrete Models and their Application to Seismic Response Analysis of Structures. *Nuclear Engineering and Design*, 48, 207-229.
- Kent, D., and Park, R. (1971). Flexural Members with Confined Concrete. *ACI Journal of the Structural Division*, 7, 1969-1990.
- Klingner, R. (1994). Review of Masonry Construction in the United States of America. *Masonry in the Americas*, 205-237.
- Klingner, R., and Bertero, V. (1976). Infilled Frames in Earthquake-Resistant Construction. Report for the Earthquake Engineering Research Center. University of California, Berkeley, CA.
- Kollegger, J., and Mehlhorn, G. (1990). Experimentelle Untersuchungen zur Bestimmung der Druckfestigkeit des gerissenen Stahlbetons bei einer Querkzugbeanspruchung. Deutscher Ausschuss für Stahlbeton. Berlin.
- Kupfer, H., Hilsdorf, H., and Rusch, H. (1969). Behavior of Concrete under Biaxial Stress. *ACI Journal*, 656-666.
- Kurt, E., Binici, B., Kurç, O., Canbay, E., and Özcebe, G. (2011). Seismic Performance of a Deficient Reinforced Concrete Test Frame with Infill Walls. *Earthquake Spectra*, 27(3), 817.
- Li, B., Tran, C., and Pan, T. (2009). Experimental and Numerical Investigations on the Seismic Behavior of Lightly Reinforced Concrete Beam-Column Joints. *Journal of Structural Engineering*, 135, 1007-1018.
- Li, B., Wang, Z., Mosalam, K., and Xie, H. (2008). *Wenchuan Earthquake Field Reconnaissance on Reinforced Concrete Framed Buildings with and without Masonry Infill Walls*. Paper presented at the 14th World Conference on Earthquake Engineering, Beijing, China.

- Li, B., Wu, Y., and Pan, T. (2003). Seismic Behavior of Non-Seismically Detailed Interior Beam-Wide Column Joints-Part II: Theoretical Comparisons and Analytical Studies. *ACI Structural Journal*, 100(1), 56-65.
- Lotfi, H., and Shing, B. (1991). Appraisal of Smeared Crack Models for Masonry Shear Wall Analysis. *Computers and Structures*, 41(3), 413-425.
- Lotfi, H., and Shing, B. (1994). Interface Model Applied to Fracture of Masonry Structures. *Journal of Structural Engineering*, 120(1), 63-80.
- Lourenco, P. B. (1996). *Computational Strategies for Masonry Structures*. PhD dissertation, Delft University, Delft, The Netherlands.
- Lynn, A., Moehle, J. P., Mahin, S. A., and Holmes, W. T. (1998). Seismic Evaluation of Existing Reinforced Concrete Building Columns. *Earthquake Spectra*, 12(4), 715-739.
- Madan, A., Reinhorn, A., Mander, J., and Valles, R. (1997). Modeling of Masonry Infill Panels for Structural Analysis. *Journal of Structural Engineering*, 123, 1295-1302.
- Magenes, G., and Calvi, G. (1992). *Cyclic Behaviour of Brick Masonry Walls*. Paper presented at the 10th World Conference on Earthquake Engineering, Madrid, Spain.
- Mahini, S. (2005). *Rehabilitation of Exterior RC Beam-Column Joints using CFRP Sheets*. PhD dissertation, University of Queensland, Australia.
- Manfredi, G., Verderame, G., and Lignola, G. (2008). *A FEM Model for the Evaluation of the Seismic Behavior of Internal Joints in Reinforced Concrete Frames*. Paper presented at the 14th World Conference on Earthquake Engineering, Beijing, China.
- Manzuri, T. (1995). *Nonlinear Finite Element Analysis and Experimental Evaluation of Retrofitting Techniques for Unreinforced Masonry Structures*. PhD dissertation, University of Colorado at Boulder. Boulder, CO.
- Mattock, A. (1974). Shear Transfer in Concrete having Reinforcement at an Angle to the Shear Plane. *Shear in Reinforced Concrete* (pp. 17-42). American Concrete Institute. Farmington Hills, MI.
- Mehrabi, A. (1994). *Performance of Masonry-Infilled RC Frames Under In-Plane Lateral Loads*. PhD dissertation, University of Colorado at Boulder. Boulder, CO.
- Mehrabi, A., and Shing, B. (1997). Finite Element Modeling of Masonry Infilled RC Frames. *Journal of Structural Engineering*, 123(5), 604-614.

- Mehrabi, A., Shing, B., Schuller, M., and Noland, J. (1994). Performance of Masonry Infilled RC Frames under In-Plane Lateral Loads *Structural Engineering and Structural Mechanics Research Series*: University of Colorado at Boulder. Boulder, CO.
- Mehrabi, A., Shing, B., Schuller, M., and Noland, J. (1996). Experimental Evaluation of Masonry Infilled RC Frames. *Journal of Structural Engineering*, March, 228-237.
- Meli, R. et. al. (2011). Seismic Design Guide for Low-Rise Confined Masonry Buildings. A Project of the World Housing Encyclopedia. Earthquake Engineering Research Institute.
- Minaie, E. (2009). *Behavior and Vulnerability of Reinforced Masonry Shear Walls*. PhD dissertation. Drexel University, Philadelphia, PA.
- Mitra, N. (2007). *An Analytical Study of Reinforced Concrete Beam-Column Joint Behavior under Seismic Loading*. PhD dissertation, University of Washington, Seattle, WA.
- Moghaddam, H., and Dowling, P. (1987). State of the Art in Infilled Frames. Report for ESEE. Imperial College of Science and Technology. London, England.
- Mohebkhah, A., Tasnimi, A., and Moghadam, H. (2007). A Modified Three Strut Model for Masonry-Infilled Steel Frames with Openings. *Journal of Seismology and Earthquake Engineering*, 9(1), 39-48.
- Mohr, O. (1900). Welche Umstände Bedingen die Elastizitätsgrcnze und den Bruch eines Materiales. *Zeitschrift des Vereines Deutscher Ingenieure*, 44, 1524-1530, 1572-1577.
- Mojsilovic, N., and Marti, P. (1997). Strength of Masonry Subjected to Combined Actions. *ACI Structural Journal*, 94(57), 633-641.
- Moroni, M., Astroza, M., and Acevedo, C. (2004). Performance and Seismic Vulnerability of Masonry Housing Types used in Chile. *Journal of Performance of Constructed Facilities*, 18(3), 173-179.
- Mosalam, K. (2005). *Shake Table Test on One-Story RC Structure with and without Masonry Infill*. Paper presented at the NATO International Workshop on Advances in Earthquake Engineering for Urban Risk Reduction, Istanbul, Turkey.
- MSJC. (2011). *TMS 402-11 Building Code Requirements and Specification for Masonry Structures*. The Masonry Society.
- Murty, C., and Jain, S. (2000). *Beneficial Influence of Masonry Infill Walls on Seismic Performance of RC Frame Buildings*. Paper presented at the 12th World Conference on Earthquake Engineering Auckland, New Zealand.

- NCMA. (2004). TEK 14-7A Allowable Stress Design of Concrete Masonry. National Concrete Masonry Association.
- Ngo, D., and Scordelis, A. C. (1967). Finite Element Analysis of Reinforced Concrete Beams. *Journal of American Concrete Institute*, 64(14), 152-163.
- Nilson, A. H. (1968). Nolinear Analysis of Reinforced Concrete by the Finite Element Method. *Journal of American Concrete Institute*, 65(9), 757-766.
- Nilsson, L., and Oldenburg, M. (1983). *Nonlinear Wave Propagation in Plastic Fracturing Materials--A Constitutive Modeling and Finite Element Analysis*. Paper presented at the IUTAM Symposium of Nonlinear Deformation Waves, Swansea.
- Nosho, K., Stanton, J., and MacRae, G. (1996). *Retrofit of Rectangular Reinforced Concrete Columns using Tonen Forca Tow Sheet Carban Fiber Wrapping*. Masters thesis, University of Washington, Seattle, WA.
- Oliver, J. (1989). A Consistent Characteristic Length for Smeared Cracking Models. *International Journal for Numerical Methods in Engineering*, 28, 461-474.
- Oluokun, F. (1991). Prediction of Concrete Tensile Strength from its Compressive Strength: Evaluations of Existing Relations for Normal Weight Concrete. *ACI Materials Journal*, 88(302-309).
- Ortiz, M., Leroy, Y., and Needleman, A. (1987). A Finite Element Method for Localized Failure Analysis. *Computer Methods in Applied Mechanics and Engineering*, 61, 189-214.
- Ottosen, N. (1977). Failure and Elasticity of Concrete. *Journal of Engineering Mechanics*, 103, 527-535.
- Ozbolt, J., and Bazant, Z. P. (1992). Microplane Model for Cyclic Triaxial Behavior of Concrete. *Journal of Engineering Mechanics*, 118(7), 1365-1386.
- Ozbolt, J., Li, Y., and Kozar, I. (2001). Microplane Model for Concrete with Relaxed Kinematic Constraint. *International Journal of Solids and Structures*, 38, 2683-2711.
- Papadrakakis, M., Papadopoulos, V., Georgioudakis, M., Hofstetter, G., and Feist, C. (2005). Reliability Analysis of a Plain Concrete Beam. IALAD Project Report. Austria.
- Perez-Gavilan, J., Flores, L., and Cruz, O. (2009). *Testing of Masonry Walls with Different lengths: Kinematics and Lateral Stiffness*. Paper presented at the XVII National Conference on Earthquake Engineering, Puebla, Mexico.

- Pieruszczak, S., and Moroz, Z. (1981). Finite Element Analysis of Strain Softening Materials. *International Journal for Numerical Methods in Engineering*, 17, 327-334.
- Puglisi, M., Uzcategui, M., and Flórez-López, J. (2009). Modeling of Masonry of Infilled Frames, Part I: The Plastic Concentrator. *Engineering Structures*, 31(1), 113-118.
- Rankine, W. (1857). On the Stability of Loose Earth (Vol. 147). Royal Society of London.
- Rashid, Y. (1968). Ultimate Strength analysis of Prestressed Concrete Pressure Vessels. *Nuclear Engineering and Design*, 7, 334-344.
- Redmond, L., Stroecker, R., and DesRoches, R. (2013). *Impact of Seismic Codes on Building Performance in the Caribbean*. Paper presented at the 4th International Conference on Computational Methods in Structural Dynamics and Earthquake Engineering, Kos, Greece.
- Redmond L., Stavridis A., and DesRoches R. (2014). Evaluation of Modeling Scheme for Unreinforced Masonry under Seismic Loading. *The Masonry Society Journal*, December.
- Reimann, H. (1965). Kritische Spannungszustände der Betons bei mehrachsiger. *Ausches Stahlbeton*, 175.
- Rice, J. R. (1968). *Mathematical Analysis in the Mechanics of Fracture* (Vol. 2). Academic Press. New York, N.Y.
- Rodrigues, H., Varum, H., and Costa, A. (2010). Simplified Macro-Model for Infill Masonry Panels. *Journal of Earthquake Engineering*, 14(3), 390-416.
- Rots, J. G., and Blaauwendraad, J. (1989). Crack Models for Concrete: Discrete or Smeared? Fixed, Multi-Directional or Rotating? *Heron*, 34(1), 1-59.
- Rots, J. G., Nauta, P., Kusters, G. M. A., and Blaauwendraad, J. (1985). Smeared Crack Approach and Fracture Localization in Concrete. *Heron*, 30(1), 1-48.
- San Bartolome, A., Bernardo, J., and Pena, M. (2010). *The Effect of Column Depth on Seismic Behavior of Confined Masonry Walls*. Paper presented at the Chilean Conference on Seismology and Earthquake Engineering, Valdivia-Santiago, Chile.
- Saouma, V., and Ingraffea, A. (1981). Fracture Mechanics Analysis of Discrete Cracking. Reports of the working commissions for IABSE (Vol. 34).
- Schlegel, R., and Rautenstrauch, K. (2004). *Failure Analysis of Masonry Shear Walls*. Paper presented at the 1st International UDEC/3DEC Symposium on Numerical Modeling of Discrete Materials in Geotechnical Engineering, Civil Engineering, and Earth Science, Bochum, Germany.

- Schneider, S., Zagers, B., and Abrams, D. (1998). Lateral Strength of Steel Frames with Masonry Infills having Large Openings. *Journal of Structural Engineering*, 124, 896-904.
- Schultz, A. (1994). Performance of Masonry structures in Extreme Lateral Loading eEvents. *Masonry in the Americas*, 85-125.
- Shapiro, D., Uzarski, J., Webster, M., Angel, R., and Abrams, D. (2004). Estimating Out-of-Plane Strength of Cracked Masonry Infills. Report for the National Science Foundation. SOH and Associates. San Francisco, CA.
- Spencer, B., and Shing, B. (2002). Stress Hybrid Embedded Crack Element for Analysis of Concrete Fracture. *American Concrete Institute Structural Journal*, 205, 323-345.
- Sritharan, S., Priestly, M., and Seible, F. (2000). Nonlinear Finite Element Analyses of Concrete Bridge Joint Systems Subjected to Seismic Actions. *Finite Elements in Analysis and Design*, 36, 215-233.
- Stafford-Smith, B. (1967). Methods for Predicting the Lateral Stiffness and Strength of Multi-Storey Infilled Frames. *Building Science*, 2, 247-257.
- Stavridis, A. (2009). *Analytical and Experimental Study of Seismic Performance of Reinforced Concrete Frames Infilled with Masonry Walls*. PhD dissertation. University of California, San Diego.
- Stavridis, A., Koutromanos, I., and Shing, B. (2012). Shake-Table Tests of a Three-Story Reinforced Concrete Frame with Masonry Infill Walls. *Earthquake Engineering and Structural Dynamics*, 41(6), 1089-1108.
- Stavridis, A., and Shing, B. (2010). Finite-Element Modeling of Nonlinear Behavior of Masonry-Infilled RC Frames. *Journal of Structural Engineering*, 136(3), 285-296.
- Stone, W., Yokel, F., Celebi, M., Hanks, T., and Leyendecker, E. (1985). Engineering Aspects of the September 19, 1985 Mexico Earthquake. *National Bureau of Standards Building Science Series 165*.
- Suidan, M., and Schnobrich, W. (1973). Finite Element Analysis of Reinforced Concrete. *ASCE Journal of the Structural Division*, 99, 2109-2122.
- Tajima, K., Mishima, T., and Shirai, N. (2004). *3-D Finite Element Cyclic Analysis of RC Beam/Column Joint using Special Bond Model*. Paper presented at the 13th World Conference on Earthquake Engineering, Vancouver, BC, Canada.
- Taylor, G. (1938). Plastic Strain in Metals. *Journal of the Institute of Metals*, 62, 307-324.

- Tena-Colunga, A., Juárez-Ángeles, A., and Salinas-Vallejo, V. H. (2009). Cyclic Behavior of Combined and Confined Masonry Walls. *Engineering Structures*, 31(1), 240-259.
- Teymur, P., Pala, S., and Yuksel, E. (2012). Retrofitting of Vulnerable Reinforced Concrete Frames with Wet-Mixed Shotcrete Panels. *Advances in Structural Engineering*, 15(1), 1-14.
- USGS. (2014). Earthquake Hazards Program, from earthquake.usgs.gov
- Uva, G., Raffaele, D., Porco, F., and Fiore, A. (2012). On the Role of Equivalent Strut Models in the Seismic Assessment of Infilled RC Buildings. *Engineering Structures*, 42, 83-94.
- Varela-Rivera, J. L., Navarrete-Macias, D., Fernandez-Baqueiro, L. E., and Moreno, E. I. (2011). Out-of-Plane Behaviour of Confined Masonry Walls. *Engineering Structures*, 33(5), 1734-1741.
- Vecchio, F. (2000). Disturbed Stress Field Model for Reinforced Concrete: Formulation. *Journal of Structural Engineering*, 126, 1070-1077.
- Vecchio, F., and Collins, M. (1986). The Modified Compression-Field Theory for Reinforced Concrete Elements Subjected to Shear. *ACI Journal*, 219-231.
- Walraven, J., and Reinhardt, H. (1981). Theory and Experiments on the Mechanical Behavior of Cracks in Plain and Reinforced Concrete. *Heron*, 26(1A), 1-68.
- William, K., and Warnke, E. (1974). Constitutive Model for the Triaxial Behaviour of Concrete. *IABSE reports of the working commissions* (Vol. 19).
- Xu, S., and Zhu, Y. (2007). Experiment Studies on Fracture Energy of Cement Paste and Mortar. *Key Engineering Materials*, 348-349, 169-172.
- Yoshimura, K., Kikuchi, K., Okamoto, T., and Sanchez, T. (1996). *Effect of Vertical and Horizontal Wall Reinforcement on Seismic Behavior of Confined Masonry Walls*. Paper presented at the 11th World Conference on Earthquake Engineering.
- Zarnic, R., and Tomazevic, M. (1988). *An Experimentally Obtained Method for the Evaluation of Behaviour of Masonry Infilled R/C frames*. Paper presented at the Ninth World Conference on Earthquake Engineering, Tokyo-Kyoto, Japan.